

UNIVERSITY OF OKLAHOMA
GRADUATE COLLEGE

DESIGN AND ANALYSIS OF ROVER WHEEL TESTBED

A DISSERTATION

SUBMITTED TO THE GRADUATE FACULTY

in partial fulfillment of the requirements for the

Degree of

DOCTOR OF PHILOSOPHY

By
DANIEL FLIPPO
Norman, Oklahoma
2009

DESIGN AND ANALYSIS OF ROVER WHEEL TESTBED

A DISSERTATION APPROVED FOR THE
SCHOOL OF AEROSPACE AND MECHANICAL ENGINEERING

BY

Dr. David Miller, Chair

Dr. Zahed Siddique

Dr. Takumi Hawa

Dr. Amy Cerato

Dr. Cengiz Altan

© Copyright by DANIEL FLIPPO 2009
All Rights Reserved.

*To my God who created me to learn about his creation... and to my parents, who
always built confidence even when it meant their worldly items got taken apart.*

Acknowledgements

I would like to thank my committee, especially Dr Miller, for their time in making this a reality. Also I could not have done this without my wife who has followed me in this and continues to support me, there is a reason God gave me you before he sent me to do this. To the University of Oklahoma I would like to say "so long and thanks for all the fish".

Contents

Acknowledgements	iv
List of Tables	ix
List of Figures	xiv
Abstract	xv
1 Introduction	1
1.1 Purgatory Dune	1
1.2 Is Wheel Design Important?	3
1.3 Increased Wheel Testing as a Solution	3
1.4 Single Wheel Testing as a Better Solution	4
1.5 Thesis	5
1.6 Overview of Dissertation	5
1.6.1 Chapter 2	5
1.6.2 Chapter 3	5
1.6.3 Chapter 4	5
1.6.4 Chapter 5	5
1.6.5 Chapter 6	6
1.6.6 Chapter 7	6
1.6.7 Chapter 8	6
1.6.8 Chapter 9	6
1.6.9 Chapter 10	6
1.6.10 Chapter 11	6
2 Literature Review	7
2.1 Introduction	7
2.2 Lunakhod	7
2.3 Lunar Rover Vehicle	10
2.4 Sojourner	12
2.5 SR2	13
2.6 Rovers and their wheels currently in use on Mars	13
2.7 Proposed Rover Designs	15
2.8 Current Test Beds	19
2.9 Summary	27
2.10 Conclusions	27

3	SWEET	28
3.1	Introduction	28
3.2	SWEET Design	28
3.2.1	Motion	29
3.2.2	Test leg	32
3.2.3	Electrical	34
3.2.4	Counterbalance	34
3.2.5	Force Torque Sensor	35
3.2.6	Z Drive Actuator	36
3.2.7	Programming	38
3.2.8	Turn Simulation	40
3.2.9	Force Assist	42
3.2.10	Testing Medium	44
3.2.11	Experiments	45
3.3	Calibration	46
3.3.1	Setup	47
3.3.2	Test Results	52
3.4	Differences with current and past test beds	56
4	Skid Steer Turning Prediction Theory	59
4.1	Introduction	59
4.2	Generalized Equations of Motion	59
4.3	Rover Equilibrium Turn	61
4.4	Turning Rate Targets	62
4.5	Wheel Kinetics	65
4.6	Increasing turning efficiency	66
4.6.1	Increasing Longitudinal Friction	66
4.6.2	Offsetting Lateral Friction	66
4.6.3	Decreasing Lateral Friction	68
4.6.4	Bow Wave Reduction	70
4.7	Further Observations of Data	75
4.7.1	Equilibrium Point Slope	75
4.7.2	Wheel Slip	76
4.8	Isotropic behavior	76
4.9	Prospective uses for skid steering turning rate prediction	76
4.9.1	ω vs Ω	77
4.9.2	Soil Characterization	77
4.10	Summary	79
5	Error Propagation	80
5.1	Introduction	80
5.2	Sensor Measurement Errors	80
5.3	SWEET Errors	81
5.4	SR2 Validation Test Errors	82
5.5	Combination of Errors	83

5.6	Summary	83
6	Blank and Omni Wheel Experiments	84
6.1	Introduction	84
6.2	Blank Wheel Tests	84
6.2.1	Test Set Up	84
6.2.2	Results	85
6.2.3	Auxiliary Blank Wheel Observations	88
6.3	Omni wheel tests	89
6.3.1	Test Set Up	89
6.3.2	Results	89
6.3.3	Auxiliary Omni wheel observations	92
6.4	Conclusions	93
7	Experiments with Non-Blank Wheels	94
7.1	Introduction	94
7.2	Test set up	94
7.3	Results	94
7.4	Auxiliary treaded wheel observations	95
7.4.1	Y Slip Rate	95
7.4.2	F_X shift due to tread	95
7.4.3	Reduction of bulldozing by higher ω	100
7.4.4	Equilibrium force intersection points	100
7.4.5	Isotropic observations	100
7.5	Conclusions	102
8	Skid Steer Experiments on Sand	103
8.1	Introduction	103
8.2	Test set up	103
8.3	Test Results	105
8.4	Auxiliary treaded wheel observations	114
8.4.1	Y Slip Rate	114
8.4.2	F_X shift due to tread	115
8.4.3	Reduction of bulldozing by higher ω	115
8.4.4	Equilibrium force intersection points	115
8.5	Conclusions	115
9	Paint or no paint experiment	117
9.1	Introduction	117
9.2	Test Set Up	117
9.3	Results	120
9.4	Conclusions	120

10 Power Prediction with Single Wheel Testing	124
10.1 Introduction	124
10.2 Test Set Up	124
10.3 Results	124
10.4 Power Usage Observations for the Four Wheels Tested	124
10.5 Conclusions	124
11 Observations and Conclusions	127
11.1 Introduction	127
11.2 Validation of single wheel testing	127
11.3 Drag Testing	128
11.4 Validation of SWEET as an Effective Test Bed	128
11.5 Limits of SWEET	131
11.6 Future Improvements of SWEET	131
11.7 Limits of What can be Learned from Single Wheel Testing	131
11.8 Overview of wheel test results	133
11.9 Future work	133
Bibliography	136
A Appendices	142
A.0.1 NI boxes specs	142
A.0.2 DC Motor specs	146
A.0.3 HEDS Optical Encoder	147
A.0.4 HIP4081A H Bridge Driver	148
A.0.5 Main SWEET Schematic	150
A.0.6 H bridge	151
A.0.7 INA126 Instrumental Amplifier	152
A.0.8 Current Sense	153
A.0.9 Motor Torque Sensor	154
A.0.10 FT sensor	155
A.0.11 Post Processor Code	158
A.0.12 Test Procedure Populator Code	162
A.0.13 Numerical Iteration Program Code	163
A.0.14 Parallax Stamp Code for Servo and Light Control	166
A.0.15 Example Test Procedure Files Used	167
A.0.16 Design Equations for SWEET	171

List of Tables

2.1	MER rover problems and events	15
3.1	Test Procedure Turning Sample	40
3.2	Test Result File Sample	40
3.3	Test Description	46
3.4	Applicable Test Apparatus Comparison	57
5.1	Possible errors with validation tests on the SR2 rover	83
6.1	Calculated uncertainties for blank wheels in $\frac{rad}{sec}$	85
6.2	Ω_{SR2} and $\Omega_{SWEETPredicted}$ results for blank wheels in $\frac{rad}{sec}$	88
6.3	Calculated uncertainties for Omni wheels in $\frac{rad}{sec}$	89
6.4	Ω_{SR2} and $\Omega_{SWEETPredicted}$ results for Omni wheels in $\frac{rad}{sec}$	90
7.1	Calculated uncertainties for treaded wheels in $\frac{rad}{sec}$	95
7.2	Ω_{SR2} and $\Omega_{SWEETPREDICTED}$ results for treaded wheels @ $.3 \frac{rad}{sec}$ on carpet	96
8.1	Play sand Characteristics Calculated from Scion Image [10]	104
8.2	Ω_{SR2} and $\Omega_{SWEETPredicted}$ results for treaded wheels @ $.3 \frac{rad}{sec}$	114
8.3	Calculated uncertainties for wheels in sand in $\frac{rad}{sec}$	115
9.1	Wheel Performance in Sand in Dragging Test	120
11.1	Results for all single wheel tests	127

List of Figures

1.1	Waterfall design process	2
1.2	Iterative design process	3
1.3	SCARAB rover vehicle [68]	4
2.1	Lunokhod I	7
2.2	Lunokhod wheel (Picture taken at exhibit in the Kansas Cosmosphere)	8
2.3	Skid Steer Method used by Lunokhod	8
2.4	Lunar Roving Vehicle [6]	10
2.5	LRV Ackerman Geometry [50]	10
2.6	LRV Wheel in Testing Apparatus [71]	11
2.7	Sojourner Rover <i>image by NASA</i>	12
2.8	University of Oklahoma’s SR2 [60]	13
2.9	Mars Exploration Rover <i>image by NASA</i>	14
2.10	MER Rover Wheels <i>image by NASA</i>	14
2.11	Wheels from Sojourner (left) MER (center) and MSL (right) <i>image by NASA</i>	15
2.12	Mars Science Laboratory <i>image by NASA</i>	16
2.13	Rocker Bogie Zero Radius Steering Method	17
2.14	NASA Athlete <i>image by NASA</i>	18
2.15	NASA Truck <i>image by NASA</i>	18
2.16	NASA Lunar Electric Vehicle <i>image by NASA</i>	19
2.17	Lunar Rover Vehicle Wheel in Testing Apparatus [71]	20
2.18	LRV Low Gravity Test Bed Inside [53]	20
2.19	LRV Low Gravity Test Bed Outside [53]	21
2.20	GM Testbed for LRV Wheel [71]	21
2.21	GM Testbed for LRV Wheel [71]	22
2.22	Variable Terrain Tilt Platform (VTTP) <i>image by NASA</i>	22
2.23	MIT Single Wheel Test Bed [19]	23
2.24	Tohoku University Single Wheel Test Apparatus Drawing [40]	24
2.25	Tohoku University Single Wheel Test Apparatus [40]	24
2.26	RCET Single-Wheel Testbed at DLR [65]	25
2.27	Japanese Consortium Testing Apparatus [38]	26
2.28	STL Radial Fatigue Test Apparatus [66]	27
3.1	Testbed	29
3.2	Motor Configuration	30
3.3	Omniwheel Specifications [43]	30
3.4	A Swedish wheel and its parameters [64]	31
3.5	Test leg	33

3.6	Control box	33
3.7	Counterbalance	35
3.8	Force torque sensor device	36
3.9	Z Drive Actuator	37
3.10	Z Drive Actuator Front	37
3.11	Labview Interface PID Control	38
3.12	Labview Interface FT Sensor Readings	38
3.13	Labview Interface Motion and Wattage Results	39
3.14	Force Feedback axis and Force Vector	39
3.15	Turning Geometry	41
3.16	Discontinuous Obstacle Situation	43
3.17	F_y behavior in a Force Assisted test	43
3.18	Turning Bin	44
3.19	Slope Bin	45
3.20	Labview Calibration VI	47
3.21	Setup for F_X calibration	48
3.22	Setup for F_Y calibration	48
3.23	Setup for F_Z calibration	49
3.24	Moment about Y Calibration	50
3.25	Moment about X Calibration	50
3.26	Gain adjusting	51
3.27	Motor Torque Sensor Calibration	52
3.28	F_X Results	53
3.29	F_Y Results	53
3.30	F_Z Results	54
3.31	M_X Results	54
3.32	M_Y Results	55
3.33	M_Z Results	55
3.34	M_τ Results	56
3.35	Tohoku University Steering Test	58
4.1	Skid Steer Force Body Diagram	60
4.2	Rover Coordinate Axis	62
4.3	Skid Steer Kinematics	63
4.4	a) Slender Skid Steer Rover b) Ackerman Skid Steer Rover	64
4.5	Force vs Spin Rate Example	65
4.6	Ω -Force graph offset illustration	67
4.7	Kinematic explanation of treaded wheel	67
4.8	Measuring α on a treaded wheel	68
4.9	Fx Reduction Example	69
4.10	Chrysler Marsh Screw Amphibian [2]	69
4.11	Omni Wheel [43]	70
4.12	Rowe and Hegedus's study on wakes of different shaped wheels [63]	71
4.13	Rowe and Hegedus's Wheel Wake Experiment [63]	72

4.14	Three cases of wheel to soil interaction: (a) Rolling wheel (b) Towed locked wheel (c) 100% skid wheel	73
4.15	Illustration of side bow wave on a wheel in a skid steer turn	74
4.16	SR2 chamfered wheel with side mounted grousers	74
4.17	Illustration of Equilibrium Point Slope for two different ω rates	75
4.18	Magnitude vs Power	76
4.19	Terrain characterization from measured power and ω variables	78
4.20	Terrain characterization from measured values, ω and Ω	79
5.1	Ω force graph with error bars	81
6.1	a) SR2 rover with blank test wheels	85
6.2	Black Blank Test Wheel Dimensions in mm	86
6.3	Results for $\omega = .3 \frac{rad}{sec}$	86
6.4	Results for $\omega = .4 \frac{rad}{sec}$	87
6.5	Results for $\omega = .5 \frac{rad}{sec}$	87
6.6	Combination of wheel rates for blank wheel on carpet	88
6.7	Omni wheel test wheel dimensions in mm [43]	90
6.8	Omni-wheel mounted on SWEET	90
6.9	Results for Omni wheel spinning at $.3 \frac{rad}{sec}$	91
6.10	Results for Omni wheel spinning at $.5 \frac{rad}{sec}$	91
6.11	Combination of graphs for Omni Wheel	92
7.1	Unpadded test carpet surface	95
7.2	Padded test carpet surface with 5 lb weight	96
7.3	Correctly orientated wheel on carpet	97
7.4	Results for correctly orientated treaded wheel rotating at $\omega = .3 \frac{rad}{sec}$ on unpadded carpet	98
7.5	Results for oppositely orientated treaded wheel rotating at $\omega = .3 \frac{rad}{sec}$ on unpadded carpet	98
7.6	Treaded Wheel Dimensions	99
7.7	Results for correct treaded wheel rotating at $\omega = .3 \frac{rad}{sec}$ on padded carpet	99
7.8	Results for opposite treaded wheel rotating at $\omega = .3 \frac{rad}{sec}$ on padded carpet	100
7.9	Combination of wheel rates for the correctly orientated wheel on carpet	101
7.10	Combination of wheel rates for the oppositely orientated wheel on carpet	101
8.1	Sand Grain Size Sifting Results	103
8.2	Example Magnified Image of Sand Used in Experiment	104
8.3	Wheels tested in Sand: (a) Opposite Painted (b) Correct Painted (c) Opposite Plastic (not tested) (d) Blank (e) Correct Plastic	104
8.4	Results of Blank wheel on sand at $\omega = .3 \frac{rad}{sec}$	105
8.5	Results of Blank wheel on sand at $\omega = .4 \frac{rad}{sec}$	106
8.6	Results of Blank wheel on sand at $\omega = .5 \frac{rad}{sec}$	106
8.7	Combination of Blank Wheel results in sand	107
8.8	Results of Oppositely Oriented Painted wheel on sand at $\omega = .3 \frac{rad}{sec}$	107

8.9	Results of Oppositely Oriented Painted wheel on sand at $\omega = .35 \frac{rad}{sec}$	108
8.10	Results of Oppositely Oriented Painted wheel on sand at $\omega = .4 \frac{rad}{sec}$	108
8.11	Results of Oppositely Oriented Painted wheel on sand at $\omega = .5 \frac{rad}{sec}$	109
8.12	Combination of Oppositely Orientated Painted wheel in sand	109
8.13	Results of Correctly Oriented Painted wheel on sand at $\omega = .3 \frac{rad}{sec}$	110
8.14	Results of Correctly Oriented Painted Wheel on Sand at $\omega = .4 \frac{rad}{sec}$	110
8.15	Results of Correctly Oriented Painted wheel on sand at $\omega = .5 \frac{rad}{sec}$	111
8.16	Combination of all Correctly Orientated Painted Wheel tests	111
8.17	Results of Correctly Oriented Plastic wheel on sand at $\omega = .3 \frac{rad}{sec}$	112
8.18	Results of Correctly Oriented Plastic wheel on sand at $\omega = .4 \frac{rad}{sec}$	112
8.19	Results of Correctly Oriented Plastic wheel on sand at $\omega = .5 \frac{rad}{sec}$	113
8.20	Composite of all Correctly Orientated Plastic Wheel tests	113
8.21	Force graph for Painted wheel in sand at $\Omega = 0$	114
9.1	<i>Metal rover wheels, right bare wheel used on SR2 rover [61]. Left wheel is painted with Herculiner [39] high friction paint.</i>	118
9.2	Painted wheel mounted on SWEET in static friction test on paving stone	118
9.3	Painted wheel mounted on SWEET in static friction test on sand	119
9.4	Painted wheel mounted on SWEET pulling load in sand	119
9.5	Longitudinal force generated by actuated wheel in Sand	121
9.6	Longitudinal force generated by actuated wheel on rock	121
9.7	Sinkage comparison of painted and bare wheels on sand	122
9.8	Power comparison of painted and bare wheels on sand	122
9.9	Power comparison of painted and bare wheels on rock	123
9.10	Power comparison of painted and bare wheels dragging 17 Newtons on sand	123
10.1	Linear comparison between measured power from SWEET single wheel test and SR2 actual.	125
10.2	Ω per Unit Power for all wheels tested	125
10.3	Results for power usage of each wheel	126
11.1	Total results of wheel as a percent of Target values	129
11.2	Efficiency of wheels as Ω per unit Power	129
11.3	Percentage of Slip on Carpet	130
11.4	Percentage of Slip on Sand	130
11.5	Proposed SWEET Electrical System	132
11.6	Example of SR2 in non-continuous Terrain	133
11.7	Ω vs ω	134
A.1	National Instruments 6020E DAQ	142
A.2	National Instruments 6020E DAQ	143
A.3	National Instruments 6602 DAQ	144
A.4	National Instruments 6602 DAQ	145
A.5	Groschopp 55018 DC Motor	146
A.6	HEDS Optical Encoder	147

A.7	HIP4080	148
A.8	Main SWEET Schematic	150
A.9	H Bridge Schematic. Adapted from A.9	151
A.10	INA126 Amplifier	152
A.11	Current Sense Schematic	153
A.12	Motor Mount Torque Sensor and Amplifier Circuit	154
A.13	Force Torque Sensor Schematic [33]	155
A.14	Exaggerated stress of FT sensor along X axis	156

Abstract

Wheel performance has been one of the limiting factors in interplanetary rover missions. Because the rigors of space restrict use of conventional tire materials, rover wheels suffer from lack of traction, high risk of snagging, and little or no compliance, which limits the rover's ability to explore and traverse discontinuous terrain. What is worse is that these limitations go unresolved by the current lack of testing. The concept that wheel utilization and design are enhanced by testing is not new. The Apollo program enjoyed substantial testing of the Lunar Rover Vehicle's wheel but at a tremendous cost in time and money, which is probably the reason for its current low priority. Single wheel testing is a solution to this problem because it can cheaply provide data for a full rover assembly's performance. This paper details these problems and provides solutions to several road blocks of using single wheel testing as a substitute for full rover testing. The Suspension and Wheel Experimentation and Evaluation Testbed (S.W.E.E.T), which is specifically designed to test single wheels in situations previously neglected, will enable engineers to iteratively improve wheel design and to develop more accurate and encompassing mission contingency strategies without the cost and time of full rover testing.

CHAPTER 1

Introduction

1.1 Purgatory Dune

"A note to all you Opportunity fans: Get used to the current scenery, because we're going to be here awhile," [24]

Steve Squyres, lead scientist on the Mars Exploration Rover (MER) effort at Cornell University, said these words on April 26, 2005 after assessing the current situation of the Mars rover Opportunity. The rover had just rolled into a 10-centimetre-high sand dune ominously named "Purgatory Dune" and became mired up to its axles on all 6 wheels. Opportunity stayed in its rut for more than a week as engineers and scientists ran tests on Earth to determine the best strategy to free the mired rover. By implementing the newly tested strategies, the rover only inched out over a four week narrow escape.

Opportunity is one of two Mars rovers that have started their fifth year of exploration on the red planet. Their mission is to take pictures and analyze Martian terrain for any signs of water. These two rovers, Opportunity and Spirit, have vastly exceeded NASA's original expectation of a 90 day mission and have done well reaching their scientific goals, but why did Opportunity get stuck in a 10 centimeter sand drift when other drifts, of the same size, had caused no problems? The consistency of the sand turned out to be the culprit. After scrutinizing video of the sand trap and testing in similar conditions at the Jet Propulsion Laboratory, engineers were able to recreate the same wheel behavior that created the predicament and repeated the event with the same mired results. Steve Squyres stated,

"We're going to take lots of pictures of all the terrain around the vehicle, to get a very complete picture of the situation. We're going to do lots of testing with the rovers that we have on the ground to simulate the situation on Mars. This testing will be aimed not just at finding a plan that will work, but at finding the very best plan that will work" [24]

The problem, it turns out, was that the sand clung to the wheels, which is termed "stacking" or "caking" and basically diminished their traction to the point they were merely spinning and sinking [31, 24, 48, 9]. Spirit, the other MER rover, has had its own trials and at the time of this paper, has been embedded for almost five months in a location named Troy. Like with Opportunity, Earth tests have been ongoing since Spirit stopped progressing so that NASA engineers can invent and test new escape methods. The terrain is very similar to Purgatory Dune's in which the wheels become caked with soil and lose their traction [4], but Spirit has a lame wheel handicap, an

underbelly rock causing high centering, and is positioned in such a way that causes the rover to slip more into the pit with every action.

NASA has employed two different rovers for Earth testing dubbed SSTB (surface system test bed). One of these rovers is the same mass as Spirit or Opportunity while the other is a slimmed down version (no solar panel or batteries) to try to mimic MER's weight on Mars. According to John Callas, the MER project manager, they use the larger massed rover more for testing even though the tests are less realistic because the scaled down version does not work as well [55]. NASA also incorporates a simple "shoebox" test to do preliminary tests on single wheels. This seemingly problematic test is composed of a shoe box filled with simulant and placed under a fully assembled rover's wheel [55]. Some research points out that NASA's simulant might not be adequate for the Mars silt that is causing so much grief for Spirit and Opportunity [57].

The testing performed, on the MER rover wheels before launching the mission to Mars, consisted of driving the rover around in the Mars yard at JPL for a photo shoot and to discern if there were any large mobility problems. NASA uses the waterfall design approach (fig 1.1) which does not incorporate any intensive wheel design, and by the time that NASA tests its wheels they are on the full rover assembly which is too late for iterative wheel design enhancements. If a design change is needed either the specifications are rewritten or Congress may get involved [21]. With a low priority for wheel to soil interaction enhancements MER's wheel designer's main design concern was to design a wheel that would not catch on the lander's air bags in the event they did not deflate properly [55]. Had there been more adequate testing on the rovers, contingency strategies for problems, such as purgatory dune or Spirit's current dilemma could have been in place before the mission started. Every situation cannot be foreseen, however planning, having strategies in place, and extensive testing [49] will always be prudent.

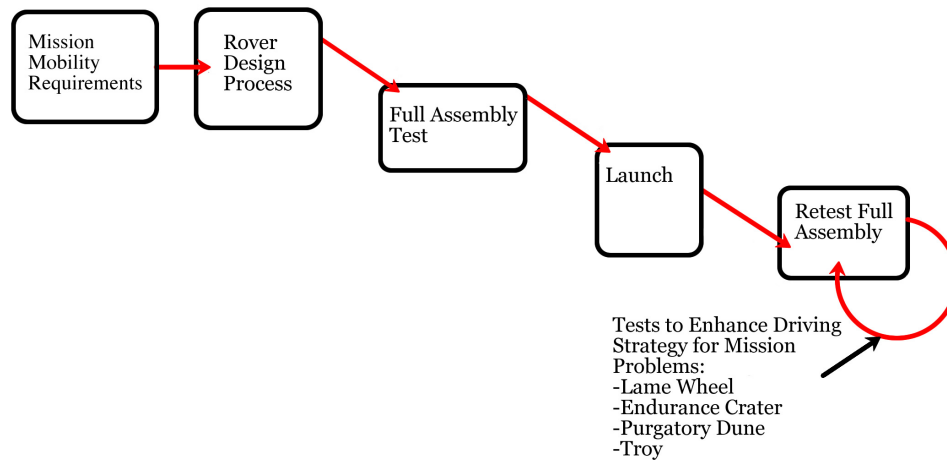


Figure 1.1: Waterfall design process

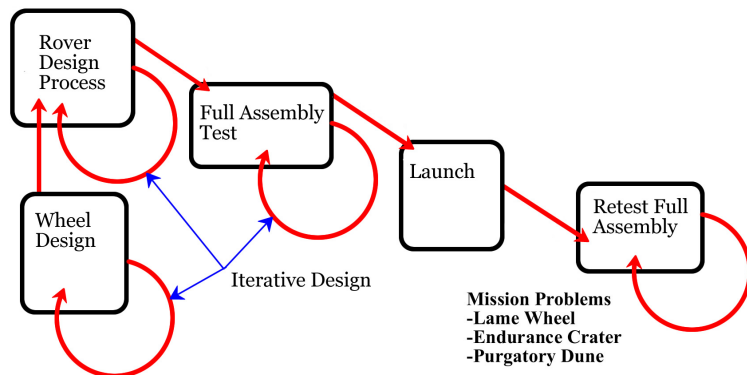


Figure 1.2: Iterative design process

1.2 Is Wheel Design Important?

"The most significant effect on traction has resulted in wheel design. Experiments involving different traction surfaces, wheel diameter and ground pressures have shown a large range of drawbar pull values. Differences of 50% have been achievable through traction surface/grouser modifications. Lowering ground pressure and reducing sinkage has moderate effects on traction but results in large differences in driving power (up to 50% during experiments). Drawbar pull tests performed as lab and field experiments have highlighted wheel design as a leading element in tractive and power design requirements. This is important because wheel design is generally independent of the suspension design and can be optimized for traction and power efficiencies." [68]

This quote is from research done by Wettergreen et al. 2009 on a full rover assembly. Other research [38, 17, 49] states as well that wheel design, even wheel tread or grouser design, is an important part of a rover's performance. This priority for wheel design is, sadly, not shared by NASA at the moment, and is in contrast to the Apollo program.

1.3 Increased Wheel Testing as a Solution

Interestingly, the little research that has been done in the area of interplanetary wheel tread and wheel design has not made it to the current rovers in use or slated for missions. As NASA and other agencies expand their endeavors to other worlds, and establish a presence on Mars and again on the Moon, they must close in the gaps on current testing to improve rover performance. To do this new test beds that will extract data for design improvement and strategy planning, will need to be

implemented. Closing the gaps in current rover wheel testing will enable scientists and engineers to design new wheels and plan strategies that will enhance rover wheel performance. The added testing does add cost and time to an already over budget and over scheduled process. NASA with its current methodology cannot afford to do iterative design on wheels even if it was a priority, which is why wheels are only tested in very few rover situations at a full rover assembly level. In this limited testing method, there is no clear direction what needs to be changed in order to improve aspects of the performance, and the benefits of iterative design are harder to realize.

1.4 Single Wheel Testing as a Better Solution

If NASA, or any agency designing a rover, had the capability to iteratively design their rover wheels separate from the rest of the rover systems the rover performance would be enhanced and the wheels could be designed to fit specific missions without the cost or hassle of fully assembled tests. Exclusively testing one wheel can be a simpler process and allow more detailed analysis in more situations and terrain types. If performance in a particular soil type is found lacking, the ease of single wheel testing allows different modifications to the wheel or suspension to be tried then evaluated to see if those changes improve. Full rover testing can glean valuable performance data such as in figure 1.3 which shows the Scarab rover towing a weighted sled to measure wheel performance [68]. This type of full rover evaluation test can be valuable but would be impractical to use in an iterative design process for the wheel. Single wheel testing would supply the same data in a much cheaper and timelier manner. Once wheels have been selected that perform well in single wheel test then more expensive system level testing could be done for final verification.

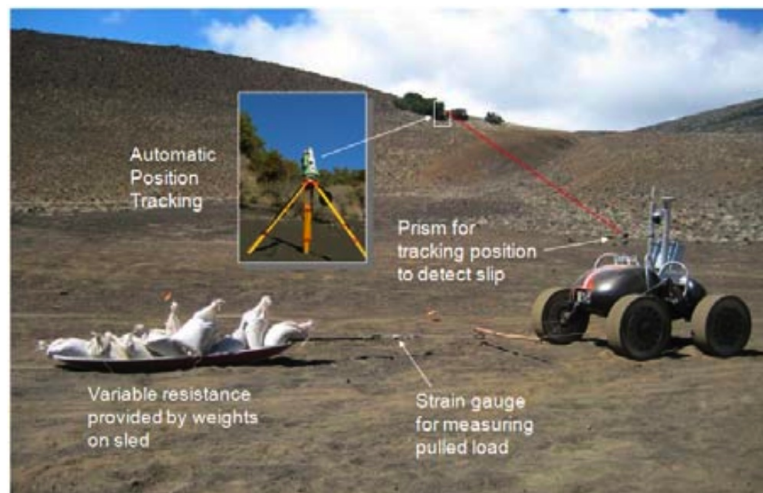


Figure 1.3: SCARAB rover vehicle [68]

1.5 Thesis

Single Wheel testing allows for low cost iterative improvement in wheel performance as well as preliminary evaluation of a rover in a new soil or terrain situation. This low cost evaluation will improve wheel performance and further understanding in wheel to soil interaction by allowing more practical extensive testing. All of which will contribute to overall rover performance. The work presented below is broken into three main topics and will show that single wheel testing is very feasible and is an accurate prediction of mobility performance at the system level. The first topic is covered in chapters 1 and 2 and details the background and problem. Chapter 3 covers the second topic of the test bed proposed in SWEET while the rest of the chapters discuss the mapping of the data from SWEET to real life rover prediction and the experiments done to validate it.

1.6 Overview of Dissertation

1.6.1 Chapter 2

Chapter 2 will review the history and progress of rover design, application, and testing and will cover different programs starting with the Russian Lunokhod rover, the Apollo program, and up to current concepts being looked at by NASA.

1.6.2 Chapter 3

Chapter 3 will unveil SWEET and explain its design specifications, function, as well as its sensor calibration. In this chapter SWEET is also compared to other tests beds currently being used.

1.6.3 Chapter 4

Chapter 4 explains the process of mapping the measured values of SWEET into performance values of a full assembly rover for a skid steer turn, as well as exploring different methods to enhance skid steer rover's turning efficiency. These qualities will be looked at in later chapters on several different wheels.

1.6.4 Chapter 5

Chapter 5 discusses the possible errors of the single wheel skid steer tests as well as their propagation through the system. With all instruments there are uncertainties inherent in the design and fabrication and SWEET is no exception. Also the validation tests are looked at for their possible uncertainties all of which propagated together give a practical range of error for the system.

1.6.5 Chapter 6

Chapter 6 begins the results for single wheel tests and evaluates a blank wheel to serve as a control group to compare other wheels to. Another wheel looked at in this chapter is the Omni wheel which is a wheel with orthogonal wheels around its circumference, both wheels are tests on padded and unpadded carpet.

1.6.6 Chapter 7

Chapter 7 expands testing with treaded wheels and compares their results. Treaded wheels, specifically directionally treaded wheels are tested on carpet and evaluated in both directions to observe their behavior in a skid steer turn.

1.6.7 Chapter 8

Chapter 8 evaluates four wheels in skid steer turns on sand. Sand is a very non cohesive soil that slows down a skid steer turn, several avenues are explored slightly to improve this consequence.

1.6.8 Chapter 9

Chapter 9 details a different experiment on sand that involves coated and non coated metal wheels. To better illustrate the iterative design ease to which a wheel can be enhanced an experiment was done to compare a change in a wheel to its original design. In this case a high friction paint was added to the wheel which did change its behavior.

1.6.9 Chapter 10

Chapter 10 discusses SWEET's ability to predict the power usage of a rover by single wheel testing. Power is very important to a rover on a different planet so any improvement in the wheel's power usage would be a vast improvement in the rover performance.

1.6.10 Chapter 11

Chapter 11 concludes the dissertation as well as details out future work, limitations, and proposed SWEET improvements.

CHAPTER 2

Literature Review

2.1 Introduction

To better appreciate and understand the work described in this paper a background of past rovers and wheel test beds are presented. Conclusions important to this thesis are drawn from current and historical work presented here.

2.2 Lunakhod

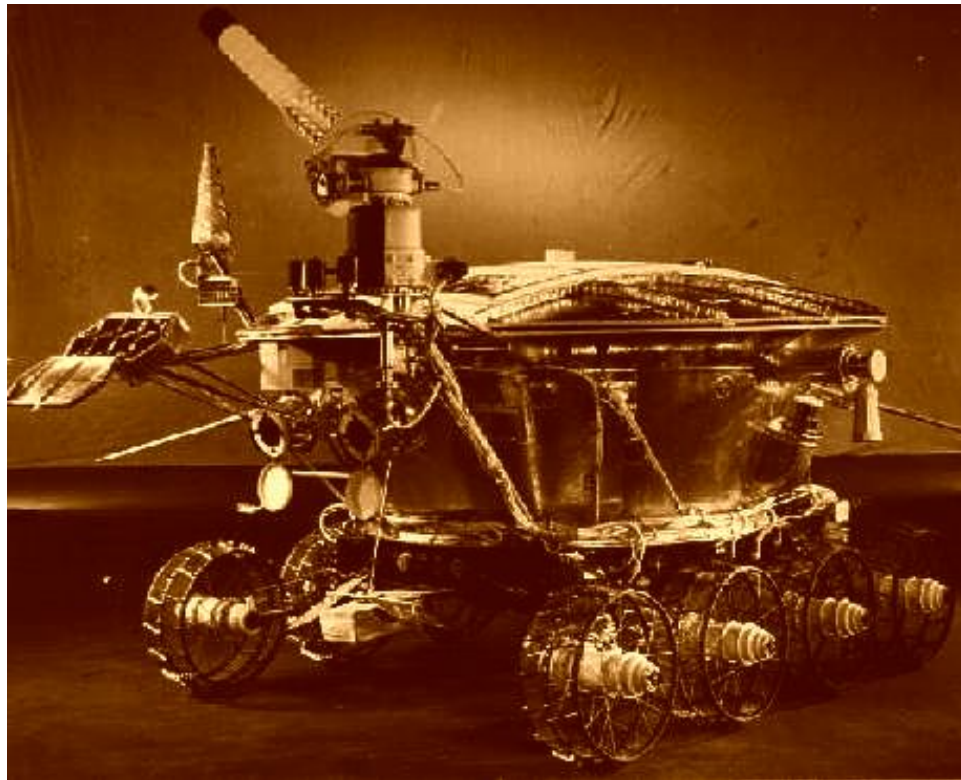


Figure 2.1: Lunokhod I
Lunokhod (image reproduced from NASA)

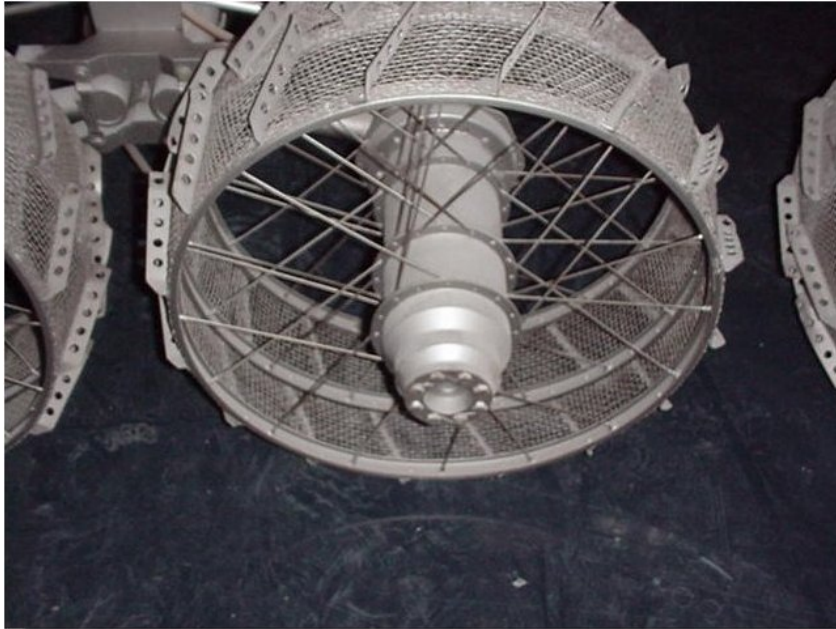


Figure 2.2: Lunokhod wheel (Picture taken at exhibit in the Kansas Cosmosphere)

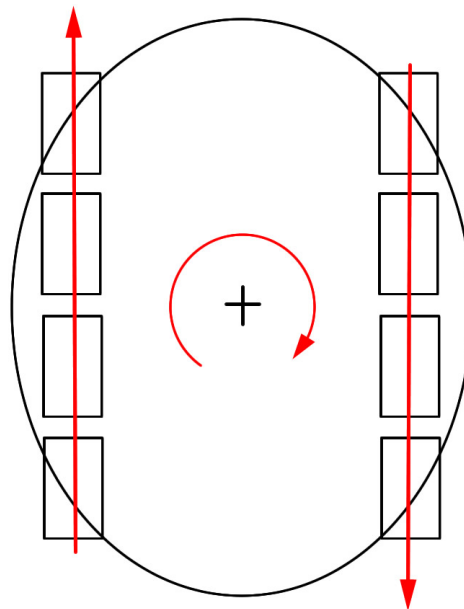


Figure 2.3: Skid Steer Method used by Lunokhod

On November 17, 1970 the former U.S.S.R. landed the first rover on the Moon. Figure 2.1 shows the Lunakhod I Moon rover, which was the Soviet's Cold War answer to the extremities of space. Weighing in at 840 kilograms the huge Russian rover advanced on eight motorized wire mesh wheels each having a diameter of .51 meters and a width of .2 meters (figure 2.2) with a wheelbase of 1.6 meters [45]. Each wheel had independent suspension and was fitted with small cleats called grousers, for traction. The rover had two speeds (1 or 2 km/hr) and maneuvered using a skid steer method (figure 2.3), which allowed the rover to pivot about any point depending on the difference between the left and right velocities. Skid Steer rovers are able to pivot about their center if the velocity on their left side is equal but opposite of the right side. The skid steer method is a very simple design that allows for high maneuverability but with less efficiency in turning than other methods. Much is still to be learned of the forces involved between wheel and soil with this steering method.

For almost a year the Lunokhod I was very successful in studying the moon, travelling 10.54 km in the Sea of Rains while performing over 500 soil tests and transmitting more than 20,000 pictures before it was shut down on Oct 4th, 1971 [14].

Lunokhod's original mission included surveying sites for later manned landings and lunar bases and providing a radio homing beacon for precision landings of later manned spacecraft. However, because America had won the manned moon race, the mission objectives refocused more on collecting images of the lunar surface, examining ambient light levels to determine the feasibility of astronomical observations from the Moon, performing laser ranging experiments from Earth, observing solar X-rays, measuring local magnetic fields, and studying mechanical properties of lunar surface material. [15]

In 1973 Lunokhod 2, identical to Lunokhod 1 except with an upgraded camera, went more than three times as far as its predecessor in four lunar days while taking more than 80,000 pictures. The pilots of Lunokhod 2, drawing on experience and confidence gained with Lunokhod 1, were a little more daring and drove the rover at twice the velocity of its predecessor. Several times the rover sank up to its hubs in loose regolith and was able to traverse 25 degree slopes with 80 percent skidding without getting permanently stuck [16]. Testing for the Lunokhods consisted of drop testing and sand pit maneuvering, assisted by a counterbalance system to simulate the moon's gravity [3].

2.3 Lunar Rover Vehicle



Figure 2.4: Lunar Roving Vehicle [6]

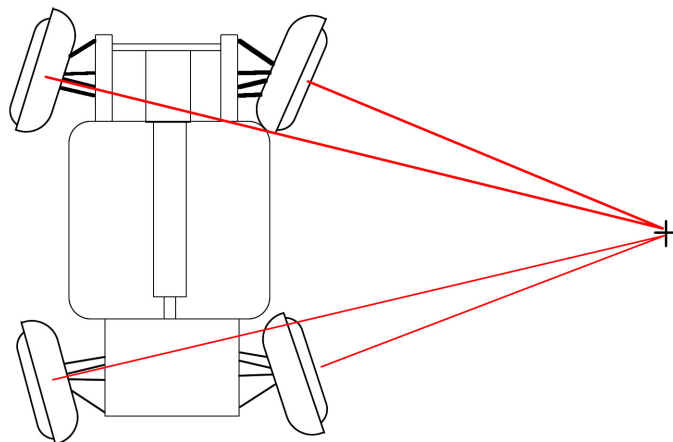


Figure 2.5: LRV Ackerman Geometry [50]

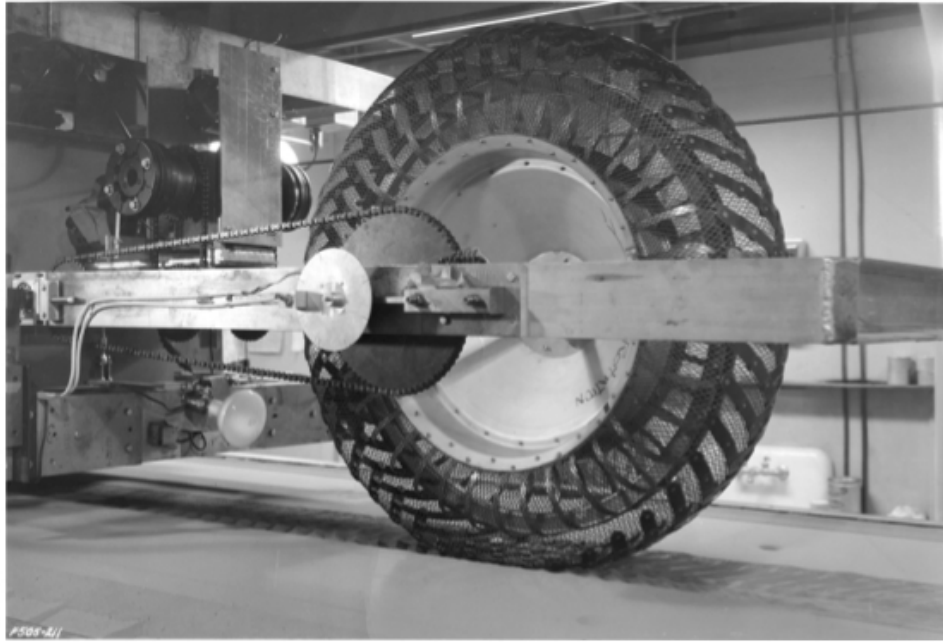


Figure 2.6: LRV Wheel in Testing Apparatus [71]

On July 31st, 1971 America's lunar rover vehicle was used for the first time on the Apollo 15 mission (figure 2.4). The LRV hotrod weighed 210 kg and could hold an additional 490 kg on the moon. The design criterion for the LRV included being able to climb a 25 degree slope fully loaded, while sustaining a speed of 16 km/hr. The Lunar Rover Vehicle utilized the Ackerman steering method (figure 2.5) which keeps all the wheels orthogonal to the radius of the turning circle. With its four wheel steering capability, the LRV was capable of a turning radius of 122 inches [18].

Each of the LRV's wheels was made of woven Zinc coated piano wire attached to a spun aluminum hub, which gave the wheels large flexibility or compliancy (figure 2.6). Several cleat designs were tested resulting in the chevron shaped Titanium cleats that were attached to the wire and covered 50 percent of the contact area. The tire was 81.8 cm in diameter and 23 cm wide with a 64.8 cm diameter titanium bumper inside the wire mesh to protect the hub in the case of extreme impact. The vehicles were used on the Apollo 15, 16, and 17 missions and where highly successful. Harrison Schmitt of Apollo 17 commented,

"...the Lunar Rover proved to be the reliable, safe and flexible lunar exploration vehicle we expected it to be. Without it, the major scientific discoveries of Apollo 15, 16, and 17 would not have been possible; and our current understanding of lunar evolution would not have been possible."
[13],[22]

The only problem with the LRV was that two fenders in separate missions were broken by astronauts that resulted in a covering of dust that caused numerous problems with electronics.

Testing for the LRV was extensive, especially for the LRV's wire mesh wheels because testing was not done just on the vehicle main assembly but additionally on single wheel subassemblies. Wheels were tested individually for traction, sinkage, stacking (collection of material in wheel) and slinging (due to mesh), dust agitation, and fatigue. At least four complicated and expensive testbeds were used in testing the LRV's wheels, which produced data to study tread design and the effects it had on speed, acceleration, load, pull performance and efficiency [50, 49]. Also a true iterative design study was accomplished with its grousers which found that 50% cleat tread area was the best performing [49].

2.4 Sojourner

A quarter of a century after the LRV, America resumed its rover endeavors with the Pathfinder mission and sent the Sojourner rover (figure 2.7) to Mars. It landed on July 4th, 1997, and traveled more than 100 meters in 83 days. It was a small rover weighing in at approximately 16 kg with small wheels 13 cm in diameter [54], with steel cleats as grousers. Some of the wheels were coated with a special paint designed to wear off with use. This gave the designers of future rovers data on how abrasive Martian soil can be [7].

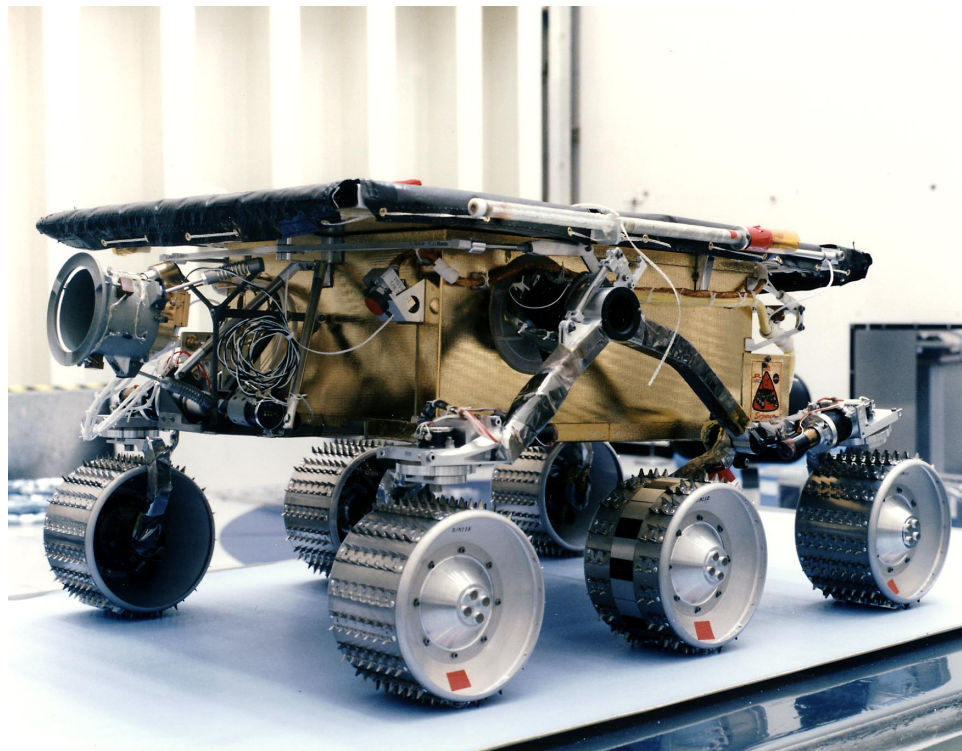


Figure 2.7: Sojourner Rover *image by NASA*

2.5 SR2

The SR2 (Solar Rover 2) (figure 2.8) was designed at the University of Oklahoma and used in a proof of concept proposal for a cheaper, faster, and simpler rover design. Much like the Lunokhod, SR2 uses a skid steer approach in turning but with only four wheels. The newest SR2 wheel iteration incorporates springs in its design to gain compliancy [61]. Tests for compliancy, of the spring wheels, were conducted by dropping the whole assembly and measuring the acceleration acting on the rover. Rolling efficiency was evaluated by measuring the distance travelled down an incline plane [52].



Figure 2.8: University of Oklahoma's SR2 [60]

2.6 Rovers and their wheels currently in use on Mars

At the time of this paper, the twin rovers Spirit and Opportunity are operating on Mars (figure 2.9). These rovers are almost three times the size of Sojourner and weigh approximately 180 kg a piece. Their wheels are milled from a solid piece of aluminum billet with spiral compliance springs incorporated into the design. The grousers on the 26 cm wheels are nothing more than small paddles on a curved wheel surface (figure 2.10) and were designed not to catch on the deflated air bag material [12].

Testing for the MER rovers consist of driving through the Mars yard at JPL. No known single wheel testing was performed.

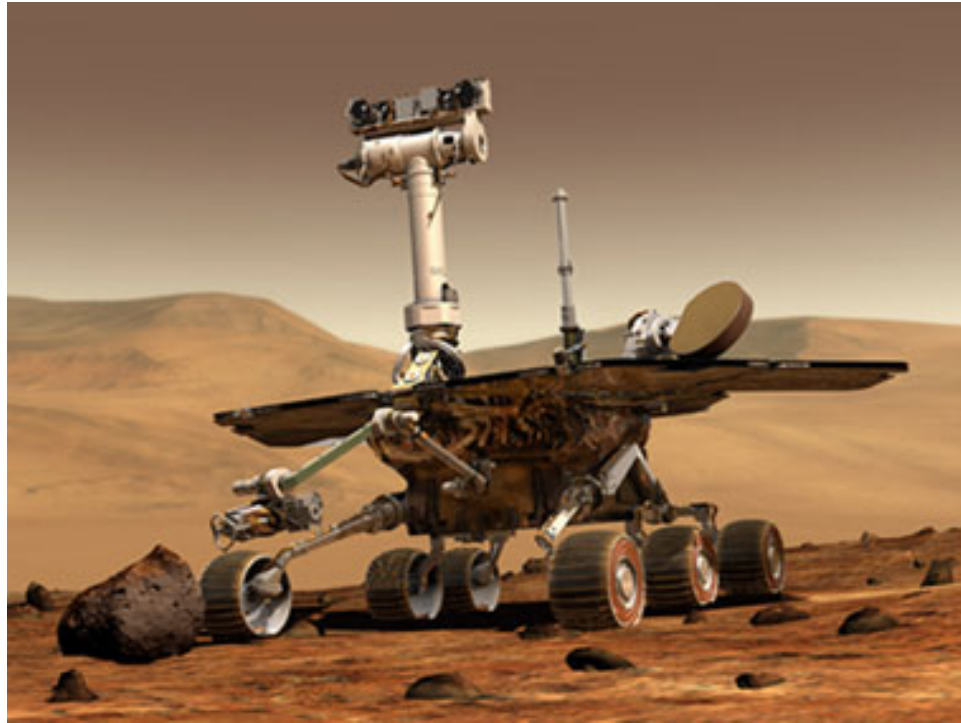


Figure 2.9: Mars Exploration Rover *image by NASA*

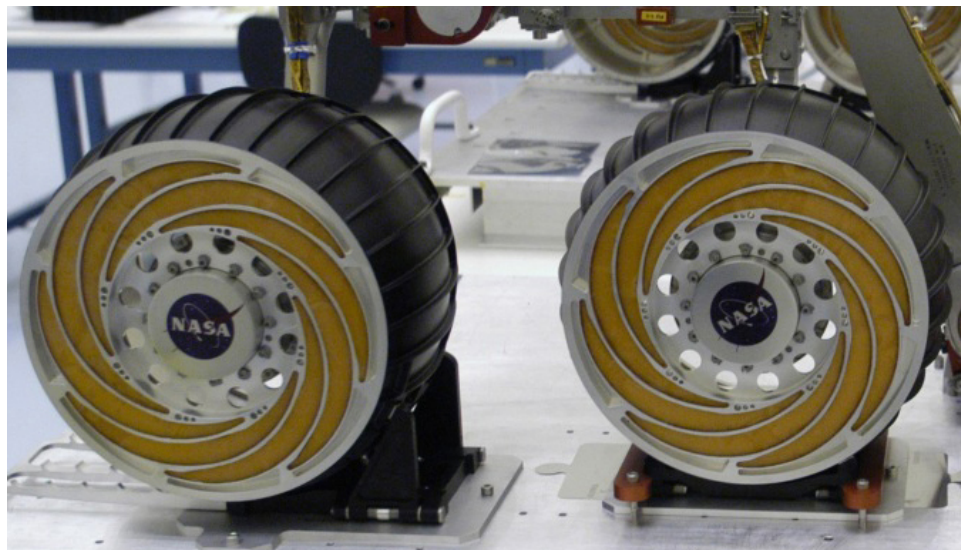


Figure 2.10: MER Rover Wheels *image by NASA*



Figure 2.11: Wheels from Sojourner (left) MER (center) and MSL (right) *image by NASA*

Due to the amazing time spent roving on Mars, the MER rovers have a long history of successes and problems. Table 2.1 shows some of the problems and events they encountered related to wheels or drive train.

Rover	Date	Problem Description	Result
Spirit	April 28, 2005	Due to sinkage, at Columbia hills, failed to climb 12-15 degree slope with 25-30 cm stones and sand.	Aborted path
	March 13, 2006	Right front wheel failed.	Drag wheel
	Nov 29, 2007	Struggles in sand at bottom of shallow bowl	Successfully navigated out
	May 07, 2009	Embedded in ultra non cohesive soil "Troy"	Currently still embedded
Opportunity	June 2004	Stood at edge of endurance crater waiting for engineers to do confidence testing.	Successful ingress and Egress of crater.
	April 26, 2005	Dug into 30 cm sand dune.	Stuck until June 4, 2005. New software alarms implemented.
	Oct 11, 2005	Slip check reported at Erebus crater of 44.5% slip.	Backed out 5.3 meters.
	June 12, 2007	Right front wheel drawing more current.	Waiting to see if it mimics Spirit.

Table 2.1: MER rover problems and events

2.7 Proposed Rover Designs

The Mars Science Laboratory (MSL) is scheduled to launch in 2011 (figure 2.12). The proposed 800 kg [8] dune buggy sized rover will be nuclear powered and carry

a multitude of science equipment with the same basic mission as the MER rovers. The current wheels on MSL are cylindrically shaped, 50 cm in diameter, and have small almost nonexistent chevron shaped cleats (figure 2.11) even though there are no lander bags to worry about snagging in this mission. The MSL, MER, and Sojourner rovers all use a Rocker Bogie suspensions that utilizes 6 wheels. The front and rear wheels can pivot about their own Z axis allowing the rovers to pivot about their center, which is a variation of the Ackerman steering methodology (figure 2.13).

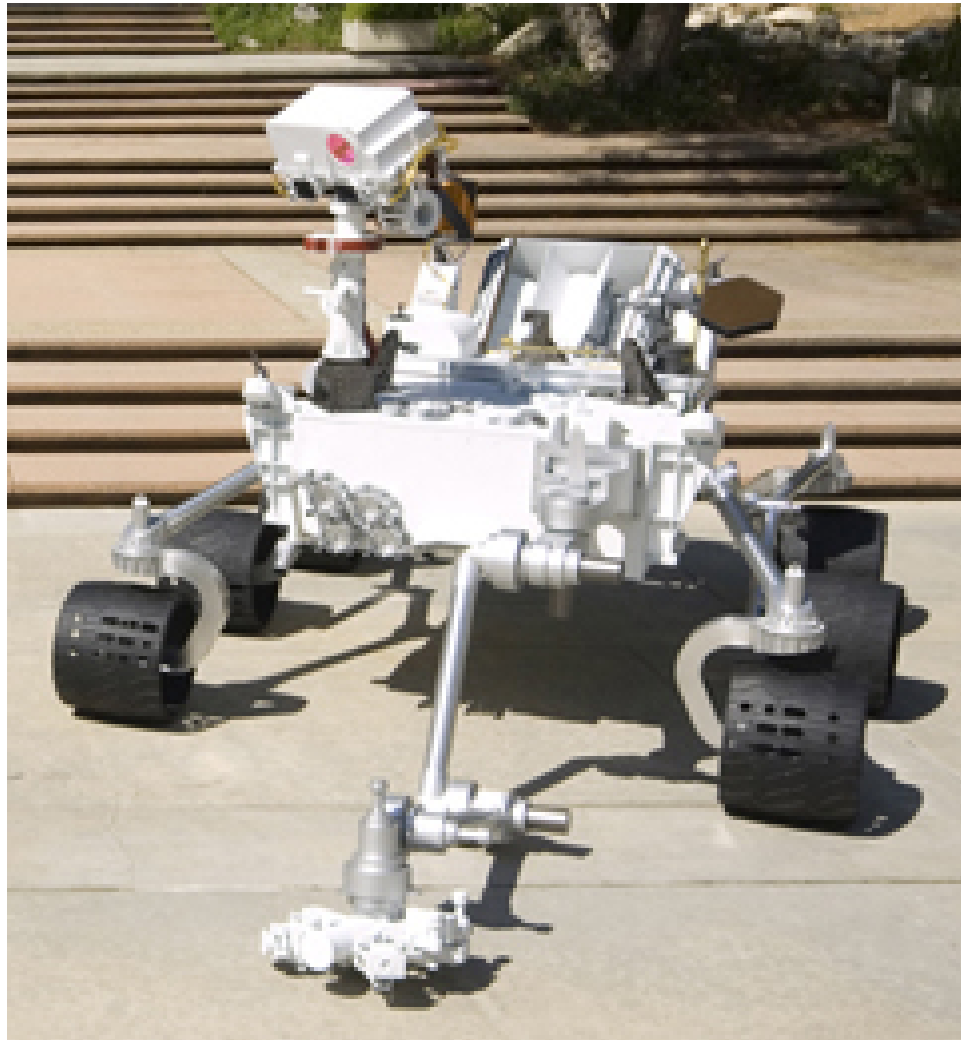


Figure 2.12: Mars Science Laboratory *image by NASA*

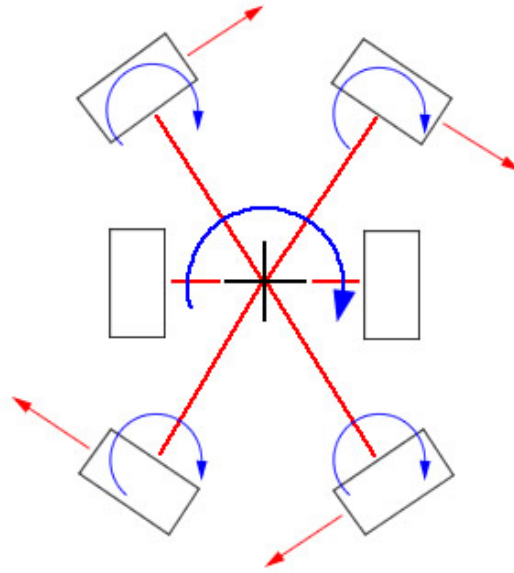


Figure 2.13: Rocker Bogie Zero Radius Steering Method

To meet the demand of the future of non-exploratory work, two other space vehicles have been designed and are being evaluated. Athlete, figure 2.14, moves in a complicated combination of legged and rolling motion due to its six wheeled legs. Athlete can bend down and pick up equipment needed for exploration and manipulate it as needed. Its wheel-leg design is hoped to be useful in cohesive as well as non cohesive soils. NASA's new Truck design (figure 2.15) is an astronaut driven six wheeled vehicle with the ability of lowering itself for easier loading and unloading of materials. The truck will also be used for the chassis for NASA's new Lunar Electric Rover (figure 2.16) which will provide accommodations for two astronauts for up to two weeks on the moon. The steering methodology for the Athlete and Truck is a variation of the MER's except all the wheels are designed to pivot, about their Z axis, making maneuvering complicated but versatile.



Figure 2.14: NASA Athlete *image by NASA*



Figure 2.15: NASA Truck *image by NASA*



Figure 2.16: NASA Lunar Electric Vehicle *image by NASA*

2.8 Current Test Beds

To fill the gap in the understanding of rover wheel design and wheel-to-soil interaction, testing machines have been designed and used by various institutions. In 1971, NASA tested the Lunar Rover Vehicle's wheels on a testing device called a dynamometer system which measured load, sinkage, pull, torque, as well as horizontal and angular velocity. The testbed (figure 2.17) consisted of a truck pulled by the rover wheel along a linear path through crushed basalt [50]. Along with the Dynamometer System, NASA used several other test beds for the LRV wheel. Figure 2.18 and 2.19 show the one sixth gravity and 1% atmosphere test bed that was actually flown aboard a C-135 aircraft and depressurized for a better understanding of wheel to regolith interaction on the moon's vacuum environment. Figures 2.20 and 2.21 show two test beds that allow for continuous linear motion for the LRV wheels. These test beds helped NASA prove that the innovative wire mesh wheel, slated for the LRV, was able to satisfy the design requirements given.

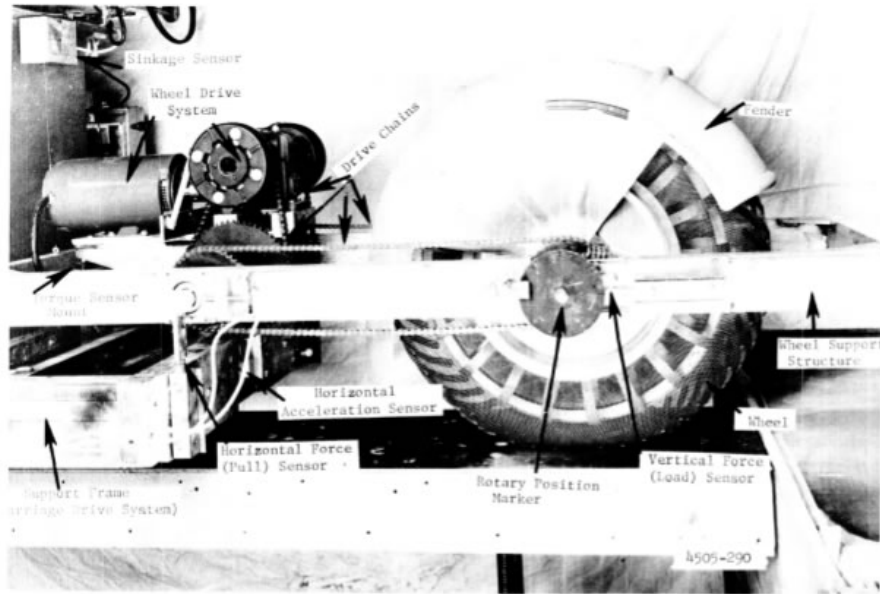


Fig. 3. LRV wheel mounted in dynamometer system

Figure 2.17: Lunar Rover Vehicle Wheel in Testing Apparatus [71]



Figure 2.18: LRV Low Gravity Test Bed Inside [53]

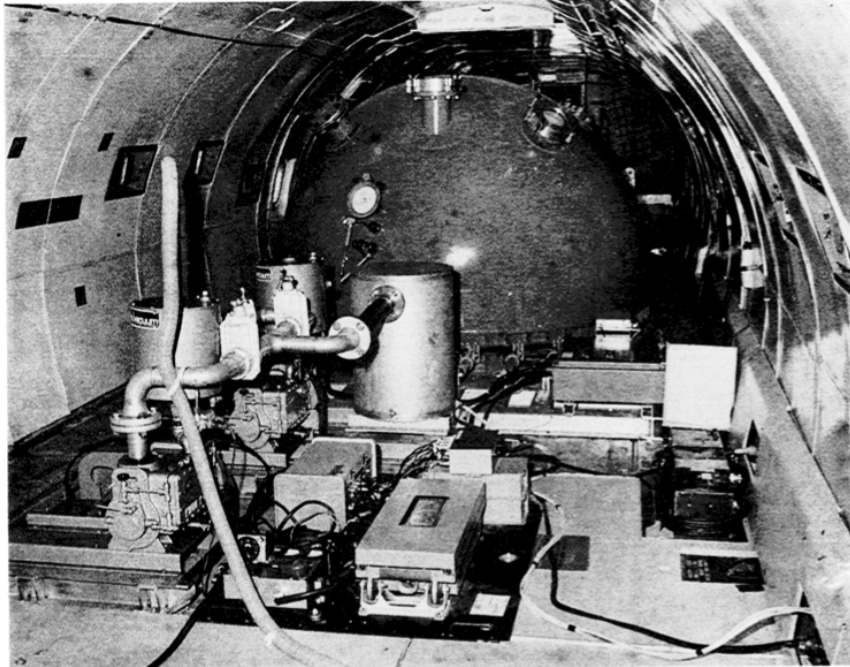


Figure 2.19: LRV Low Gravity Test Bed Outside [53]



Figure 2.20: GM Testbed for LRV Wheel [71]



Figure 2.21: GM Testbed for LRV Wheel [71]



A Model Robotic Vehicle was driven over 25-cm obstacles on simulated terrain at a tilt of 20°.

Figure 2.22: Variable Terrain Tilt Platform (VTTP) *image by NASA*

NASA now uses devices such as the variable terrain tilt platform (VTTP) (figure 2.22), at JPL, to gain a better understanding of entire rover systems in a sloped environment. The VTTP is a 16 x 16 ft table that can tilt up to 25 degrees and can be left bare or covered with terrain [46]. These types of test beds have no mechanical tether to the rover. The rovers, as a whole assembly, move freely along the test bed and their performance is observed as they traverse various obstacles.

In June of 2004, the VTTP was put to use when the rover Opportunity sat on the ridge of Endurance crater waiting till engineers at NASA decided if it was safe for it to traverse down into the hole. The testing consisted of covering the VTTP platform with concrete flagstones purchased at a large-chain hardware store and then covering the flagstones with a texture from mixed sand and quick-drying cement. Then they tilted the platform to 25 degrees and evaluated the rover on it. Using a fish scale they pulled backward on the rover with a cord to make the rover lose its footing and slip [5].

The Massachusetts Institute of Technology has had success with their testing apparatus designated the "Field and Space Robotics Laboratory terrain characterization testbed" (figure 2.23). The FSRL tests a single driven wheel through different mediums to better understand wheel to soil interaction [36, 37, 34, 35, 17], providing data for a motor torque vs slippage relationship, as well as a novel way to measure sinkage given an image of the wheel in sand. Measuring slippage, motor torque, and wattage used along the Y axis, via a drawbar pull, the FSRL is a standard design that is widely used.

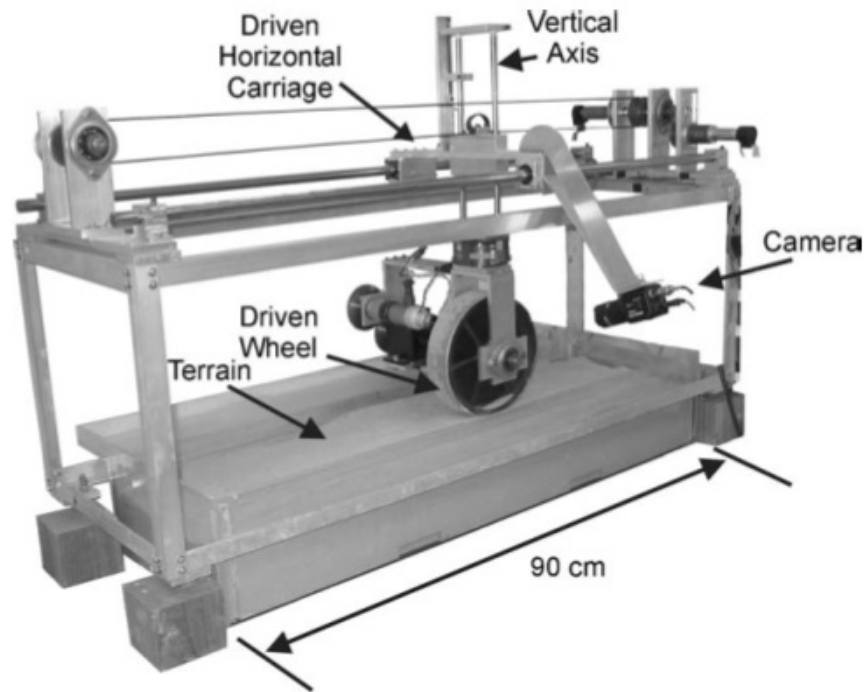


Figure 2.23: MIT Single Wheel Test Bed [19]

A similar design is used at Tohoku University to refine rover steering and other parameters [70, 42, 40]. The Tohoku apparatus (figure 2.24) is different from FSRL in that the test wheel can be rotated and locked before being pushed through the media. This ability allows a closer examination of how lateral forces of the wheel are related to slip angle and slip ratio.

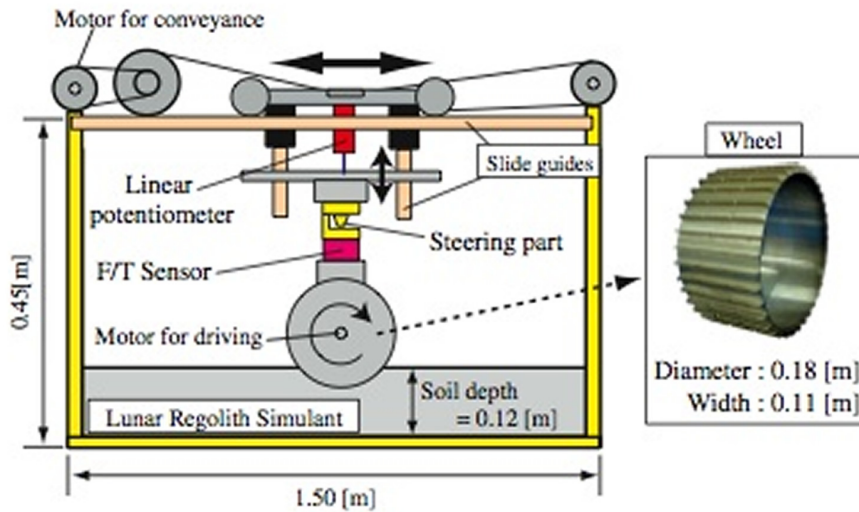


Figure 2.24: Tohoku University Single Wheel Test Apparatus Drawing [40]

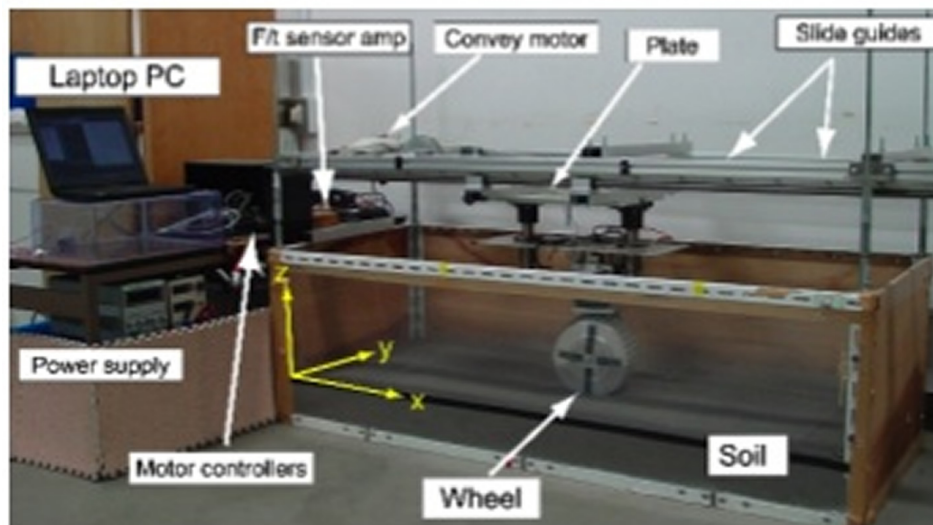


Figure 2.25: Tohoku University Single Wheel Test Apparatus [40]

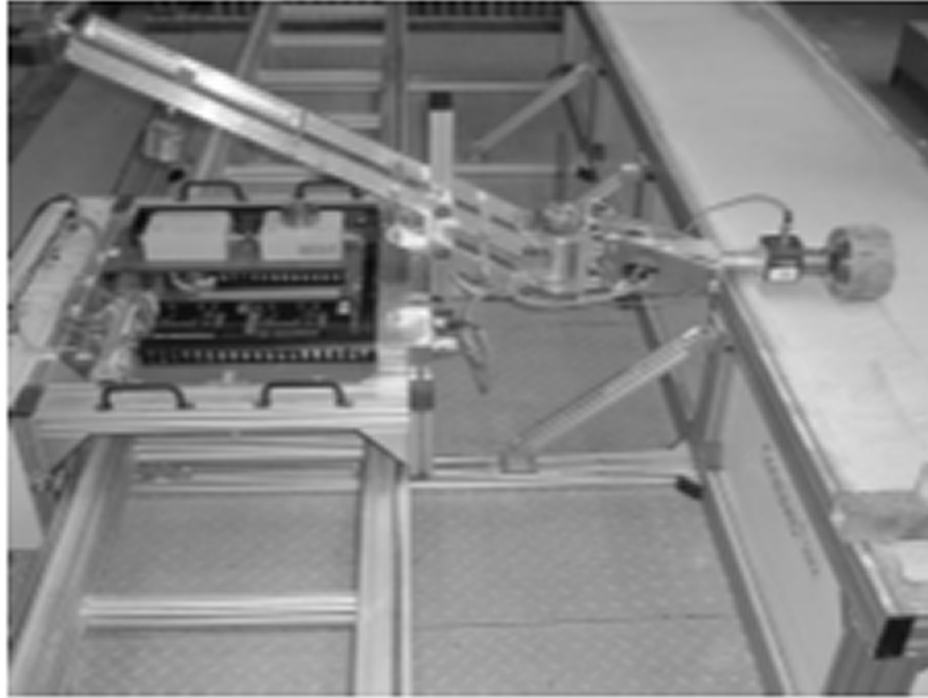


Figure 2.26: RCET Single-Wheel Testbed at DLR [65]

RCET (Rover Chassis Evaluation Tools) (figure 2.26) is a single wheel testbed at the DLR Institute of Space Simulation. RCET is a variation of the FSRL design and its main purpose is to measure a vehicle's tractive ability on homogeneous surfaces under controlled situations [65].

A coalition of Japanese institutions: the School of Physical Sciences in Sagami-hara; Meiji University in Kanagawa; and ISAS/JAXA have designed a testing apparatus for small applications (figure 2.27). Their experimental system uses a parallel link attached to a guide rail that actuates the wheel along a linear path. New wheels with better non-stacking ability than conventional wheels, have been evaluated using this device [38].

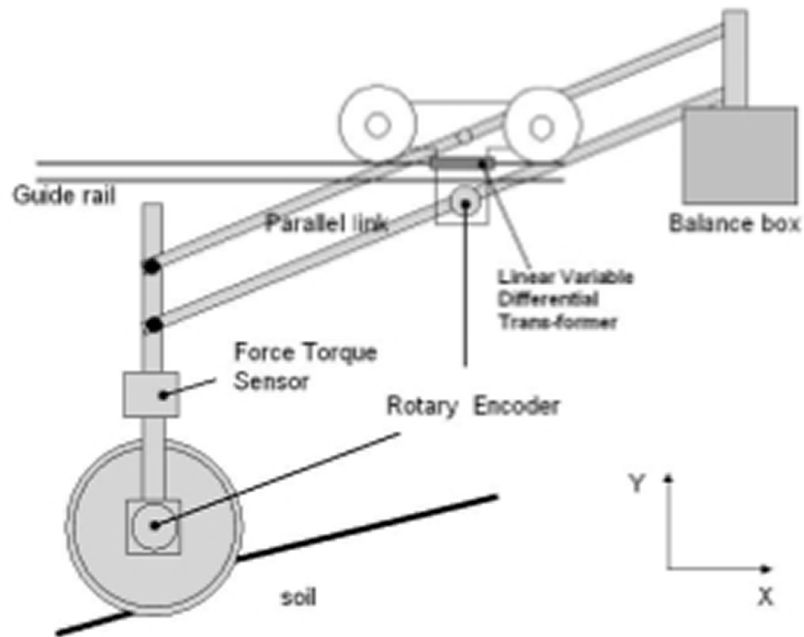
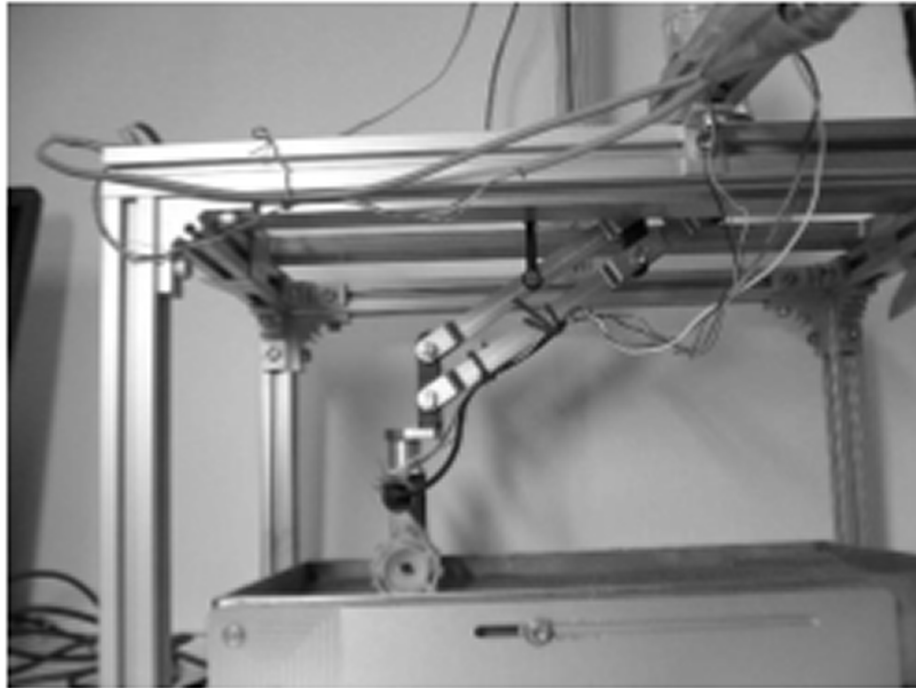


Figure 2.27: Japanese Consortium Testing Apparatus [38]

Analogous to space vehicle wheel testing is the testing that is conducted on automotive wheels and tires (figure 2.28). These tests usually deal with fatigue and performance at high speeds or impacts.



Figure 2.28: STL Radial Fatigue Test Apparatus [66]

2.9 Summary

From the past, present, and future examples of rovers and their wheels, it is shown that there are gaps in the current testing methodology. The Lunar Rover Vehicle's wheel was tested extensively both as a total assembly and even more as a single wheel. Iterative design played a big role in the LRV's wheel [50]. As the space program has evolved single wheel evaluation and iterative design have fallen out of fashion not because it wasn't a worthwhile tool but due to the excessive cost in time and resources that only the Apollo mission budget could support.

2.10 Conclusions

1. Skid steer rovers can be highly maneuverable, but the forces involved are complicated and power intensive in turning. Further testing needs to be done to find better grouser patterns to aid in these disadvantages.
2. Athlete and NASA's Truck mark the expanding role of robots into more working roles instead of just exploration, which requires different performance characteristics. One characteristic is the ability to drag or push with a given force which would be needed in order to perform new tasks such as excavating regolith [1] and move equipment.

CHAPTER 3

SWEET

3.1 Introduction

To better understand, characterize, and enable enhancement of rover performance, several new wheel characteristics need to be tested that are currently overlooked. Data from a testing apparatus specifically designed to test in situations previously neglected, such as shock absorption, turning, and simulated force, will enable better wheel designs and provide for better strategy in dealing with mission contingencies. The requirements for a test bed to fit these accommodations include a large enough vertical drop off to simulate the design criteria, actuated motion along the X , Y , and rotation about the Z axis to adequately study turning, and a means to provide repeatable simulated force along the direction of motion.

3.2 SWEET Design

The purpose of SWEET (Suspension and Wheel Experimentation and Evaluation Testbed) is to fill the previously discussed need for more adequate testing of rover wheels. SWEET (Figure 3.1) has a 10 x 10 ft footprint and is fabricated from modular aluminum. A weighted vertical test leg, incorporating a driven wheel and a six axis force torque sensor, stays stationary in the X and Y directions but allows movement along the Z -axis via a counterbalance system.

SWEET differs from the test beds discussed earlier in that the table can move in the X and Y directions underneath the test stand, as well as rotate about any point in the X and Y plane. This added advantage gives the apparatus the unique ability to measure forces and torques in a true turn. This testbed can also evaluate traction, sinkage, lateral forces, turning efficiency, compliancy, rolling efficiency, and the effects of simulated drag for each wheel tested. The table can move along the X and Y axis at velocities faster than $20 \frac{cm}{sec}$, which is more than needed when considering Spirit or Opportunity but will allow for testing the emerging, faster rover concepts [61]. SWEET is also large enough to be used to test other assemblies such as a suspension system or an entire rover.

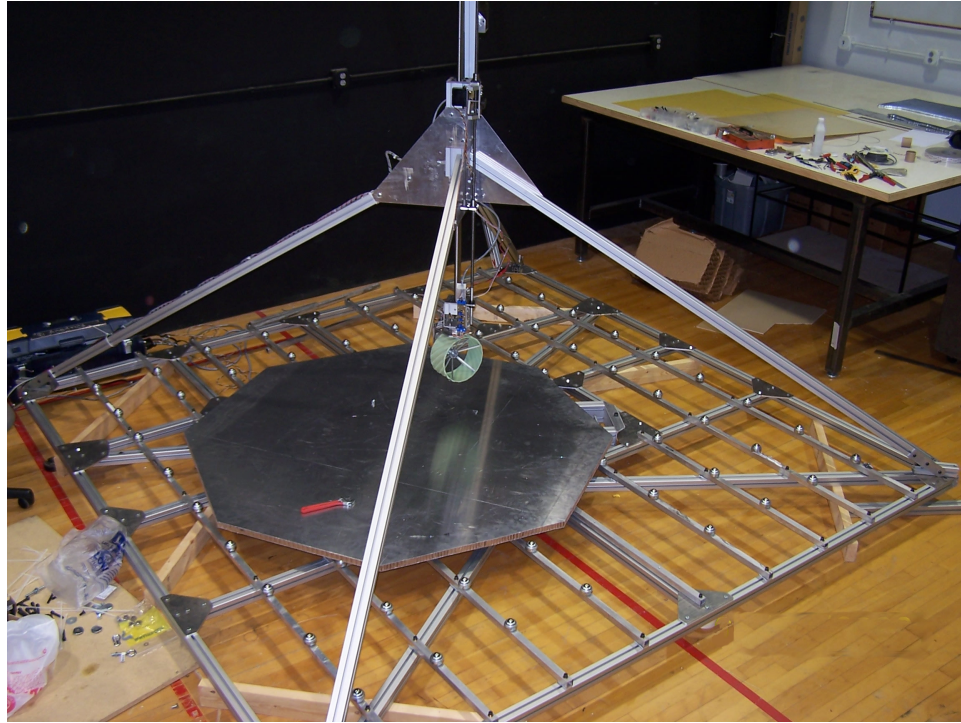


Figure 3.1: Testbed

3.2.1 Motion

To simulate motion on the testbed, the table moves under the test leg. This motion is accomplished by three DC motors that are offset 120 degrees from each other (Figure 3.2). Each of these motors have a 120 mm Kornylac omnidirectional wheel mounted on their shaft (figure 3.3), and create the desired table motion discussed earlier.

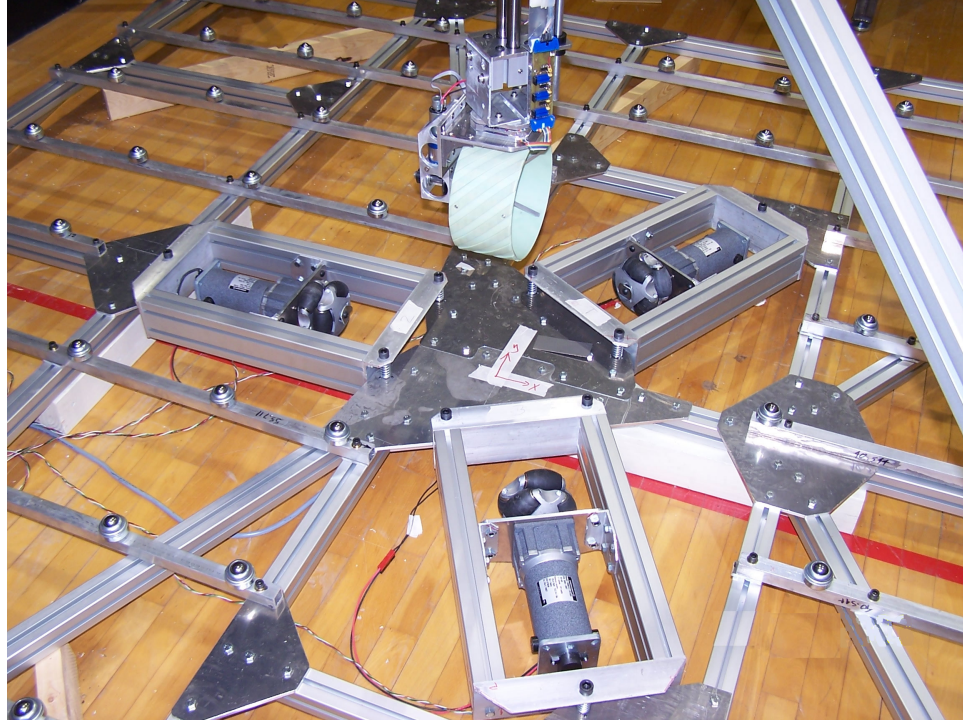


Figure 3.2: Motor Configuration

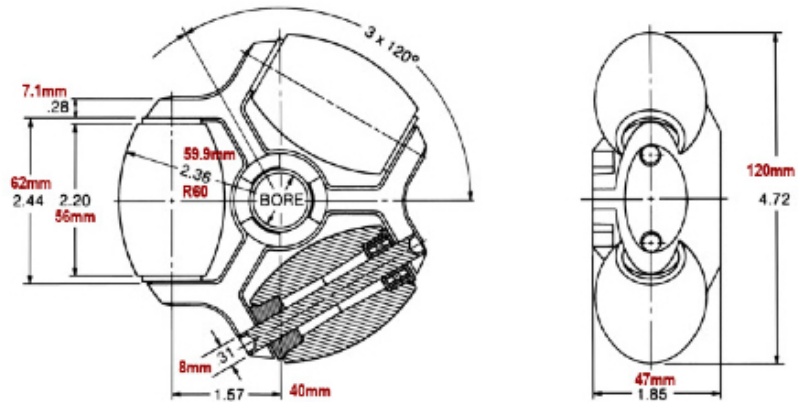


Figure 3.3: Omniwheel Specifications [43]

To transform the desired cartesian table motion of \dot{X} , \dot{Y} , and $\dot{\Theta}$ to the angular speed of each of the three motors, a transformation equation (3.1) is used [64]:

$$\dot{\phi} = J_2^{-1} J_f R(\Theta) \dot{\xi} \quad (3.1)$$

In this equation, $\dot{\xi}$ is a vector containing the desired table motion parameters of \dot{X}, \dot{Y} , and $\dot{\Theta}$, represented as equation 3.2

$$\dot{\xi} = \begin{pmatrix} \dot{X} \\ \dot{Y} \\ \dot{\Theta} \end{pmatrix} \quad (3.2)$$

In equation 3.3 $R(\Theta)$ is the rotational transformation matrix that is dependent on the angular position of the table Θ .

$$R(\Theta) = \begin{pmatrix} \cos(\Theta) & -\sin(\Theta) & 0 \\ \sin(\Theta) & \cos(\Theta) & 0 \\ 0 & 0 & 1 \end{pmatrix} \quad (3.3)$$

J_f is a matrix made up of three constraint equations, one for each wheel. J_f transforms the desired motion values of $\dot{\xi}$ into the control parameter, $\dot{\phi}$, which is a vector containing the three motor angular speeds. Equation (3.4) shows how J_f is dependent on the three angles and the distance, l , the wheel is away from the center of the rover (figure 3.4 and 3.2).

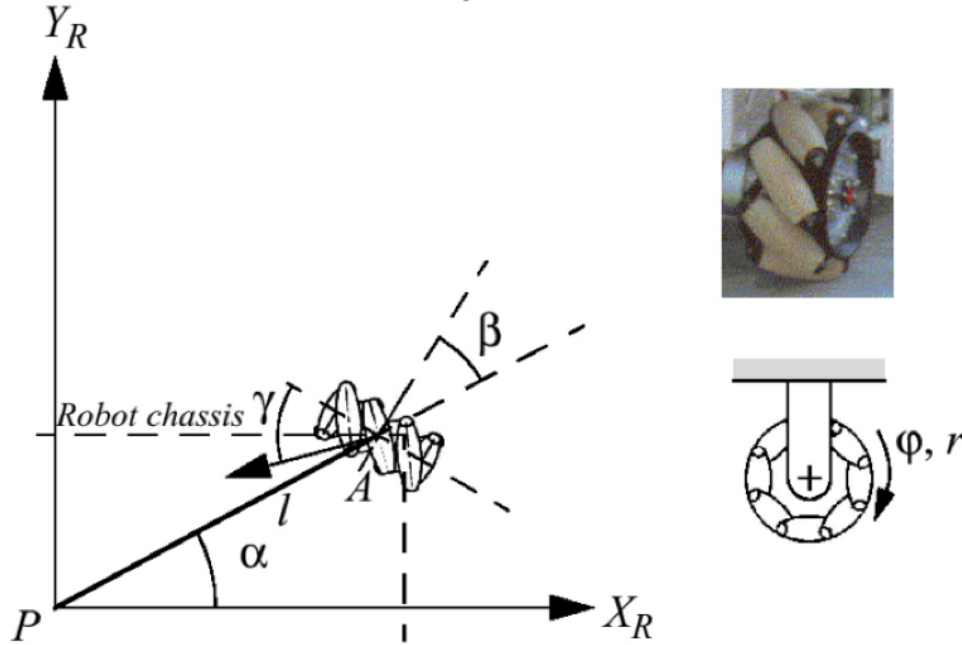


Figure 3.4: A Swedish wheel and its parameters [64]

$$J_f = \sin(\alpha_1 + \beta_1 + \gamma_1) - \cos(\alpha_1 + \beta_1 + \gamma_1) - l \cos(\beta_1 + \gamma_1) \quad (3.4)$$

For the configuration in this apparatus, β and γ are zero, making J_f dependent

only on α . If all three wheels are taken into account and set up in matrix form, the result is equation (3.5):

$$J_f = \begin{pmatrix} \sin(\alpha_1) & -\cos(\alpha_1) & -l \\ \sin(\alpha_2) & -\cos(\alpha_2) & -l \\ \sin(\alpha_3) & -\cos(\alpha_3) & -l \end{pmatrix} \quad (3.5)$$

J_2 is a matrix holding the radius values of each wheel. Since each radius is the same J_2 can be simplified to a scalar value r (equation 3.6).

$$J_2 = \begin{pmatrix} rad_1 & 0 & 0 \\ 0 & rad_2 & 0 \\ 0 & 0 & rad_3 \end{pmatrix} \quad (3.6)$$

Taking into account equations (3.2) and (3.6), we can simplify equation (3.1) into equation (3.7) which maps a relation between the table motion ($\dot{X}, \dot{Y}, \dot{Z}$) and the motor angular velocities (ϕ_1, ϕ_2, ϕ_3).

$$\begin{pmatrix} \phi_1 \\ \phi_2 \\ \phi_3 \end{pmatrix} = \frac{1}{r_{wheel}} J_f R(\Theta) \begin{pmatrix} \dot{X} \\ \dot{Y} \\ \dot{\Theta} \end{pmatrix} \quad (3.7)$$

If the user wishes to use the table as the global coordinates then the $R(\Theta)$ rotational matrix must be left in equation 3.7, otherwise if global coordinates rest on the wheel, or rover, $R(\Theta)$ can be left out and equation 3.7 simplifies to equation 3.8:

$$\begin{pmatrix} \phi_1 \\ \phi_2 \\ \phi_3 \end{pmatrix} = \frac{1}{r_{wheel}} J_f \begin{pmatrix} \dot{X} \\ \dot{Y} \\ \dot{\Theta} \end{pmatrix} \quad (3.8)$$

With the configuration that SWEET utilizes ($l = .3$ m, $\alpha_1 = \frac{\pi}{3}$, $\alpha_2 = \pi$, $\alpha_3 = \frac{5\pi}{3}$, and $r_{wheel} = .06$ m) equation 3.8 is placed in the controller program with equation 3.9:

$$\begin{pmatrix} \phi_1 \\ \phi_2 \\ \phi_3 \end{pmatrix} = \frac{1}{.06} \begin{pmatrix} (.866\dot{X}) - (.5\dot{Y}) - (.3\dot{\Theta}) \\ (.5\dot{Y}) - (.3\dot{\Theta}) \\ (-.866\dot{X}) - (.5\dot{Y}) - (.3\dot{\Theta}) \end{pmatrix} \quad (3.9)$$

3.2.2 Test leg

The test leg (Figure 3.5) is a fully adjustable assembly that hangs from the center of the pyramid shaped apparatus, and is free to move along the Z -axis sliding on linear bearings. The test wheel is powered by a Faulhaber DC motor geared down to (43:1) and then again geared down (4:1) or (2:1) via a chain drive and varying sprockets. The ratio of (172:1) was used to mimic the in-house rover. Gearing adjustments can be made for varying gear ratios or wheel sizes. An encoder is used on the motor for PID control along with a motor torque sensor that is incorporated into the motor mount, and is comprised of eight uniaxial, 350 Ω strain gages. These strain gages are configured in a wheat stone bridge (Appendix B) and their signals amplified before being fed into a National Instruments 6020E DAQ box. The test leg also holds the force torque sensor, discussed in section 3.2.5.

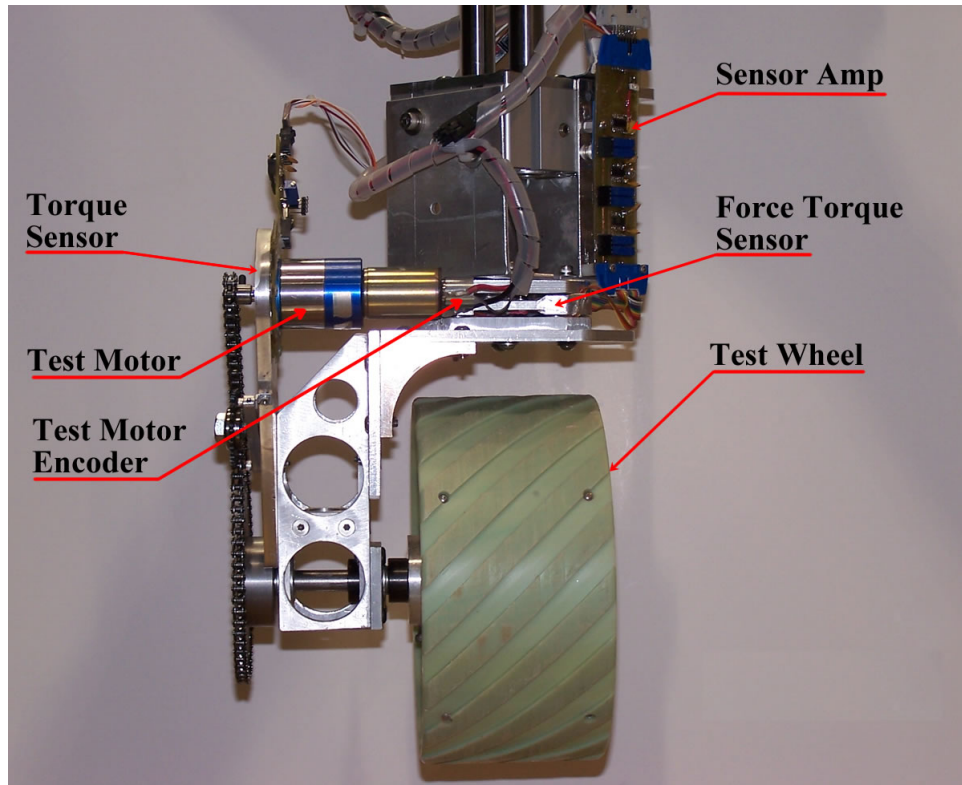


Figure 3.5: Test leg

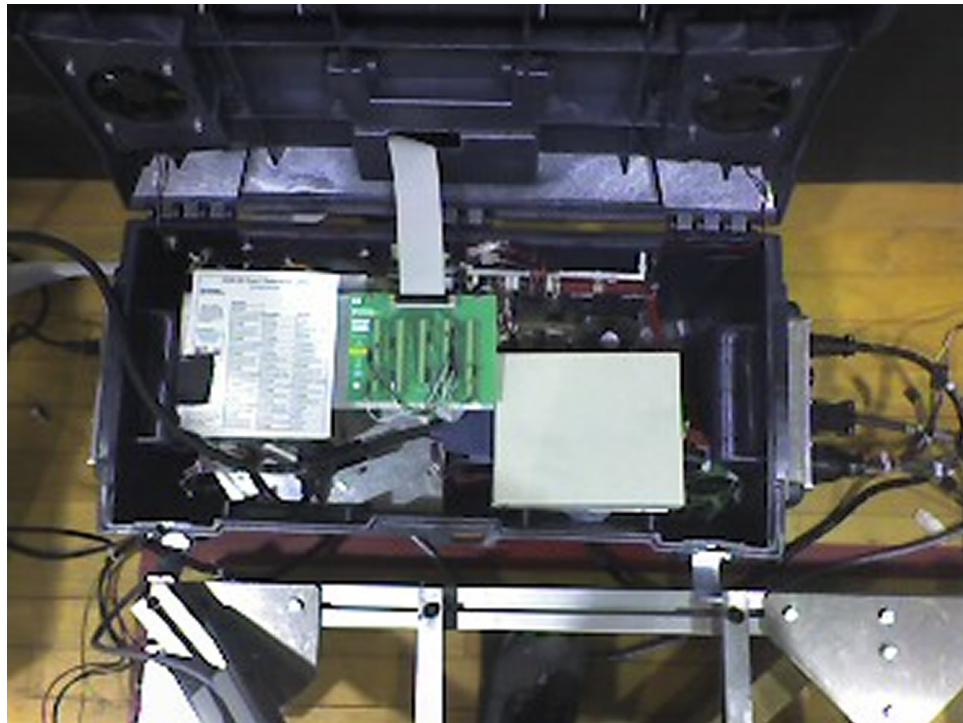


Figure 3.6: Control box

3.2.3 Electrical

Most of the electrical system is housed entirely in the control box shown in Figure (3.6). The mobile control box allows for easier testing and diagnostics on the electrical components.

Three 240 Watt power supplies, each connected to a 40 Amp PWM controlled H-bridge provide power and control for the main motors. The control box is also equipped with a 200 Watt power supply that powers the encoders, testing wheel, Z drive actuator, and force torque sensors. A dual separate channel, PWM controlled, H-bridge controls the test wheel and the Z drive actuator.

The apparatus utilizes two National Instruments data acquisition boards interfaced to a computer. A PCI-6602 DAQ board handles most of the digital and counter pins which give PWM signals to the H-bridges, while a USB-6020E DAQ board handles all the force torque analog signals, as well as encoder signals of the three motors, Z -axis displacement encoder, And the voltage value from an inline current sense circuit. The current sense measures the amperage and voltage used by the test wheel which is passed on to the analog input of the 6020E. Also incorporated in the control box is a Parallax Stamp, which supplies a pulse output to the Z drive engaging servo. The stamp in this configuration decreases the number of counter pins needed on the more expensive DAQ boards. The Stamp microprocessor also controls SWEET's test warning lights and any auxiliary lower level hardware to be added later.

3.2.4 Counterbalance

The apparatus incorporates a counterbalance system (figure 3.7) that allows the user to vary the wheel loading on the test wheel which allows different simulated gravities and or different rover weights.



Figure 3.7: Counterbalance

3.2.5 Force Torque Sensor

Like most of the test beds discussed earlier, the main sensor used is located on the test leg, along with the sensor's adjustable gain amplifier, just above the wheel. It is a six degree of freedom force torque sensor (figure 3.8) machined from 2024 aluminum, incorporating 32 strain gages networked together [33] [32] (see Appendix B,C). This sensor gives us a full view of the forces and torques (F_x , F_y , F_z , M_x , M_y , and M_z) being applied to the test wheel which is located six inches directly under the sensor. Both the force torque sensor and the gain adjustable amplifier were fabricated by the

author at the University of Oklahoma.

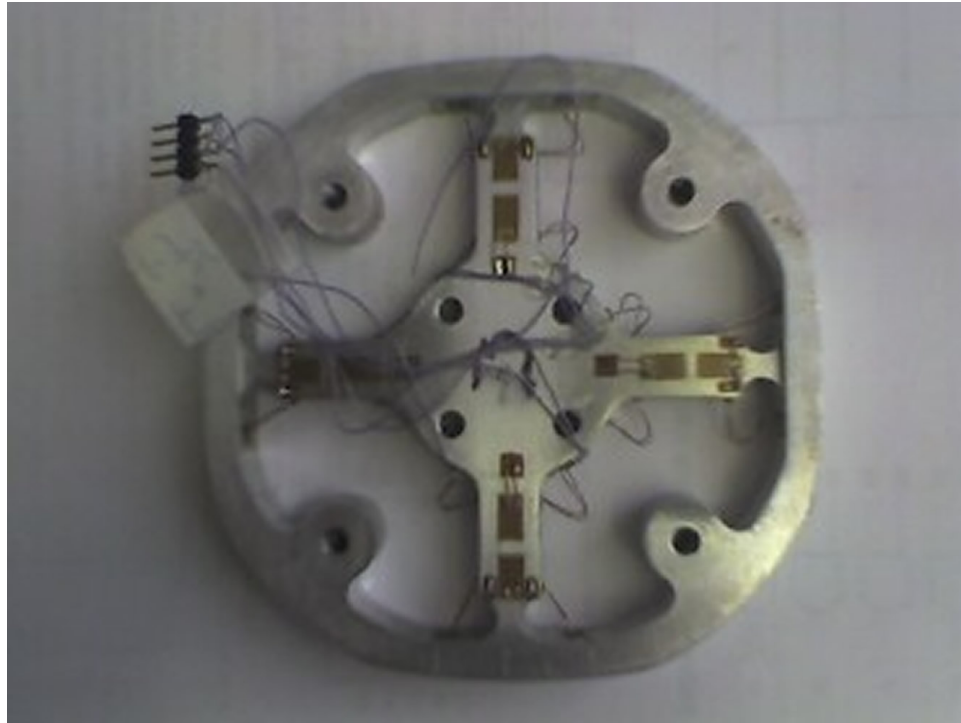


Figure 3.8: Force torque sensor device

3.2.6 Z Drive Actuator

To aid in testing and maintenance a Z axis actuator is used (figure 3.9 and 3.10). The actuator is a 12V geared DC motor which, when engaged, slides the test foot up and down along its Z axis. This actuator is engaged and disengaged by a servo so as to not hamper testing that requires the Z axis to move freely. The housing for the Z drive actuator also is the mount for the Z axis displacement encoder.

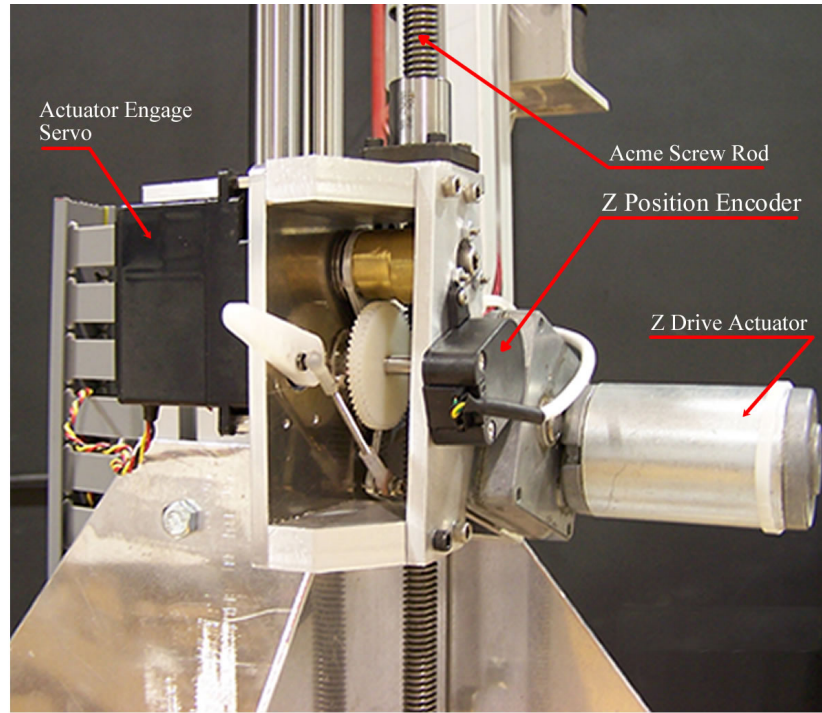


Figure 3.9: Z Drive Actuator

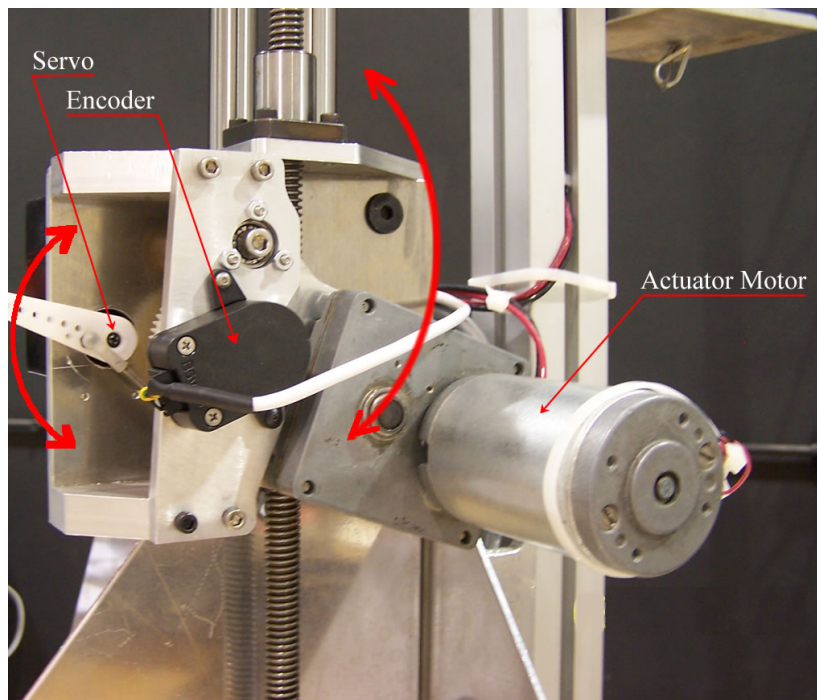


Figure 3.10: Z Drive Actuator Front

3.2.7 Programming

SWEET is computer controlled because of the complicated nature of the tri-omniwheel system, which makes manual control not practical. Labview 8.2 (National Instruments programming language) is used in programming SWEET since two National Instruments data acquisition boards are used for data gathering. The programming incorporates proportional, integral, differential (PID) control algorithms for each of the main motors as well as the test motor, force feedback, and force assist feature.

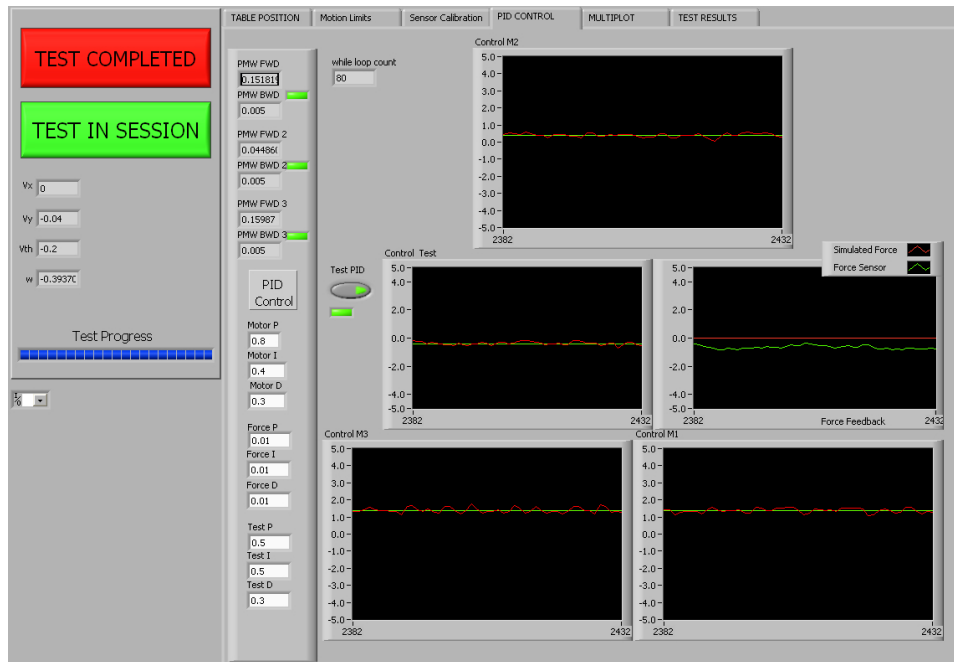


Figure 3.11: Labview Interface PID Control

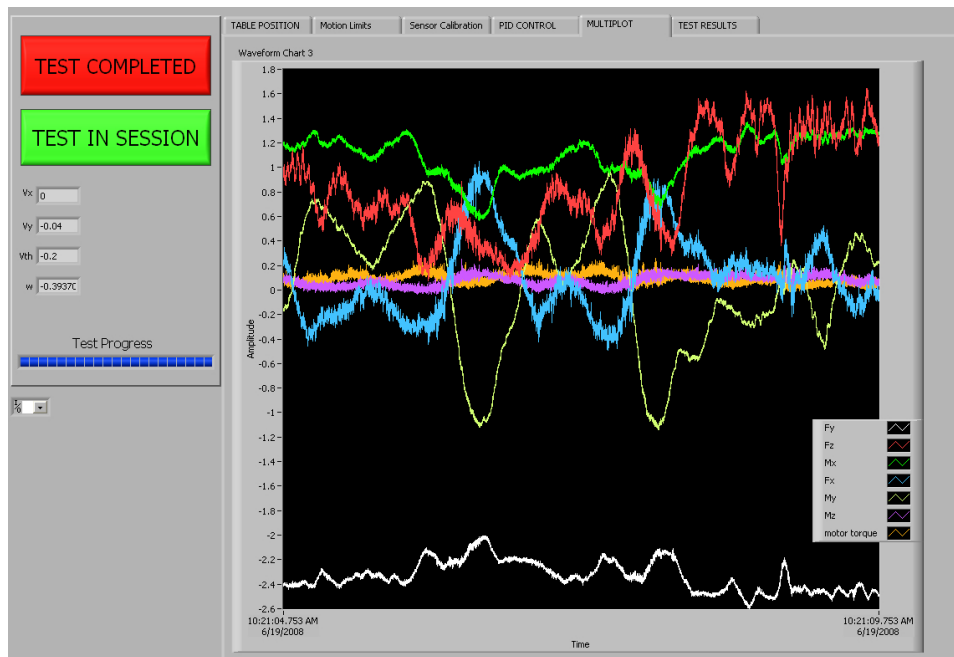


Figure 3.12: Labview Interface FT Sensor Readings

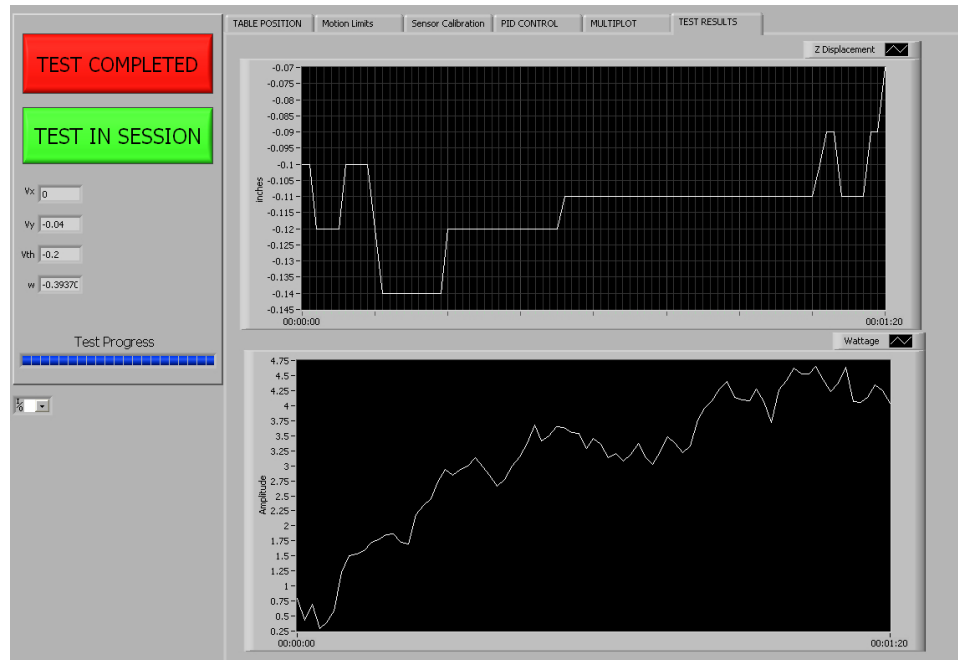


Figure 3.13: Labview Interface Motion and Wattage Results

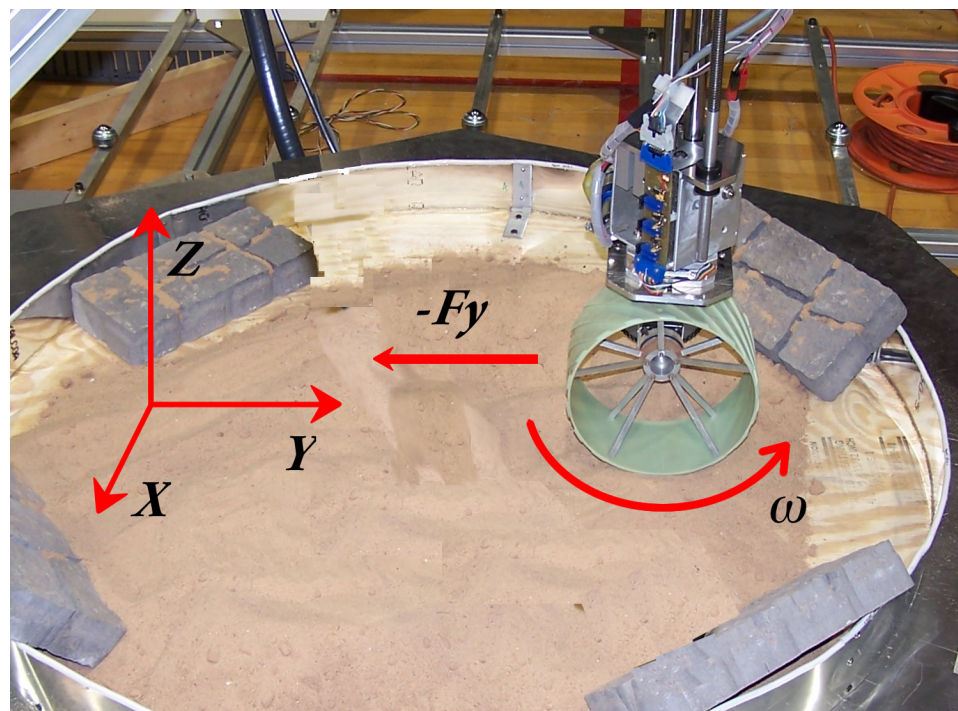


Figure 3.14: Force Feedback axis and Force Vector

When executed, the program initially asks which preprogrammed test procedure file to use. The test procedure file (TP file) is a text file that is read into an array and

Table 3.1: Test Procedure Turning Sample

Δt	V_x	V_y	Ω	F_A	F_y
.1	$\dot{\Theta} \cdot R_x$	$\dot{\Omega} \cdot R_y$	$\dot{\Theta}$	0	0
.2	$\dot{\Theta} \cdot R_x$	$\dot{\Omega} \cdot R_y$	$\dot{\Theta}$	0	0
.3	$\dot{\Theta} \cdot R_x$	$\dot{\Omega} \cdot R_y$	$\dot{\Theta}$	0	0

Table 3.2: Test Result File Sample

Δt	V_x	V_y	Ω	F_y	RH%	T°	F_x	F_y	F_z	M_τ	M_x	M_y	M_z
.1	0	.1	0	0	34	84	0.358	-1.102	-0.961	3.988	-0.337	0.973	0.026
.1	0	.1	0	0	34	84	0.162	-1.221	-1.32 3	.995	-0.372	-0.289	0.038
.1	0	.1	0	0	34	84	0.042	-1.261	-1.476	3.998	-0.391	-0.571	0.032

governs SWEET as it proceeds through the test (table 3.1). Different experiments can be executed by the preprogrammed TP file that controls the table, wheel motion, and force feedback function.

1. When F_y is non-zero SWEET switches into force feedback mode. This F_y value becomes the force value that the wheel is to drag or be pulled by. SWEET will move the table accordingly (using PID control) to keep the measured F_y equal to the force value read from the TP file (figure 3.14).
2. V_x , V_y , and $\dot{\Omega}$ are table velocity values that control SWEET's motion when not in the force feedback mode.
3. Δt column controls the timing and length of the test.

The control page (figure 3.11) is where PID gains can be set for all motors and for the force feedback control. After the test is finished preliminary results can be seen on several pages (figure 3.12 and 3.13). These results consist of all the forces and torques measured, Z displacement, and wattage used by the test wheel.

Wattage used by the test wheel is useful in measuring how efficiently the wheel performs its tasks and is calculated as:

$$Wattage = V_{test} \cdot I_{test} \quad (3.10)$$

in equation 3.10 d_{test} is voltage of the test wheel and I_{test} is the Current Measured from the test wheel.

Data from the test procedure file is appended to sensor readings, environmental factors, and written to a test result file (table 3.2).

3.2.8 Turn Simulation

In order to produce a simulated turn of radius R (figure 3.15) the table will have to be in motion in the X and Y directions as well as spin with a Ω . As the table rotates about a point R_x along the X axis and R_y along the Y axis with a radius R and angular velocity of Ω the velocity V_t of the table at the wheel will be equation 3.12.

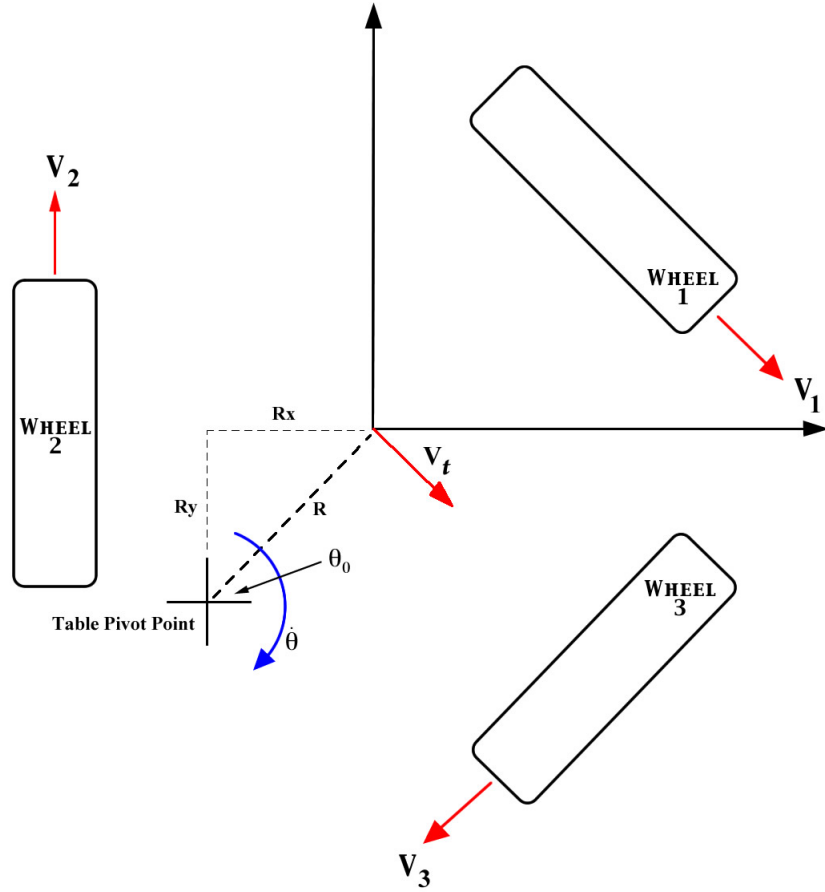


Figure 3.15: Turning Geometry

$$V_t = \Omega \cdot R = \Omega \cdot \sqrt{R_x^2 + R_y^2} \quad (3.11)$$

To calculate the velocities in the X and Y directions (V_x and V_y) the components are found for V_t .

$$V_y = V_t \cdot \text{Cos}(\Theta_0) = \Omega \cdot \text{Cos}(\Theta_0) \cdot \sqrt{R_x^2 + R_y^2} \quad (3.12)$$

$$V_x = V_t \cdot \text{Sin}(\Theta_0) = \Omega \cdot \text{Sin}(\Theta_0) \cdot \sqrt{R_x^2 + R_y^2} \quad (3.13)$$

By definition :

$$\text{Cos}(\Theta_0) = \frac{R_x}{\sqrt{R_x^2 + R_y^2}} \quad (3.14)$$

$$\text{Sin}(\Theta_0) = \frac{R_y}{\sqrt{R_x^2 + R_y^2}} \quad (3.15)$$

By combining equations 3.12, 3.13, 3.14, and 3.15 then simplifying.

$$V_x = \Omega \cdot R_y \quad (3.16)$$

$$V_y = \Omega \cdot R_x \quad (3.17)$$

The table will also rotate about its own axis (Ω_t) at the same rate (Ω) as the wheel rotates about the simulated circle.

Table 3.1 shows a sample Test procedure file for this motion would be for a turn of radius R and angular velocity $\dot{\Theta}$.

3.2.9 Force Assist

One limitation of single wheel testing is that it is hard to simulate a rover on discontinuous terrain. Since all the wheels are working together with dissimilar forces and varying conditions it is hard to approximate by one wheel. To alleviate this limitation SWEET incorporates another feature in that it can simulate the assisted force from the other wheels. If one wheel on a four wheel rover were to make contact with an obstacle (figure 3.16) the remaining wheels would produce a force assisting the stopped wheel allowing it to climb the obstacle. This value, termed F_A for force assistance, can be changed in the test procedure file and applied to a wheel test. In this category of tests called assisted tests the table motion is governed by equation 3.18.

$$V_y = \omega r - KF_y \quad (3.18)$$

Where ω and r are the angular velocity and radius of the test wheel. K in this function is defined in equation 3.19

$$K = \frac{\omega r}{F_A} \quad (3.19)$$

To implement a force assisted test ω (angular velocity of the test wheel) and F_A (limit of assistance force) must be non zero in the test procedure file. Figure 3.17 shows the behavior of F_y versus time in an assisted force test in which $\omega = .06 \frac{rad}{sec}$ and $F_A = 7.26 \text{ kg}$.

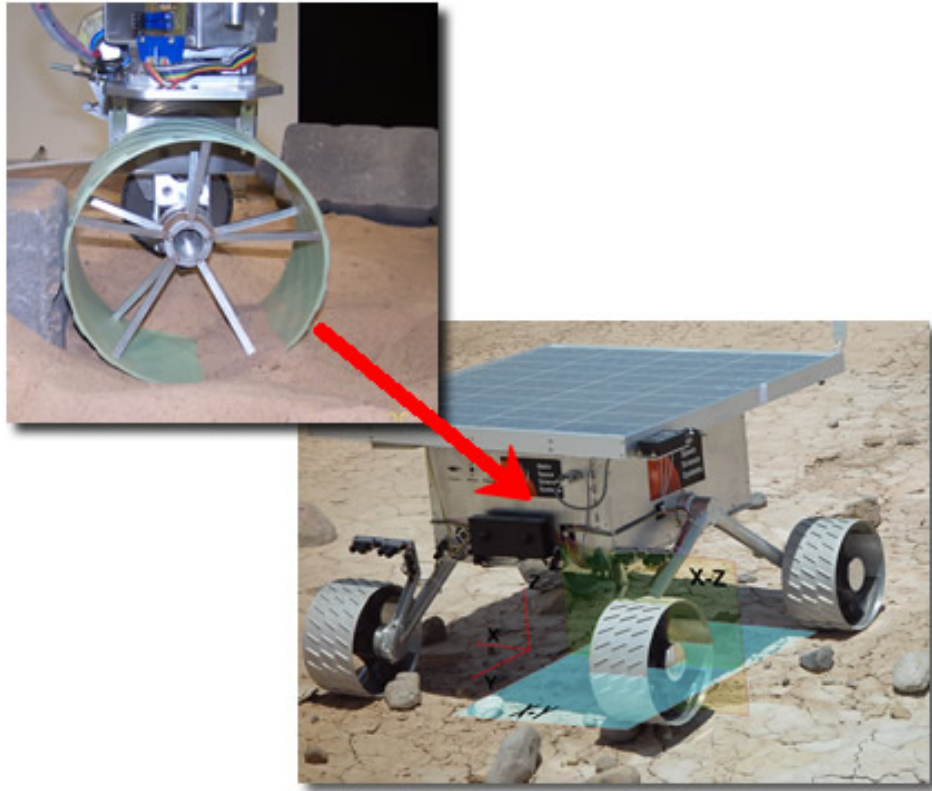


Figure 3.16: Discontinuous Obstacle Situation

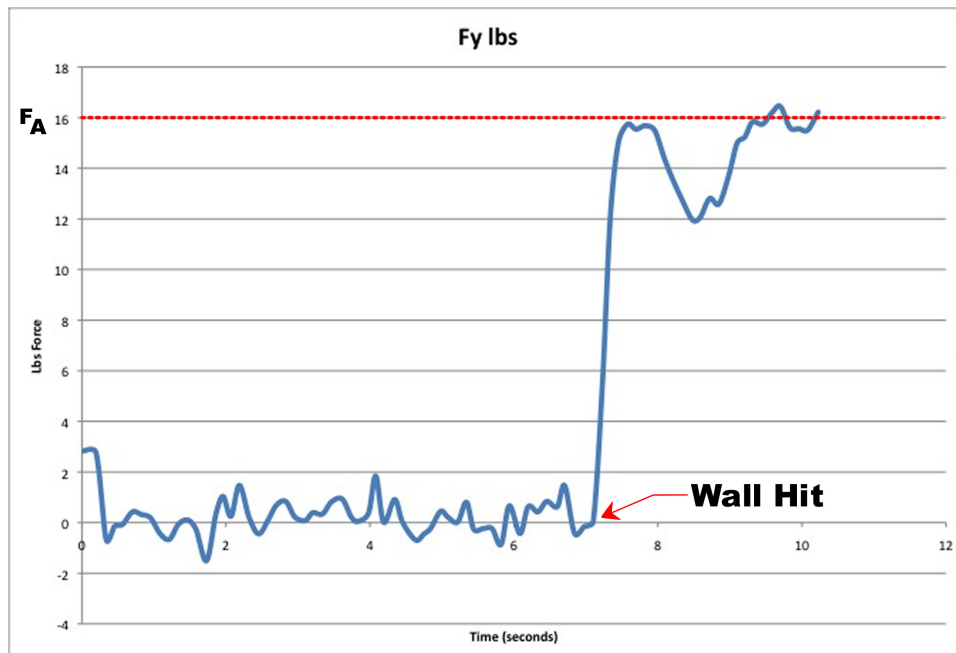


Figure 3.17: F_y behavior in a Force Assisted test

3.2.10 Testing Medium

Different terrain mediums can be used for testing. Those of particular interest are non-cohesive mediums that mimic the terrain of Mars and our Moon. As an preliminary evaluation surface, carpet will be used to test the theories discussed in chapter 4 and also sand will be used due to its low cost and safety in chapter 8. Eventually diatomaceous earth and regolith stimulant will be incorporated to better simulate the Moon and Mars. Rocks will also be used as a medium in varying sizes and orientations depending on the test. Each of the differing terrains will be housed in bins that are easily rolled in and out of the machine for the different tests being done.

The turning bin is 111 cm in diameter and used for skid steering and Ackerman turning and drop compliancy tests (figure 3.18), while the "slope bin" can be adjusted for slope angles of 0-45 degree (figure 3.19) to study a wheel's performance in such a situation.



Figure 3.18: Turning Bin



Figure 3.19: Slope Bin

3.2.11 Experiments

As discussed earlier SWEET loads a pre-programmed test procedure file into an array and progresses through it until the experiment is done. Below are some of the main experiments that would give a good account of a wheel's performance. Vertical loading, via weight on the counter balance, is a variable in each test as well as the surface media.

Static Traction With the table in a fixed position the test wheel power is slowly ramped up to full power until the wheel loses traction. The force in the Y direction (F_y at slipping) is recorded and used to find the static coefficient of friction for that particular wheel to media interaction by the equation: $F_y = \mu_s N$ where N is the normal force from the ground to the wheel. Since N and F_y are known μ_s can be calculated for each wheel. A number of tests will be run to see how μ_s changes with change in weight and sinkage.

Dynamic Traction Similar to Static Traction this test will fix the table position but full power will be given to the wheel throughout the test to ensure constant slipping. The measured F_y in this case will be used to find μ_k by the equation $F_y = \mu_k N$. Also friction can be monitored as the wheel sinks, to gain a better understanding of wheel to soil interaction at differing depths.

Steering Efficiency Steering efficiency is tested by moving the table at a certain ω about an axis that is parallel to the Z axis and recording the wattage that the test motor used during the turn as well as the lateral forces exhibited by the wheel. Simulated dragging can also be used to measure how well the wheel turns under varying working conditions. Several variations to this experiment are possible depending upon what type of turning mobility is being tested. The test apparatus can simulate Ackerman steering by moving the table beneath the stationary wheel in a curving motion and measuring the forces and moments incurred. If a skid steer wheel is being tested, the table is programmed to go at an angle, dependent upon the rover’s geometry, while the test wheel rotates at a set speed. Zero-radius testing is a simple matter of turning the table under the test wheel and measuring M_z .

Rolling Efficiency Much like steering efficiency, rolling efficiency can be measured although this test measures the efficiency on a straight path. This test also uses the wattage used by the test motor and can utilize differing weights and simulated dragging. Rolling efficiency can also be measured on different mediums, composite mediums, and slopes.

Sinkage Using the Z axis encoder the sinkage can be measured as the test is performed. This performance parameter will be recorded for differing loads, slopes, and simulated drags.

Drop/Compliance The SWEET apparatus is able to do drop testing to measure compliancy for each wheel. This test can be executed by disengaging the test leg from a certain height, or can be done by driving the test wheel over a small cliff. Varying weights as well as media can be incorporated. δZ is measured to verify the velocity along the Z axis. The measured F_z is also analyzed in each case to evaluate a wheel’s ability to absorb impact.

Table 3.3: Test Description

Test Name:	Variables	Purpose
Static Traction	F_z , Media	μ_s
Dynamic Traction	F_z , Media, Test Wheel ω	μ_k
Steering Efficiency	F_z , Media, Velocity, Slope (θ) Turning Radius,	$F_{lateral}$, Wattage, ΔZ
Rolling Efficiency	F_z , Media, Velocity, Slope (θ)	Wattage
Sinkage	F_z , Media, Slope (θ), $-F_y$ (drag)	Wattage
Drop	F_z , Media, V_z	F_z , ΔZ

3.3 Calibration

Calibration of the force torque sensor is important to getting useful data from SWEET. Significant detail is presented about the calibration since SWEET’s sensor is unique.

3.3.1 Setup

Calibration was done using a CCI HS-15 commercial force sensor. Figure 3.21 shows the calibration set up for the F_x calibration process. The commercial force sensor is attached to a special calibration axle, in lieu of the test wheel, on one end and to the mount (via a screw) on the other end. Different forces are acquired, on the test foot, by screwing the wing nut in and out. This set up gives adequate control to place forces on the test foot with a accuracy of $\pm 0.044N$. The forces in the X and Y direction was varied from 0 to $4.45N$ with a step of $.445N$ and from 4.45 to $8.90N$ with a step of $.89N$ and finally from $8.90 \rightarrow 22.24N$ with a step of $4.45N$. There were a total of eighteen measurements taken in the X and Y directions and recorded by a Labview calibration VI (figure 3.20). The calibration virtual interface (VI) accepts given forces or torques and records them into a file alongside the average voltage readings of all the sensor channels.

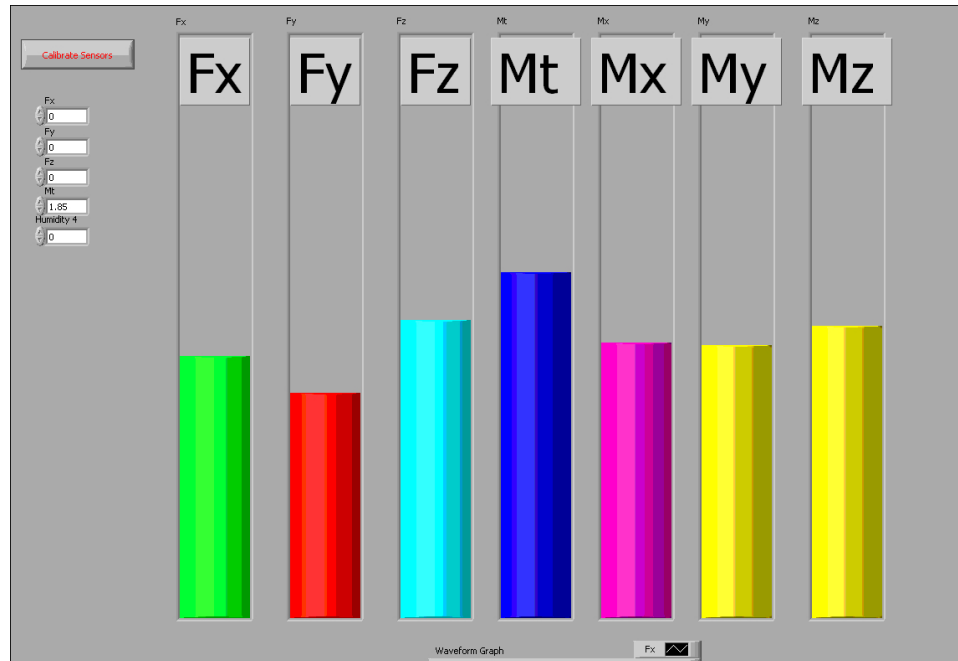


Figure 3.20: Labview Calibration VI

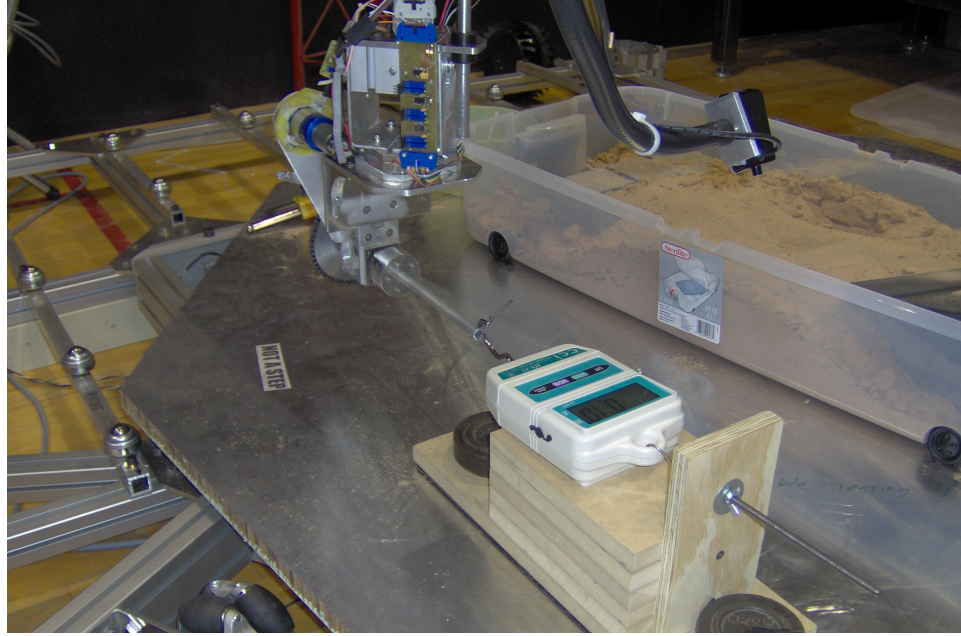


Figure 3.21: Setup for F_X calibration

The test set up for the Y direction (figure 3.22) was much the same as in the X but rotated ninety degrees. The same range of measurements was taken as well as the same total amount.

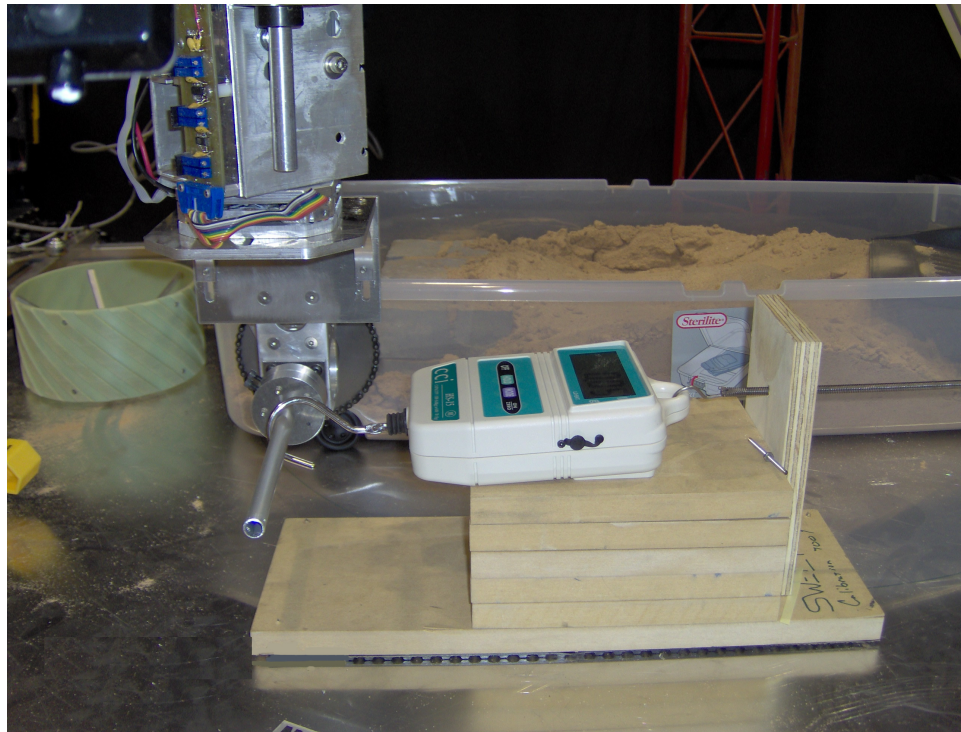


Figure 3.22: Setup for F_Y calibration

Figure (3.23) shows the set up for all the calibration done in the Z direction. At this point the test foot was raised to an adequate height to give enough room for the force sensor and weights. The first measurement was taken with the test axle only, with the next measurement being taken with the force sensor hanging from the calibration axle. After that, weights were hung on the sensor they were added to the force sensor's weight of $5.87N$ and the voltages were read.

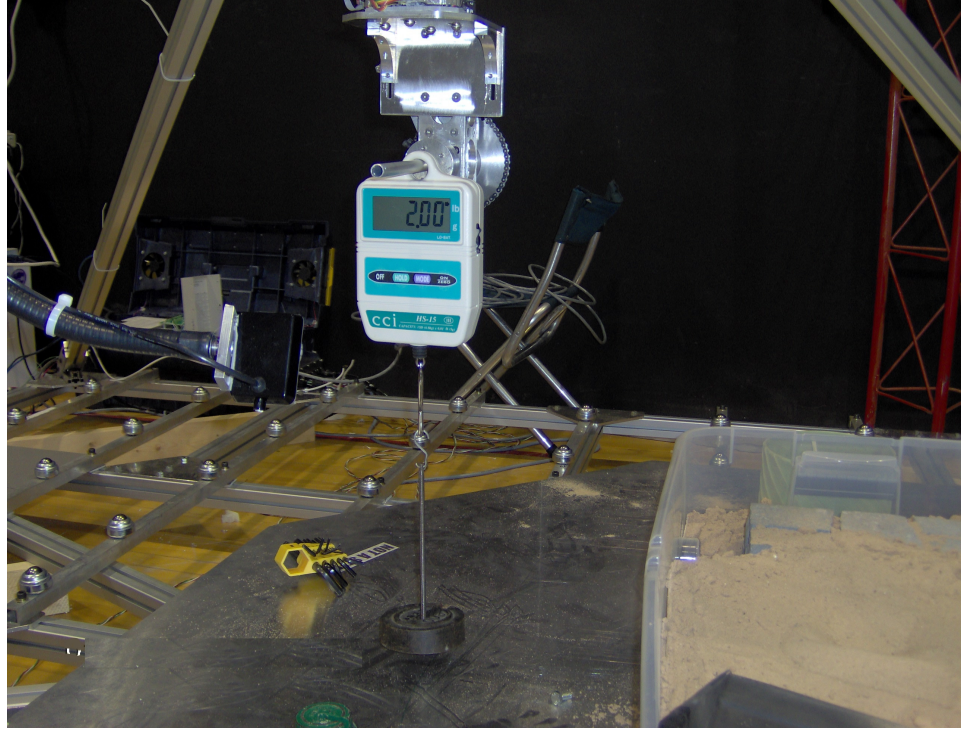


Figure 3.23: Setup for F_Z calibration

Having calibrated the forces for the sensor the torques also need a mapping from voltage to $N \cdot m$. This calibration is done by initially taking the readings with the test foot hanging, and without any outside forces acting on it, then using a $30.48cm$ long, $.49N$, moment arm, that is attached to the base of the force torque sensor, a second reading is done and recorded as the voltage for $.075N \cdot m$. Voltage is then recorded for the commercial force sensor attached to the end of the moment arm. Weights are then added up to $22.24N$ at $.89N$ increments (figure 3.25). This procedure is done for M_y as well (figure 3.24). To calibrate M_z the moment is attached to the side of the force torque sensor base and the commercial force sensor is attached to the end parallel with the floor. The same increments in the calibration of M_z are the same as with M_x and M_y .

The torque sensor directly mounted to the test motor also was in need of calibration. Figure 3.27 illustrates the setup showing an attached 1 ft long .10 lb moment arm parallel to the floor. By using this calibration setup torques can be applied to the sensor in the same way as the force torque sensor was. Measurements are taken from $0 \rightarrow 1.36N \cdot m$ every $.27N \cdot m$ and from $2.72 \rightarrow 6.78N \cdot m$ every $1.36N \cdot m$ for a total of nine measurements.

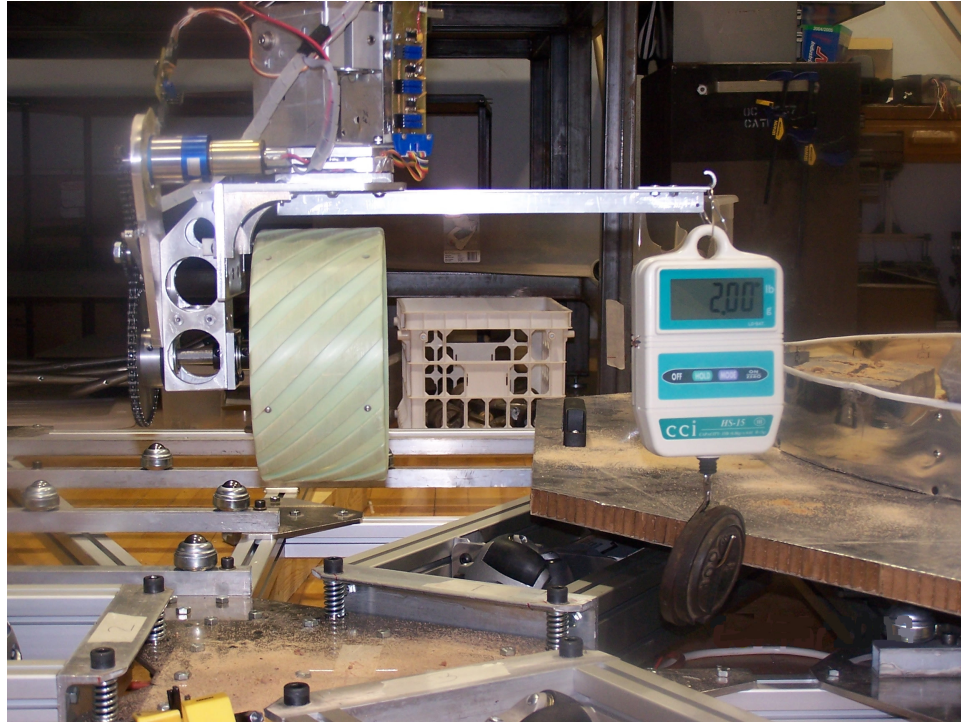


Figure 3.24: Moment about Y Calibration

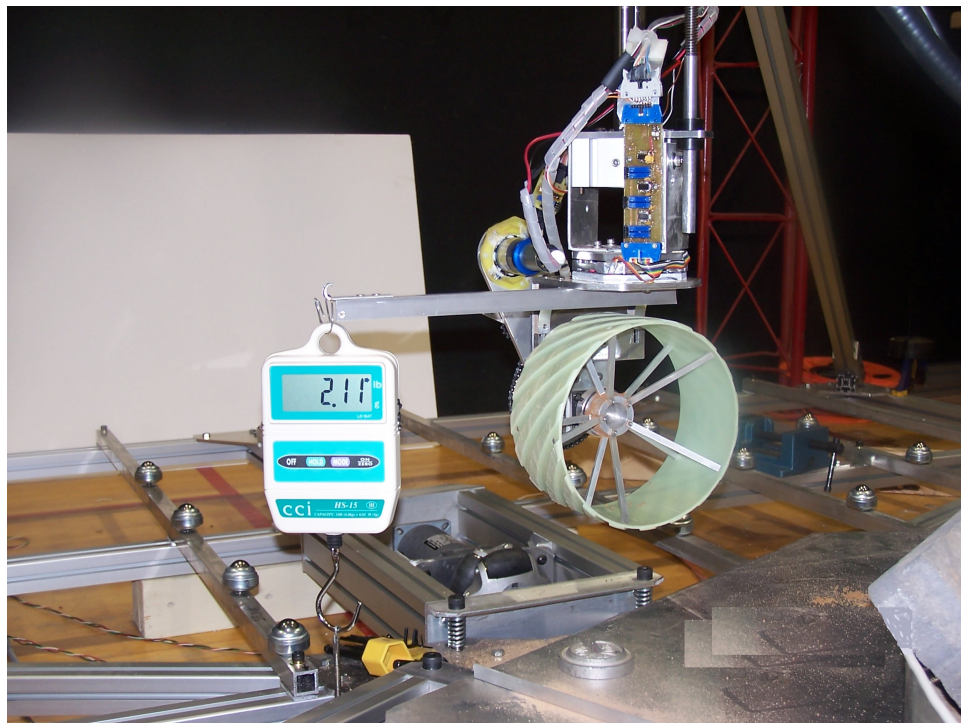


Figure 3.25: Moment about X Calibration

The gains, of the sensors, are easily adjusted by changing the resistance on the FT sensor amplifier (figure 3.26) and are calculated by equation 3.20 [11].

$$G = 5 + \frac{80\Omega}{R_g} \quad (3.20)$$

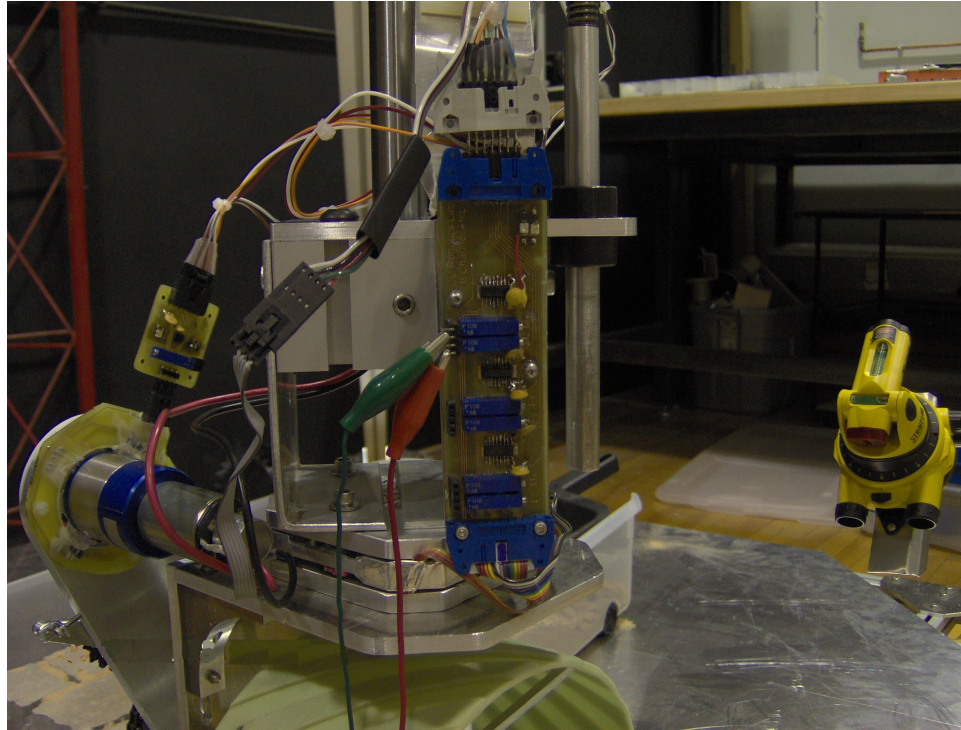


Figure 3.26: Gain adjusting

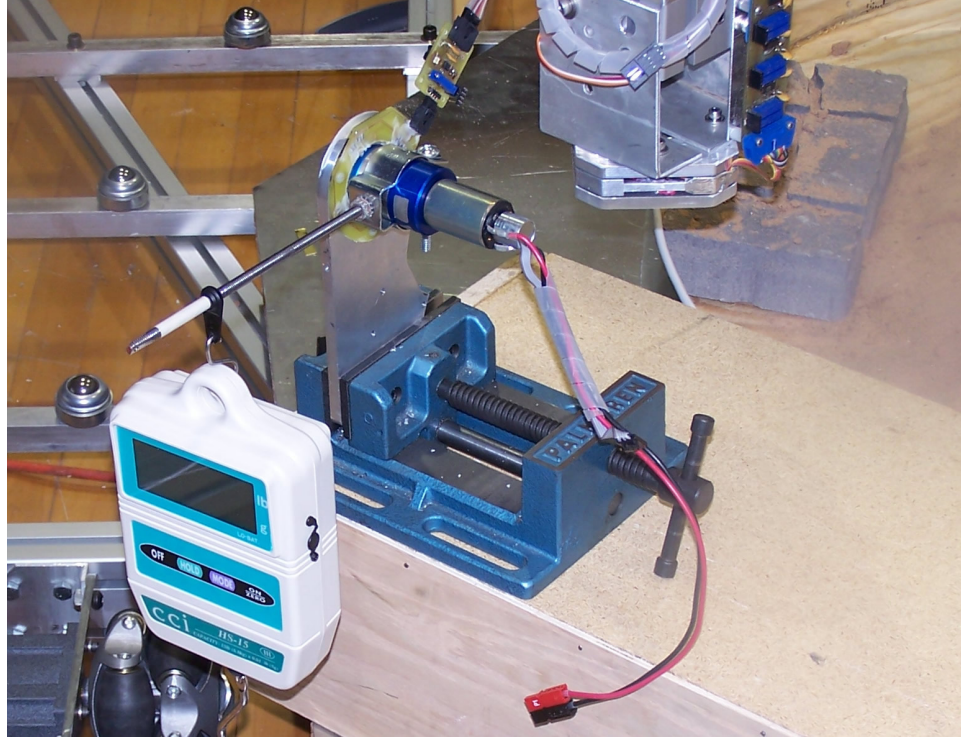


Figure 3.27: Motor Torque Sensor Calibration

3.3.2 Test Results

Graph 3.28 shows the results of the F_x calibration. As expected F_x and M_y are directly affected by pulling along the X axis. All the channels are measured to check for cross talk. Cross talk is the undesired effect of one signal or channel leaking over to another. In force torque sensors this manifests itself the same way. If there is cross talk then a force, applied along the Y axis, will register in other channels such as F_x and F_z . Crosstalk can be mitigated by decoupling the motion in each direction so that only the designated strain gages measure that direction and no other.

In the SWEET force torque sensor the highest cross talk was with F_x being approximately 15% of M_y and was due to the deflection of the moment arm used. The second largest crosstalk value was 6.4% of F_z registering as M_z .

Linearity is also an important factor in sensor design and as seen from all the result graphs 3.28, 3.29, 3.30, 3.31, 3.32, and 3.33 the lowest R^2 factor is .994.

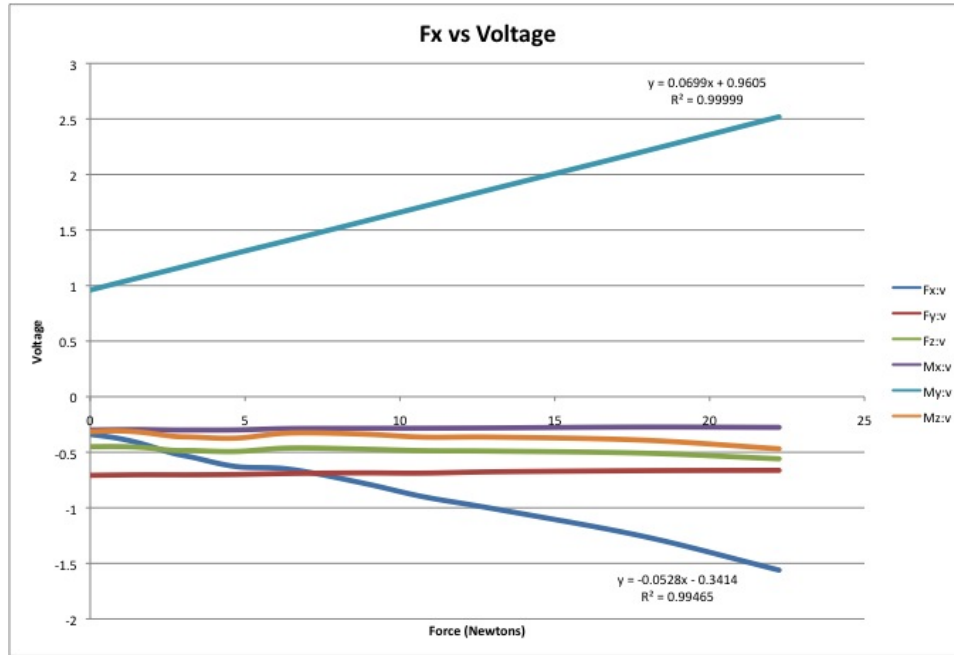


Figure 3.28: F_X Results

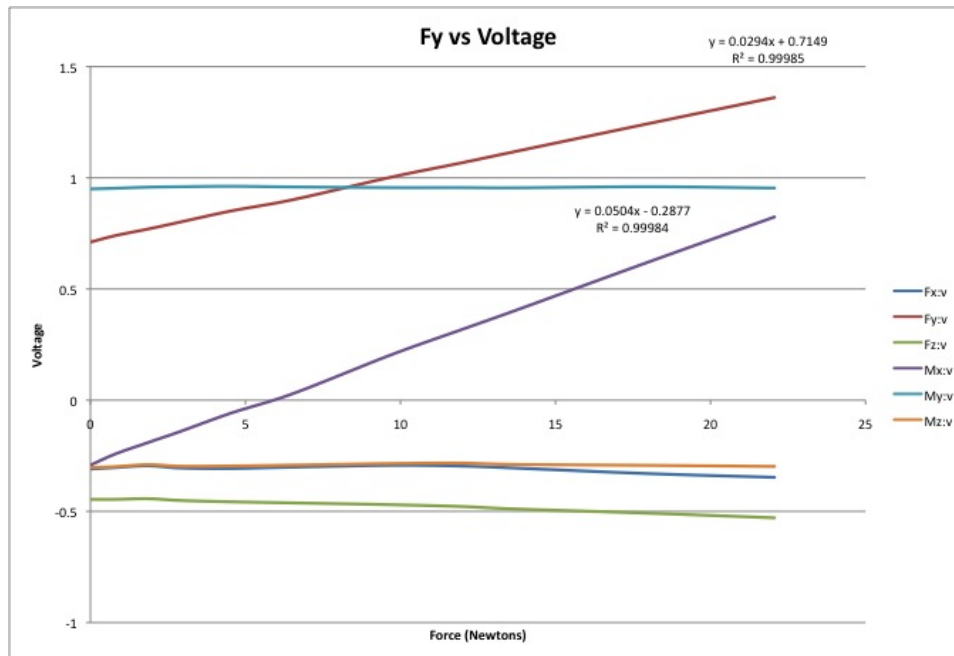


Figure 3.29: F_Y Results

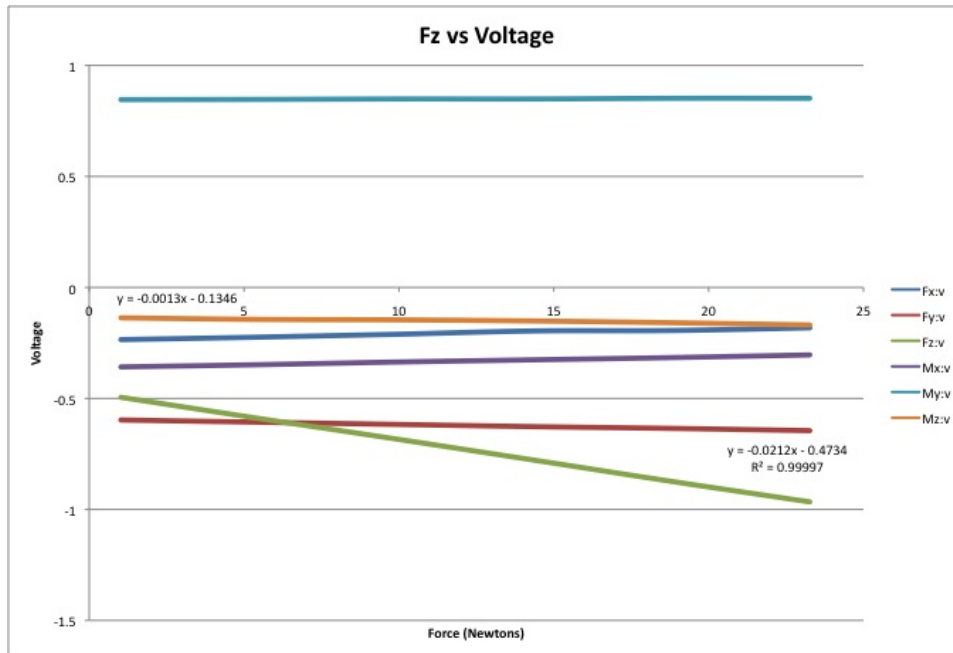


Figure 3.30: F_Z Results

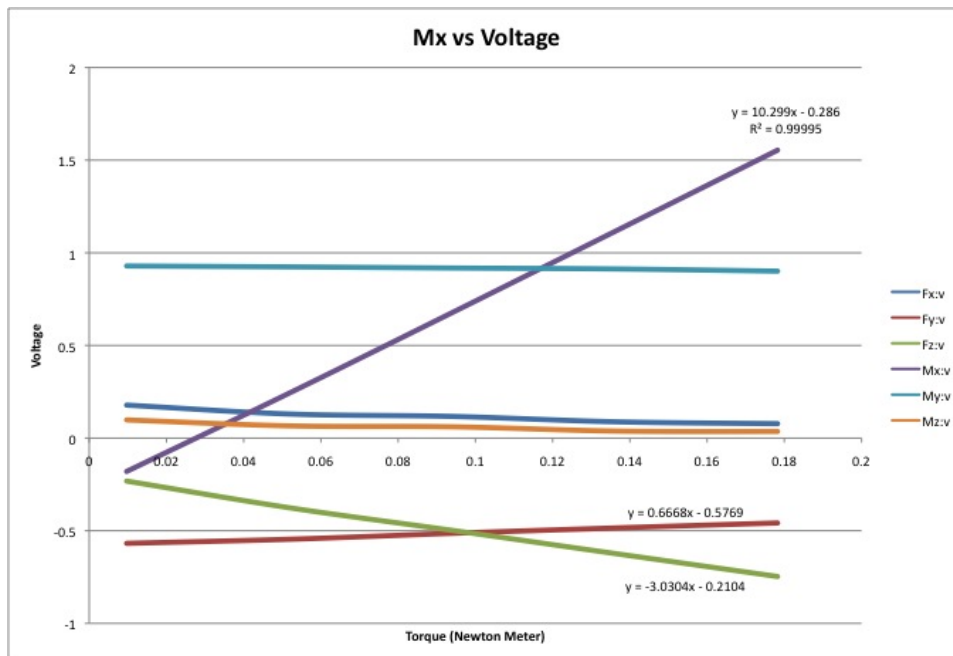


Figure 3.31: M_X Results

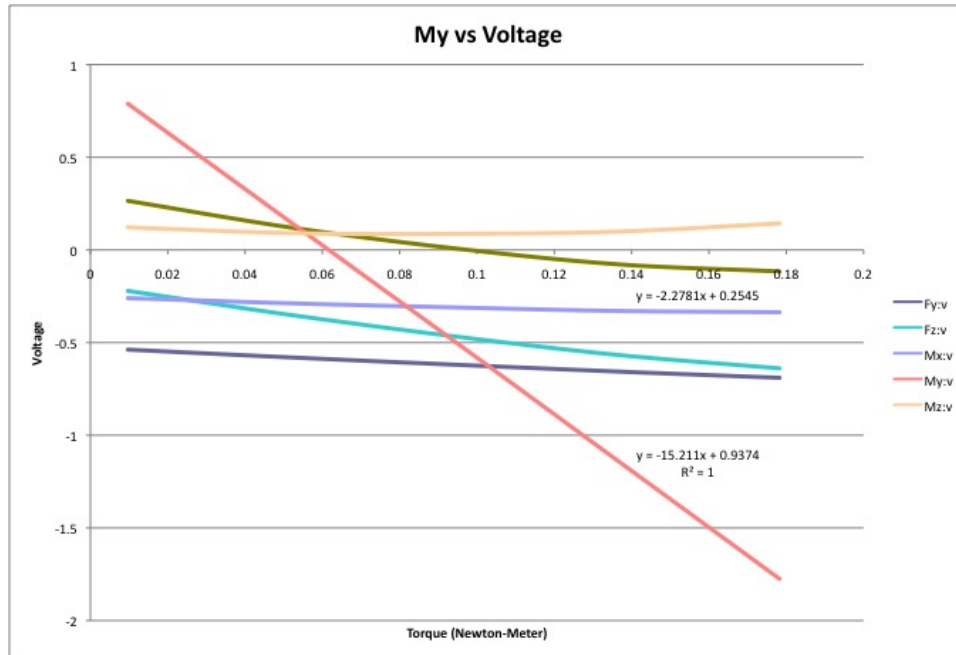


Figure 3.32: M_Y Results

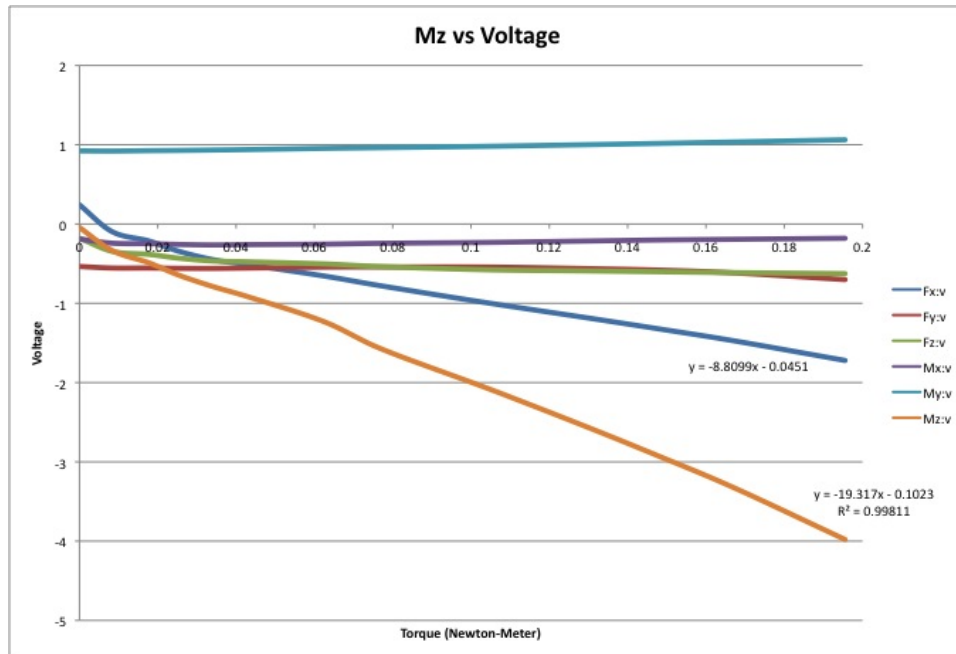


Figure 3.33: M_Z Results

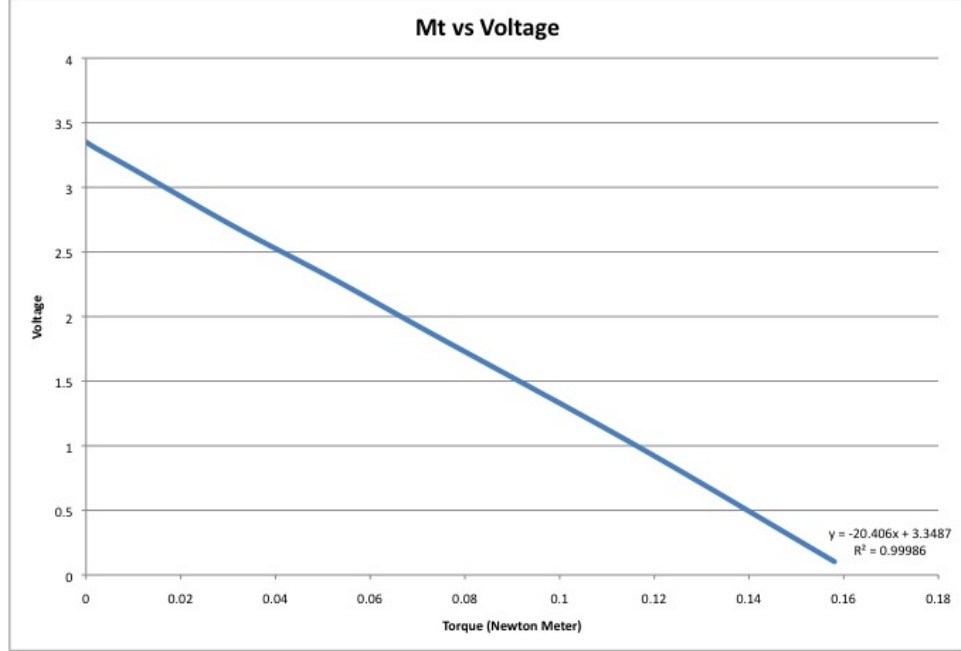


Figure 3.34: M_τ Results

$$49.77V_x - 29.3 = F_x \quad (3.21)$$

$$48.67V_y + 23.72 = F_y \quad (3.22)$$

$$-47.1798V_z - 22.3300 = F_z \quad (3.23)$$

$$.09709V_{mx} + .02777 = M_x \quad (3.24)$$

$$-.06574V_{my} + .06163 = M_y \quad (3.25)$$

$$-.05176V_{mz} - .00529 = M_z \quad (3.26)$$

$$-.049V_{m\tau} + .1641 = M_\tau \quad (3.27)$$

In summary of the calibration the highest error was in the F_z channel, of the force torque sensor, of $\pm .22N$ with a linearity high in the F_x channel of .995. The Z displacement rotary sensor has a resolution of $.013cm$.

3.4 Differences with current and past test beds

From the earlier discussion of current and past rover wheel test beds and the description of SWEET some major differences are apparent that have important possibilities for furthering rover wheel research. These differences, as seen from Table 3.4, allow for significant functionality that no other testing apparatus has.

The biggest and perhaps the most important difference is that while most testbeds can only move along Y , SWEET is additionally actuated in the X direction and is rotatable along the Z axis. This combination gives SWEET the ability to simulate turning at any given radius.

Table 3.4: Applicable Test Apparatus Comparison

Organization	OU	MIT	Tohoku U	LRV	JAXA	Lecce	DLR
Name:	SWEET	FSRL	SWTB	Dynamometer	Exp System	testbed	RCET
Motion: X	YES	NO	NO	NO	NO	NO	NO
Y	YES	YES	YES	YES	YES	YES	YES
Z	FREE/ACT	FREE	FREE	FREE	FREE	FREE	FREE
Ω	YES	NO	Not Actuated	NO	NO	NO	NO
Sensors: Z	YES	YES	YES	YES	YES	YES	YES
X	YES	NA	NA	NA	NA	NA	NA
Y	YES	YES	YES	YES	YES	NO	NA
Ω	YES	NA	NA	NA	NA	NO	NA
6DOFFT	YES	YES	YES	F_y, F_z	YES	NO	NA
Motor τ	YES	YES	YES	YES	NO	NO	YES
Wheel Dia	21 cm	14.6	18 cm	81 cm	NA	16 cm	35 cm
Max V_x	$> 50 \frac{cm}{sec}$	NA	NA	NA	NA	NA	NA
Max V_y	$> 50 \frac{cm}{sec}$	$8 \frac{cm}{sec}$	$3 \frac{cm}{sec}$	$> 3 \frac{m}{sec}$	$40 \frac{mm}{sec}$	Unknown	NA
Max Ω	$2.59 \frac{rad}{sec}$	NA	NA	NA	NA	NA	NA
Wheel ω	$12.17 \frac{rad}{sec}$	$1.1 \frac{rad}{sec}$	$.33 \frac{rad}{sec}$	$> 7.75 \frac{rad}{sec}$	Unknown	Unknown	NA
Counterbalance	YES	Z loading	YES	Z loading	YES	NO	YES
Video	YES	YES	NO	NO	NO	YES	YES
Slope	YES	Possible	Possible	NO	Possible	NO	Possible
Force Feedback	YES	NO	NO	NO	NO	NO	NA

The testing apparatus at the Tohoku University [41] does have the ability to rotate the test wheel along the Z axis and drag it at the angle through the media (figure 3.35). This set up gives a measure of tangential force as it changes with slip ratio ($\frac{V-\omega r}{V}$) and slip angle γ but does not measure efficiency in such an action, nor does it allow the wheel to experience a true turn with Ackerman, skid steer, or zero radius turning.

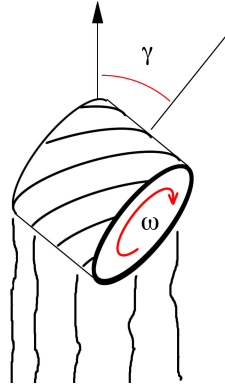


Figure 3.35: Tohoku University Steering Test

It is important to have a better understanding of how wheel design effects steering and efficiency in space vehicle design, because of the new roles these machines will play. Excavation, drilling, and equipment manipulation demand more steering traction than does a conventional rover. Also, space vehicles will always be in need of more efficient designs. If a certain wheel design saves energy in turning then it is worth pursuing as a design option and further study to evaluate the trade between steering efficiency and straight line rolling efficiency.

The second unique design feature that SWEET provides is that its size allows for a large drop test velocity. As rovers and space terrain vehicles, as well as their missions develop so will their need for more compliance in wheel and suspension design. SWEET's geometry allows for a one meter drop giving a V_z of $4.43 \frac{m}{sec}$ which would be the same as dropping from 2.63 meters on Mars.

Finally SWEET's ability to simulate a dragging force via a force feedback loop is another feature that current test beds do not enjoy. This component allows SWEET to simulate crippled scenarios such as what happened to the Mars rover Spirit on March 13th 2006 when its front right wheel stopped working [24]. SWEET can simulate Spirit's mishap and test what wheels work better on slopes or straights while dragging either a dysfunctional assembly or equipment that will be needed for occupation or science. As space vehicles are needed for more than roving there will be more of a need for dragging, pushing, or excavating, and more of a need for wheels that perform better doing these activities.

CHAPTER 4

Skid Steer Turning Prediction Theory

4.1 Introduction

Skid steering turn performance is beyond the ability of most single wheel test systems but is a very important to the performance of the entire skid steer rover. If a method can be demonstrated to transform data from a single wheel skid steer test to predict the turning efficiency of a skid steer rover, then skid steer turning is one more behavior that can be studied and improved upon cheaply and thoroughly using the a single wheel testing method. This ability to analyze skid steering through single wheel testing is also a demonstration of the utility of this work. This chapter describes a technique to take the forces incurred on the test wheel, measured in a single wheel test, and map them to a real life turning rate value for a full rover assembly. This chapter also discusses ways to augment skid steering performance in light of the acting forces.

4.2 Generalized Equations of Motion

Figure 4.1 is a force body diagram of a skid steer rover turning about its center (O). Equations of motion can be expressed as in equations 4.1, 4.2, and 4.3.

$$m\ddot{x} = \Sigma(F_x - f_x) \quad (4.1)$$

$$m\ddot{y} = \Sigma(F_y - f_y) \quad (4.2)$$

$$I\dot{\Omega} = a(-f_{x_1} - f_{x_2} + F_{x_1} + F_{x_2}) + b(-f_{x_3} - f_{x_4} + F_{x_3} + F_{x_4}) + t(\Sigma F_{y_i} - \Sigma f_{y_i}) + M \quad (4.3)$$

Where m is the mass of the rover, I is the rotational inertia, \ddot{x} and \ddot{y} are accelerations in the X and Y directions, M is any exterior moment acting on the rover, and $\dot{\Omega}$ is the angular acceleration in the XY plane. F_x and F_y are forces either directly or indirectly produced by the motors turning the wheels while f_x and f_y are frictional forces dependent on the wheel to soil coefficient of friction, velocity, and weight of the rover. If all the resistive (frictional) forces are shifted to the left side, these equations become 4.4, 4.5, and 4.6.

$$m\ddot{x} + \Sigma f_{x_i} = \Sigma F_x \quad (4.4)$$

$$m\ddot{y} + \Sigma f_{y_i} = \Sigma F_y \quad (4.5)$$

$$m\dot{\Omega} + a(f_{x_1} + f_{x_2}) + b(f_{x_3} + f_{x_4}) + t(\Sigma f_{y_i} = a(F_{x_1} + F_{x_2}) + b(F_{x_3} + F_{x_4}) + t\Sigma f_{y_i} + M \quad (4.6)$$

For the test we are only concerned with a turn about the rover's center the assumption $a=b$ can be made. Also if q is defined as the state vector with components $q = (x, y, \phi)$ where x , y , and ϕ are the rover's position and orientation. All of the resistive forces

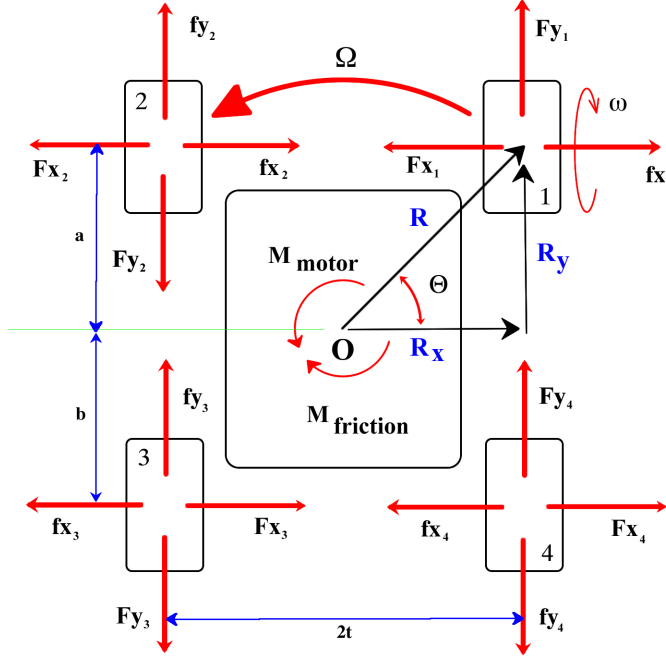


Figure 4.1: Skid Steer Force Body Diagram

and actuated forces are dependent on the state values as well as the wheel to soil coefficient of coulomb and viscous friction (μ_k and μ_v). As seen in equations 4.7 through 4.10 it is not assumed that friction is not dependent on slip as in [20] where the coulomb friction model assumes that friction jumps to a static level immediately once slippage has occurred. This assumption is not accurate at low slippage (both V_X and V_Y) rates which is discussed by [59] as well as validated by the results in following chapters. Also it can be observed that f_x is dependent on \dot{x} as well as \dot{y} since slip of the wheel ($\omega r - \dot{y}$) has a significant affect on friction. F_x and F_y are also dependent on the state vector for the same reason.

$$f_x = f(\dot{x}, \omega r - \dot{y}, \mu_k, \mu_v) \quad (4.7)$$

$$f_y = f(\omega r - \dot{y}, \mu_k, \mu_v) \quad (4.8)$$

$$F_x = f(\dot{x}, \omega r - \dot{y}, \mu_k, \mu_v) \quad (4.9)$$

$$F_y = f(\omega r - \dot{y}, \mu_k, \mu_v) \quad (4.10)$$

If all the resistive forces are grouped together (eq 4.11) then the generalized equation simplifies to equation 4.12.

$$R(\dot{q}) = \begin{bmatrix} \Sigma f_x \\ \Sigma f_y \\ a \cdot \Sigma f_x + t \cdot \Sigma f_y + M \end{bmatrix}, F_{total} = \begin{bmatrix} \Sigma F_x \\ \Sigma F_y \\ \Sigma M \end{bmatrix} \quad (4.11)$$

$$m\ddot{q} + R(\dot{q}) = F_{total}(\dot{q}) \quad (4.12)$$

4.3 Rover Equilibrium Turn

Skid steering is used on many rovers [30, 68, 61] and is an unintuitive multiple force process which is due to the longitudinal and lateral sliding that must take place for a skid steer rover to turn. Since kinetic sliding is unavoidable in a skid steer turn the system must be thought of more in a kinetic sense rather than just mapped rigidly with kinematic constraints [44]. Some research has been done with skid steering mobility [47, 23, 25, 44, 59] and lays out a similar kinematic approach as taken above, but none of the work found describes the following behavior of the forces on a wheel during a skid steer turn. When a rover initiates a turn its rotation (in the $X - Y$ plane, figure 4.1, 4.2) will accelerate up to an equilibrium spin rate Ω (Fig. 4.1) at which point it will stabilize and the moment about its center (M_o) will equal zero. With $\ddot{q} = 0$ and $M = 0$ equation 4.12 simplifies to 4.13.

$$\begin{bmatrix} \Sigma f_x \\ \Sigma f_y \\ a \cdot \Sigma f_x + t \cdot \Sigma f_y \end{bmatrix} = \begin{bmatrix} \Sigma F_x \\ \Sigma F_y \\ a \cdot \Sigma F_x + t \cdot \Sigma F_y \end{bmatrix} \quad (4.13)$$

If $F_x - f_x$ and $F_y - f_y$ are defined as F_X and F_Y meaning that F_X and F_Y are resultant forces acting on the wheel equation 4.13 gives equations 4.14.

$$\begin{bmatrix} \Sigma F_X \\ \Sigma F_Y \\ a \cdot \Sigma F_x - t \cdot \Sigma F_y \end{bmatrix} = \begin{bmatrix} 0 \\ 0 \\ 0 \end{bmatrix} \quad (4.14)$$

If all wheels are assumed to have equal footing and equal forces acting on them then equation 4.14, neglecting the trivial solutions, can be further reduced as equation 4.15.

$$F_Y = \frac{a}{t} F_X = F_X \cdot \tan(\Theta) \quad (4.15)$$

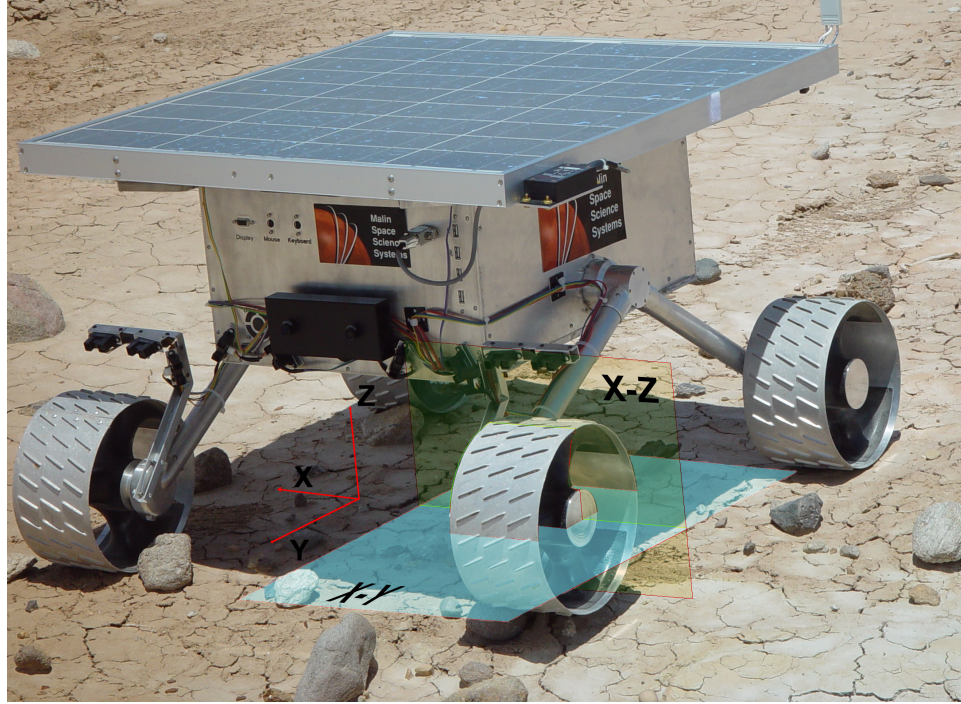


Figure 4.2: Rover Coordinate Axis

Equation 4.15 describes a relationship between F_X and F_Y at the turning equilibrium point and is dependent upon the rover geometry (Θ) with the assumption of a single point contact between wheel and soil. If the rover were slender (Fig. 4.4-a) then Θ would be larger than $\frac{\pi}{4}$ and F_X would be much smaller than F_Y . If $\Theta = \frac{\pi}{2}$ then $F_Y = \infty$. This would mean that no matter how much force a blank wheel could exert on the ground the rover's spin rate Ω would always be zero as if two wheels were pulling directly opposite of each other and canceling each other out. If, on the hand, Θ were equal to zero, as in Fig. 4.4-b, then F_X and F_Y (the net force of power and friction) would also be equal to zero. This configuration is better known as Ackerman steering which means that the wheels have no lateral slip and if there is no longitudinal slip then the turning rate can be calculated precisely by equation 4.16. For further reading on the force behavior consult [28].

$$\Omega_{Ackerman} = \frac{\omega r}{R}, F_Y = 0. \quad (4.16)$$

where ω is the wheel angular velocity in radians per second, r is the wheel radius, and R is the distance from the center of the wheel to the center of rotation of the rover in the $X - Y$ plane.

4.4 Turning Rate Targets

Equation 4.16 refers to the target turning rate $\Omega_{Ackerman}$ without longitudinal slipping for an Ackerman steering geometry. To calculate the target turn rate for a skid steer rover where $\Theta \neq 0$, Θ must be taken into account and is reflected in equation 4.17.

If an Ackerman wheel was pivoted Θ degrees such as with a Skid Steered wheel, a target value for its turning rate might be equation 4.17.

$$\Omega_{Target} = \frac{\omega r}{R} \cos(\Theta), F_y \neq 0 . \quad (4.17)$$

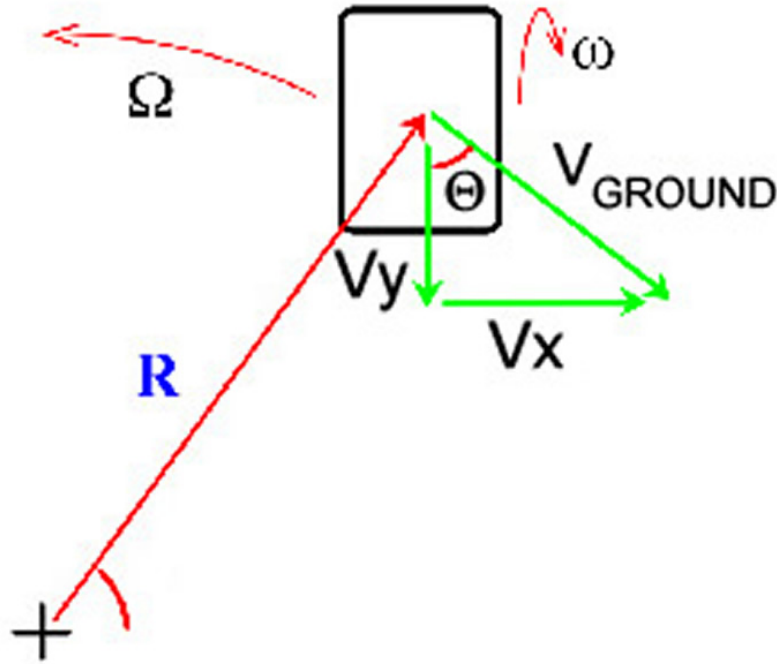


Figure 4.3: Skid Steer Kinematics

Ω_{Target} is the turn rate if the wheel could produce the same forward velocity as it would if in an Ackerman turn. This is impossible because V_Y of a skid steer wheel will always be less than V_Y of an Ackerman wheel since the wheel is sliding due to the realities of skid steering. Even though $V_{Y-SKIDSTEER} < V_{Y-Ackerman}$ the spin rate of a rover (Ω) could be larger than Ω_{Target} if:

- Due to the tread there exists a resultant f_X that turns the rover faster.
- The frictional force f_X is much smaller than the f_Y force. If in the extreme idealistic case where $f_X = 0$ then according to equation 4.15 the rover would accelerate its spin up to the point where $F_Y = 0$.

To find the value of $\Omega_{F_Y=0}$, which is the spin rate at which there is no longer a net force in the Y direction, the longitudinal velocity (V_y)(Fig. 4.3) of the ground under the wheel must be equal to the velocity of the wheel rim (ωr) therefore making $F_y = 0$ (no slip). Equation 4.22 explains this relationship, and is the same kinematic relationship that an Ackerman steered wheel would be described by if it were R_X distance from the center of the turn.

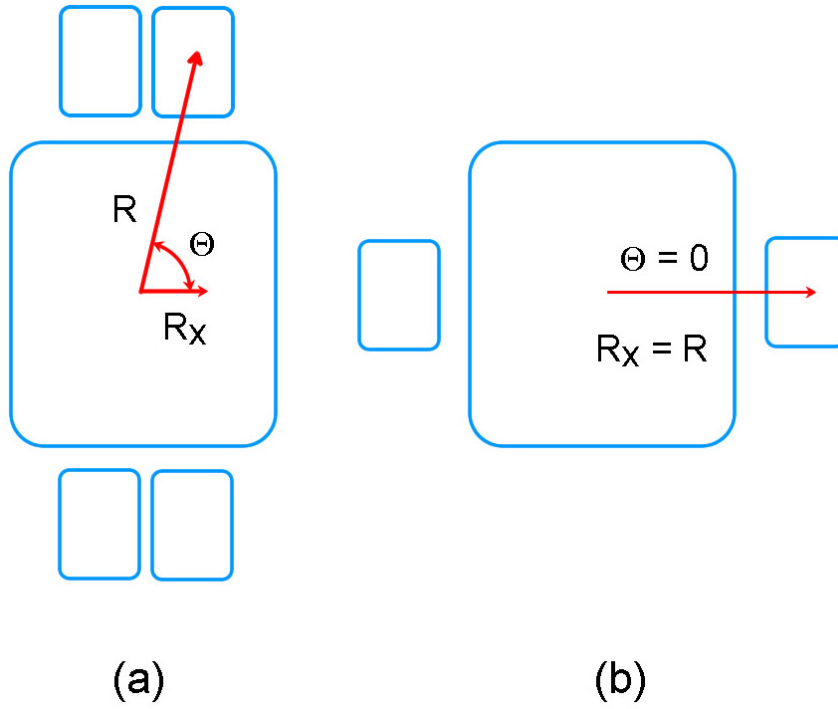


Figure 4.4: a) Slender Skid Steer Rover b) Ackerman Skid Steer Rover

$$V_y = \omega r . \quad (4.18)$$

$$V_y = \cos(\Theta) V_{ground} . \quad (4.19)$$

$$V_{ground} = \Omega R . \quad (4.20)$$

$$\omega r = \Omega R \cos(\Theta) . \quad (4.21)$$

$$\Omega_{F_y=0} = \frac{\omega r}{R \cos(\Theta)} = \frac{\omega r}{R_x} . \quad (4.22)$$

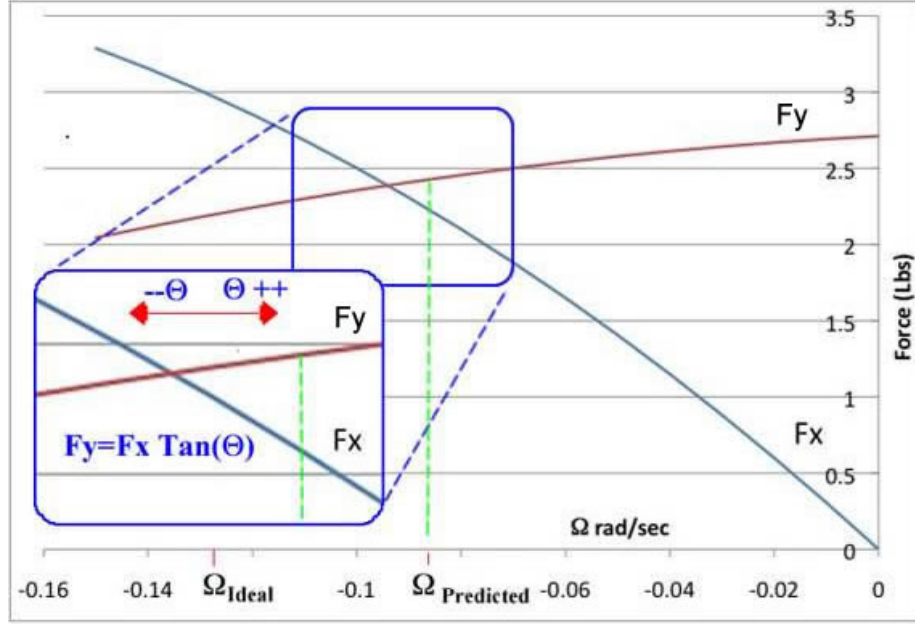


Figure 4.5: Force vs Spin Rate Example

4.5 Wheel Kinetics

For the right front wheel of a rover pivoting in the counter clockwise direction, the ground must move under it in the opposite direction ($-\Omega \frac{rad}{sec}$) and the relationship of the forces on the wheel, as the spin rate ($|\Omega|$) of the ground under the wheel increases, can be shown in illustration 4.5. When Ω is equal to zero the wheel being tested rotates ($\omega \frac{rad}{sec}$) but does not move. This causes a force to be measured on the force torque sensor and is just the Coulomb kinetic friction ($F_Y = \mu_k N$) between the wheel and ground in the Y direction. For a blank wheel on smooth ground there is no F_X at this point. F_X increases with the spin rate of the ground under the wheel while F_Y decreases due to the table moving more and more along the wheel's direction of motion. When the two graphs intersect ($F_Y = F_X$) the corresponding Ω at this point would represent the equilibrium spin rate ($\Omega_{Predicted}$) of a square rover ($\Theta = \frac{\pi}{4}$). To find the equilibrium point, of a rectangular rover, equation 4.15 adds the needed constraint between F_X and F_Y . For the SR2 [62] rover $\Theta = .8477 rad$ when combined with equation 4.15 this simplifies to equation 4.23.

$$F_y = 1.133F_x . \quad (4.23)$$

In essence what we are doing is operating the test wheel and the ground under the wheel independently by varying the table speed (Ω) and keeping the wheel spin rate (ω) constant as the table moves in a simulated skid steer turn based on the rover geometry that we are predicting for. By observing the behavior of the forces acting on the wheel it can be seen when the forces satisfy equation 4.23 which means the corresponding Ω is the predicted rover spin rate. In Fig. 4.5 this relationship gives

a point just right of the intersection point, for the SR2 rover, and corresponds to a $\Omega_{Predicted}$ value which is the predicted spin rate of a rover fitted with four wheels with the same orientation and identical tread to the wheel tested on the same soil. This mapping, of the forces measured on a single wheel test to the full rover performance, gives a means to predict a rover's performance by single wheel testing.

It should be noted again how a rover's geometry affects this relationship. As Θ increases above $\frac{\pi}{4}$ the rover is thinner (Fig. 4.4-a) which makes turns less efficient and $\Omega_{Predicted}$ becomes smaller. If, on the other hand, Θ decreases its $\Omega_{Predicted}$ value increases until $\Theta = 0$ thus making $\Omega_{Predicted} = \frac{\omega r}{R}$ which is an Ackerman steering geometry.

4.6 Increasing turning efficiency

Turning efficiency in this case is the turning speed of the rover per a given ω wheel spin rate. If efficiency was 100% then the rover's spin would only be dependent on ω and its geometry. Since there is friction, especially in skid steering, the efficiency is reduced and is also dependent on the soil and wheel properties. From the kinetic behavior of a wheel in a skid steer turn a few observations can be made for how to increase the efficiency of a turn by looking at the Ω -Force graph of figure 4.5. The objective would be to increase the $\Omega_{Predicted}$ and move it to the left which means moving the intersection constraint point ($F_Y = F_X \cdot \tan(\Theta)$) in that direction giving the rover a more efficient turn. The efficiency discussed thus far has been turning rate per wheel rad/sec ($\frac{\Omega}{\omega}$) and does not factor in power usage of the turns, which will be discussed in chapter 10. The following are a few observations on how to accomplish increasing skid steering turning efficiency.

4.6.1 Increasing Longitudinal Friction

One way to increase Ω is by increasing F_Y which translates as increasing the frictional force in the wheel's forward Y direction. If this can be accomplished without increasing the friction along the wheel's axis (X direction), or at least not proportionally, then the skid steer turn rate will increase and a more efficient turn will be realized. Adding grousers or changing wheel material are two ways the frictional force, can be augmented. Space rovers are limited in their useable materials due to the harshness of space. Adding grousers can be done but other factors such as sinkage might be adversely affected along with turning. The key in any change, especially in light of the decoupled nature of the component forces discussed in this chapter, is to increase the friction along Y while decreasing it along X .

4.6.2 Offsetting Lateral Friction

Another way to move the equilibrium constraint point further to the left of the Ω -Force graph is to decrease f_X . In figure 4.6 there are three f_X graphs depicting three different f_X zero intercepts. These intercepts symbolize the inherent frictional force

along the axis of the wheel, for a given angular velocity ω which should be zero for a blank wheel but not necessarily for a treaded wheel.

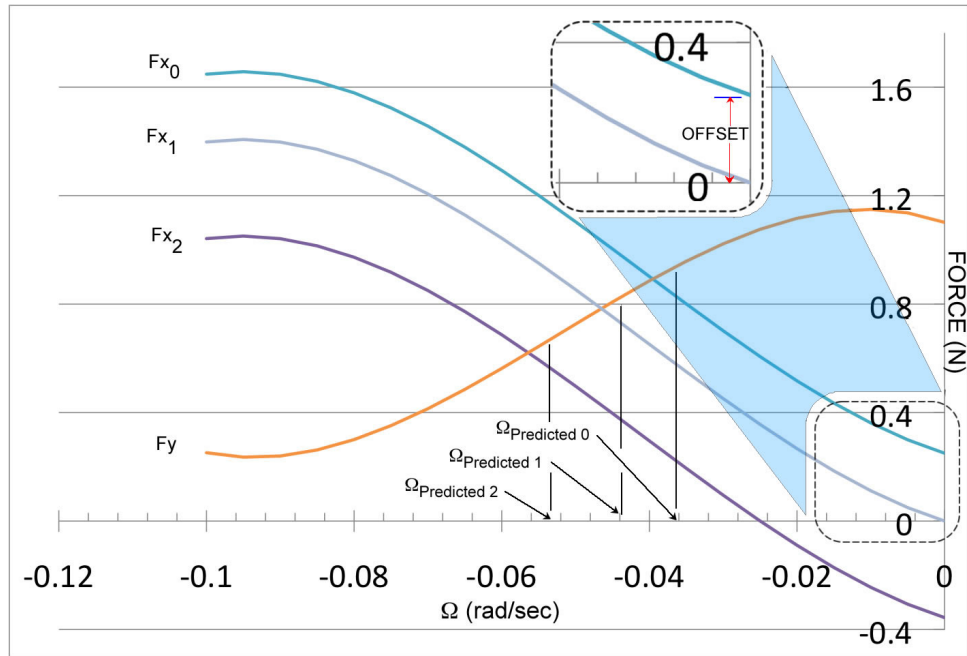


Figure 4.6: Ω -Force graph offset illustration

In considering a non-blank wheel, particularly a directional patterned wheel such as figure 4.8 there is a possibility of a force along the X axis induced by the tread pattern dependent on ω . If the wheel is mounted in the correct orientation then the additional force will benefit the turning efficiency by offsetting the frictional force, f_X , produced by the turn therefore increasing Ω . The theoretical target turning rate for a directional treaded wheel has to include any V_x produced by the tread (eq 4.24 and figure 4.8).

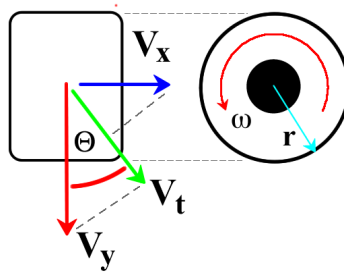


Figure 4.7: Kinematic explanation of treaded wheel

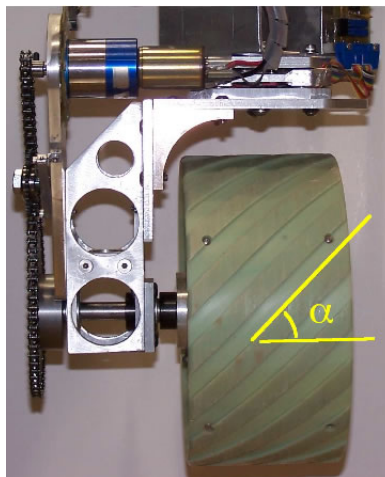


Figure 4.8: Measuring α on a treaded wheel

$$V_t = V_y \cos(\Theta) + V_x \sin(\Theta) . \quad (4.24)$$

$$V_y = \omega r . \quad (4.25)$$

$$V_t = \Omega R . \quad (4.26)$$

$$\Omega_{Target} = \frac{1}{R} (\omega r \cos(\Theta) + V_x \sin(\Theta)) . \quad (4.27)$$

If Ω_{Target} were related to the tread design only (such as a bolt screwing into a nut), and ignored any soil interaction, V_x would be a function of ω , α , and r (equation 4.28) which would give the Ω_{Target} in equation 4.29. If the wheels were to be switched and placed on the rover in the opposite orientation the inherent F_X force would work against the turn and decrease the Ω (figure 4.9). There are precedent cases of vehicles that rely on this behavior to maneuver such as the Chrysler Marsh Screw Amphibian (figure 4.10).

$$V_x = \frac{\omega r}{\tan(\alpha)} . \quad (4.28)$$

$$\Omega_{Target} = \frac{\omega r}{R} \left(\cos(\Theta) + \frac{\sin(\Theta)}{\tan(\alpha)} \right) . \quad (4.29)$$

4.6.3 Decreasing Lateral Friction

From the Ω -force graphs it can also be seen that as $F_x(\Omega)$ is reduced (F_{x1} and F_{x2} in figure 4.9) along all values of Ω then the $\Omega_{Predicted}$ value would be increased. This can be explained physically as the effect of reducing the rover's kinetic friction in the X direction. If F_x were reduced enough, without reducing F_Y or at least not proportionally, making the wheel anisotropic, then it is possible to increase Ω above the target rate given by equation 4.17.

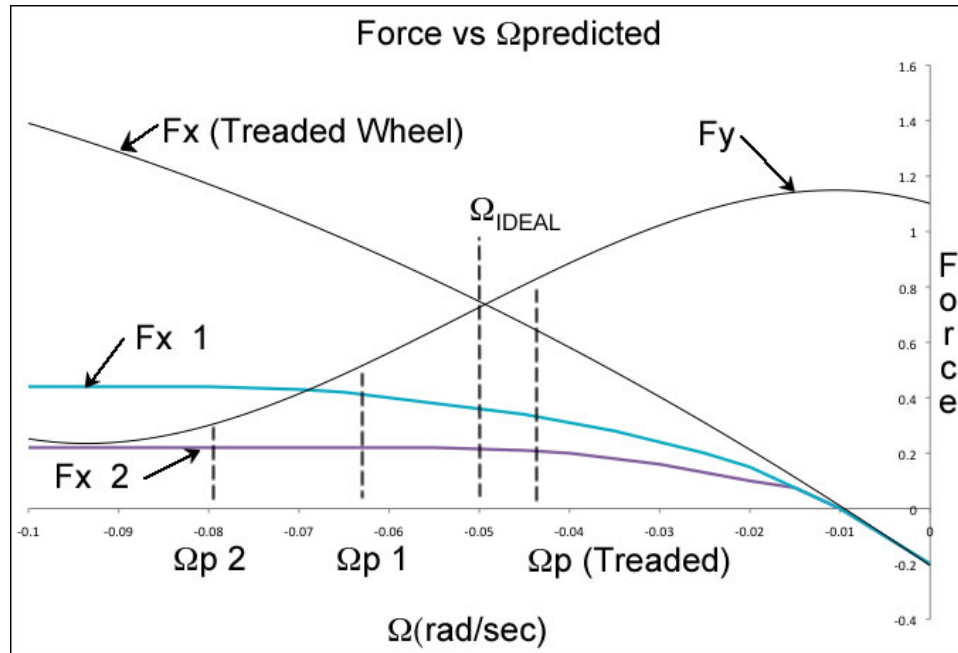


Figure 4.9: Fx Reduction Example



Figure 4.10: Chrysler Marsh Screw Amphibian [2]

One wheel that reduces lateral friction is an Omni wheel (figure 4.11). Omni wheels are wheels fitted with rollers orthogonally placed along the circumference which allow for an extra degree of freedom along the wheel's axis and have been studied and used in several applications [67, 27, 72, 29]. Chapter 6.3 discusses results from an Omni wheel in a skid steer test.

4.6.4 Bow Wave Reduction



Figure 4.11: Omni Wheel [43]

Figures 4.12, 4.13, and 4.14 illustrate the bulldozing phenomenon that happens in certain wheel to soil interactions. Unless a wheel has a high slip rate it will experience a bulldozing effect of some sort or a bow wave forming directly in line of its motion especially in non-cohesive soil such as sand. In effect the wheel is pushing soil out of the way and doing work which causes a force in the opposite direction of travel. Bulldozing works against turning in both the X and Y directions. The Y direction exhibits more of the bow wave behavior while the X direction could be described more as plowing (figure 4.15) which causes a greater frictional force. Larger grousers and directional chamfers (figure 4.16) could possibly help with this resistance to try to dig away and stay on top of the bow wave as the wheel spins. More experiments would need to be done on these non-cohesive soils to validate these designs. Other work that has been done in this area is Yoshida et al. discusses how F_X decreases with increasing wheel spin rate (ω) [70], also Rowe and Hegedus [63] (figure 4.12 and 4.13) show how a bow wave can be diminished by different wheel shapes. figure Although the bow wave phenomenon is a significant effect on wheel to soil interaction it is extremely hard to analytically calculate without making many approximations [69].

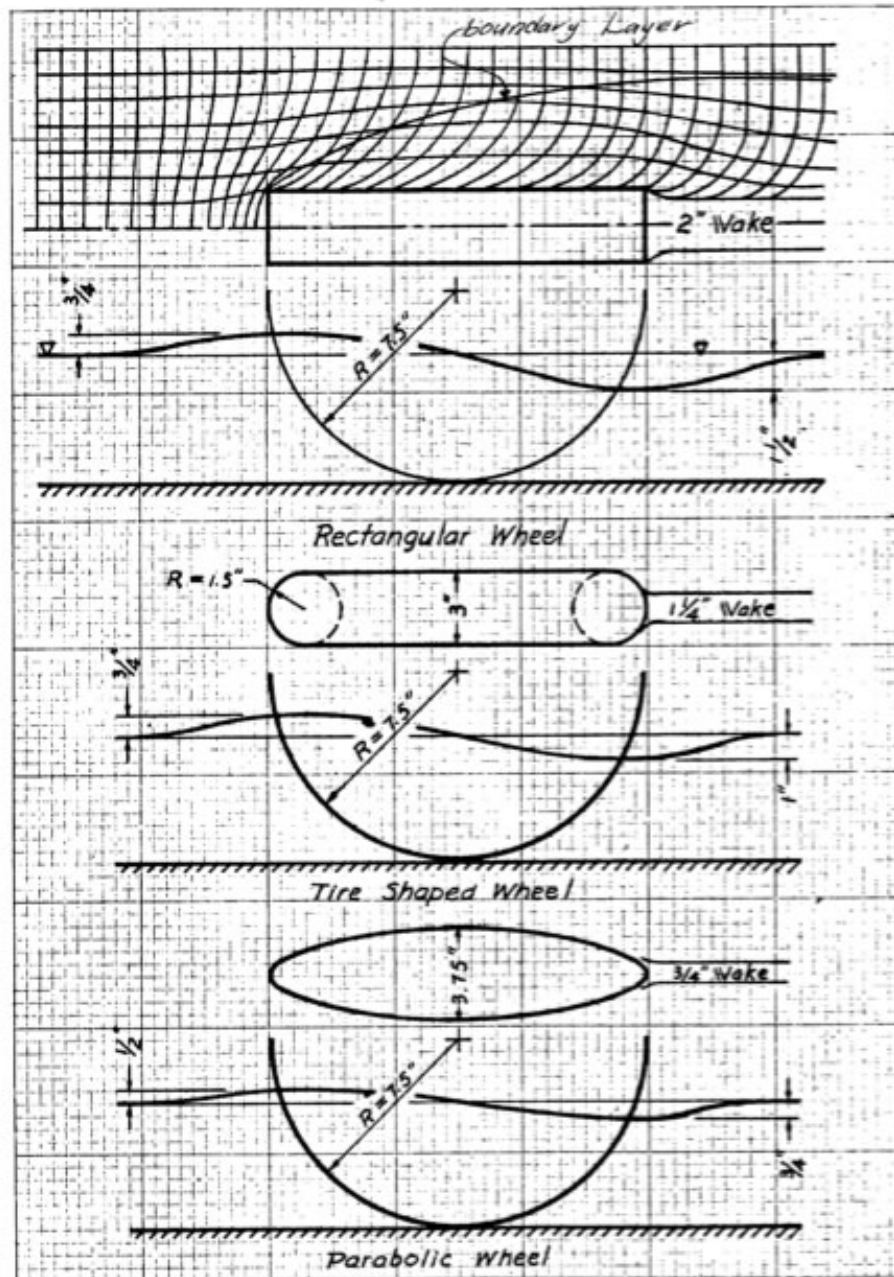


Fig. 2 Sketches showing the Pressure Wave and Wake for Different Wheel Forms

Figure 4.12: Rowe and Hegedus's study on wakes of different shaped wheels [63]

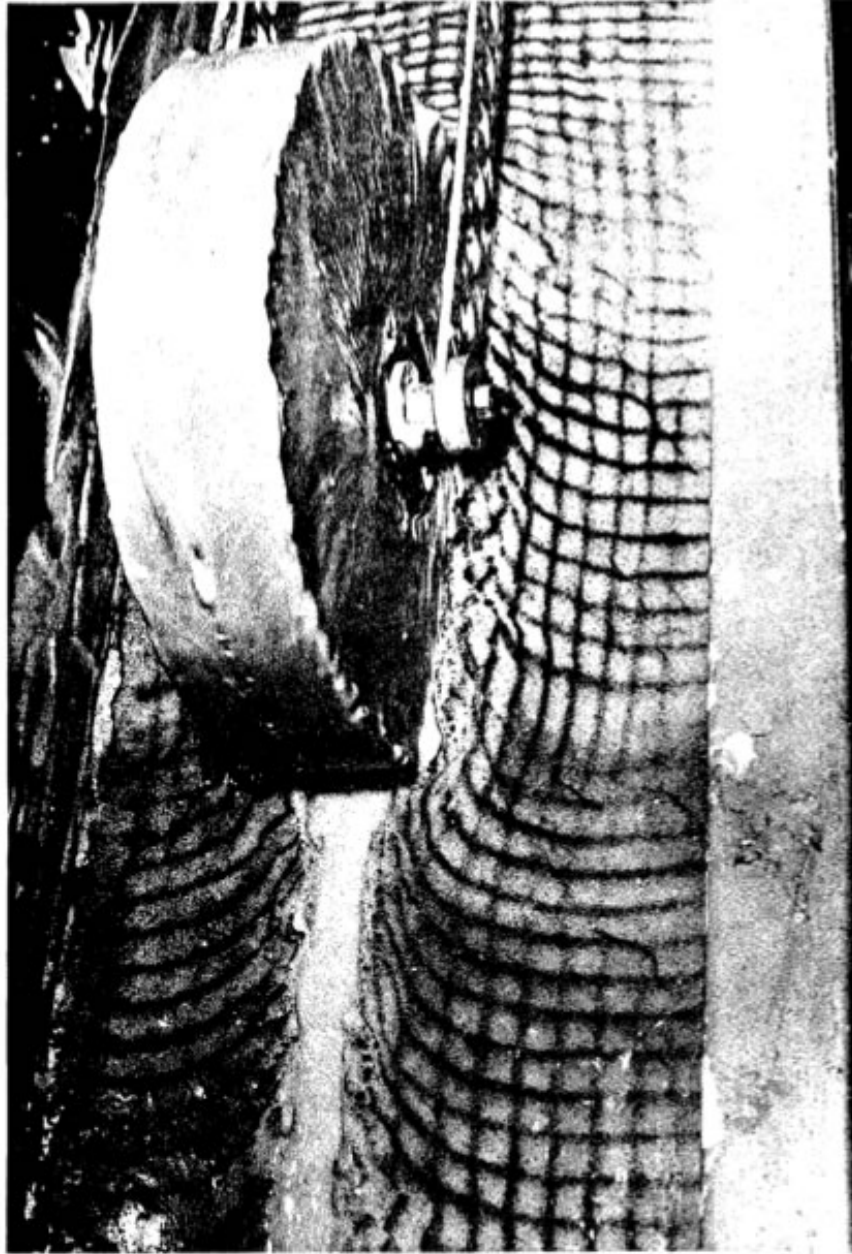


Figure 1a. - Viscous Drag. Viscous field.

Figure 4.13: Rowe and Hegdus's Wheel Wake Experiment [63]

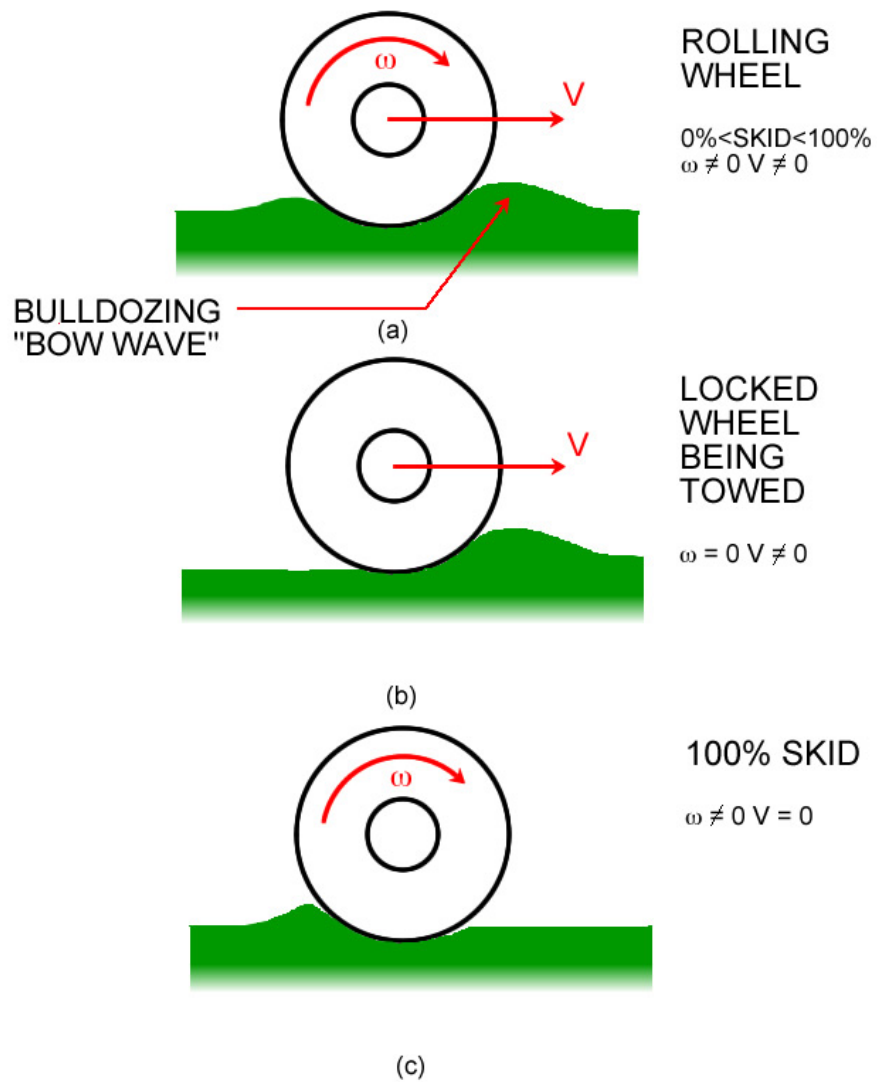


Figure 4.14: Three cases of wheel to soil interaction: (a) Rolling wheel (b) Towed locked wheel (c) 100% skid wheel

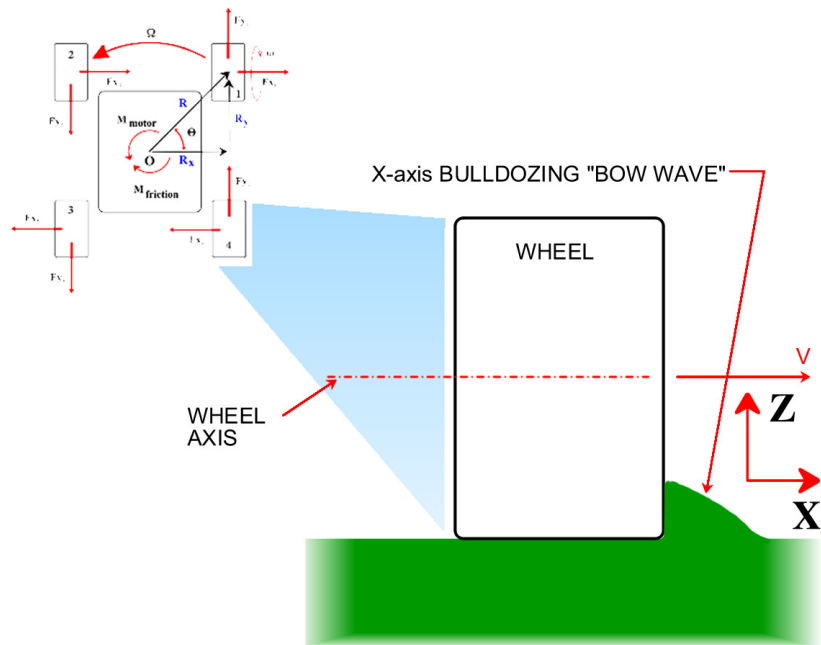


Figure 4.15: Illustration of side bow wave on a wheel in a skid steer turn



Figure 4.16: SR2 chamfered wheel with side mounted grousers

4.7 Further Observations of Data

From multiple experiments it is possible to see patterns in the large amount of data, which may help in designing wheels for specific missions as opposed to a general wheel used for all missions.

4.7.1 Equilibrium Point Slope

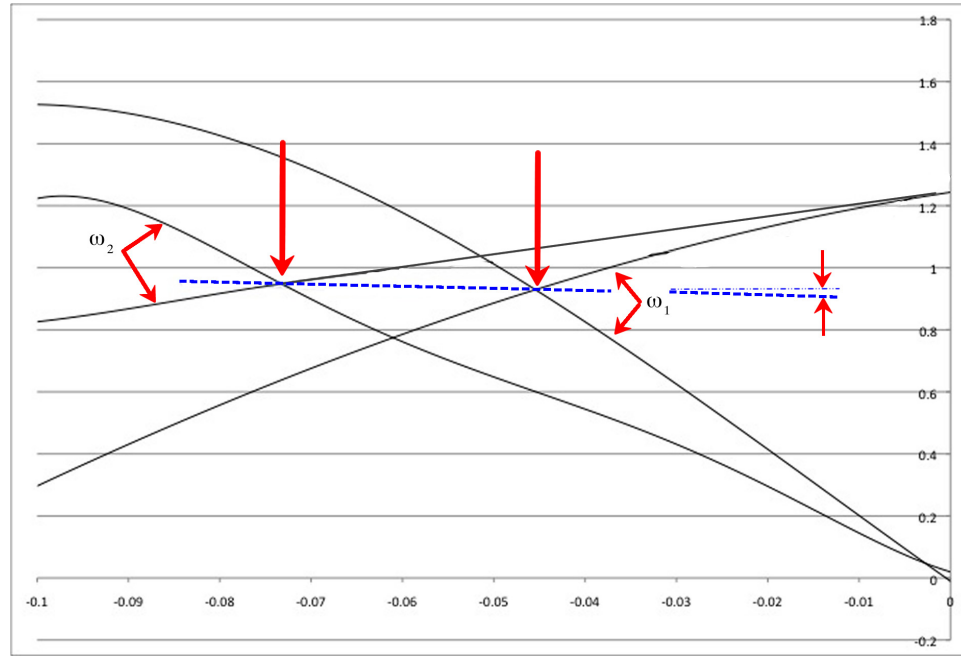


Figure 4.17: Illustration of Equilibrium Point Slope for two different ω rates

Intuitively as a rover's wheel velocity (ω) increases so does its turning rate (Ω) and the forces acting on the wheel (figure 4.1). At the equilibrium turning point the forces can be combined into a resultant force with magnitude $\sqrt{F_X^2 + F_Y^2}$ and direction along R (to the center of the rover). If several ω values are sampled a line can be drawn through all the equilibrium points (figure 4.17). The slope of this line signifies the dependence of the force magnitude on rover turn rate Ω . The lower the slope, of this line, the less ground friction has an effect on the rover's turning rate and the more the rover can increase its turning velocity without overly increasing the magnitude of forces on the wheel. Obviously this is only linear over a certain domain of Ω but can still be useful in classifying wheel designs. If it can be shown that this force magnitude is proportional to a rover's power need (figure 4.18) then this value would be useful in predicting power requirements for higher speed turns.

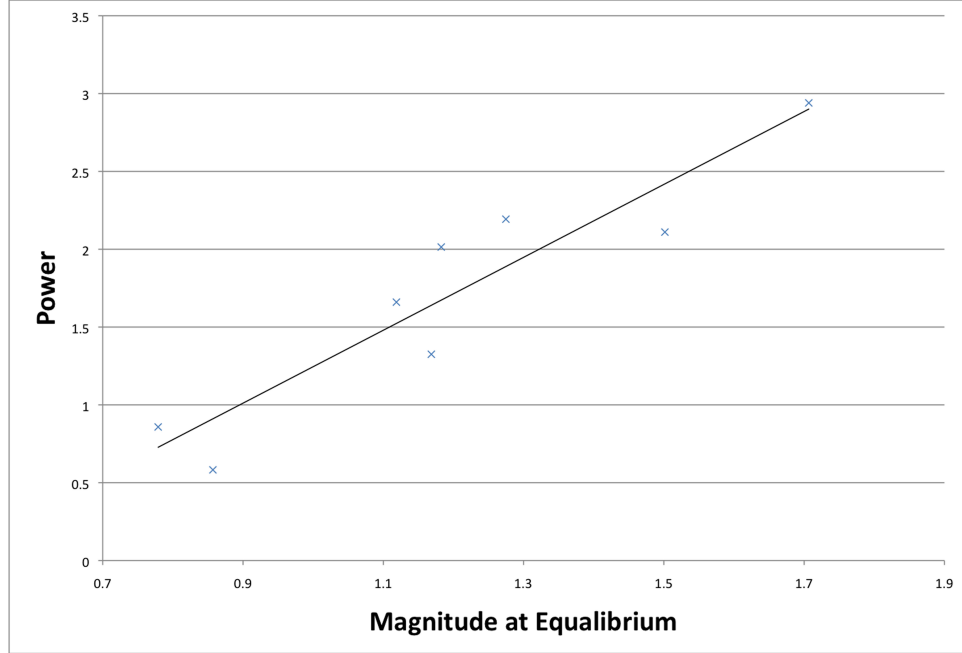


Figure 4.18: Magnitude vs Power

4.7.2 Wheel Slip

The longitudinal slippage of the wheels can also be calculated from single wheel tests. The results can be used to bolster or discourage use of any assumptions in control theory dealing with wheel slip [30, 44]. Percent slip can be calculated with equation 4.30.

$$Slip = \frac{\omega r - V_y}{\omega r} \quad (4.30)$$

V_y is calculated from the table velocity of the single wheel test (equation 4.31).

$$V_y = \Omega R \cos(\Theta) \quad (4.31)$$

4.8 Isotropic behavior

Since a wheel's skid steering efficiency is dependent on the proportion of f_X and f_Y forces acting on the wheel the isotropic nature of the wheel (whether the frictional forces are equal in all directions) is a major factor governing its performance.

4.9 Prospective uses for skid steering turning rate prediction

Being able to predict rover turning rate of a specific wheel has a few applications. These application take advantage of the ease and low cost of single wheel testing and are discussed below.

4.9.1 ω vs Ω

Single wheel testing allows a designer to test a specific wheel on a variety of soils and catalog the relationship between the rover's ω (wheel spin rate) and its predicted Ω spin rate. This information would be useful in rover control, when the rover knows the soil it is on and needs to know how much it has turned for a given ω for a period of time. This relationship would give a more accurate positional reading [61, 30], as well as give the controller a better idea of what ω should be for a given turn on a given soil.

4.9.2 Soil Characterization

An issue with planetary rovers is how to classify the soil on which the rover is driving [36]. This can be done with scientific equipment but at a weight and space cost. Ojeda et al. [56] came up with a solution to this by using the rover's power measurement and an onboard gyro to characterize terrains by predefined turns. They proved that a soil can be defined by the power used in a predefined turn in a rover using a specific wheel. The problem with this is that the data needed to catalog this relationship could be work intensive using a full rover assembly, especially if considering different wheel types and suspension configurations. The same catalog could be created much easier using a single wheel testing procedure which will save time and cost. Figure 4.19 shows a possible decision tree based on the measured wattage and ω parameters cross referenced with a catalog of known wattage to ω relationships indicative to varying soils that was created earlier using single wheel testing.

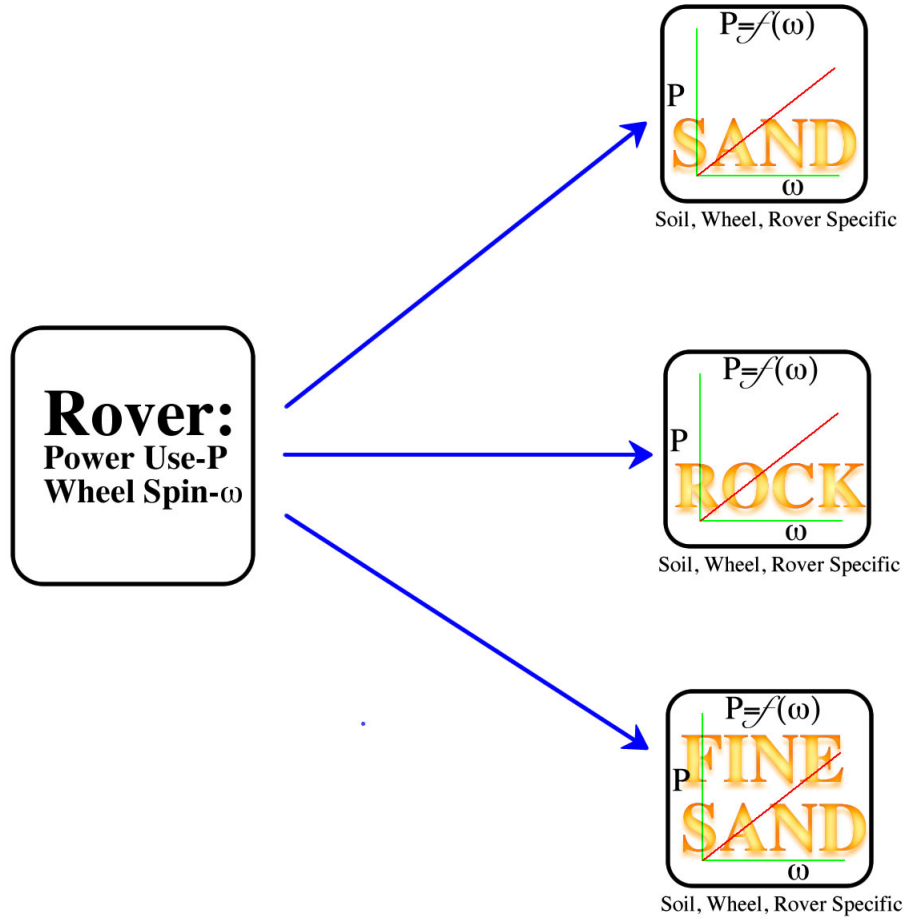


Figure 4.19: Terrain characterization from measured power and ω variables

Another way to characterize the soil would be to measure the rover's spin rate from an onboard inertial measurement unit (IMU) and compare it to another catalog of soil parameters that compares Ω and ω (figure 4.20), which would also be composed of data from single wheel tests. Force components can be estimated in a similar way. If enough tests are run and cataloged for a specific wheel and soil then a relationship between power used and magnitude of the forces in an equilibrium turn can be established (figure 4.18). By using the constraint equation derived earlier (eq 4.15) the force components can be calculated.

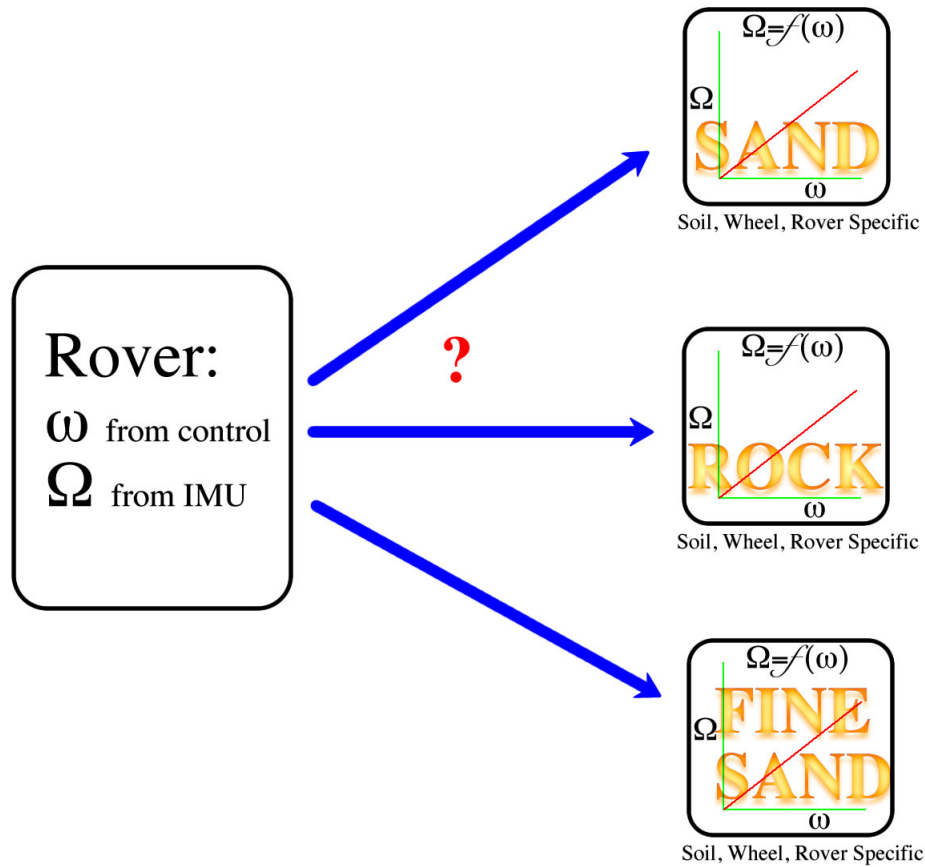


Figure 4.20: Terrain characterization from measured values, ω and Ω

4.10 Summary

This chapter set the framework for skid steer turning prediction by describing the equations of motion of a skid steer rover and the mapping of a single wheel test to full rover's performance. Also discussed are the avenues of possible ways to augment skid steering efficiency along with applications that might result. Chapter 11 will discuss the results for this relationship and any further applications, also chapters 6.2.2 and 7 discuss the experimental validation results of the theory discussed in this chapter and the possible ways to increase the skid steering spin rate of a rover.

CHAPTER 5

Error Propagation

5.1 Introduction

In any testing apparatus the sensors are of primary importance and can also be the cause of most the errors. As discussed in chapter 3 SWEET uses a 6 axis Force-Torque sensor that is interfaced to a computer via a National Instruments data acquisition board.

5.2 Sensor Measurement Errors

The accuracy of the calibration force sensor is $\pm.044N$ while the accuracy of the National Instruments DAQ 6020-E is $.557mV$. (specs on the NI box are in appendix A) Using the conversion equations that were calculated (Equations 3.21, 3.22, and 3.23) we can find the error that is propagated through the analysis.

$$\frac{\delta F}{\delta V_x} = 49.77 \quad \frac{\delta F}{\delta F_x} = 1 \quad (5.1)$$

$$\frac{\delta F}{\delta V_y} = 48.67 \quad \frac{\delta F}{\delta F_y} = 1 \quad (5.2)$$

$$\frac{\delta F}{\delta V_z} = -47.1698 \quad \frac{\delta F}{\delta F_z} = 1 \quad (5.3)$$

$$\frac{\delta F}{\delta V_{M_x}} = .09709 \quad \frac{\delta F}{\delta M_x} = 1 \quad (5.4)$$

$$\frac{\delta F}{\delta V_{M_y}} = -.06574 \quad \frac{\delta F}{\delta M_y} = 1 \quad (5.5)$$

$$\frac{\delta F}{\delta V_{M_z}} = -.05176 \quad \frac{\delta F}{\delta M_z} = 1 \quad (5.6)$$

$$\frac{\delta F}{\delta V_{M_\tau}} = -.049 \quad \frac{\delta F}{\delta M_\tau} = 1 \quad (5.7)$$

Using the error propagation equation (5.8):

$$E = \sqrt{\left(\frac{\delta F}{\delta V_x}\right)^2 U_v^2 + \left(\frac{\delta F}{\delta F_x}\right)^2 (U_x)^2} \quad (5.8)$$

The errors can be calculated (5.9, 5.10, 5.11, 5.12, 5.13, 5.15):

$$E_x = \pm.052N \quad (5.9)$$

$$E_y = \pm.052N \quad (5.10)$$

$$E_z = \pm.22N \quad (5.11)$$

$$E_{M_x} = \pm.044 \frac{N}{M} \quad (5.12)$$

$$E_{M_y} = \pm.044 \frac{N}{M} \quad (5.13)$$

$$E_{M_z} = \pm.044 \frac{N}{M} \quad (5.14)$$

$$E_{M_\tau} = \pm.044 \frac{N}{M} \quad (5.15)$$

In the case of predicting skid steering performance (chapter 4) these errors in force readings need to be mapped to the turn rate prediction. Figure 5.1 shows how these errors would propagate to $\Omega_{SWEETPREDICTION}$ errors.

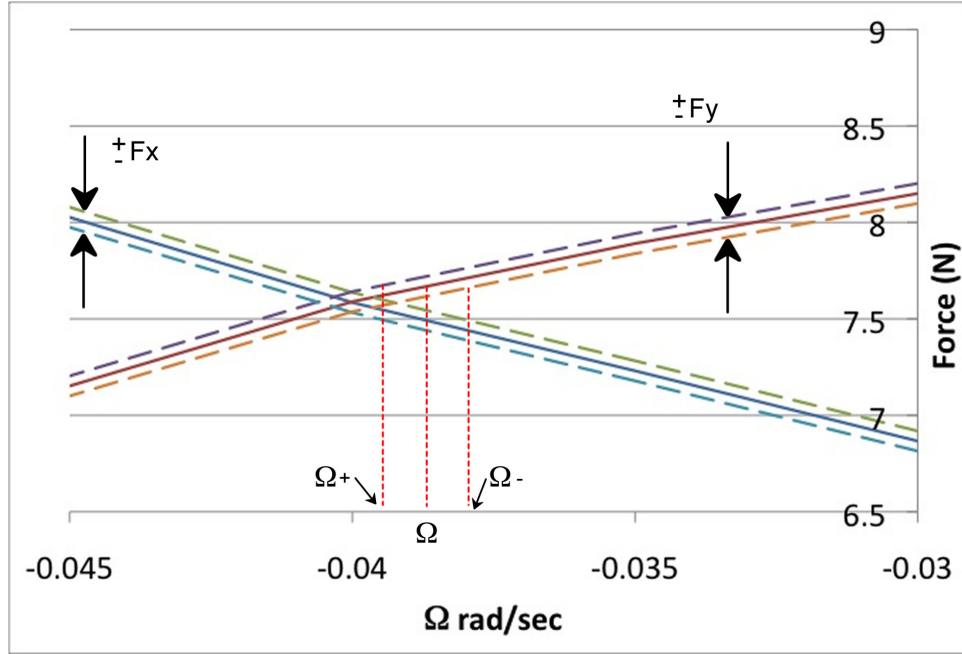


Figure 5.1: Ω force graph with error bars

5.3 SWEET Errors

Along with the FT sensor errors there are also errors incurred when SWEET moves the table and the test wheel. The test wheel and the Omni wheels controlling the table are controlled using a Proportional Derivative Integral control (PID) loop which keeps the wheels turning at a desired rpm. The Test wheel has an encoder that is interfaced with proper counter inputs on the DAQ board which gives an exact count relationship to the rpm of the wheel. The main motors, on the other hand, are not done this way but are fed through analog inputs because of the lack of counter pins.

The analog signal is then processed and a frequency is used for PID control. This process is adequate for testing although it is necessary to calibrate the main motors to get the correct rpm which is a cause of systemic error in the system. The main motors are calibrated to within $\pm .02 \frac{rad}{sec}$. The motor control equations derived in chapter 3 are used to calculate how this error propagates (figs 5.16, 5.17, and 5.18) in a skid steer turn.

$$\begin{pmatrix} \dot{\phi}_1 \\ \dot{\phi}_2 \\ \dot{\phi}_3 \end{pmatrix} = \frac{1}{.06} \begin{pmatrix} (.866\dot{X}) - (.5\dot{Y}) - (.3\dot{\Theta}) \\ (.5\dot{Y}) - (.3\dot{\Theta}) \\ (-.866\dot{X}) - (.5\dot{Y}) - (.3\dot{\Theta}) \end{pmatrix} \quad (5.16)$$

$$V_x = \Omega \cdot R_y \quad (5.17)$$

$$V_y = \Omega \cdot R_x \quad (5.18)$$

$$\dot{\Theta} = \Omega \quad (5.19)$$

If \dot{X} , \dot{Y} , and $\dot{\Theta}$ in equation 5.16 are substituted using equations 5.17, 5.18, and 5.19 then three equations can be solved for Ω . R_X and R_Y are the geometry measurements of the rover in question and are .289 and .322 meters respectively for the SR2 rover.

$$\dot{\phi}_1 = \frac{1}{r} [.866\Omega R_Y - .5\Omega R_X - .3\Omega] \quad (5.20)$$

$$\dot{\phi}_2 = \frac{1}{r} [.5\Omega R_X - .3\Omega] \quad (5.21)$$

$$\dot{\phi}_3 = \frac{1}{r} [-.866\Omega R_Y - .5\Omega R_X - .3\Omega] \quad (5.22)$$

$$\Omega = \pm .00726 \frac{rad}{sec} \quad (5.23)$$

$$\Omega = \pm .00772 \frac{rad}{sec} \quad (5.24)$$

$$\Omega = \pm .001658 \frac{rad}{sec} \quad (5.25)$$

Motor number two will cause the most error in this type of skid steer turn since it is required to go the slowest and will be the error that is used when compiling. Another source of error with SWEET is the possibility of the table slipping on the omni wheels that move it which can become a problem if the table is not loaded properly otherwise it is an intermittent random error that can be decreased by longer averaged tests.

5.4 SR2 Validation Test Errors

When testing the SR2 rover several errors crop up due to the methodology or lack of more accurate testing equipment. Since SR2 is a full assembly rover it is sometimes difficult to get an accurate measurement of performance. The validation tests consist of running the rover for a certain amount of time then measuring the angle turned in that time. If no other factors were involved then the longer the turn test the better

since it is an average measurement, but with sand a rover proceeds through virgin sand differently than rutted sand. If a rover turns more than a quarter turn then its wheels will be traveling in disturbed soil which will change the rate of turn. So in these validation tests care was taken to keep the time of the tests short enough to keep the rover on virgin sand. For the lower wheel rates the tests could be run up to 45 sec while the faster wheel rates only turned for 30 seconds. The difference in time will also make a difference in possible error. Other sources of error could be the resolution and accuracy of the measurement as well as the start up time for the rover's motor variance. Table 5.1 shows the errors tied to these possible error sources. The equations used in finding the weighting of the small errors on the final composite

Error	Description	Value	Units
Protractor	reading and resolution	$\pm .035$	radians
Time	start up	$\pm .2$	seconds
Motor Variance	wheel rpm	$\pm .01$	$\frac{rad}{sec}$

Table 5.1: Possible errors with validation tests on the SR2 rover

error are 5.26 and 5.27.

$$\Omega = \frac{\beta}{Time} \tag{5.26}$$

$$\Omega = \frac{\omega r}{R} \cdot \cos \Theta \tag{5.27}$$

Where β is the measured angle, Time is the length of the test, and equation 5.27 is the target value for a isotropic wheel which will give the worst case error scenario. Using a propagation equation similar to 11.5 the combined error for the SR2 validation tests can be calculated using equation 5.28.

$$E = \sqrt{\left(\frac{1}{time}\right)^2(\Delta\beta)^2 + \left(\frac{\beta}{time^2}\right)^2(\Delta time)^2 + \frac{(\Delta\omega)r}{R} \cos \Theta} \tag{5.28}$$

As can be seen from equation 5.28 the error for the different tests will be different because they depend on the time of the test and the angle of the final measurement.

5.5 Combination of Errors

The three categories of errors discussed is in units of $\pm\Omega \frac{rad}{sec}$ and will be calculated and added for each wheel.

5.6 Summary

Discussed in this chapter is the possible errors in the testing system as well as their propagation. Three categories of errors were laid out and explained. Each wheel will have its own error depending on its specific testing parameters.

CHAPTER 6

Blank and Omni Wheel Experiments

6.1 Introduction

Several experiments were conducted to validate that a rover's turning efficiency can be predicted by a single wheel test. These single wheel tests were performed on SWEET and then validated with experiments conducted on a full rover assembly. This chapter discusses two of these tests done on a blank wheel and an Omni wheel. A blank wheel was used to attempt to isolate key forces in a skid steer turn, and the Omni wheel was tested to help explore possible turning enhancements allowed by the Omni wheel's low lateral friction.

6.2 Blank Wheel Tests

6.2.1 Test Set Up

In the first experiments SWEET was programmed to simulate a skid steer turn and fitted with a .109 meter radius blank wheel (figure 6.1 and 6.2) while unpadded high density low height pile carpet was placed on the table as a simulated surface. Parameters of the test skid steer turn were set to mimic our in-house four wheel skid steer rover's (SR2 [62]) geometry and loading. Loading was calculated by weighing SR2 (the test rover) and dividing by four since there are four wheels. The test variables were wheel spin rates ($\omega = .3, .4, \text{ and } .5 \frac{\text{rad}}{\text{sec}}$) and turn rates ($\Omega = 0, -.005, -.01, -.015, -.02, \dots, -.12 \frac{\text{rad}}{\text{sec}}$) with 5 trials of each. The only measured values, for these tests, were the forces f_Y and f_X from the force torque sensor. Post data processing was done with a C program that averaged all trials, performed 2nd and 3rd order regression curve fitting, and calculated $\Omega_{\text{SWEETPREDICTED}}$ (appendix A.0.11). Microsoft Excel was also used to graph the data as well as calculate the higher order curve fitting. The higher order (3-6 degree) equations need a numerical iterative program (appendix A.0.13) to solve for the $\Omega_{\text{SWEETPREDICTED}}$ values. Results are shown in figures. 6.3, 6.4, and 6.5.

To validate the $\Omega_{\text{SWEET-PREDICTED}}$ values SR2 (figure 6.1) was fitted with four identical blank wheels and turned on the same carpet used in the SWEET tests. Tests were done for the same three wheel speeds ($\omega = .3, .4, \text{ and } .5 \frac{\text{rad}}{\text{sec}}$) measuring the spin rate of the rover during each test (by measuring the angle between an onboard laser level mark and the initial position and dividing by the elapsed time).

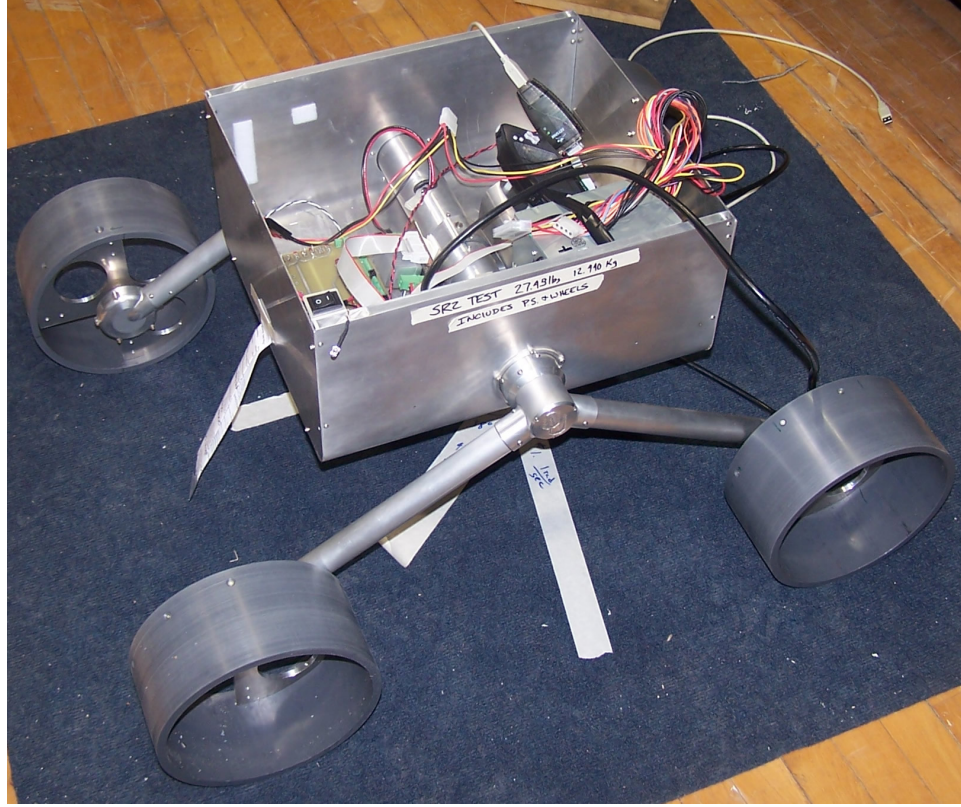


Figure 6.1: a) SR2 rover with blank test wheels

6.2.2 Results

Results for the blank wheel test are given in table 1 along with $\Omega_{SWEET-PREDICTED}$ results, percentage error, the Target turning rate (eq 4.22), percentage of Target, and slip along the Y direction. These results show a definite validation of the SWEET single wheel test prediction on carpet within 3% of the full assembly rover's spin rate with the same wheel rotation rate (ω). Error analysis, for this test, is given in table 6.1 and shows that every test is within the uncertainty calculated.

Table 6.1: Calculated uncertainties for blank wheels in $\frac{rad}{sec}$

ω	FT sensor	SWEET	Combined	SR2 validation
0.3	-0.0384 to -0.0457	$\pm .00772$	-0.03116 to -0.0529	$\pm .00342$
0.4	-0.0522 to -0.0615	$\pm .00772$	-0.0450 to -0.0692	$\pm .00345$
0.5	-0.0583 to -0.0714	$\pm .00772$	-0.0506 to -0.0786	$\pm .00349$

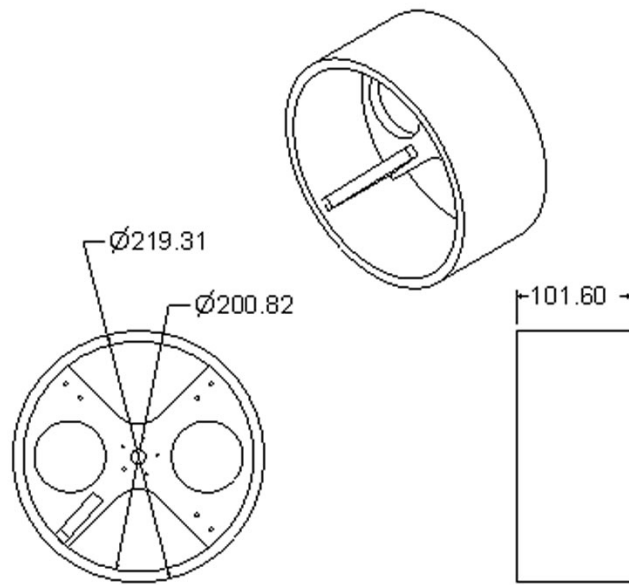


Figure 6.2: Black Blank Test Wheel Dimensions in mm

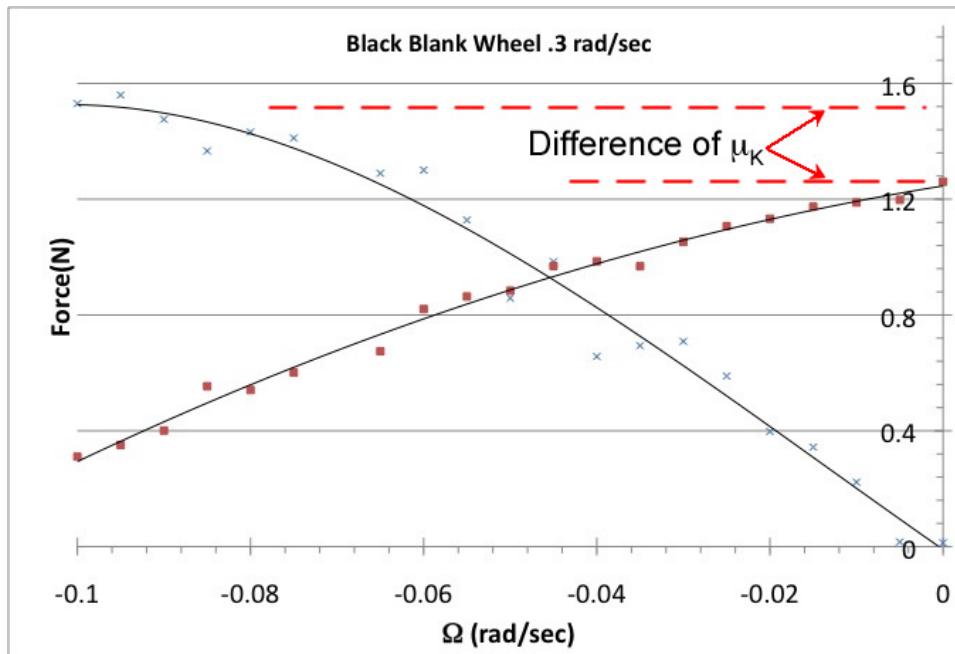


Figure 6.3: Results for $\omega = .3 \frac{rad}{sec}$

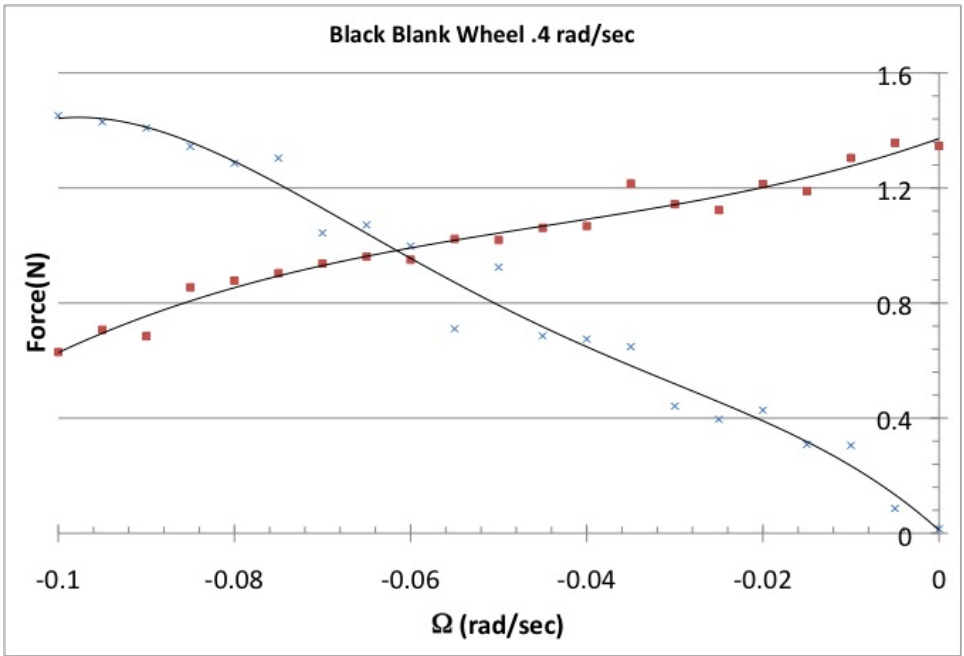


Figure 6.4: Results for $\omega = .4 \frac{rad}{sec}$

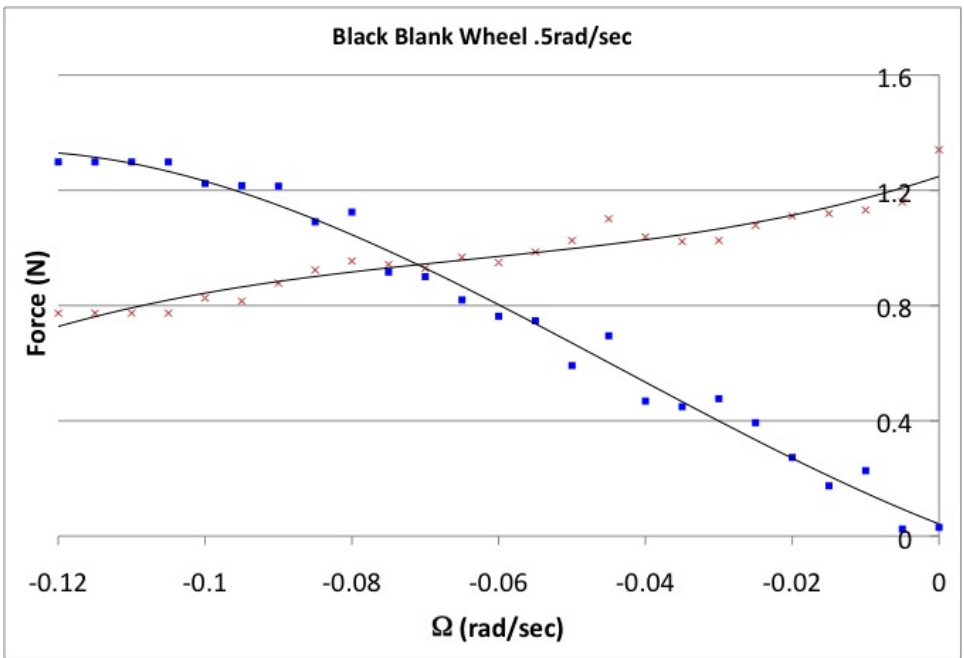


Figure 6.5: Results for $\omega = .5 \frac{rad}{sec}$

Table 6.2: Ω_{SR2} and $\Omega_{SWEETPredicted}$ results for blank wheels in $\frac{rad}{sec}$

ω	Ω_{SR2}	$\Omega_{SWEETPredicted}$	Difference	$F_Y = 0$ Target	% of Target	Y slip
0.3	-0.042	-0.042	0%	-0.11	37%	62.8%
0.4	-0.056	-0.057	1.8%	-0.15	37%	62.1%
0.5	-0.066	-0.064	3.0%	-0.19	35%	66%

6.2.3 Auxiliary Blank Wheel Observations

Slip

Slip rate (Y direction) for the blank wheel is around 63% for all speeds tested. Obviously a blank wheel on carpet in a skid steer turn will slip considerably but the calculated slip rate will be a useful comparison to other wheels. The optimal case would be is the wheel slipped in the X direction and did not slip in the Y .

Forces as a function of ω

Figure 6.6 also illustrates how F_X and F_Y are dependent on ω . As ω increases the frictional force incurred laterally decreases which agrees with Yoshida [70] that frictional forces are affected by the wheel spin rate. The longitudinal (F_Y) forces also increase as ω increases. This is simply due to the higher frictional force of the wheel spinning faster.

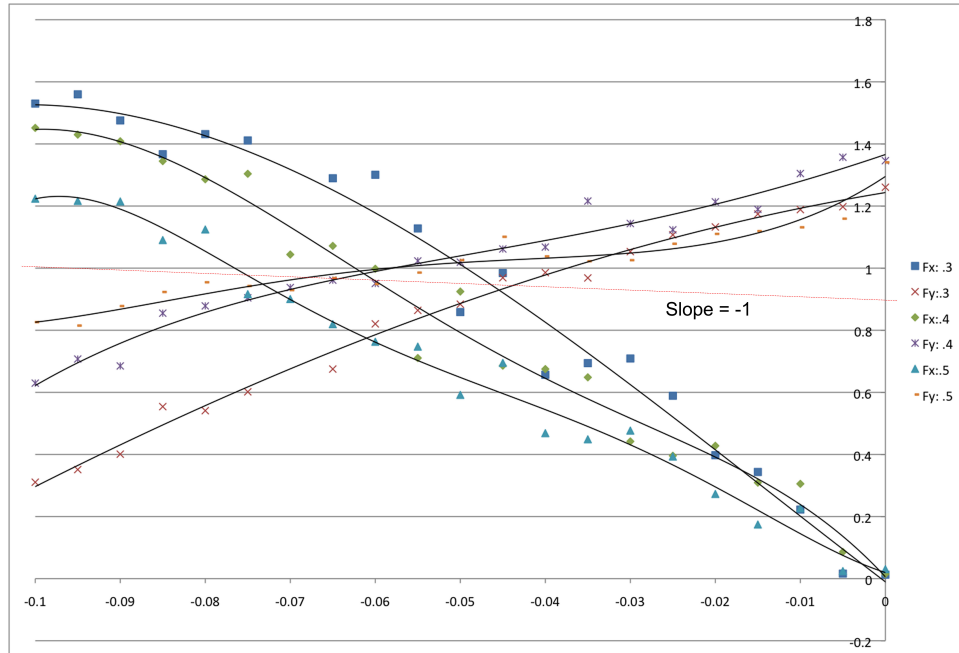


Figure 6.6: Combination of wheel rates for blank wheel on carpet

Equilibrium force intersection points

Figure 6.6 illustrates the linearity of the equilibrium points with a slope of -1. This value represents how much the magnitude of the force changes with changing Ω . In other words this value shows how quickly the magnitude of forces on the wheel increase as the rover spin rate (Ω) increases.

Isotropic Behavior

The difference between the dynamic frictional forces, f_Y found at $\Omega = 0$ and f_X found at the larger spin rates, are slight and depend on the wheel spin rate (ω) (figure 6.3). The biggest difference in forces being when ω is slowest, this can be attributed to the added friction of the bow wave catching on the wheel's side. At higher ω 's the difference is negligible making the blank wheel isotropic.

6.3 Omni wheel tests

As stated in chapter 4, Omni wheels (figure 6.7) are designed such that they do not restrict motion parallel to their axis. This anisotropic feature, in theory, allows the rover turn rate (Ω) to increase without increasing wheel spin rate (ω) up to where mechanical friction becomes more dominant. Tests were run on these Omni wheels to validate this theory and the algorithm as a whole.

6.3.1 Test Set Up

An Omni wheel (figure 6.8) was mounted on SWEET and taken through a skid steer turn identical to the earlier blank wheel skid steer tests. Two wheel velocities were tested ($.3$ and $.5 \frac{rad}{sec}$) with the range of Ω from 0 to $.1$ rad/sec by $.005$ increments with five trials each.

6.3.2 Results

Figure 6.9 shows the results for the wheel velocity of $.3 \frac{rad}{sec}$ and figure 6.10 gives the results for $.5 \frac{rad}{sec}$. Table 6.3.2 shows the uncertainty calculated for the test and the SR2 validation tests. Table 6.3.2 shows the results and that they are within the uncertainty calculated.

Table 6.3: Calculated uncertainties for Omni wheels in $\frac{rad}{sec}$

ω	FT sensor	SWEET	Combined	SR2 validation
0.3	-.0546 to -.0607	$\pm .00772$	-.0474 to -.0680	$\pm .00346$
0.5	-.102 to -.107	$\pm .00772$	-.0948 to -.115	$\pm .00363$

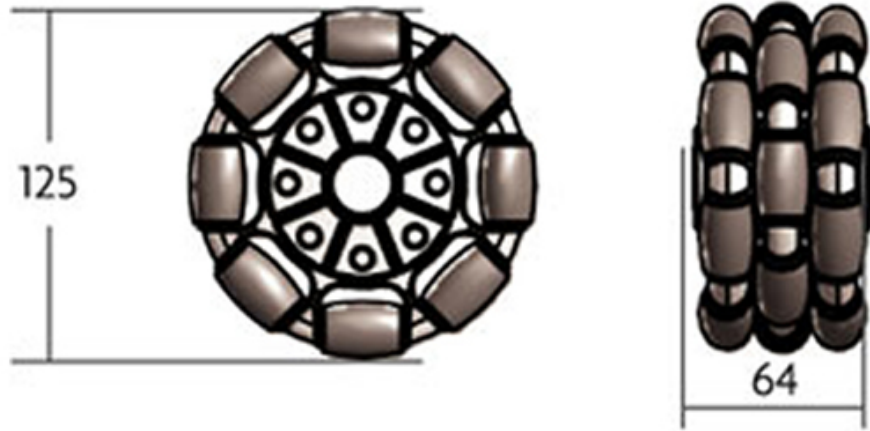


Figure 6.7: Omni wheel test wheel dimensions in mm [43]

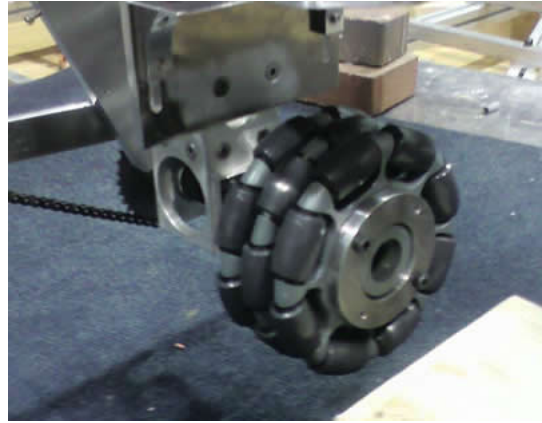


Figure 6.8: Omni-wheel mounted on SWEET

Table 6.4: Ω_{SR2} and $\Omega_{SWEETPredicted}$ results for Omni wheels in $\frac{rad}{sec}$

ω	Ω_{SR2}	$\Omega_{SWEETPredicted}$	Difference	$F_Y = 0$ Target	% of Target	Y slip
$.3 \frac{rad}{sec}$	-0.059	-0.058	1.7%	-0.065	90.9%	6.9%
$.5 \frac{rad}{sec}$	-0.1	-0.105	5.0%	-0.108	92.5%	1.2%

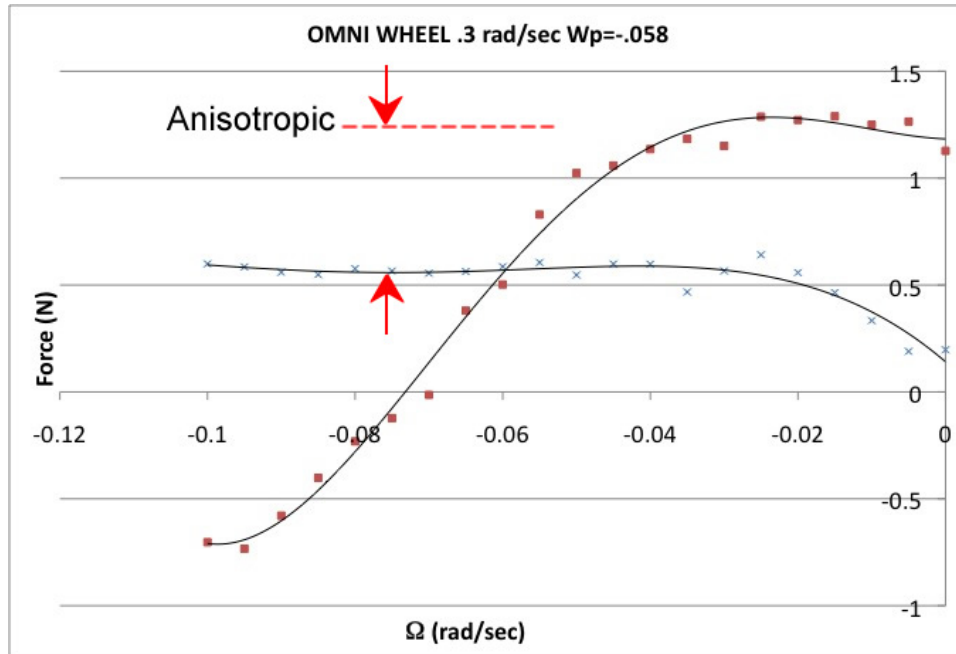


Figure 6.9: Results for Omni wheel spinning at $.3 \frac{rad}{sec}$

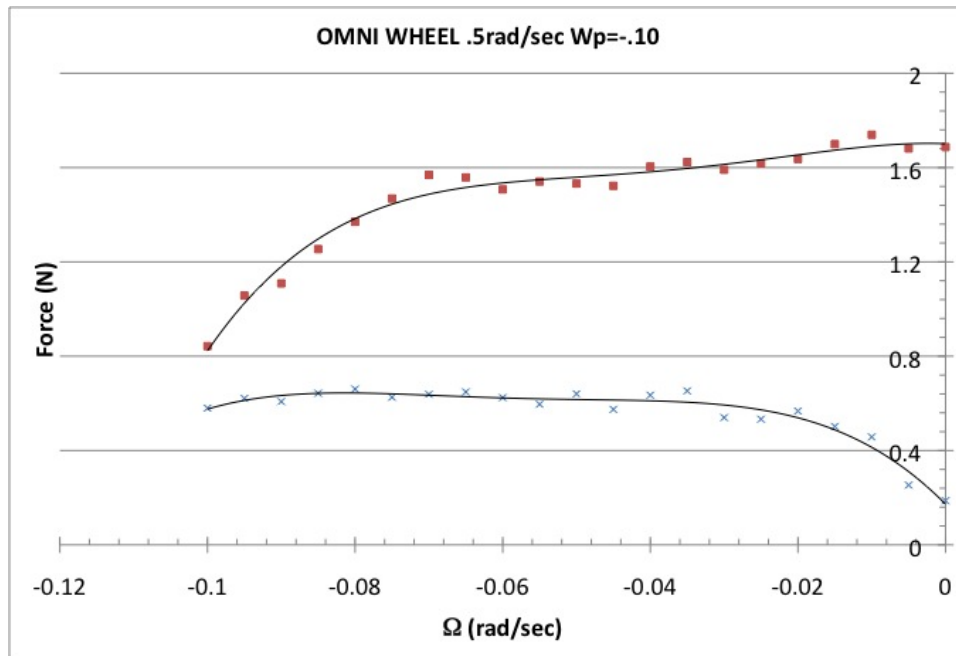


Figure 6.10: Results for Omni wheel spinning at $.5 \frac{rad}{sec}$

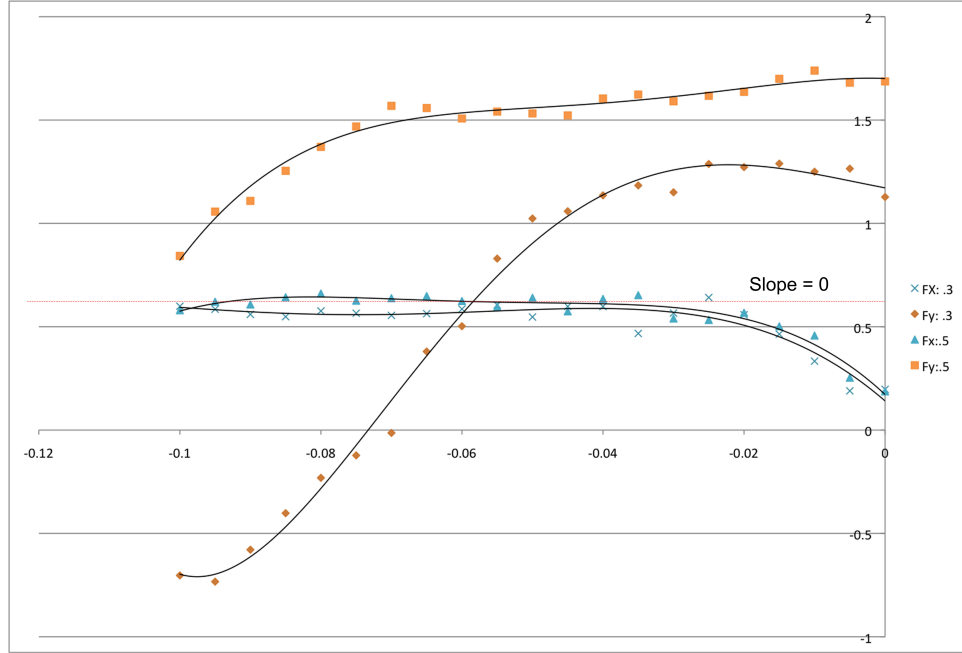


Figure 6.11: Combination of graphs for Omni Wheel

6.3.3 Auxiliary Omni wheel observations

Y Slip

Slip rate is a very low 3.7-5.3% which while consuming less energy also helps in maintaining a more linear frictional force in the longitudinal direction as can be seen by graphs 6.9 through 6.11.

f_X reduction

Because of the Omni wheel's inherent low lateral friction, f_X is reduced for all Ω values. f_X reaches its terminal friction value earlier than conventional wheels giving it a lower value at higher Ω . This "flattened out" the f_X graph while increasing the $|\Omega|$ value giving the rover, with omni wheels, a much more efficient turn.

Equilibrium force intersection points

Due to f_X reaching its terminal value the slope of the equilibrium points is zero as seen in figure 6.11. This shows that the turning rate Ω is mostly dependent on ω which will prove to be much more efficient since the power needed is only for overcoming mechanical friction in the gear train. This relationship is only valid to a certain Ω until other viscous forces will increase and start to impede the turn.

Isotropic Behavior

The Omni wheel is a highly anisotropic wheel, meaning that its frictional force along its axis is much different than along its path of motion. This parameter is one more way to judge its skid steering ability. This attribute can be measured in the difference of f_Y at $\Omega = 0$ and its terminal f_X value (figure 6.9).

6.4 Conclusions

This chapter analyzes the results of the tests done to validate the theory discussed in chapter 4 for non treaded and Omni wheels. From the results it is shown that the real world tests come to within 5% of what was predicted by SWEET in a single wheel test for both a blank wheel and an Omni wheel in a skid steer turn on carpet. Also shown was how an Omni wheel increased the turning efficiency, by its reduction of longitudinal slipping and lateral friction, to better than 90% of Target ($F_Y = 0$) values while the blank wheel was only at about 37%. Also the magnitude of forces on an Omni wheel is not as dependent on wheel to soil friction as with the blank wheel This makes the turn rate more dependent on motor limitations and mechanical friction than of wheel to soil interaction.

CHAPTER 7

Experiments with Non-Blank Wheels

7.1 Introduction

As discussed, in chapter 4, non blank wheels have the potential to change the turning efficiency depending on their tread. Wheels that have a non axial symmetry or that generate forces dependent on there direction of rotation can be classified as directionally treaded, experience has proved that directionally treaded wheels do better on the SR2 if mounted in a certain orientation or worse if mounted opposite. These experiments show that using SWEET we can predict a rover's performance with non blank wheels as well as start to understand how grouzers can effect wheel and rover performance specifically in skid steer turns.

7.2 Test set up

Two directional patterned wheels, with radius of .102 meters (Figs. 7.6 and 7.3), were tested in SWEET with a wheel rotation rate of $.3 \frac{rad}{sec}$. Tests were run at $.005 \frac{rad}{sec}$ intervals for 0 to .1 for the unpadded trials and every .01 interval from 0 to .06 for the padded tests. Five trials of each test where again averaged and curve fitted and solved with Excel or a C program (appendix A.0.11).

Figures 7.4, 7.5, 7.7, and 7.8 show the performance of the two oppositely patterned wheels dubbed 'correct' and 'opposite' which correspond to their proper orientation on the actual rover. The 'correct' wheel would be the wheel that enhances the turn and the 'opposite' would diminish the rover's spin efficiency. The tests were also run simulating the right front side of a rover turning in a counter-clock-wise direction. The wheels were tested on padded and unpadded carpet (figs 7.2, 7.1) to focus on how the tread itself interacts with the surface and the interactions affect on turning performance on different terrains. In a skid steer turn the opposite directional wheel can be visualized as trying to screw itself to the right fighting against the turn when mounted on the right side, the correct wheel mounted on the right side is trying to screw itself left which benefits the turn. Figures 7.1, 7.2, and 7.3 also show the two types of carpet tested. Validation tests were again accomplished using SR2 on both the padded and unpadded carpets. The SR2 tests were run for 20 seconds and then the angle travelled was measured.

7.3 Results

As can be seen from table 7.3 the $\Omega_{PREDICTED}$ results are higher for the unpadded carpet but with less distinction between the correct and opposite wheels. Separate

Omega-Force graphs are shown in figures 7.4 , 7.5, 7.7, and 7.8 while table 7.3 shows the uncertainty calculated.



Figure 7.1: Unpadded test carpet surface

Table 7.1: Calculated uncertainties for treaded wheels in $\frac{rad}{sec}$

Carpet	Wheel	FT sensor	SWEET	Combined	SR2 validation
padded	Opposite	NA	$\pm .00772$	-.0297 to -.0451	$\pm .00340$
padded	Correct	-.0521 to -.0476	$\pm .00772$	-.0399 to -.0598	$\pm .00342$
unpadded	Opposite	-.0456 to -.0374	$\pm .00772$	-.0296 to -.0534	$\pm .00341$
unpadded	Correct	-.0445 to -.0502	$\pm .00772$	-.0368 to -.0579	$\pm .00343$

7.4 Auxiliary treaded wheel observations

7.4.1 Y Slip Rate

Slip rate (table 7.3) for the treaded wheel shows that the opposite wheel slipped more in the Y direction which accounts for its lower efficiency.

7.4.2 F_X shift due to tread

From figures 7.4, 7.5, 7.7, and 7.8 and it can be seen that the correct wheel's f_x graph is shifted down below zero and the f_x for the opposite wheel is shifted above.



Figure 7.2: Padded test carpet surface with 5 lb weight

Table 7.2: Ω_{SR2} and $\Omega_{SWEETPREDICTED}$ results for treaded wheels @ $.3 \frac{rad}{sec}$ on carpet

Carpet	Wheel	Ω_{SR2}	$\Omega_{SWEETPREDICTED}$	Difference	% of Target	Y slip
padded	Opposite	-.0367	-.0374	1.9%	35%	65.2%
padded	Correct	-.0454	-.0498	9.7%	43%	57.0%
unpadded	Opposite	-.041	-.0417	1.7%	39%	61.1%
unpadded	Correct	-.0471	-.0472	.4%	45%	55.3%

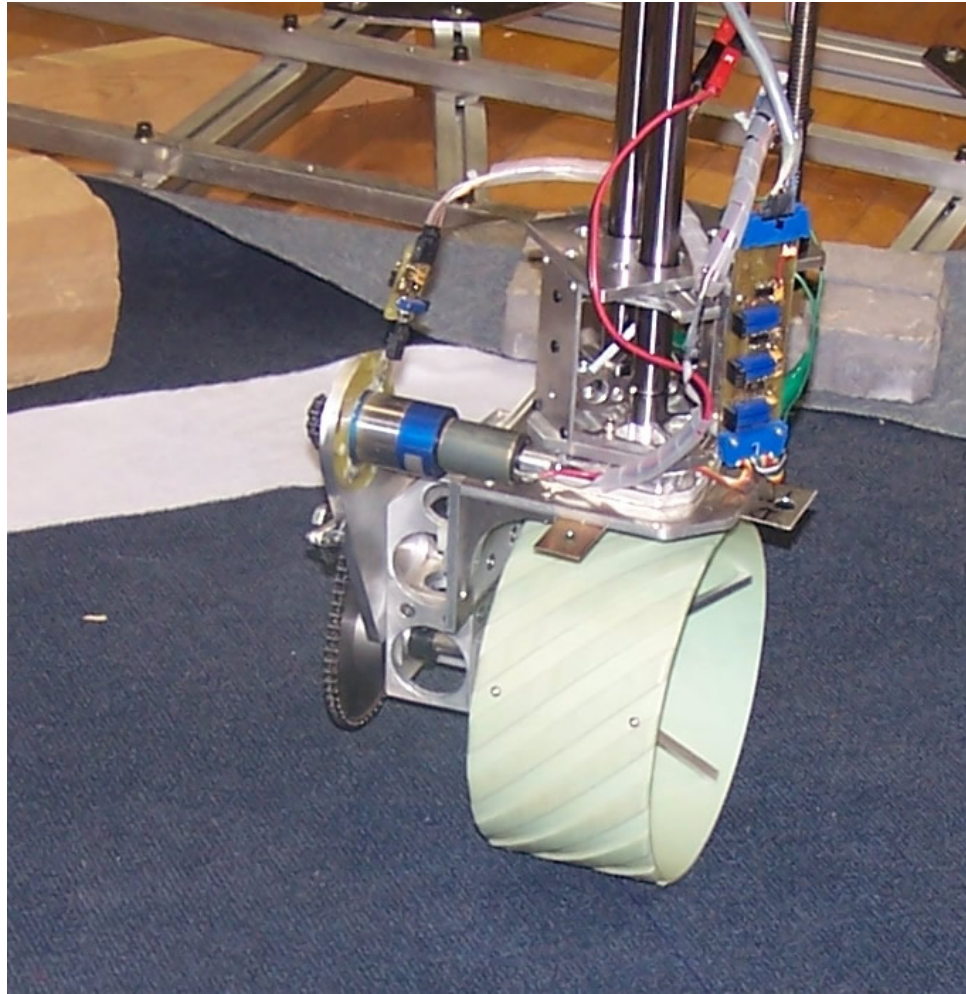


Figure 7.3: Correctly orientated wheel on carpet

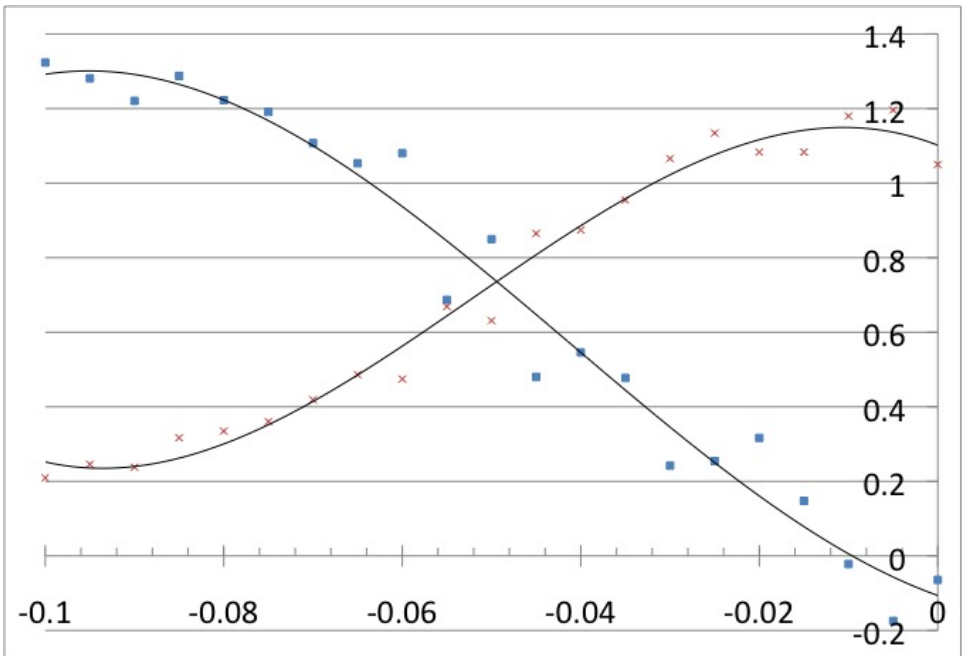


Figure 7.4: Results for correctly orientated treaded wheel rotating at $\omega = .3\frac{rad}{sec}$ on unpadding carpet

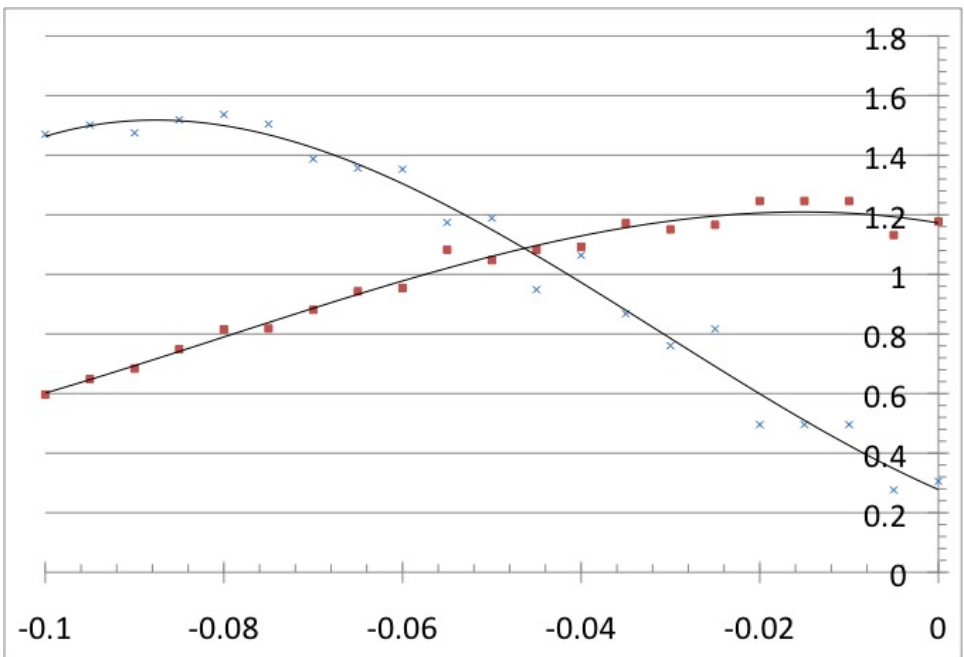


Figure 7.5: Results for oppositely orientated treaded wheel rotating at $\omega = .3\frac{rad}{sec}$ on unpadding carpet

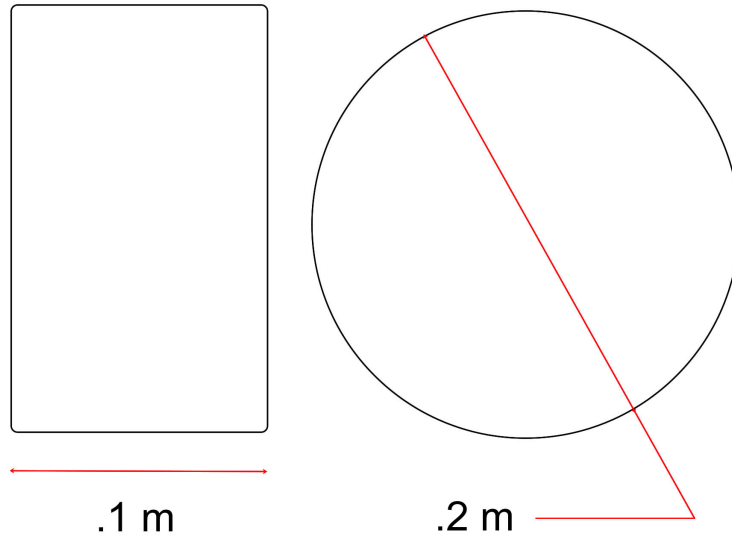


Figure 7.6: Treaded Wheel Dimensions

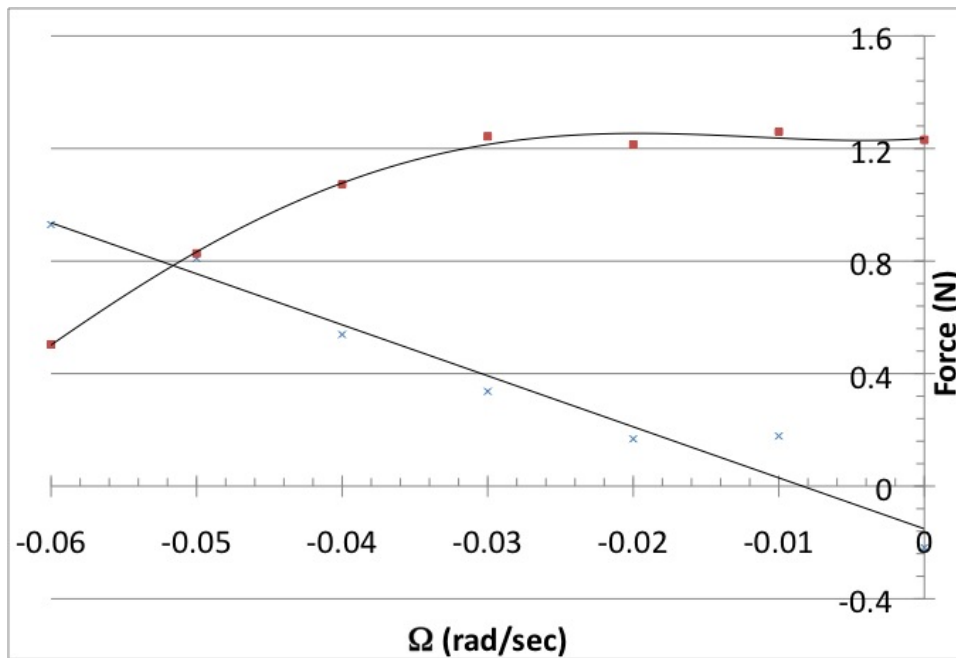


Figure 7.7: Results for correct treaded wheel rotating at $\omega = .3 \frac{rad}{sec}$ on padded carpet

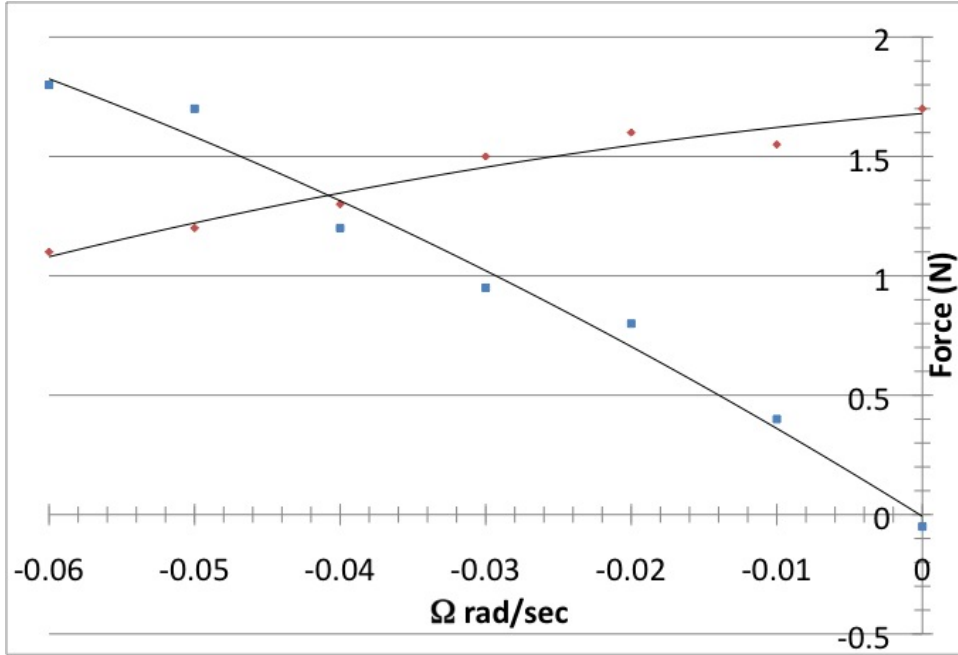


Figure 7.8: Results for opposite treaded wheel rotating at $\omega = .3 \frac{rad}{sec}$ on padded carpet

The shift below zero is the benefit of a correctly oriented wheel causing f_x and f_y to intersect at a higher Ω . The opposite wheel's $|\Omega|$ is smaller for the same reason. This shift is caused by the inherent force due to the tread spoke of in chapter 4 and shows that tread does have a significant effect on turning performance.

7.4.3 Reduction of bulldozing by higher ω

Again it can be seen in figures 7.9 and 7.10 that f_x is dependent on slip (ω), as with yoshida [70].

7.4.4 Equilibrium force intersection points

Figures 7.9 and 7.10 show a combination of different ω values tested with a correctly and oppositely orientated wheel on unpadded carpet. If we take the equilibrium point line the slope, for the correct wheel, equals -3.4. This value is less than third of the opposite wheel at -12.6. This means that the opposite wheel's power needs are much more dependent on Ω than the correct wheel, and if ω were to be increased the opposite wheel would require more power for less turn rate.

7.4.5 Isotropic observations

From figures 7.4, 7.5, 7.7, and 7.8 it can be seen that the frictional forces in the Y direction (when $\Omega = 0$) are lower than the peak frictional forces in the X direction. This could be attributed to the combination of treads on the wheel, catching the carpet on the wheels edge, and the wheel angular velocity.

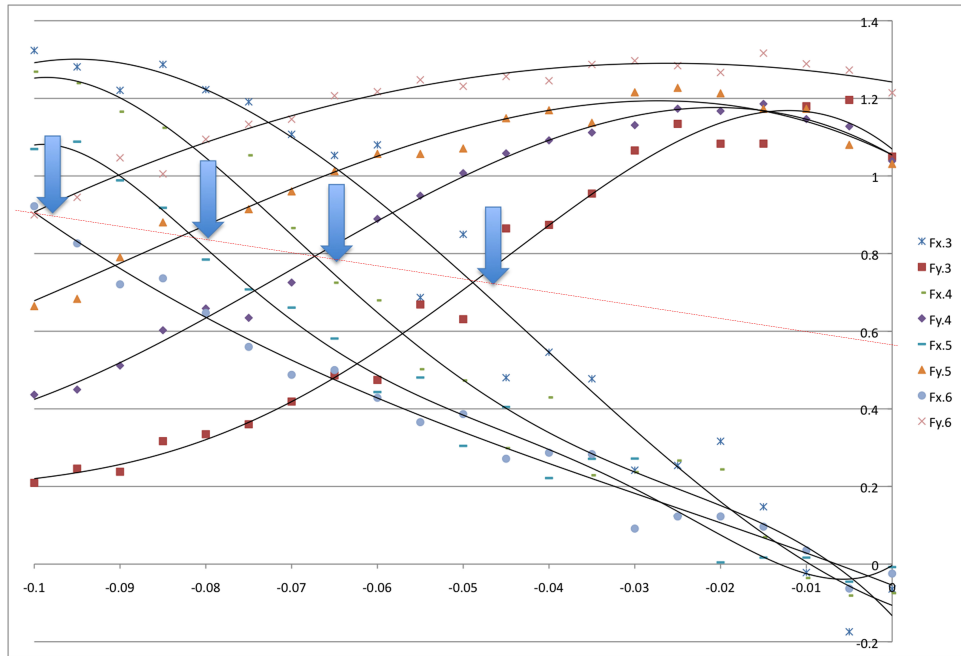


Figure 7.9: Combination of wheel rates for the correctly orientated wheel on carpet

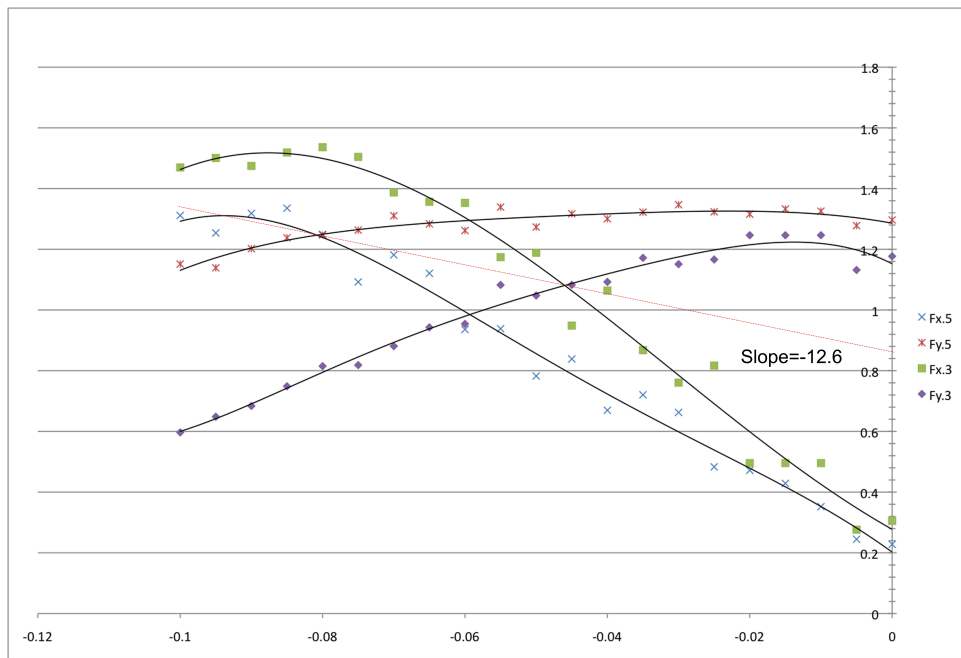


Figure 7.10: Combination of wheel rates for the oppositely orientated wheel on carpet

7.5 Conclusions

This chapter showed the results for several skid steer experiments done with directionally treaded wheels on carpet. These wheels show that their small tread was enough to significantly alter their performance both for and against in skid steer turning. Even though the rover performance is impossible to analytically calculate, SWEET was able to predict it within 10% using a single wheel test which was well within the calculated uncertainty values. Also shown was that soil, in this case carpet, will change the efficiency of a skid steer turn and could exaggerate the difference between correctly and incorrectly oriented directional wheels. Single wheel testing can help distinguish and quantify the amount that tread design can positively or negatively effect a rover's performance during maneuvers.

CHAPTER 8

Skid Steer Experiments on Sand

8.1 Introduction

The carpet discussed in chapter 7 was a simple terrain to start experimenting with but with planetary rover applications a better non-cohesive Mars or Moon simulate is needed to validate single wheel testing in such environments. The terrain on Mars contains mixed fine, course, and hardened soils as well as wind blown silt [57] in the dunes and creater floors which is where both spirit and opportunity had most of their mobility problems. An experimental terrain that is less cohesive would better simulate these harsh environments. This chapter discusses the finding from skid steer tests performed on sand.

8.2 Test set up

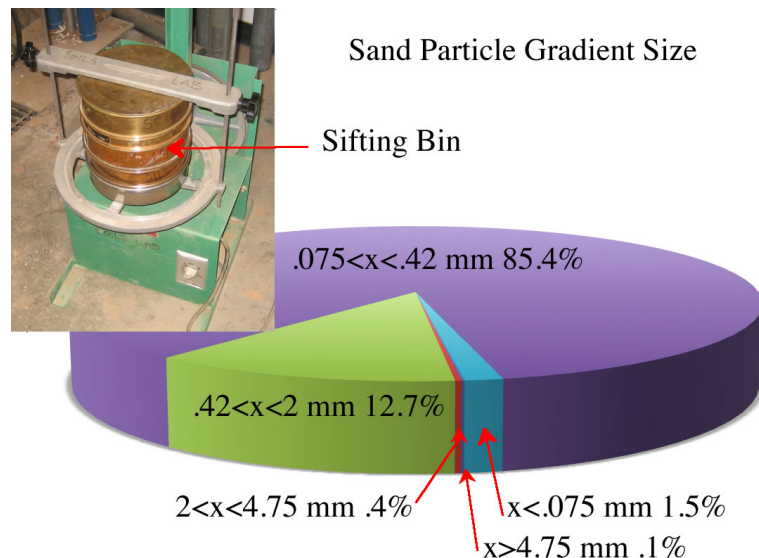


Figure 8.1: Sand Grain Size Sifting Results

The sand used in these experiments has an averaged particle size between .42 and .075 mm (figure 8.1) which can be classified as a med-fine sand [26], and is a typical play sand purchased at a hardware store. The density was $1.56 \frac{Kg}{L}$ and room humidity was 45% at about 27 degrees centigrade. The sand was a loose very dry terrain typical of sand dunes found on Mars except for the slightly larger particle size. Table 8.1 shows the sand specs calculated from a Scion Image [10] analyzation using pictures

taken similar to figure 8.2. The calculated specifications of the sand is described as rounded to well rounded [58] and fits the typical play sand characteristics.



Figure 8.2: Example Magnified Image of Sand Used in Experiment

Form Factor	Angularity	Aspect Ratio	Roundness
.65	1.58	1.32	.74

Table 8.1: Play sand Characteristics Calculated from Scion Image [10]

Four wheels were tested (fig 8.3) on sand. The first being the blank wheel tested in chapter 6.2.2 on carpet. The next wheel was a metal wheel used on SR2 [61] but with a coating of high friction rubber based paint. This wheel is a directionally treaded wheel so it is evaluated in the correct and opposite orientations. The final wheel, to be evaluated on sand, is the plastic cylindrical correctly oriented wheel that was tested in chapter 7.

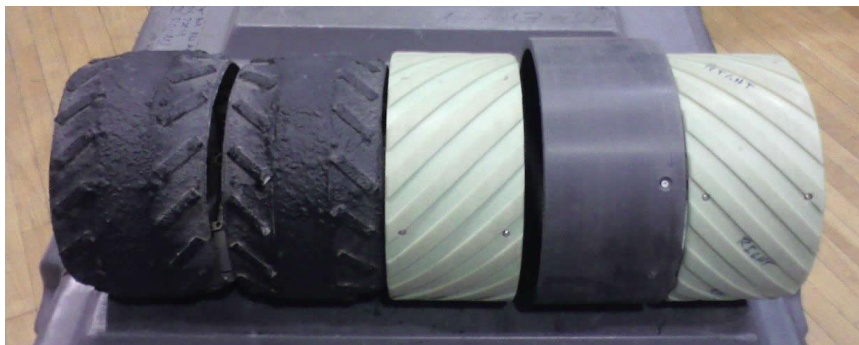


Figure 8.3: Wheels tested in Sand: (a) Opposite Painted (b) Correct Painted (c) Opposite Plastic (not tested) (d) Blank (e) Correct Plastic

In a non-cohesive soil test careful attention needs to be given to the sequences of a single wheel skid steer test. Wheel rotation and table rotation need to start simultaneously. If the wheel initiates its turn first then it will dig down in the sand before the table moves which will cause a larger bow wave which, in turn, will cause false force data.

Complications arose due to some force torque sensor voltage offsets that made calibration more frequent and made it necessary to get f_X zero force value readings from running a blank wheel in sand and averaging the values. f_Y was found again using the blank wheel but sitting it on a level board and recording the values.

8.3 Test Results

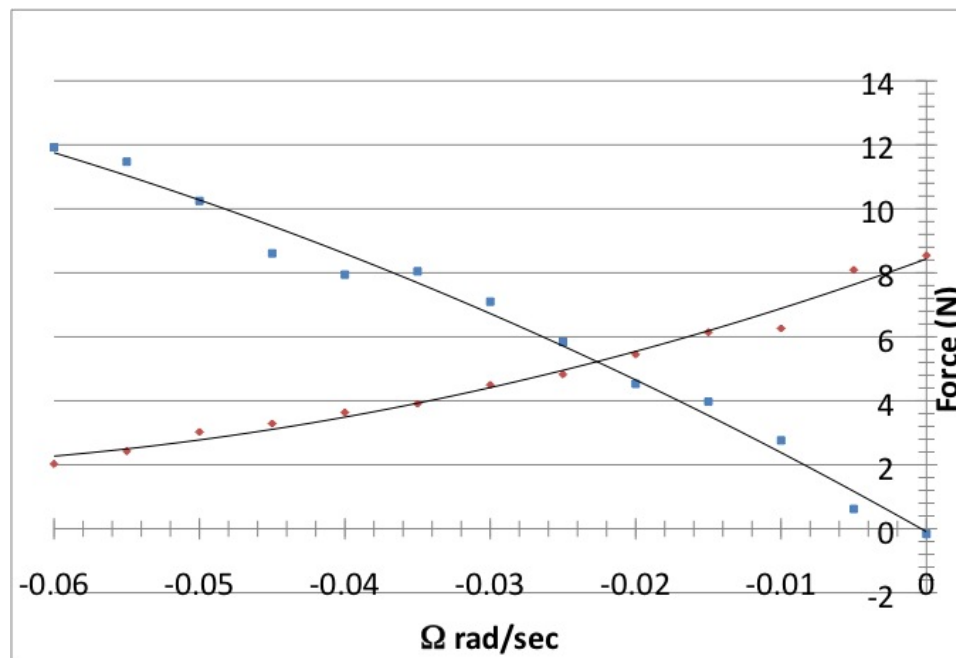


Figure 8.4: Results of Blank wheel on sand at $\omega = .3 \frac{rad}{sec}$

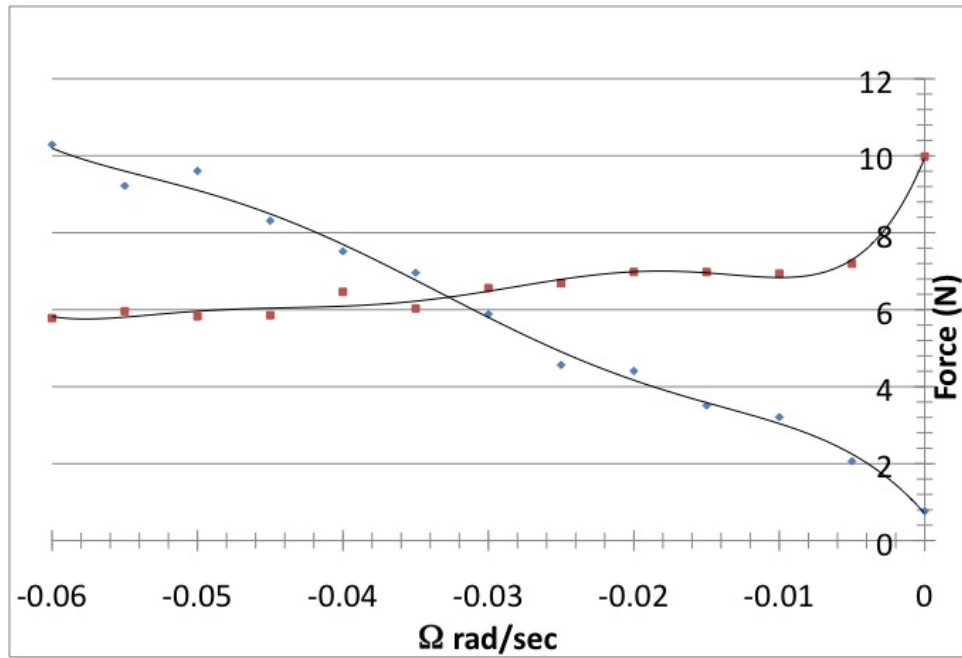


Figure 8.5: Results of Blank wheel on sand at $\omega = .4 \frac{rad}{sec}$

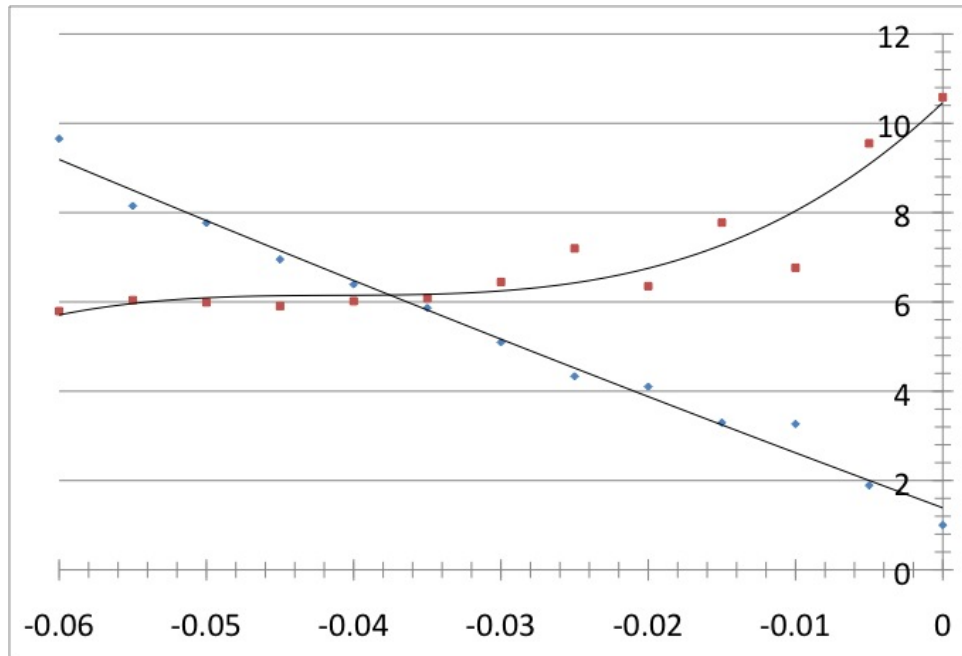


Figure 8.6: Results of Blank wheel on sand at $\omega = .5 \frac{rad}{sec}$

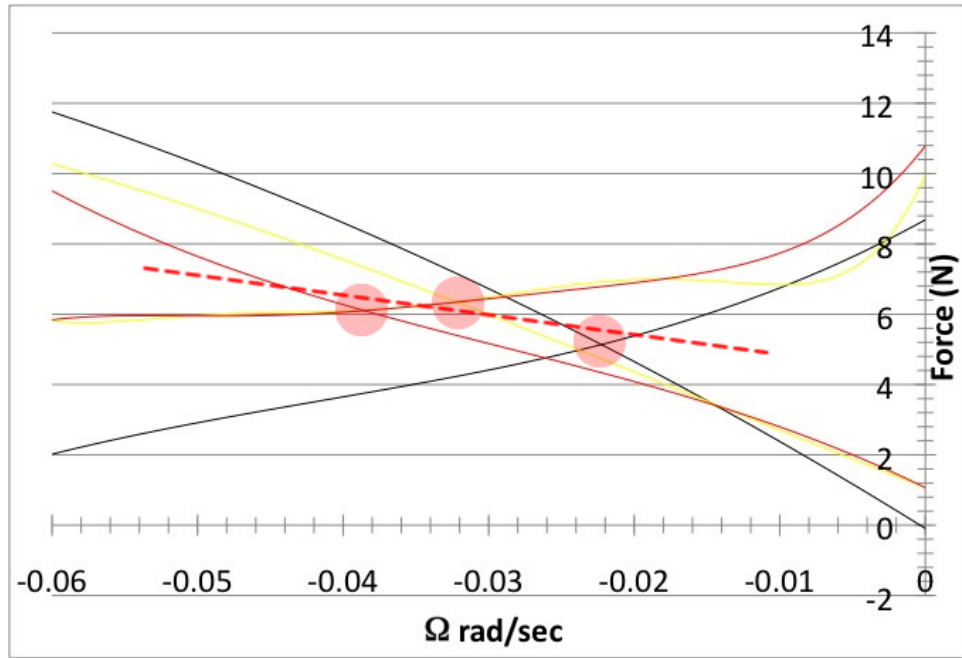


Figure 8.7: Combination of Blank Wheel results in sand

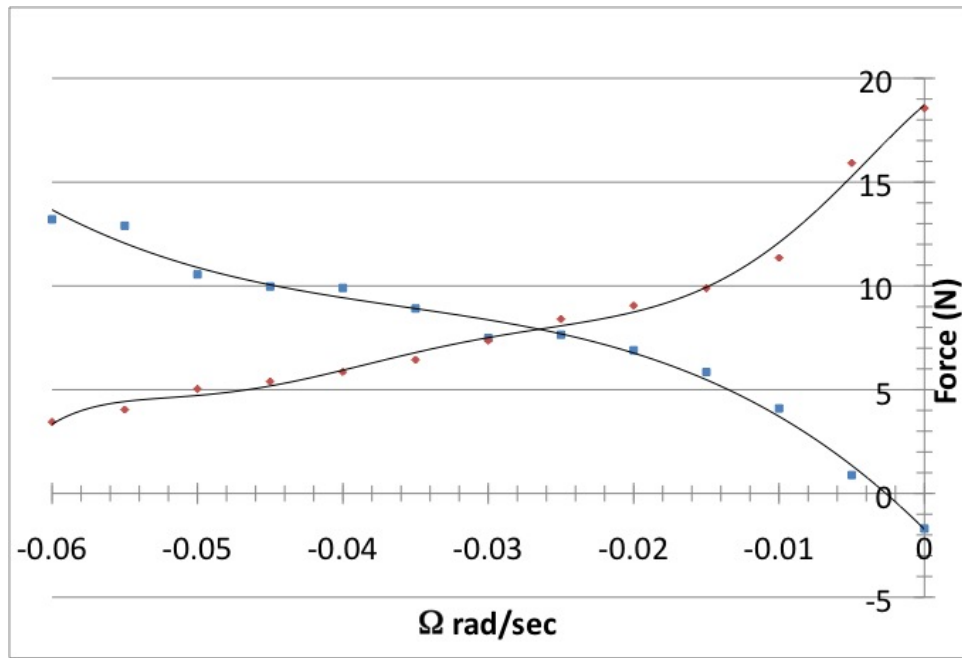


Figure 8.8: Results of Oppositely Oriented Painted wheel on sand at $\omega = .3 \frac{rad}{sec}$

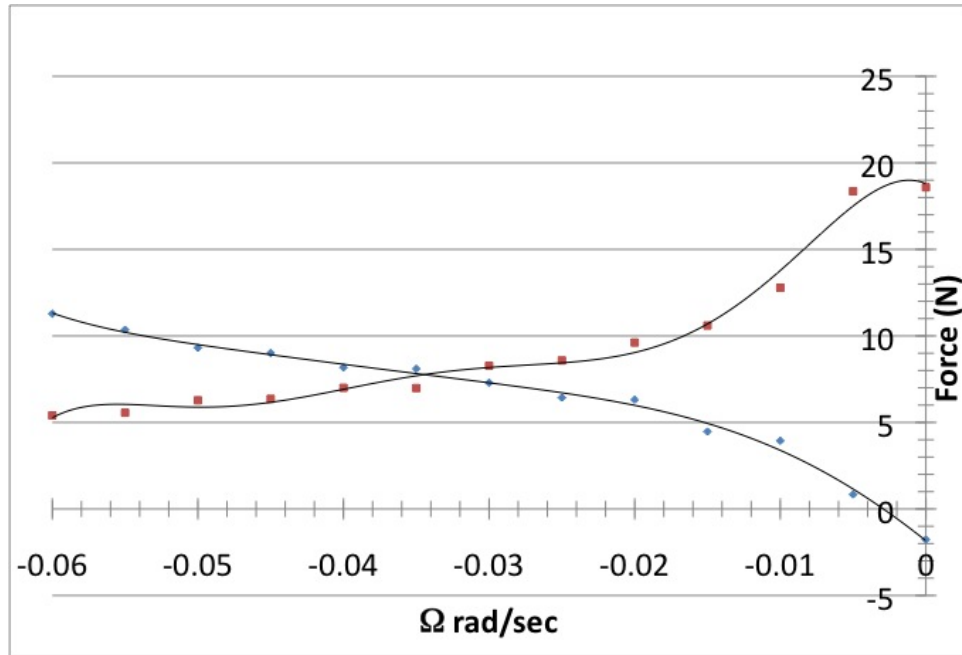


Figure 8.9: Results of Oppositely Oriented Painted wheel on sand at $\omega = .35 \frac{rad}{sec}$

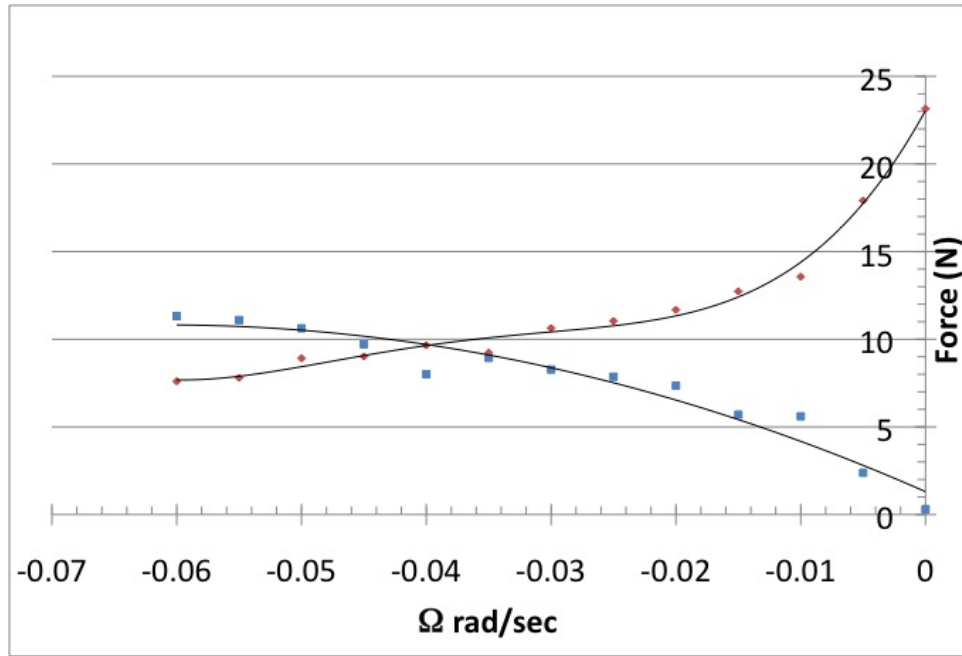


Figure 8.10: Results of Oppositely Oriented Painted wheel on sand at $\omega = .4 \frac{rad}{sec}$

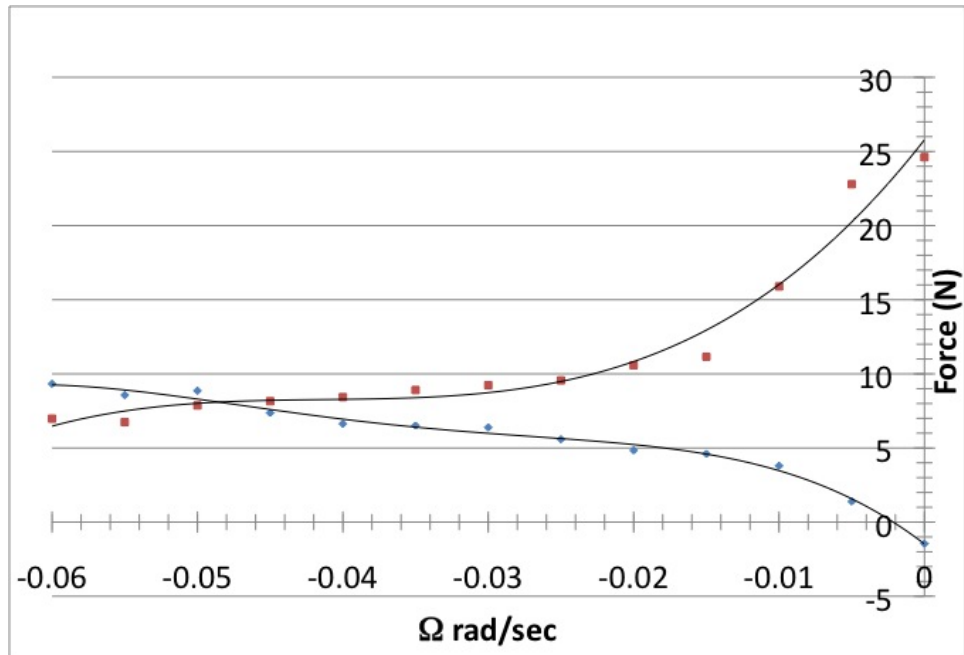


Figure 8.11: Results of Oppositely Oriented Painted wheel on sand at $\omega = .5 \frac{rad}{sec}$

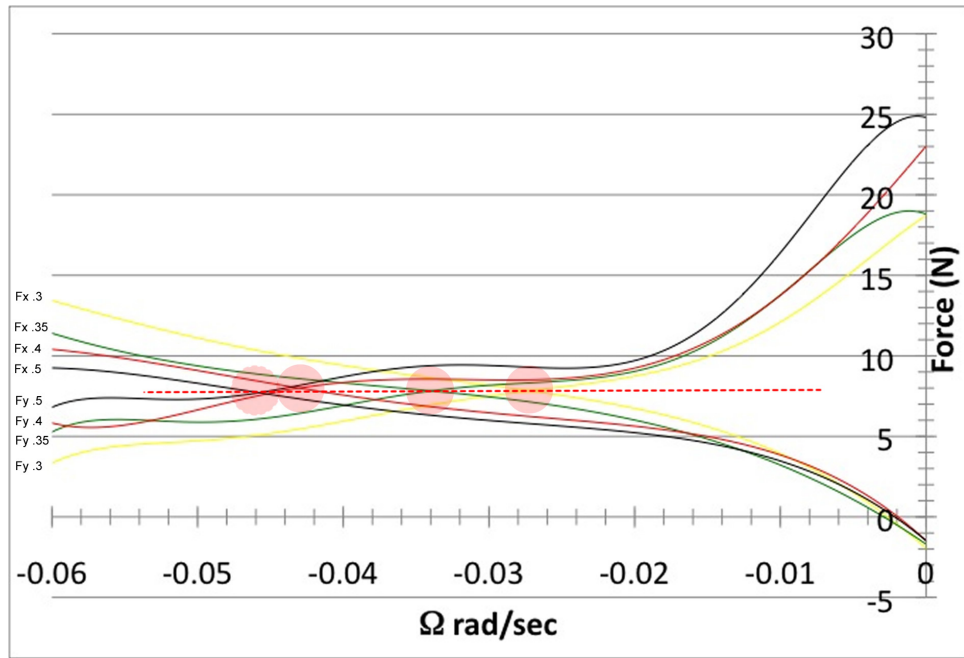


Figure 8.12: Combination of Oppositely Orientated Painted wheel in sand

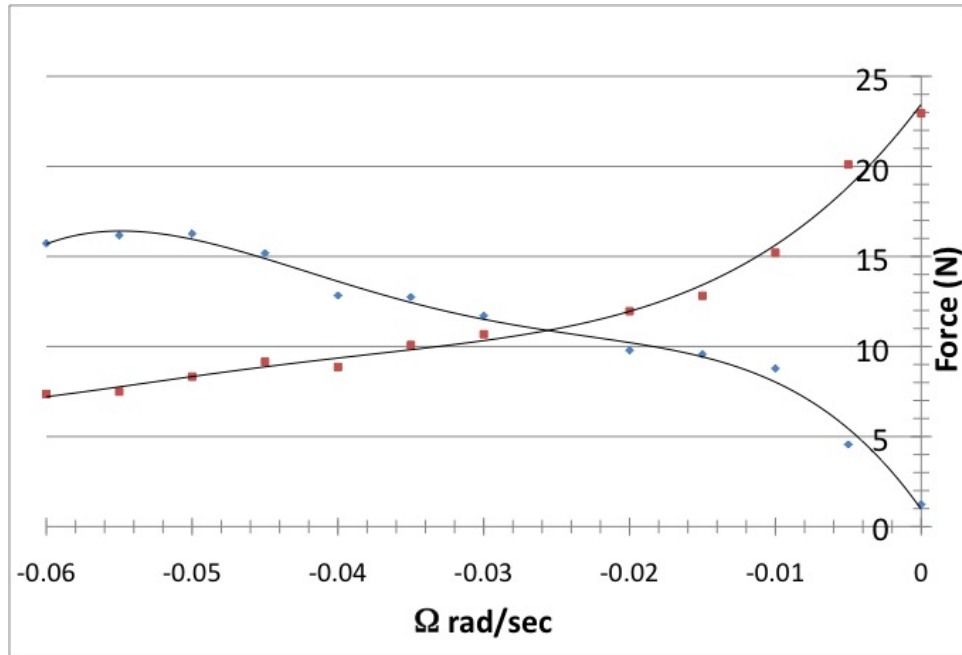


Figure 8.13: Results of Correctly Oriented Painted wheel on sand at $\omega = .3 \frac{rad}{sec}$

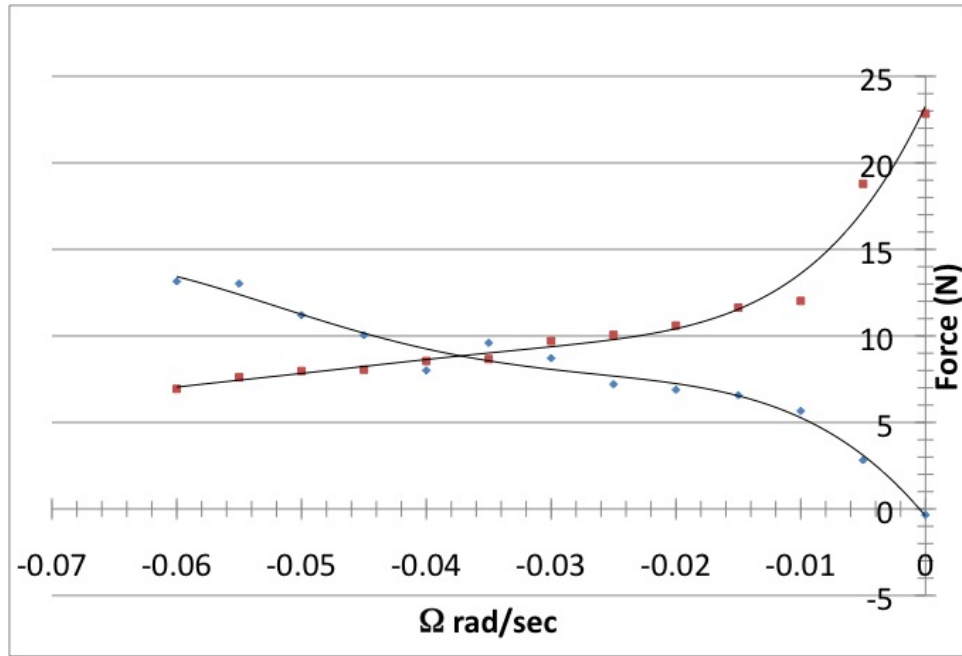


Figure 8.14: Results of Correctly Oriented Painted Wheel on Sand at $\omega = .4 \frac{rad}{sec}$

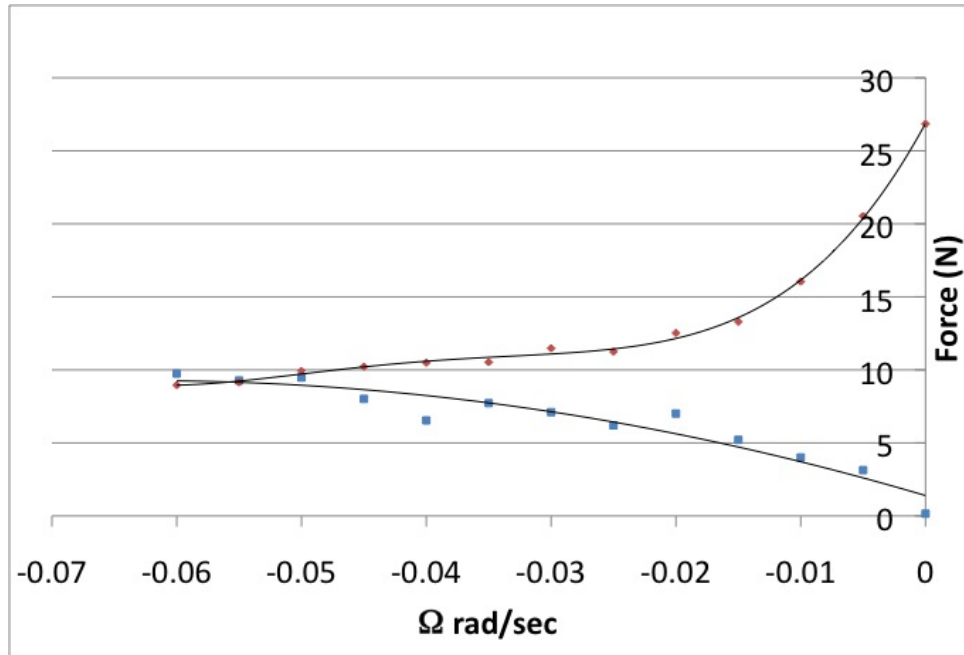


Figure 8.15: Results of Correctly Oriented Painted wheel on sand at $\omega = .5 \frac{rad}{sec}$

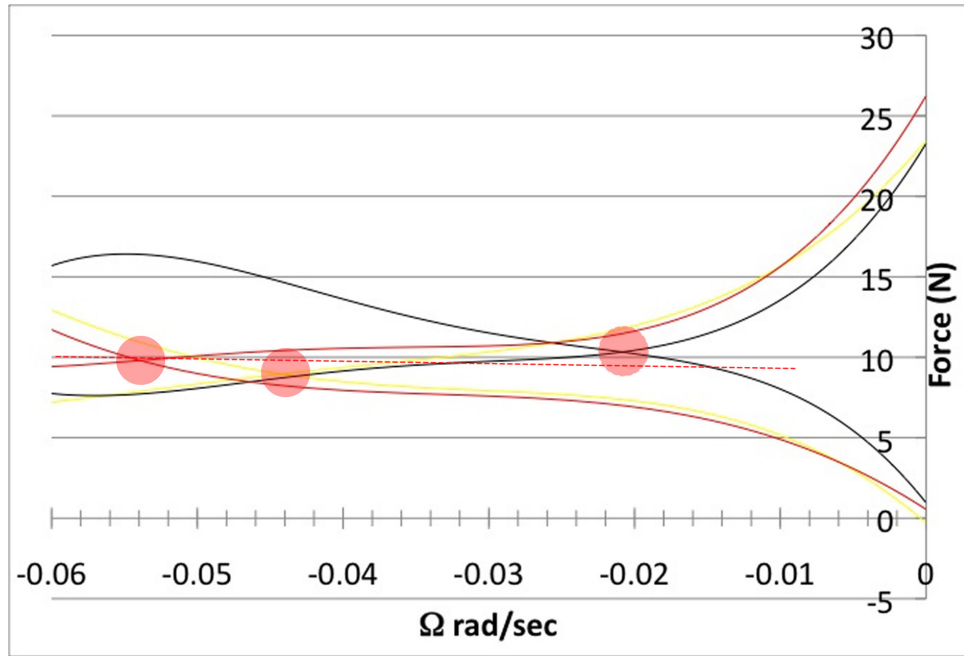


Figure 8.16: Combination of all Correctly Orientated Painted Wheel tests

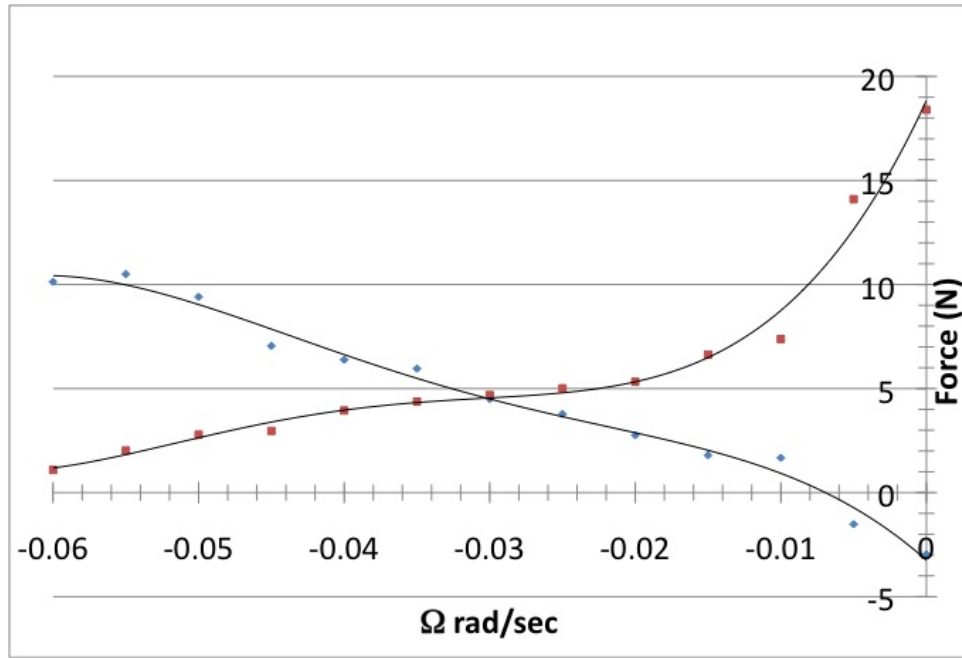


Figure 8.17: Results of Correctly Oriented Plastic wheel on sand at $\omega = .3 \frac{rad}{sec}$

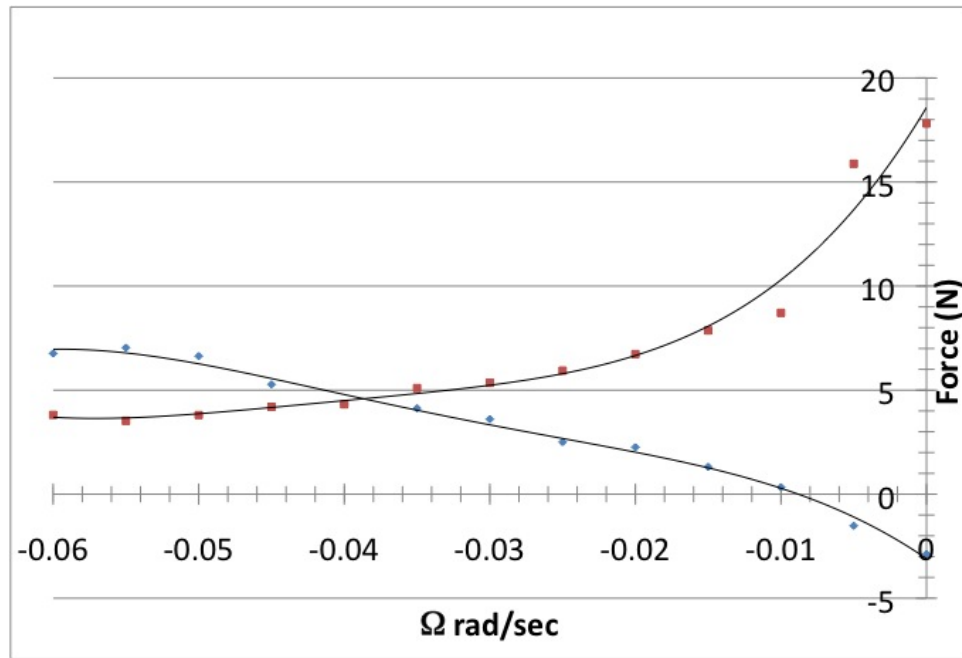


Figure 8.18: Results of Correctly Oriented Plastic wheel on sand at $\omega = .4 \frac{rad}{sec}$

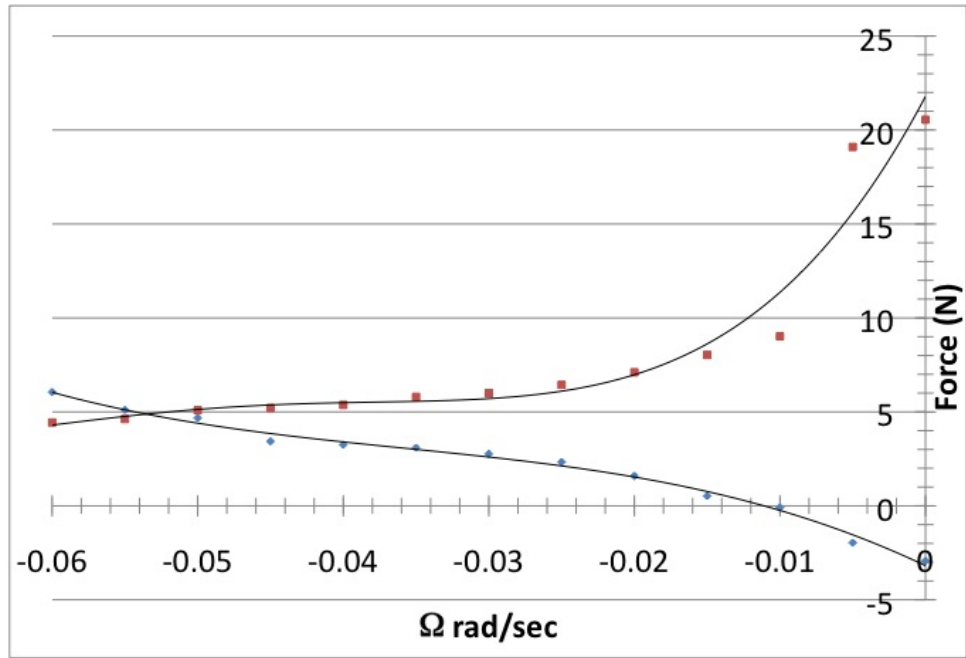


Figure 8.19: Results of Correctly Oriented Plastic wheel on sand at $\omega = .5 \frac{rad}{sec}$

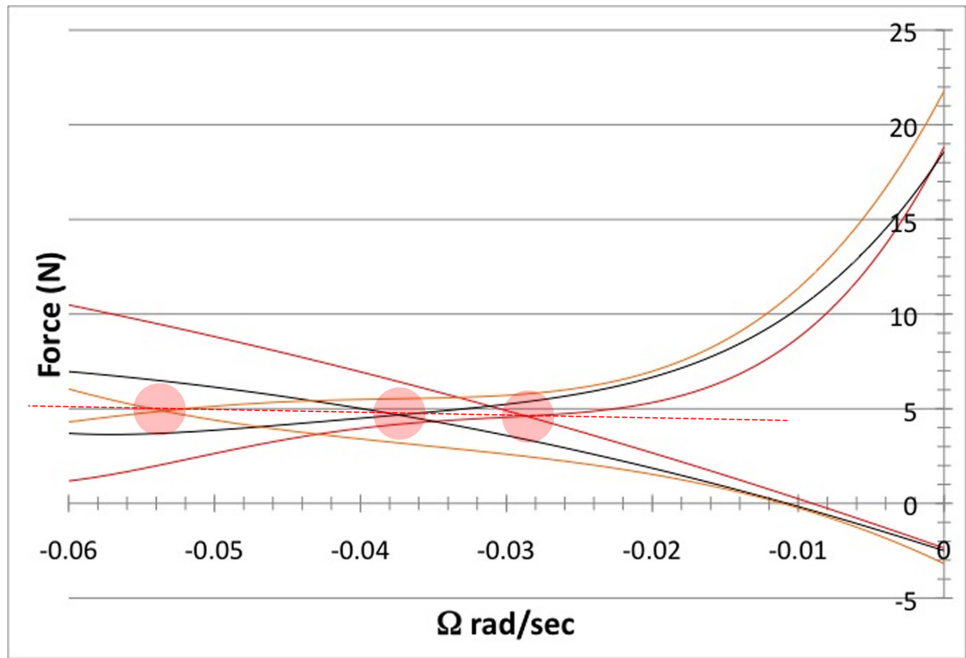


Figure 8.20: Composite of all Correctly Orientated Plastic Wheel tests

Graphs 8.4 through 8.20 show force results for all the wheels tested while table 8.3 tabulates the $\Omega_{PREDICTED}$ values compared with the SR2 tests. All test results were within ten percent of the SR2 validation values. Table 8.3 shows the test results while table 8.3 shows the calculated uncertainty.

Table 8.2: Ω_{SR2} and $\Omega_{SWEETPredicted}$ results for treaded wheels @ $.3 \frac{rad}{sec}$

ω	Wheel	Ω_{SR2}	$\Omega_{SWEETPredicted}$	Difference	% of Target	Y slip
.3	Blank	-.02	-.021	5.0%	17.7%	81.4%
.4	Blank	-.0291	-.0291	90.0%	19.3%	80.7%
.5	Blank	-.035	-.033	5.7%	18.6%	82.5%
.3	Painted Opposite	-.0265	-.0243	8.3%	25.1%	77.0%
.35	Painted Opposite	-.031	-.0322	3.9%	25.2%	73.8%
.4	Painted Opposite	-.0355	-.0337	5.1%	25.2%	76.0%
.5	Painted Opposite	-.044	-.04	9.1%	25.0%	77.2%
.3	Painted	-.025	-.0228	8.8%	23.7%	78.4%
.4	Painted	-.0345	-.0323	6.4%	24.5%	77.0%
.5	Painted	-.0466	-.0447	4.1%	26.5%	74.6%
.3	Plastic	-.0263	-.0281	6.8%	24.9%	73.4%
.4	Plastic	-.0373	-.0377	1.1%	26.5%	73.2%
.5	Plastic	-.0487	-.0511	4.9%	27.0%	71.0%

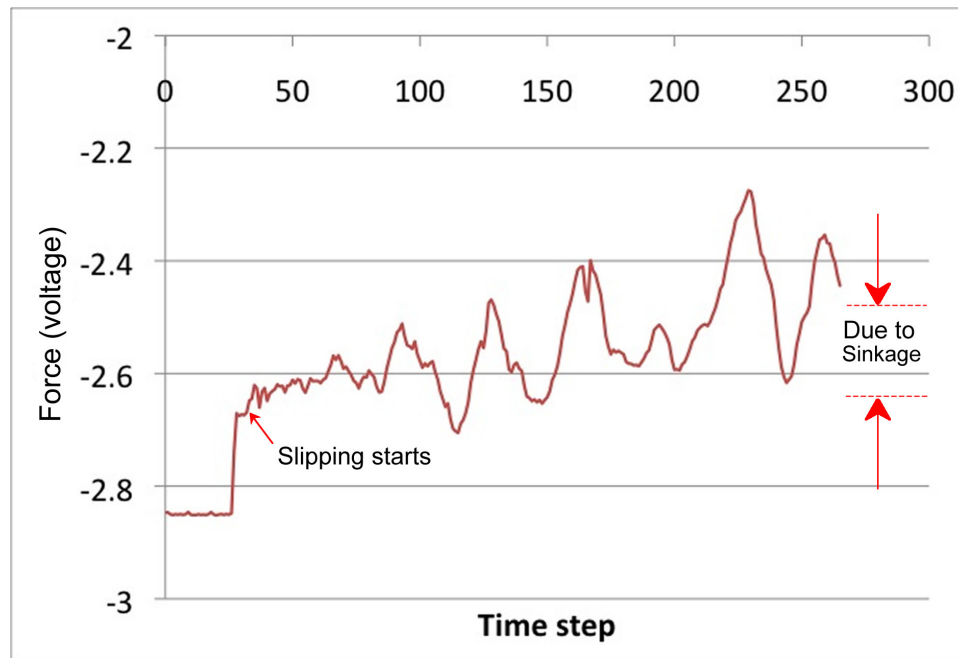


Figure 8.21: Force graph for Painted wheel in sand at $\Omega = 0$

8.4 Auxiliary treaded wheel observations

8.4.1 Y Slip Rate

Slip rate (table 8.3) for the treaded wheel shows that the blank wheel slipped more in the Y direction than all the other wheels which accounts for its lower efficiency.

Table 8.3: Calculated uncertainties for wheels in sand in $\frac{rad}{sec}$

ω	Wheel	FT sensor	SWEET	Combined	SR2 validation
0.3	Blank	-.0207 to -.0213	$\pm .00772$	-.0130 to -.0290	$\pm .00248$
0.4	Blank	-.0323 to -.0337	$\pm .00772$	-.0246 to -.0414	$\pm .00249$
0.5	Blank	-.0287 to -.0295	$\pm .00772$	-.0209 to -.0372	$\pm .00249$
0.3	Painted Opp	-.0239 to -.0247	$\pm .00772$	-.0162 to -.0324	$\pm .00238$
0.35	Painted Opp	-.0317 to -.0327	$\pm .00772$	-.0240 to -.0405	$\pm .00238$
0.4	Painted Opp	-.0329 to -.0346	$\pm .00772$	-.0254 to -.0423	$\pm .00279$
0.5	Painted Opp	-.0393 to -.0408	$\pm .00772$	-.0316 to -.0485	$\pm .00280$
0.3	Painted	-.0225 to -.023	$\pm .00772$	-.0148 to -.0307	$\pm .00238$
0.4	Painted	-.0317 to -.0329	$\pm .00772$	-.0239 to -.0406	$\pm .00238$
0.5	Painted	-.0441 to -.0453	$\pm .00772$	-.0364 to -.0530	$\pm .00239$
0.3	Plastic	-.0276 to -.0286	$\pm .00772$	-.0199 to -.0363	$\pm .00238$
0.4	Plastic	-.0372 to -.0382	$\pm .00772$	-.0295 to -.0459	$\pm .00279$
0.5	Plastic	-.0506 to -.0516	$\pm .00772$	-.0429 to -.0594	$\pm .00281$

8.4.2 F_X shift due to tread

From figures 8.4 through 8.16 it can be seen that there was no shift due to tread. The wheels tested have non aggressive treads which make little directional difference in sand.

8.4.3 Reduction of bulldozing by higher ω

Again it can be seen in figures 8.4 through 8.16 that F_x is dependent on slip (ω), as with Yoshida [70].

8.4.4 Equilibrium force intersection points

In both the painted and plastic wheels the slope of equilibrium points (shown in figures 8.12, 8.16, and 8.20 the grey dot is focused on the equilibrium point) was level, while the blank wheel had a larger negative value (figure 8.7). This can be interpreted as the blank wheel creating more F_X and F_Y forces as the wheel speed increased which consumes more power. The plastic and painted wheels remained constant over this domain.

8.5 Conclusions

This chapter showed the results for several skid steer experiments done on sand. Although impossible to analytically calculate, SWEET was able to predict within 10% on all experiments and be well within uncertainty values. Other observations are:

- Treaded wheels did better than the blank wheel with all speeds.

- All the wheels in sand had a positive equilibrium force intersection slope which means that for this speed domain the wheels did better at higher ω speeds.
- Due to sinkage at lower Ω rates F_Y at $\Omega = 0$ is not an accurate value for dynamic friction and registered a much higher force than on carpet. Figure 8.21 shows the raw data of the $\Omega = 0$ tests for the painted wheel in sand. A clear step can be seen in the graph showing the beginning of slip which can be used to calculate μ_K .

CHAPTER 9

Paint or no paint experiment

9.1 Introduction

Chapters 1 and 2 detailed the MER rover's wheel design priorities of not being entangled in the landing bags. This no snag priority led to a design of very small grousers and lack of traction. This chapter further explores the SWEET single wheel testing methodology potential and explores avenues to allay NASA's fears of snagging while simultaneously increasing wheel traction. There are several problem with metal wheels for planetary rovers. The first is that their traction is much less than that of their pneumatic rubber counterparts which can be seen in their dismal performance. Another problem is their potential for snagging on rocks or landing bags which could possibly bring the mission to an embarrassing end. To combat the second evil, designers have made the metal wheels less aggressive, these emaciated grouser patterns makes the wheel performance even worse. In light of this any new wheel design that enhances its performance as well as alleviates the risks of a potential wheel snag would be advantageous. In an attempt to better the performance of these wheels, as well as decrease their potential as a snagging hazard, a test was conducted evaluating two metal wheels. One wheel is left bare and is compared with its twin (fig. 9.1) coated with Herculiner, a polyurethane and rubber based paint [39]. Painting rover wheels is not a new concept and was done on the Sojourner rover [7] but not for traction; the paint was designed to wear off to show the abrasion properties of the Martian soil.

9.2 Test Set Up

The wheels tested were the metal wheels tested in chapter 8. Two categories of tests were done on the wheels, the first being a static friction test which evaluated the wheels frictional force on play sand and paving stone (Fig. 9.2 and Fig. 9.3). This test keeps the table from moving under the wheel while the test wheel motor was slowly ramped up until the wheel begins to slip. The longitudinal force acting on the wheel (along the Y axis) is measured and recorded which allows the maximum frictional force of the wheel, which is also when it begins to slip, to be seen clearly. This gives an easy comparison between the two wheels tested showing and comparing static and kinetic friction. Ten trials of each wheel on each surface were done with the values averaged in the results.

The second test was run on sand only and measures the performance of the wheels as they drag a constant longitudinal force (f_Y). The SWEET apparatus is capable of a force feedback test in which it simulates a dragging force, which in this test was an arbitrary 17 Newtons for 13 seconds. The drag footprint is shown in figure 9.4. The



Figure 9.1: Metal rover wheels, right bare wheel used on SR2 rover [61]. Left wheel is painted with Herculiner [39] high friction paint.

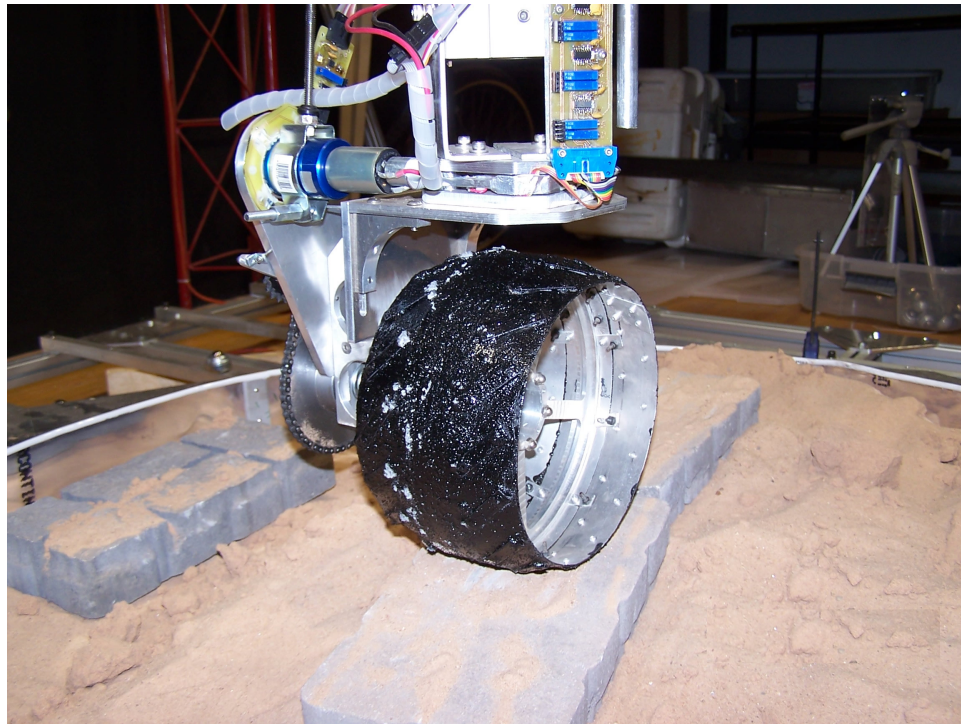


Figure 9.2: Painted wheel mounted on SWEET in static friction test on paving stone



Figure 9.3: Painted wheel mounted on SWEET in static friction test on sand



Figure 9.4: Painted wheel mounted on SWEET pulling load in sand

wheels were run 5 times and their performance values averaged. Both wheels in all tests were loaded with a 40 N normal load and run through 5 centimeters of sand.

Table 9.1: Wheel Performance in Sand in Dragging Test

Wheel	Rotated distance (m)	Distance traveled (m)	Slip
Unpainted	1.33	.361	72.9%
Painted	1.292	.538	58.4%

9.3 Results

The static friction test in sand (fig. 9.5 Time versus Frictional Force) showed that the painted wheel (red line) recorded a larger kinetic frictional force than the bare wheel (blue line) although the bare wheel had a slightly higher kinetic and static frictional force on the paving stone (fig. 9.6). These results can be explained as follows: on rock, the sharp grousers of the bare wheel dig in and provide more resistance than the rounded grousers (rounded due to the coat of paint) on the painted wheel; in sand, the rough surface of the painted wheel provides more contact area with the sand, and moves more sand (and therefore has more force) than the smooth surface of the bare wheel. Note that the sharp grousers of the bare wheel will cut through the sand more easily than the rounded lumps of the grousers on the painted wheel.

The dragging test results show that the painted wheel travelled farther in the allotted time, and with less rotation, than the bare wheel giving the painted wheel the advantage in sand (the painted wheel slipped less). This advantage can be intuitively explained as the rougher surface of the painted wheel moving more sand than the smooth surface of the bare wheel, thereby generating more force and overcoming the simulated drag force more easily. Table 9.1 shows the average distance traveled for a given amount of wheel rotation with the slippage value for each wheel. As can be seen, wheel slippage was high in this test due to the drag force, but the coated wheels performed significantly better.

Fig 9.7 shows the sinkage in centimeters for both wheels are very similar. The painted wheel initially sinks a little faster, understandably since it is moving more sand. But as the wheels settle in, the sinkage rate of the painted wheel slows until both wheels achieve a similar rate and depth of sinkage.

9.4 Conclusions

These tests showed that the bare metal wheel did prove to catch more on the rock surface than the painted wheel. This can be explained by the metal tips and sharp points tended to catch on the porous rock surface. While advantageous in climbing over rocky obstacles, this could also be a negative attribute and might prove harmful to rover drive trains and pose possible mobility hazards such as with the fear of the MER rovers snagging on the landing bags [12]. The painted wheels cause the grousers to be smoother while showing better performance in sand both in static friction and dragging especially as the wheel sinks.

Future work should include tests on other wheel shapes as well as different space rated epoxies or paints. From these experiments it can be seen that space worthy

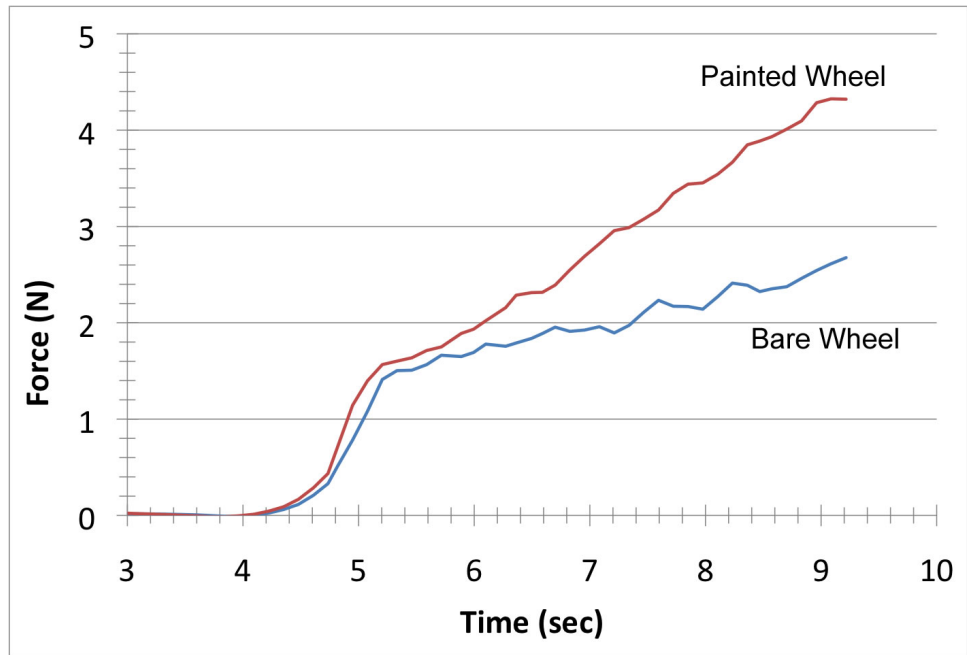


Figure 9.5: Longitudinal force generated by actuated wheel in Sand

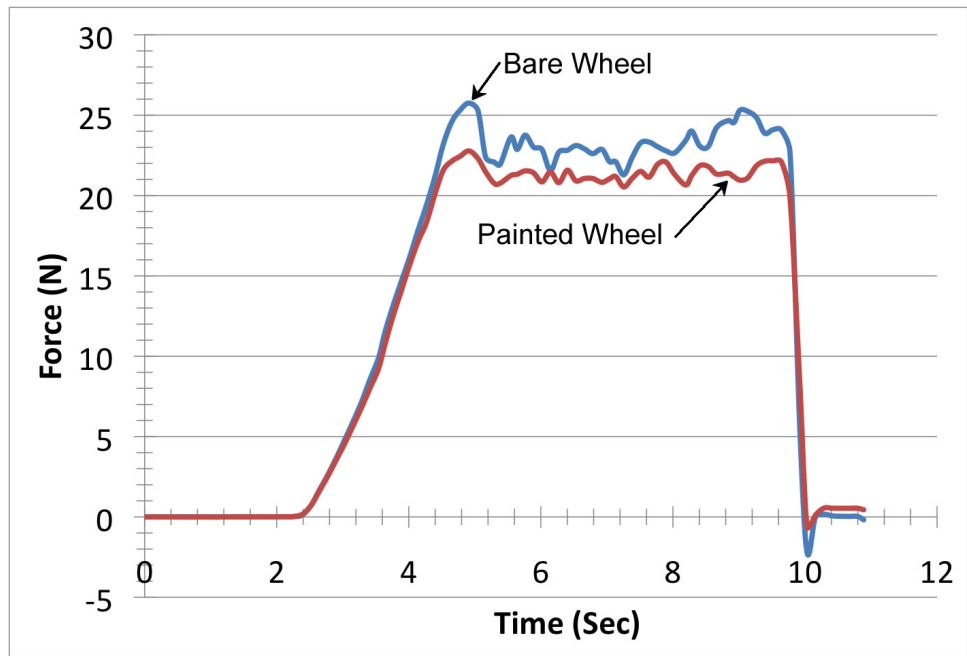


Figure 9.6: Longitudinal force generated by actuated wheel on rock

paints or epoxies will enhance a rover's performance by increasing each wheel's traction without the snagging hazards posed by bare metal wheels.

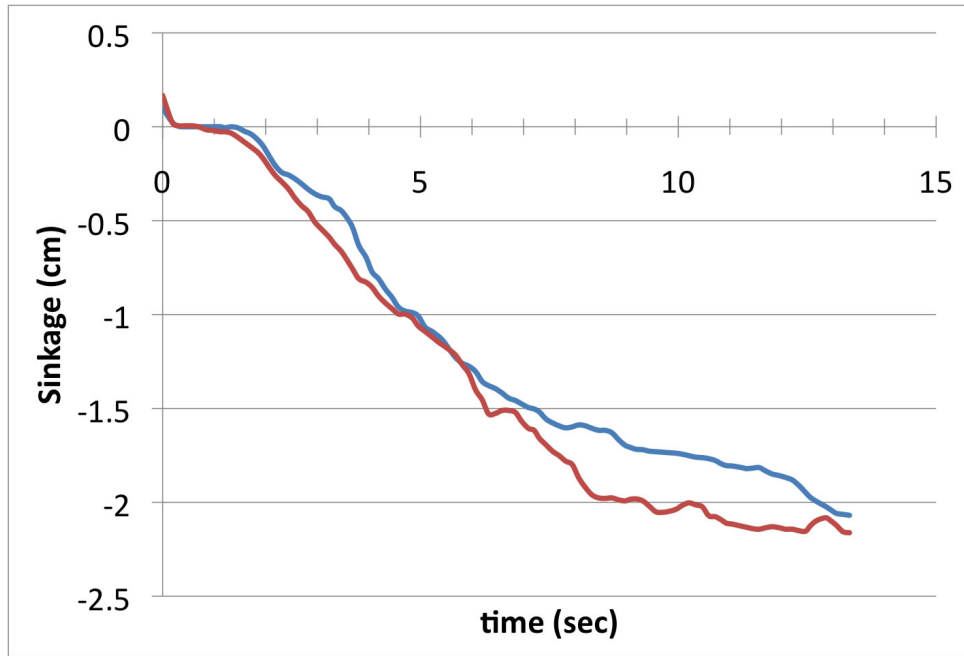


Figure 9.7: Sinkage comparison of painted and bare wheels on sand

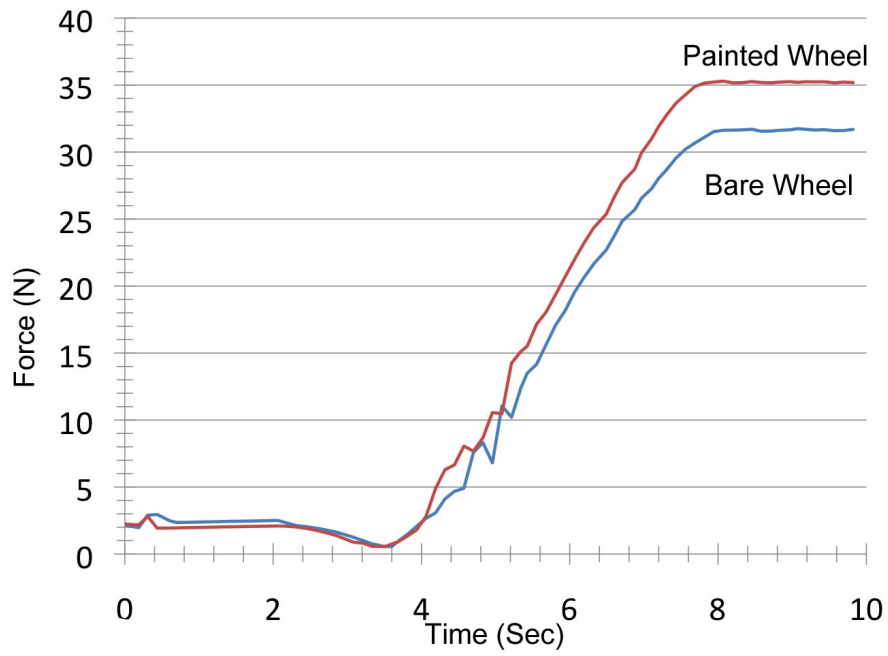


Figure 9.8: Power comparison of painted and bare wheels on sand

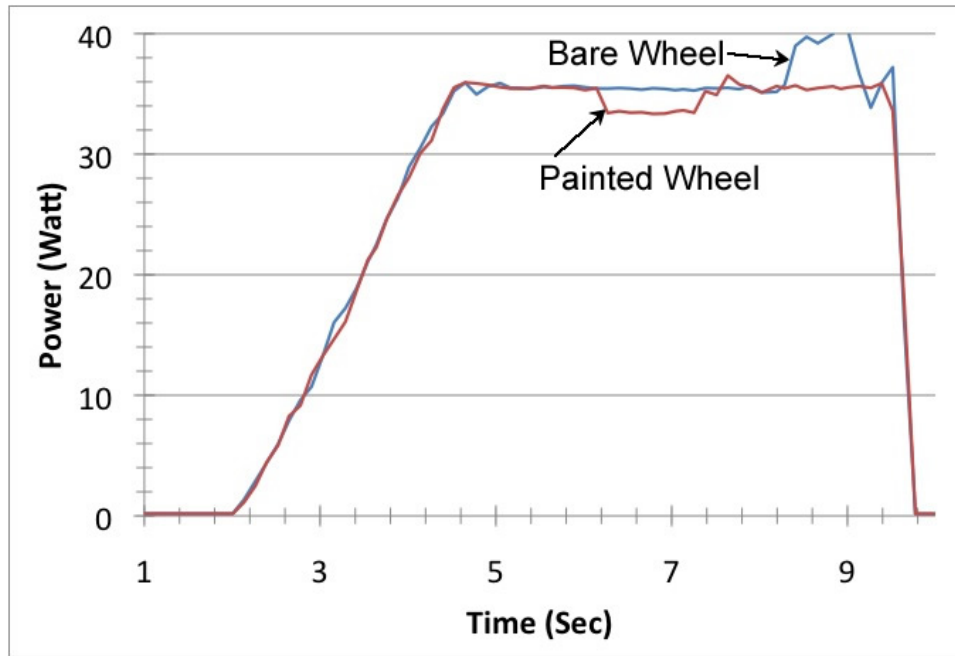


Figure 9.9: Power comparison of painted and bare wheels on rock

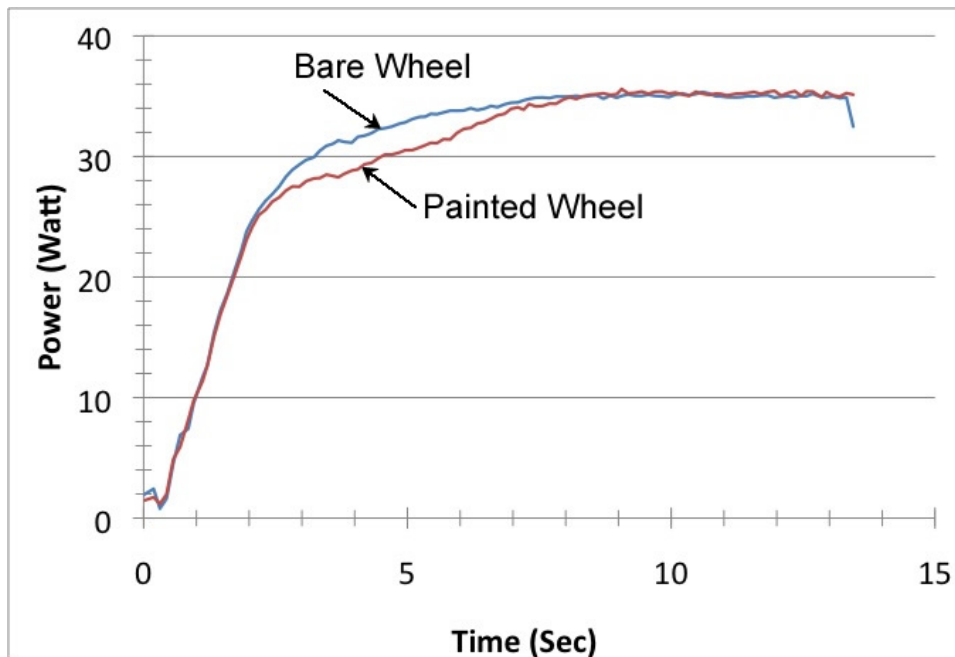


Figure 9.10: Power comparison of painted and bare wheels dragging 17 Newtons on sand

CHAPTER 10

Power Prediction with Single Wheel Testing

10.1 Introduction

Power usage is an important parameter for planetary rovers, and wheels can have a definite affect on a rover's power needs. So the amount of power a wheel takes to perform a maneuver, such as a skid turn, should also be an important parameter to be evaluated and optimized during the iterative design process. If it can be proven that a single wheel test can produce power usage measurements for a tested wheel and that value can be mapped to a total rover assembly then power usage is one more behavior that can be tested on a single wheel testbed.

10.2 Test Set Up

Four test wheels were individually loaded on SWEET and run again in a simulated skid steer turn. SWEET measured the voltage and current from the wheel test motor which is used to calculate the un-calibrated power that the wheel used in turning. These wheels were also mounted on SR2 and put through the same turn while recording the voltage and current used.

10.3 Results

The comparison between SWEET and SR2 are given in figure 10.1 showing a simple linear relationship between the two and mapping the data from a single test to a full rover assembly.

10.4 Power Usage Observations for the Four Wheels Tested

Figures 10.2 and 10.3 show the outcome of all four wheels tested on SWEET in units of $\frac{\Omega}{Power}$. As is seen the omni wheel was most efficient overall by quite a margin while the left wheel did the worst in efficiency. It should noted that the black wheel is larger and the omni wheel is smaller than the left and right, but both figures take wheel size into account. In every case the wheels were more efficient at the higher ω .

10.5 Conclusions

From the experiments done it can be seen that the power usage is one more performance measure that for a given rover on a specific soil can be predicted by a single

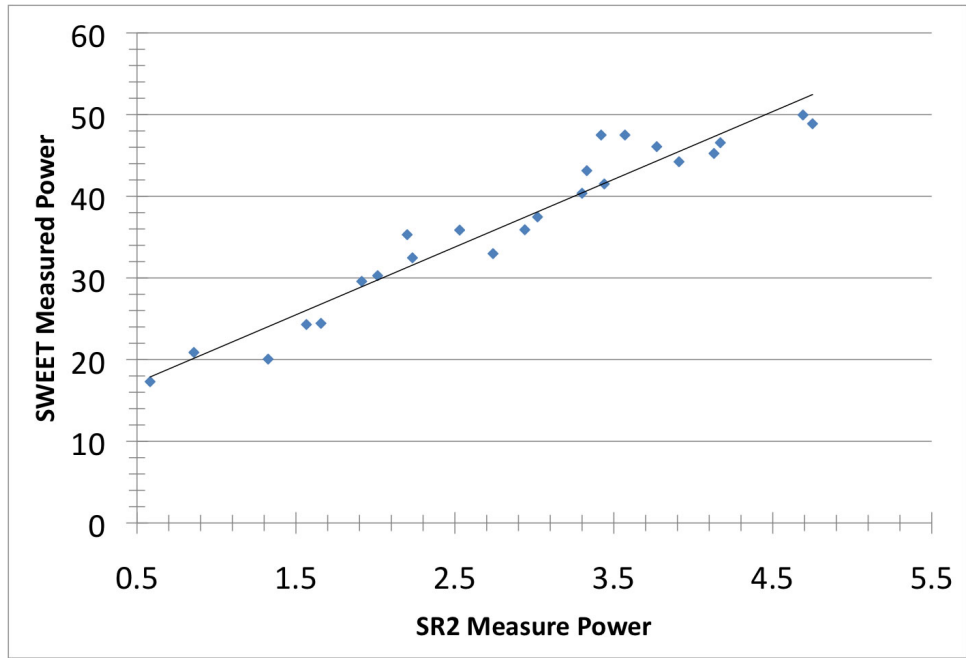


Figure 10.1: Linear comparison between measured power from SWEET single wheel test and SR2 actual.

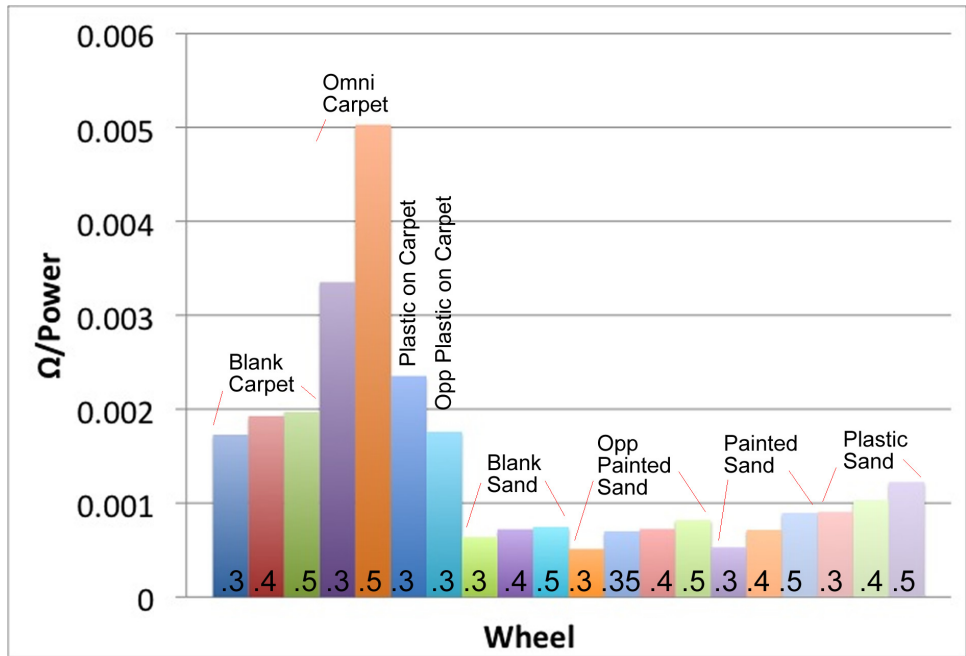


Figure 10.2: Ω per Unit Power for all wheels tested

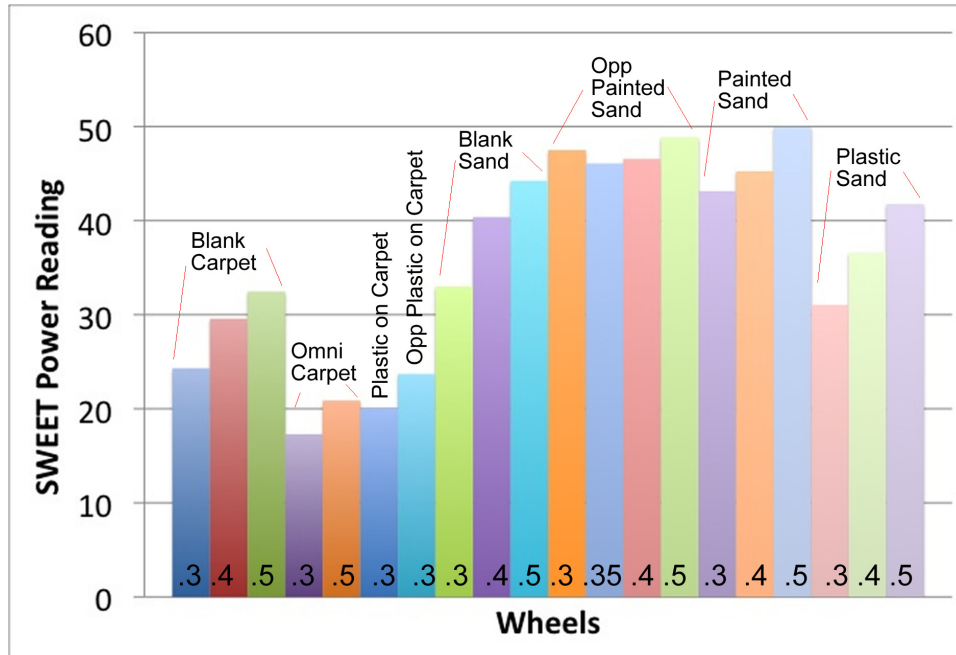


Figure 10.3: Results for power usage of each wheel

wheel test. Also from figure 10.2 it is apparent that tread does matter in skid steer turning and that these wheels were more efficient at higher ω 's with the Omni wheel being the most efficient. Graph 10.2 shows the comparison between the carpet and sand tests, which shows that the wheels on carpet are much more efficient than on sand. Also shown is that the directional wheels in sand showed very little change when oriented wrong which could change if a more aggressive grouser was used.

CHAPTER 11

Observations and Conclusions

11.1 Introduction

Rover performance can be enhanced by bringing back the practice of iterative wheel design without the cost of time and resources endured by the past programs that utilized it. Several conclusions can be brought forward dealing with this hypothesis and the experiments performed to validate it. This chapter sums up the research as well as looks forward to future work in the subject.

11.2 Validation of single wheel testing

Table 11.1: Results for all single wheel tests

Surface	Wheel	ω	Ω_{SR2} (actual)	Ω_{SWEET} (Predicted)	Difference	% Target	Y Slip
unpadded	Blank	0.3	-.042	-.042	0%	37%	62.8%
unpadded	Blank	0.4	-.056	-.057	1.8%	37%	62.1%
unpadded	Blank	0.5	-.066	-.064	3.0%	35%	66%
unpadded	Omni	.3	-.059	-.058	1.7%	90.9%	6.9%
unpadded	Omni	.5	-.1	-.105	5.0%	92.5%	1.2%
padded	Left	.3	-.0367	-.0374	1.9%	35%	60.5%
padded	Right	.3	-.0454	-.0498	9.7%	43%	55.2%
unpadded	Left	.3	-.041	-.0417	1.7%	39%	64.7%
unpadded	Right	.3	-.0471	-.0472	.4%	45%	55.2%
Sand	Blank	.3	-.02	-.021	5.0%	17.7%	81.4%
Sand	Blank	.4	-.0291	-.0291	0.0%	19.34%	80.7%
Sand	Blank	.5	-.035	-.033	5.7%	18.61%	82.5%
Sand	Opp Paint	.3	-.0265	-.0243	8.3%	25.1%	77.0%
Sand	Opp Paint	.35	-.031	-.0322	3.87%	25.2%	73.8%
Sand	Opp Paint	.4	-.0355	-.0337	5.1%	25.2%	76.0%
Sand	Opp Paint	.5	-.044	-.04	9.1%	25.0%	77.2%
Sand	Painted	.3	-.025	-.0228	8.8%	23.7%	78.4%
Sand	Painted	.4	-.0345	-.0323	6.4%	24.5%	77.0%
Sand	Painted	.5	-.0466	-.0447	4.1%	26.5%	74.6%
Sand	Plastic	.3	-.0263	-.0281	6.8%	24.9%	73.4%
Sand	Plastic	.4	-.04	-.0377	1.1%	26.5%	73.2%
Sand	Plastic	.5	-.0487	-.0511	4.9%	27.7%	70.9%

From table 11.2 and figure 11.1 it can be seen that SWEET can predict full assembly rover performance in turning efficiency and turning power usage. Chapter 9 also shows that SWEET can be used to evaluate traction, sinkage, and pulling efficiency of several wheel designs.

Single Wheel Testing provides a designer with a cheap and timely means to test, evaluate, and iterate a wheel's design. Over a 2000 tests have been run on these wheels which would have been much more costly and time consuming with a full rover assembly test.

Looking at the overall data some observations can be made about the wheels tested. Figure 11.1 is the skid steer performance results for all the wheels tested with their radius taken into account. They are the percentage of the Ω value is of the $F_Y = 0$ target value discussed in chapter 4. From this graph it can be seen that the big winner over all is the Omni wheel due to its low lateral friction. Figure 11.1 shows that all wheels did worse on sand, which was expected due to its non-conhesive nature. Also expected was that wheels travelling through sand would take more power for the same velocity which can be seen in figure 11.2. Figures 11.3 and 11.4 show the comparison of the wheels in percentage of slip for carpet and sand. The blank non-treaded wheels come in last in both carpet and sand showing how tread can benefit wheel and rover performance, while the plastic wheels did slightly better on sand and future experiments could test a coated plastic wheel of the same size and shape as tested here. Target values for the chamfered wheels may be a little inaccurate due to the realistic radius of the chamfered wheel being smaller due to its sinkage. From figure 10.2 it can be seen that in sand all the wheels tested were more efficient at higher speeds. This finding conflicts with the viscous friction bow wave concept. One way to describe this is that the rover floats better on sand at these higher speeds up until a point where the viscous friction will dominate. Future tests could explain this if the sinkage is looked at in comparison to the data and a possible sweet spot could be found for every wheel where it would be more efficient.

11.3 Drag Testing

The drag test done in chapter 9 showed SWEET's capability to test in areas other than skid steering. The tests compared two identical wheels with one difference; measuring the effect of surface finish has on wheel performance.

11.4 Validation of SWEET as an Effective Test Bed

From the experimental results SWEET has proven to be an effective single wheel test bed in skid steering and power usage experiments. SWEET is able to recreate situations and actions that closely mimic real life such as real turns, soil varieties , slope testing, force feedback, and force assist, and does these in a cheap and timely manor.

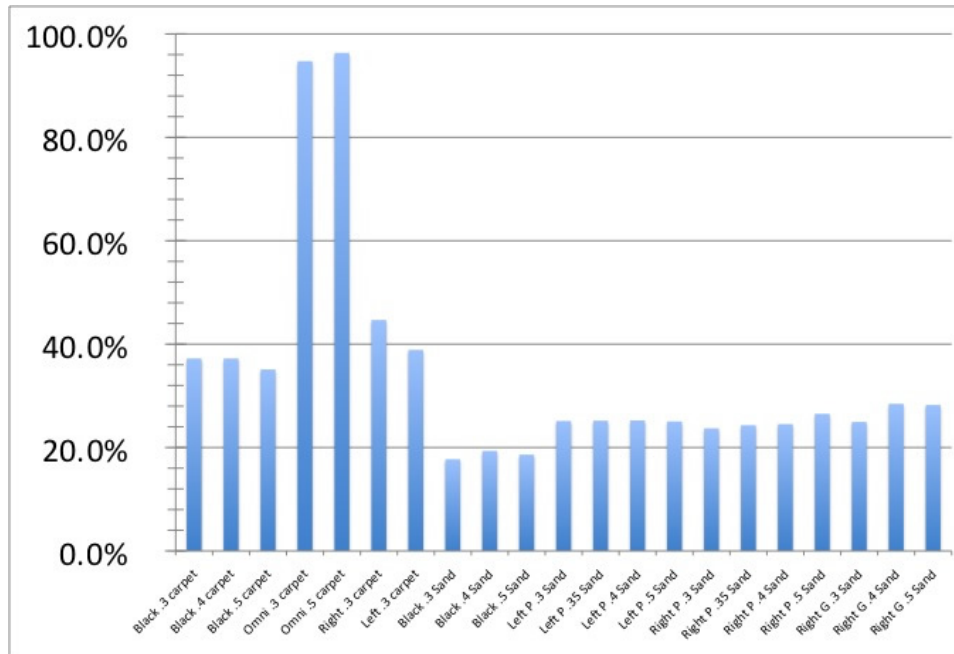


Figure 11.1: Total results of wheel as a percent of Target values

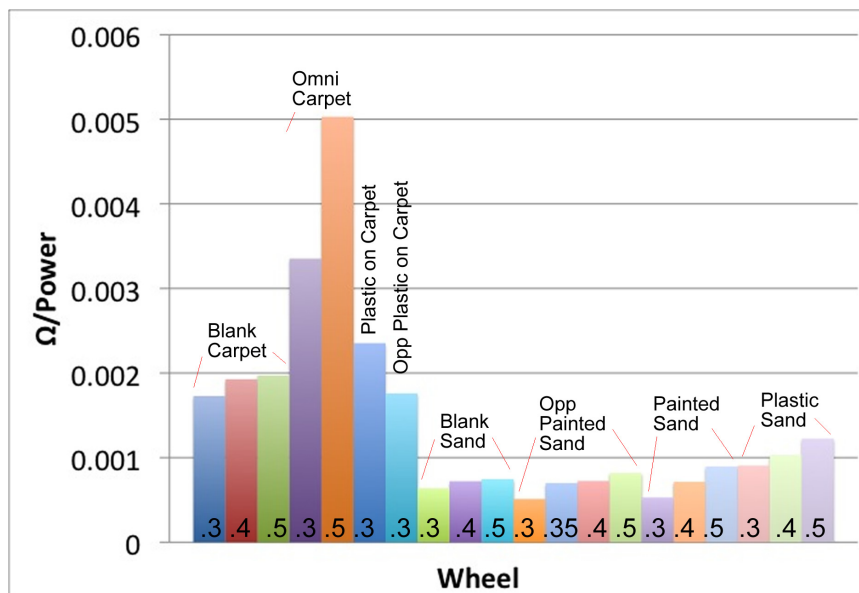


Figure 11.2: Efficiency of wheels as Ω per unit Power

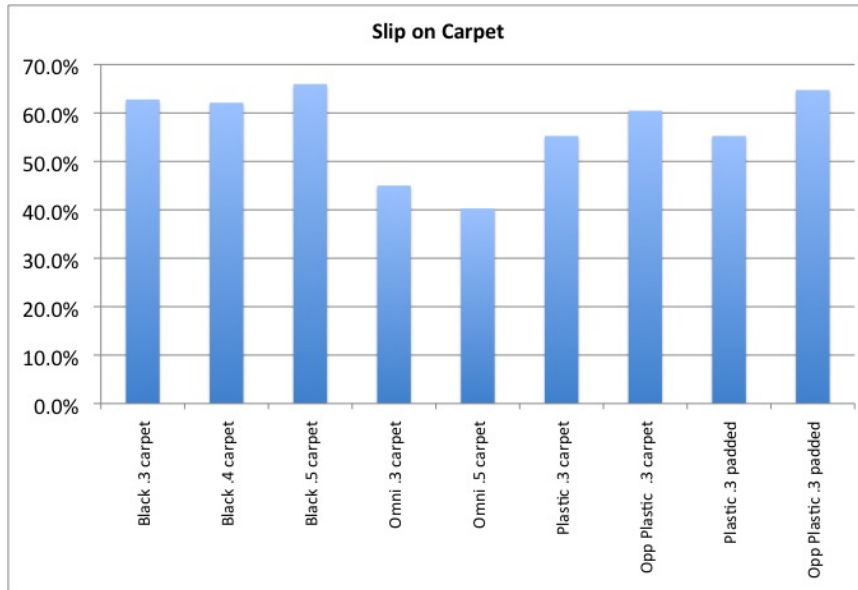


Figure 11.3: Percentage of Slip on Carpet

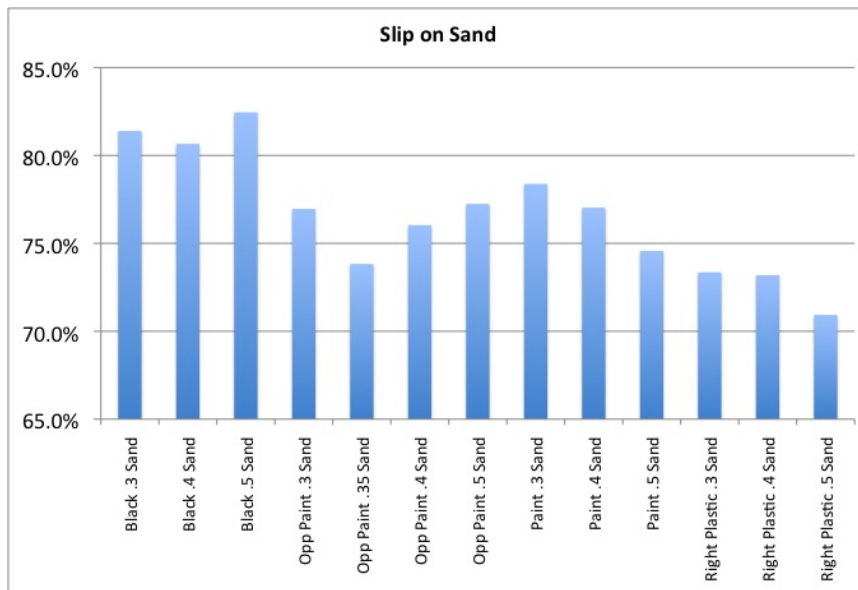


Figure 11.4: Percentage of Slip on Sand

11.5 Limits of SWEET

There are limitations to SWEET that do not prevent single wheel testing but do hamper it. First of all due to SWEET's geometry and design, its workspace is a small one meter diameter circle which is only 10% of its overall size. This limits its testing scenarios. Also, the omni wheel design is problematic in that it is very difficult to keep the table constrained and not slipping. This problem makes localization of the table unrealistic by dead reckoning. Another limitation is SWEET's dynamic response to any simulation of high frequency or acceleration in the Z direction. This limitation is due to the test foot's inertial mass being quite large. With SWEET it is also hard to get very accurate load readings due to the friction in the linear bearings.

11.6 Future Improvements of SWEET

It would be recommended that further iterations of SWEET incorporate embedded circuits to control its motion and measurements. An example chip would be the Parallax Propellor which has eight processors and video features. One chip would be adequate for measurement sensing and file recording and another for control for all the actuators (figure 11.5).

Several solutions might alleviate the limitations discussed above such as high friction paint for the underside of the table to gain better dead reckoning or laser tracking of the table for better localization, but a more broad recommendation would be to redesign SWEET as a rotatable foot on a gantry design. Such a design would solve both of the above mentioned limitations as well as provide a simpler means of testing since the table would not need changing to test on different soils and could incorporate simulated dunes or problem areas common to rover maneuvering. Also due to the dead reckoning accuracy of a non slip gantry, tests could be programmed as a set so that a wheel would undergo a battery of tests without the help of the operator. This aspect would further increase the efficiency and advantage of single wheel testing. Components from the current version could also be used to lower fabrication costs in the next iteration. The final upgrade suggested is to rebuild and upgrade the force torque sensor which exhibited some random voltage offsets. Also SWEET would benefit greatly from an automatic calibration procedure and mechanism using touch switches and springs with known force constraints. The table could push the wheel against the spring until the switch is triggered giving the ease and ability to calibrate before each testing event.

11.7 Limits of What can be Learned from Single Wheel Testing

There are limitations to what can be approximated and learned from single wheel testing. The most apparent is when the conceived soil is a non-homogenous mixture (figure 11.6) the single wheel approximation may have a more difficult time simulating the total rover's performance as different wheels contact different soils or obstacles.

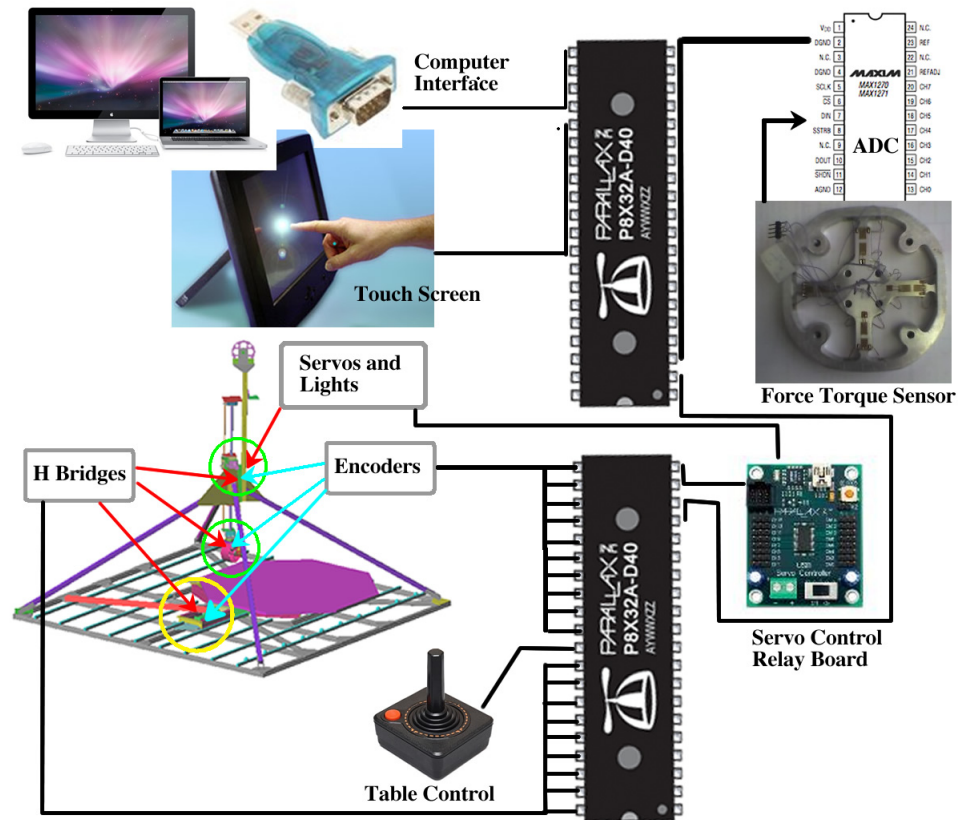


Figure 11.5: Proposed SWEET Electrical System



Figure 11.6: Example of SR2 in non-continuous Terrain

Single wheel testing could evaluate and be used to iterate how a single wheel could do on different soils but will lose some capability when considering holistic rover performance on non-homogenous soils. Another limitation would be simulating a rover in discontinuous terrain, since only one wheel can be tested in single wheel testing this could make the simulation not as accurate. The force assist mode on SWEET does mitigate this inaccuracy some by suppling the pushing force that would be from the other wheels but other solutions should be sought for better simulation in this situation.

11.8 Overview of wheel test results

It can be observed in the directional tread tests that tread and its orientation do affect the wheel's performance, especially on surfaces that are more compliant. Figure 11.7 shows the results of $\Omega = f(\omega)$ which can be used in controlling the rover if the soil is known, or if the turn rate Ω is known can be used for soil characterization.

Slip data for the wheels shows that there is considerable longitudinal slip. Which makes a no slip assumption [44] an inaccurate one.

11.9 Future work

Future work would include these open research questions that SWEET could answer.

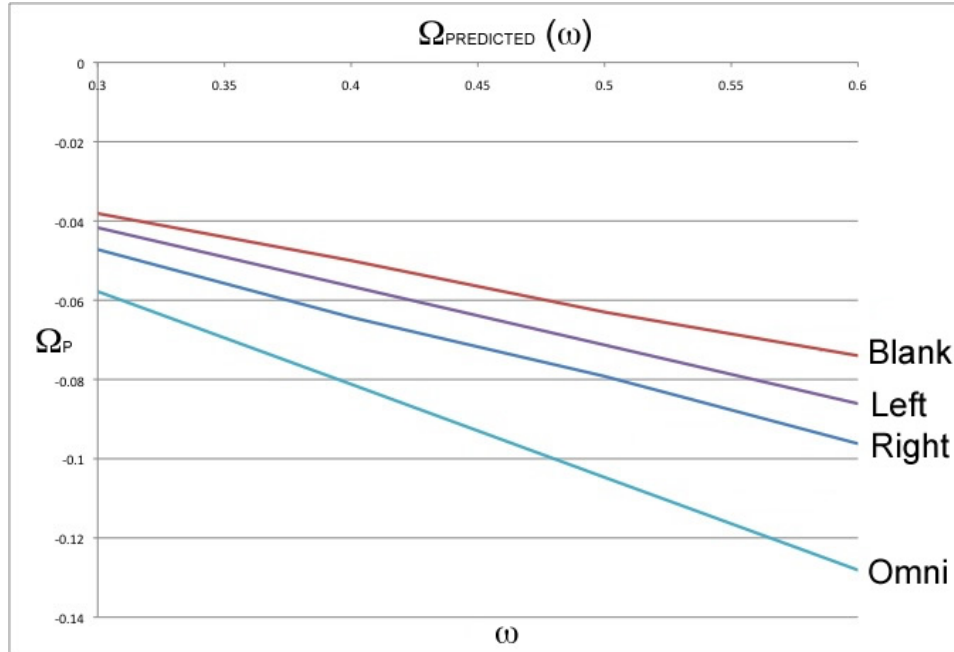


Figure 11.7: Ω vs ω

- Creating soil catalog with parameters to be compared in-situ for soil characterization. Parameters would be constructed from single wheel testing and in the form of $\Omega = f(\omega)$ and $Power = f(\omega)$ for specific rovers and wheels. Also $\Omega(\omega)$ would be of use in control when the soil is known. Tests and catalog wheel-to-soil performance is made much more possible by single wheel testing.
- Research into single directional force component alteration. From the equilibrium point graph it can be seen that augmenting F_Y while diminishing F_X a skid steer turn's efficiency can be increased. If avenues can be studied that will allow selective frictional force alteration such as directional soil agitation, skid steering rocking [51], or efficient grouser design skid steering will be a more efficient turning method.
- Wheel width experiments. At some point, if a wheel's width is increased, the single point contact assumption will not be an adequate approximation. It would be interesting to know how a wheel's F_y and F_x behavior, in a skid steer turn, depends on its width and analytically how the constraint equation $F_y = F_x \cdot \tan(\Theta)$ would change. Finally would there be a sweet spot in wheel width in turning on a certain soil? This topic would be a useful subject for single wheel testing.
- Wheel diameter experiments. It would be interesting to know how a wheel's diameter affects its turning ability and efficiency.
- Skid Steer turn testing that has a turn radius larger than 0. It would be interesting to examine the effect that tread have upon different turning radiuses

and make recommendations for best use of each tread.

- Clay and diatomaceous earth soil tests. To get a better idea of stacking/caking and how to remedy that problem different soils will need to be experimented with. These tests could explore possible new techniques such as high frequency vibration for a possible low cost remedy.
- Artificial Intelligence tread and grouser pattern generation. Using Neural Networks and Genetic Algorithms it would be interesting to set up a computer simulation of wheels, through a NN, and a generation ,through a GA.

Chapter 2, in this dissertation, discussed the past 50 years of space rover use focusing on the testing and use of rover wheels. The Apollo program, for instance, enjoyed a large iterative rover wheel testing program, but over the years this testing priority has diminished to the detriment of wheel to soil understanding and rover performance. Chapter 3 laid out the design and use of a testing apparatus known as SWEET (Suspension and Wheel evaluation and experimentation testbed) that has the capability to test rover wheels in a number of scenarios not previously achieved at a fraction of the cost and time. Chapter 4 explained algorithm to map between the measured forces in a SWEET single wheel test to predict the performance of a full rover assembly. This algorithm is a way that SWEET can be used in lieu of expensive full rover testing. Chapter 5 explored the uncertainties involved in the skid steering tests as well as the propagation of those errors. Chapter 6, 7, and 8 use the skid steering algorithm discussed in chapter 4 to predict the results of skid steering turning rate of a blank, treaded, and Omni wheels on carpet and sand for a full rover. Results are validated using the SR2 skid steer rover. In chapter 9 two wheels were compared using SWEET both with pulling efficiency, sinkage, and traction. Chapter 10 looked at power usage for different wheels and maps a linear relationship between SWEET's power measurements and that of a full rover assembly.

From this dissertation it can be seen that more testing is needed in rover wheel design, full rover testing is expensive and sometimes impractical, single wheel testing is a cheap timely way to test wheels, and single wheel tests can evaluate wheels in many ways without the need for a full rover.

Bibliography

- [1] 2008 regolith excavation challenge. <http://regolith.csewi.org/about>.
- [2] Daniel warner technician, wood research laboratory. http://web.ics.purdue.edu/~warnerd/index_files/Page1421.htm.
- [3] Lunokhod test movie clip. <http://videos.howstuffworks.com/science-channel/4963-tank-on-the-moon-improving-the-lunokhod-video.htm>.
- [4] Mars exploration rover mission. http://marsrover.nasa.gov/mission/status_spiritAll.html#sol2015.
- [5] Mars exploration rover mission. <http://marsrovers.nasa.gov/gallery/video/hardware.html>.
- [6] Nasa apollo 17 lunar roving vehicle. `{\url{http://commons.wikimedia.org/wiki/Image:NASA_Apollo_17_Lunar_Roving_Vehicle.jpg}}`.
- [7] Nasa lewis research center's contribution to the mars pathfinder mission. <http://marsprogram.jpl.nasa.gov/MPF/mpf/lewis.html>.
- [8] Nasa's 2009 mars science laboratory. file:///localhost/Users/danielflippo/research/Dissertation/Literature_review/Resources/MSL/MSL_overview_LS.pdf.
- [9] Opportunity leaving martian sand trap. <http://marsrovers.jpl.nasa.gov/gallery/video/opportunity01.html#FlyingOverOpportunityWorkSite>.
- [10] Scion image software. <http://www.scioncorp.com/index.htm>.
- [11] Micropower instrumentation amplifier. Data sheet for ina126 amp, TEXAS INSTRUMENTS, 2005.
- [12] Wheels in the sky. <http://mars.jpl.nasa.gov/mer/spotlight/wheels01.html>, October 2005.
- [13] Lunar rover. http://en.wikipedia.org/wiki/Lunar_rover, May 2007.
- [14] Lunokhod. <http://www.astronautix.com/craft/lunokhod.htm>, 2007.
- [15] Lunokhod. <http://www.astronautix.com/craft/lunokhod.htm>, 2007.
- [16] J Appleton. Lunokhod 2 on the moon. <http://www.ast.cam.ac.uk/ipswich/Miscellaneous/Lunokhod.htm>, 1973.

- [17] R. Bauer, W. Leung, and T. Barfoot. Experimental and simulation results of wheel-soil interaction for planetary rovers. *2005 IEEE/RSJ International Conference on Intelligent Robots and Systems*, pages 586 – 91, 2005.
- [18] The Boeing Company, LRV Systems Engineering Huntsville Alabama. *Lunar Roving Vehicle Operations Handbook Contract NASB-25145*, April 19 1971.
- [19] C.A. Brooks, K.D. Iagnemma, and S. Dubowsky. Visual wheel sinkage measurement for planetary rover mobility characterization. *Auton. Robots (Netherlands)*, 21(1):55 – 64, 2006/08.
- [20] L. Caracciolo, A. de Luca, and S. Iannitti. Trajectory tracking control of a four-wheel differentially driven mobile robot. In *Robotics and Automation, 1999. Proceedings. 1999 IEEE International Conference on*, volume 4, pages 2632–2638 vol.4, 1999.
- [21] STEPHEN CLARK. Amid struggles, mars science lab still targets '09 launch. *Space Flight now*, Posted: October 10, 2008.
- [22] JR Clyde S. Jones and Frank J. Nola. Mobility systems activity for lunar rovers at msfc. Technical Memorandum NASA TM X-64623, NASA, MARSHALL SPACE FLIGHT CENTER, ALABAMA, September 1971.
- [23] R.E. Colyer and J.T. Economou. Comparison of steering geometries for multi-wheeled vehicles by modelling and simulation. *Decision and Control, 1998. Proceedings of the 37th IEEE Conference on*, 3:3131–3133 vol.3, 1998.
- [24] Leonard David. Opportunity mars rover stuck in sand. *space.com*, 2005.
- [25] J.T. Economou and R.E. Colyer. Modelling of skid steering and fuzzy logic vehicle ground interaction. *American Control Conference, 2000. Proceedings of the 2000*, 1(6):100–104 vol.1, Sep 2000.
- [26] Kenneth S. Edgett and Philip R. Christensen. The particle size of martian aeolian dunes. *Journal of Geophysical Research*, 96(E5):22765–22776, December 1991.
- [27] Jefferey Farnam. Four-wheel drive wheel-chair with compound wheels,". Technical Report 4,823,900, United States Patent Office, 1989.
- [28] Dan Flippo, David P. Miller, and Richard Heller. Turning efficiency prediction for skid steer robots using single wheel testing. turning efficiency prediction for skid steer robots using single wheel testing. turning efficiency prediction for skid steer robots using single wheel testing. turning efficiency prediction for skid steer robots using single wheel testing. In *FSR*, 2009.
- [29] Daniel Flippo. Design of rover wheel testing apparatus. In *ISAIRAS*, 2008.

- [30] Y. Fuke and E. Krotkov. Dead reckoning for a lunar rover on uneven terrain. In *Robotics and Automation, 1996. Proceedings., 1996 IEEE International Conference on*, volume 1, pages 411–416 vol.1, Apr 1996.
- [31] Natalie Godwin and Dolores Beasley. Nasa’s opportunity rover rolls free on mars. *News Release*, 2006.
- [32] Richard L. Hannah and Stuart E. Reed. *Strain Gage Users Handbook*. Springer, 1992.
- [33] Junichi Hayashi. Device for measuring components of force and moment in plural directions. Patent 4448083, United States Patent Office, May 15 1984.
- [34] K. Iagnemma, Shinwoo Kang, H. Shibly, and S. Dubowsky. Online terrain parameter estimation for wheeled mobile robots with application to planetary rovers. *IEEE Trans. Robot. (USA)*, 20(5):921 – 7, 2004.
- [35] K. Iagnemma, H. Shibly, and S. Dubowsky. On-line terrain parameter estimation for planetary rovers. *Proceedings 2002 IEEE International Conference on Robotics and Automation (Cat. No.02CH37292)*, 3:3142 – 7, 2002.
- [36] Karl Iagnemma, Hassan Shibly, and Steven Dubowsky. A laboratory single wheel testbed for studying planetary rover wheel-terrain interaction. Technical report, MIT Field and Space Robotics Laboratory, 77 Massachusetts Avenue, Room 3-435a, January 2005.
- [37] K.D. Iagnemma and S. Dubowsky. Terrain estimation for high-speed rough-terrain autonomous vehicle navigation. *Proc. SPIE - Int. Soc. Opt. Eng. (USA)*, 4715:256 – 66, 2002.
- [38] K. Iizuka, Y. Sato, Y. Kuroda, and T. Kubota. Experimental study of wheeled forms for lunar rover on slope terrain. *9th IEEE International Workshop on Advanced Motion Control*, pages 266 – 71, 2006.
- [39] Old World Industries Inc. Herculiner truck bed liners. <http://www.herculiner.com/>.
- [40] G. Ishigami, A. Miwa, K. Nagatani, and K. Yoshida. Terramechanics-based model for steering maneuver of planetary exploration rovers on loose soil. *J. Field Robot. (USA)*, 24(3):233 – 50, 2007/03/.
- [41] G. Ishigami and K. Yoshida. Steering characteristics of an exploration rover on loose soil based on all-wheel dynamics model. *2005 IEEE/RSJ International Conference on Intelligent Robots and Systems*, pages 3099 – 104, 2005.
- [42] Genya Ishigami, Akiko Miwa, and Kazuya Yoshida. Steering trajectory analysis of planetary exploration rovers based on all-wheel dynamics model. *European Space Agency, (Special Publication) ESA SP*, (603):121 – 128, 2005.

- [43] KORNYLAK, 400 HEATION ST HAMILTON, OHIO 45011. *OMNIWHEEL, Heavy Duty and Lightweight Multi-directional Wheels For Conveyors, Manual and Powered Transfer Systems, and non-Powered and Powered Robot Wheels.*
- [44] K. Kozłowski and D. Pazderski. Modeling and control of a 4-wheel skid-steering mobile robot. *Int. J. Appl. Math. Comput. Sci. (Poland)*, 14(4):477 – 96, 2004//. skid-steering vehicles;time-varying control laws;Lyapunov analysis;4-wheel skid-steering mobile robot;mathematical model;kinematic controller;kinematic control law;backstepping technique;.
- [45] Andrew J. LePage. Ahead of their time: The soviet lunar program of the seventies ahead of their time: The soviet lunar program of the seventies part i. *THE ELECTRONIC JOURNAL OF THE ASTRONOMICAL SOCIETY OF THE ATLANTIC*, 7(1), January 1996.
- [46] Randel Lindemann. Platform for testing robotic vehicles on simulated terrain. Technical report, NASA, June 01 2006.
- [47] Anthony Mandow, Jorge L. Martínez, Jesús Morales, Jose-Luis Blanco, Alfonso García-Cerezo, and Javier Gonzalez. Experimental kinematics for wheeled skid-steer mobile robots. In *IROS*, pages 1222–1227. IEEE, 2007.
- [48] Maggie McKee. One mars rover gets stuck in, the other chills out. *NewScientistSpace*, 2006.
- [49] K.J. Melzer. Performance of the boeing lrv wheels in a lunar soil simulant. Technical Report 2, Mobility and Environmental Division U.S. Army Engineer Waterways Experiment Station, December 1971.
- [50] K.J. Melzer and A.J. Green. Performance of the boeing lrv wheels in a lunar soil simulant. Technical Report 1, Mobility and Environmental Division U.S. Army Engineer Waterways Experiment Station, December 1971.
- [51] S. Miller, D.P.; Li Tan; Swindell. Simplified navigation and traverse planning for a long-range planetary rover. *Robotics and Automation, 2003. Proceedings. ICRA '03. IEEE International Conference on*, 2:2436–2441 vol.2, 14-19 Sept. 2003.
- [52] Brandon Mills. Design and analysis of compliant wheels for a planetary rover design and analysis of compliant wheels for a planetary rover design and analysis of compliant wheels for a planetary rover. Master’s thesis, University of Oklahoma, 2007.
- [53] C. Howell Mullis. A study and analysis of the msfc lunar roving vehicle dust profile test program. Technical report, UNIVERSITY OF ALABAMA, 1971.
- [54] NASA. A description of the rover sojourner. <http://mpfwww.jpl.nasa.gov/rover/descrip.html>, 1996.

- [55] NASA. Free spirit: Rescuing a rover part 1 of 2. <http://www.ustream.tv/recorded/1858490>, July 2009.
- [56] Lauro Ojeda, Johann Borenstein, and Gary Witus. Terrain trafficability characterization with a mobile robot. *Proceedings of SPIE - The International Society for Optical Engineering*, 5804:235 – 243, 2005.
- [57] Howard A. Perko, John D. Nelson, and Jacklyn R. Green. Mars soil mechanical properties and suitability of mars soil simulants. *Journal of Aerospace Engineering*, 19(3):169–176, 2006.
- [58] M.C. Powers. A new roundness scale for sedimentary particles. *Journal of Sedimentary Petrology.*, 23(2):117–119, 1953.
- [59] Proceedings of the Institution of Mechanical Engineers, Part D: Journal of Automobile Engineering. *A general theory for skid steering of tracked vehicles on firm ground*, volume 215. Professional Engineering Publishing, 2001.
- [60] M. A. Ravine, J. F. Bell III, M. C. Malin, and D. P. Miller. Semi-autonomous rover operations: A mars technology program semi-autonomous rover operations: A mars technology program demonstration. *Lunar and Planetary Science XXXVI*, 2005.
- [61] Matt Roman, D.P. Miller, and Zack White. Roving faster farther cheaper. In *Proceedings for FSR*, Chamonix, France, July 2007. Field Service Robotics.
- [62] Matthew J. Roman. Design and analysis of a four wheeled planetary rover. Master’s thesis, University of Oklahoma, August 2005.
- [63] Dr R.S. Rowe and Ervin Hegedus. Drag coefficients of locomotion over viscous soils part ii. Technical Report 54, Dept of Army Ordinance tank-automotive command research division land locomotion laboratory, 1959.
- [64] Roland Siegwart and I. Nourbakhsh. *Introduction to Autonomous Mobile Robots*. MIT Press, 2004.
- [65] S.Michaud, L.Richter, T.Thueer, A.Gibbesch, T.Huelsing, N. Schmitz, S. Weiss, A.Krebs, N.Patel, L.Joudrier, R.Siegwart, B.Schäfer, and A.Ellery. Rover chassis evaluation and design optimisation using the rcet, 2006.
- [66] Standard Testing Laboratories, 1845 Harsh Ave. S.E. P.O. Box 758, Massillon, Ohio 44648-0758 USA. *Radial Fatigue Two-Position Tire and Wheel Test Machine*.
- [67] M. Wada. A 4wd omnidirectional wheelchair with a chair tilting mechanism for enhancing step climbing capability. pages 474–479, March 2008.
- [68] David Wettergreen, Dominic Jonak, David Kohanbash, Scott Moreland, Spencer Spiker, and James Teza. Field experiments in mobility and navigation with a lunar rover prototype. In *FSR*, 2009.

- [69] J.Y. Wong. *Theory of ground vehicles*. John Wiley and sons inc., 2008.
- [70] K. Yoshida and G. Ishigami. Steering characteristics of a rigid wheel for exploration on loose soil. *Intelligent Robots and Systems, 2004. (IROS 2004). Proceedings. 2004 IEEE/RSJ International Conference on*, 4:3995–4000 vol.4, 28 Sept.-2 Oct. 2004.
- [71] Anthony H Young. *From concept to reality*. Springer New York, 2007.
- [72] A. Zobova and Ya Tatarinov. Free and controlled motions of an omniwheel vehicle. *Moscow University Mechanics Bulletin*, 63(6):146–150, December 2008.

APPENDIX A

Appendices

Appendix A: Specs

A.0.1 NI boxes specs

NI DAQPad™ -6020E Family Specifications

This document lists the I/O terminal summary and specifications for the NI DAQPad-6020E family of devices. This family includes the following devices:

- NI DAQPad-6020E (Half-Size Box)
- NI DAQPad-6020E (Full-Size Box)
- NI DAQPad-6020E BNC

I/O Terminal Summary



Note With NI-DAQmx, National Instruments revised its terminal names so they are easier to understand and more consistent among NI hardware and software products. The revised terminal names used in this document are usually similar to the names they replace. For a complete list of Traditional NI-DAQ (Legacy) terminal names and their NI-DAQmx equivalents, refer to *Terminal Name Equivalents* of the *E Series Help*.

Table 1. I/O Terminals

Terminal Name	Terminal Type and Direction	Impedance Input/ Output	Protection (V) On/Off	Source (mA at V)	Sink (mA at V)	Rise Time (ns)	Bias
AI <0..15>	AI	100 GΩ in parallel with 50 pF	35/25	—	—	—	±200 pA
AI SENSE	AI	100 GΩ in parallel with 50 pF	35/25	—	—	—	±200 pA
AI GND	—	—	—	—	—	—	—
AO 0	AO	0.1 Ω	Short-circuit to ground	5 at 10	5 at -10	15 V/μs	—
AO 1	AO	0.1 Ω	Short-circuit to ground	5 at 10	5 at -10	15 V/μs	—
AO EXT REF	AI	10 kΩ	35/25	—	—	—	—
AO GND	—	—	—	—	—	—	—
D GND	—	—	—	—	—	—	—



Figure A.1: National Instruments 6020E DAQ

Table 1. I/O Terminals (Continued)

Terminal Name	Terminal Type and Direction	Impedance Input/ Output	Protection (V) On/Off	Source (mA at V)	Sink (mA at V)	Rise Time (ns)	Bias
FREQ OUT	DO	—	—	3.5 at (V _{CC} - 0.4)	5 at 0.4	1.5	50 kΩ pu

* Indicates active low.
[†] P0.<6..7> are also pulled down with a 50 kΩ resistor.
 AI = Analog Input DIO = Digital Input/Output pu = pull-up
 AO = Analog Output DO = Digital Output
 Note: The tolerance on the 50 kΩ pull-up resistors is large. Actual value might range between 17 kΩ and 100 kΩ.

Specifications

The following specifications are typical at 25 °C unless otherwise noted.

Analog Input

Input Characteristics

Number of channels	16 single-ended or 8 differential (software-selectable)	Input coupling	DC
Type of A/D converter (ADC)	Successive approximation	Max working voltage (signal + common mode)	Each input should remain within ±11 V of ground
Resolution	12 bits, 1 in 4,096	Overvoltage protection	
Max sampling rate	100 kS/s guaranteed	Powered on	±35 V
Input signal ranges		Powered off	±25 V
		Inputs protected	AI <0..15>, AI SENSE

Range (Software-Selectable)	Input Range	
	Bipolar	Unipolar
20 V	±10 V	—
10 V	±5 V	0 to 10 V
5 V	±2.5 V	0 to 5 V
2 V	±1 V	0 to 2 V
1 V	±500 mV	0 to 1 V
500 mV	±250 mV	0 to 500 mV
200 mV	±100 mV	0 to 200 mV
100 mV	±50 mV	0 to 100 mV

FIFO buffer size	4,096 samples (S)
Data transfers	Interrupts, programmed I/O
Configuration memory size	512 words (1 word = 8 bits)

Figure A.2: National Instruments 6020E DAQ

NI 660x Specifications

This document lists the specifications for the NI 660x family of devices. Specifications listed below are typical at 25 °C unless otherwise noted. Refer to the *NI 660x User Manual* for more information about NI 660x devices.

The NI 660x family includes the following devices:

- NI PCI-6601
- NI PCI-6602
- NI PXI-6602
- NI PXI-6608

Power

Power requirement	5 VDC (±5%)
NI 6601	0.4 A to 0.75 A
NI 6602	0.5 A to 1.5 A
NI 6608	1 A to 2.5 A (with 1 m shielded cable as load) varies with application and OCXO warm-up period, does not include I/O power supplied through I/O connector

Available at I/O connector 4.65 to 5.25 VDC, 1 A (maximum)

I/O Characteristics

Compatibility	TTL/CMOS
Power-on state	Input (high-Z) with weak pull-downs
Pull-down current	10 µA min to 200 µA max
Input impedance	25 kΩ to 500 kΩ
Output impedance	75 kΩ (56 kΩ from an onboard resistor and 19 Ω from the TIO ASIC)
Hysteresis	300 mV Schmitt triggers

Digital logic levels on P0.<0..7>

Level	Min	Max
Input low voltage	-0.3 V	0.8 V
Input high voltage	2.0 V	Supply +0.3 V
Input low current (V _{in} = 0 V)	—	-10 µA
Input high current (V _{in} = 5 V) -0.3 V	—	200 µA
Output low voltage (I _{OL} = 24 mA)	—	0.4 V
Output high voltage (I _{OH} = -13 mA)	2.4 V	—

Digital I/O

Number of channels	32
Data transfer	Static
Handshaking	None

Timing I/O

Number of channels	
NI 6601	4 up/down counter/timers
NI 6602	8 up/down counter/timers
NI 6608	8 up/down counter/timers
Resolution	32 bits
Maximum count	4,294,967,295



Figure A.3: National Instruments 6602 DAQ

Rollover times	NI 6608											
100 kHz timebase.....11.93 h	Without prescaling..... 80 MHz											
20 MHz timebase.....214.74 s	With prescaling..... 125 MHz											
80 MHz timebase.....53.69 s												
Prescalers.....X8 or X2 prescaler for each counter	Minimum edge separation (for two edge separation measurement).....s2/maximum timebase											
Baseclocks available	Data transfers											
NI 6601.....100 kHz and 20 MHz	NI 6601.....DMA (1 channel), interrupts											
NI 6602.....100 kHz, 20 MHz, and 80 MHz	NI 6602.....DMA (up to 3 channels), interrupts											
NI 6608.....100 kHz, 20 MHz, and 80 MHz	NI 6608.....DMA (up to 3 channels), interrupts											
Baseclock accuracy	DMA modes..... Scatter-gather											
<table border="1"> <thead> <tr> <th>Device</th> <th>Baseclock Accuracy</th> </tr> </thead> <tbody> <tr> <td>PCI-6601</td> <td>100 ppm ($\pm 0.01\%$) over temperature</td> </tr> <tr> <td>PCI-6602</td> <td>100 ppm ($\pm 0.01\%$) over temperature</td> </tr> </tbody> </table>	Device	Baseclock Accuracy	PCI-6601	100 ppm ($\pm 0.01\%$) over temperature	PCI-6602	100 ppm ($\pm 0.01\%$) over temperature	OCXO (NI 6608 Only) Frequency..... 10.000000 MHz Warm-up time..... 5 minutes (to within 20 ppb of operating frequency, power-off duration < 1 hour) Frequency stability versus supply voltage change ($\pm 5\%$) ± 5 ppb Temperature stability (0 to 50 °C) ± 5 ppb, reference to 25 °C Drift in frequency..... ± 0.45 ppb/day; ± 45 ppb/year Allowed frequency adjustment (to correct for drift in frequency)..... ± 500 ppb, typical					
Device	Baseclock Accuracy											
PCI-6601	100 ppm ($\pm 0.01\%$) over temperature											
PCI-6602	100 ppm ($\pm 0.01\%$) over temperature											
<table border="1"> <thead> <tr> <th rowspan="2">Device</th> <th colspan="2">Baseclock Accuracy</th> </tr> <tr> <th>PXI Chassis</th> <th>cPCI Chassis</th> </tr> </thead> <tbody> <tr> <td>PXI-6602</td> <td>Takes on Baseclock Accuracy of PXI CLK 10 signal</td> <td>200 ppm ($\pm 0.02\%$) over temperature</td> </tr> <tr> <td>PXI-6608</td> <td>Takes on Baseclock Accuracy of PXI CLK 10 signal¹</td> <td>200 ppm ($\pm 0.02\%$) over temperature</td> </tr> </tbody> </table>	Device	Baseclock Accuracy		PXI Chassis	cPCI Chassis	PXI-6602	Takes on Baseclock Accuracy of PXI CLK 10 signal	200 ppm ($\pm 0.02\%$) over temperature	PXI-6608	Takes on Baseclock Accuracy of PXI CLK 10 signal ¹	200 ppm ($\pm 0.02\%$) over temperature	RTSI Trigger Lines (PCI Only) Trigger lines <0..6> 7 RTSI clock 1 Minimum pulse width for Z index on position measurement NI 6601..... 200 ns NI 6602..... 50 ns
Device		Baseclock Accuracy										
	PXI Chassis	cPCI Chassis										
PXI-6602	Takes on Baseclock Accuracy of PXI CLK 10 signal	200 ppm ($\pm 0.02\%$) over temperature										
PXI-6608	Takes on Baseclock Accuracy of PXI CLK 10 signal ¹	200 ppm ($\pm 0.02\%$) over temperature										
Maximum source frequency	PXI Trigger Bus (PXI Only) Trigger lines <0..5> 6 Star trigger 1 Clock 1											
NI 6601	Bus Interface All devices Master, slave											
Without prescaling20 MHz												
With prescaling.....60 MHz												
NI 6602												
Without prescaling80 MHz												
With prescaling.....125 MHz												

Figure A.4: National Instruments 6602 DAQ

A.0.2 DC Motor specs



Customer: Groschopp.com
 Application:
 Prepared by:

Quote No: ---
 Date: **07/09/08**

Motor: **PM 8014**
 Voltage: **24 v DC**
 Speed: **2500 rpm 2 Poles**
 Gearbox: **PS 1900 20:1 Ratio**

Catalog Part No: **55018**

SPECIFICATIONS

Rating:
 Speed: 123.7 rpm
 Torque: 73.2lb-in
 Current: 7.1 amps
 Output: 107 watts
 Output: 0.1437 HP

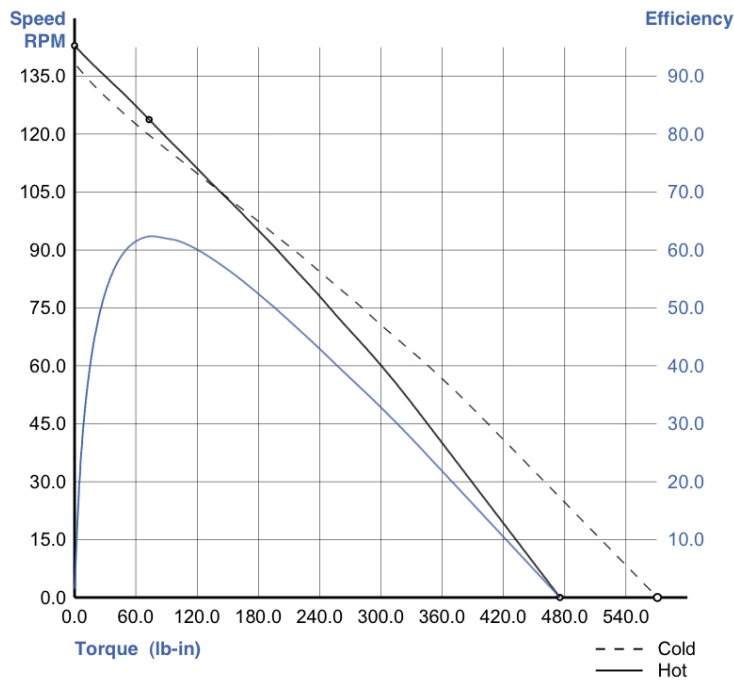
Duty Cycle:
 On: Continuous
 Off:

Efficiency:
 Gearbox: 85.1 %
 Motor: 73.3 %
 System: 62.3 %

Start/Stall Conditions:
 Current: 44.41 amps
 Torque: 570.89 lb-in

Constants:
 Ke: 8.20 v/krpm
 Kt: 0.69 lb-in/amp

Speed, Efficiency Vs. Torque



Notes:

There are not implied warranties that the goods shall be merchantable or that they are fit for a particular purpose.

© 2008 Groschopp, Inc.



Groschopp, Inc., 420 15th Street NE, Sioux Center, IA 51250-2100 USA
 (712) 722-4135 Phone · (800) 829-4135 Toll Free · (712) 722-1445 FAX

www.groschopp.com

Figure A.5: Groschopp 55018 DC Motor

Panel Mount Optical Encoders

Technical Data

HEDS-5700 Series

Features

- Two Channel Quadrature Output with Optional Index Pulse
- Available with or without Static Drag for Manual or Mechanized Operation
- High Resolution – Up to 512 CPR
- Long Rotational Life, > 1 Million Revolutions
- -20 to 85°C Operating Temperature Range
- TTL Quadrature Output
- Single 5 V Supply
- Available with Color Coded Leads

Description

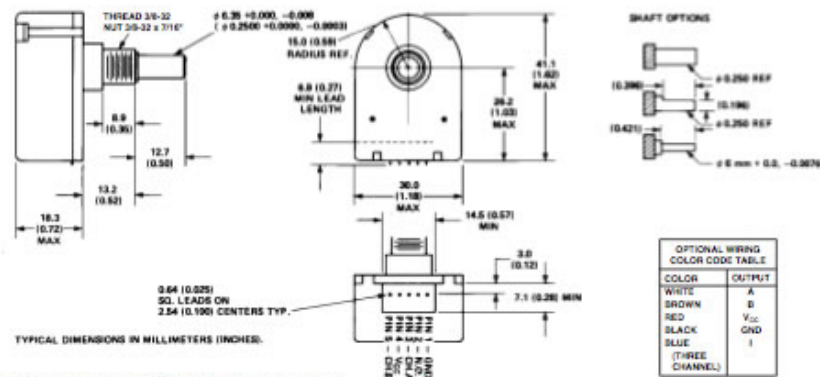
The HEDS-5700 series is a family of low cost, high performance, optical incremental encoders with mounted shafts and bushings. The HEDS-5700 is available with tactile feedback for hand operated panel mount applications, or with a free spinning shaft for applications requiring a pre-assembled encoder for position sensing.

The encoder contains a collimated LED light source and special detector circuit which allows for high resolution, excellent encoding performance, long rotational



life, and increased reliability. The unit outputs two digital waveforms which are 90 degrees out of phase to provide position and direction information. The HEDS-5740 Series provides a third Index Channel.

Package Dimensions



*Note: For the HEDS-5700, Pin #2 is a No Connect. For the HEDS-5740, Pin #2 is Channel I, the index output.

Figure A.6: HEDS Optical Encoder

A.0.4 HIP4081A H Bridge Driver



HIP4081A

Data Sheet

July 2004

FN3659.7

80V/2.5A Peak, High Frequency Full Bridge FET Driver

The HIP4081A is a high frequency, medium voltage Full Bridge N-Channel FET driver IC, available in 20 lead plastic SOIC and DIP packages. The HIP4081A can drive every possible switch combination except those which would cause a shoot-through condition. The HIP4081A can switch at frequencies up to 1MHz and is well suited to driving Voice Coil Motors, high-frequency switching power amplifiers, and power supplies.

For example, the HIP4081A can drive medium voltage brush motors, and two HIP4081As can be used to drive high performance stepper motors, since the short minimum "on-time" can provide fine micro-stepping capability.

Short propagation delays of approximately 55ns maximizes control loop crossover frequencies and dead-times which can be adjusted to near zero to minimize distortion, resulting in rapid, precise control of the driven load.

A similar part, the HIP4080A, includes an on-chip input comparator to create a PWM signal from an external triangle wave and to facilitate "hysteresis mode" switching.

The Application Note for the HIP4081A is the AN9405.

Ordering Information

PART NUMBER	TEMP RANGE (°C)	PACKAGE	PKG. DWG. #
HIP4081AIP	-40 to 85	20 Ld PDIP	E20.3
HIP4081AIPZ (Note)	-40 to 85	20 Ld PDIP (Pb-free)	E20.3
HIP4081AIB	-40 to 85	20 Ld SOIC (W)	M20.3
HIP4081AIBZ (Note)	-40 to 85	20 Ld SOIC (W) (Pb-free)	M20.3

NOTE: Intersil Pb-free products employ special Pb-free material sets; molding compounds/die attach materials and 100% matte tin plate termination finish, which is compatible with both SnPb and Pb-free soldering operations. Intersil Pb-free products are MSL classified at Pb-free peak reflow temperatures that meet or exceed the Pb-free requirements of IPC/JEDEC J Std-0208.

Features

- Independently Drives 4 N-Channel FET in Half Bridge or Full Bridge Configurations
- Bootstrap Supply Max Voltage to 95V_{DC}
- Drives 1000pF Load at 1MHz in Free Air at 50°C with Rise and Fall Times of Typically 10ns
- User-Programmable Dead Time
- On-Chip Charge-Pump and Bootstrap Upper Bias Supplies
- DIS (Disable) Overrides Input Control
- Input Logic Thresholds Compatible with 5V to 15V Logic Levels
- Very Low Power Consumption
- Undervoltage Protection
- Pb-free Available

Applications

- Medium/Large Voice Coil Motors
- Full Bridge Power Supplies
- Switching Power Amplifiers
- High Performance Motor Controls
- Noise Cancellation Systems
- Battery Powered Vehicles
- Peripherals
- U.P.S.

Pinout

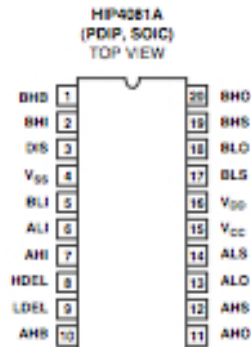


Figure A.7: HIP4080

Appendix B: Schematics

A.0.5 Main SWEET Schematic

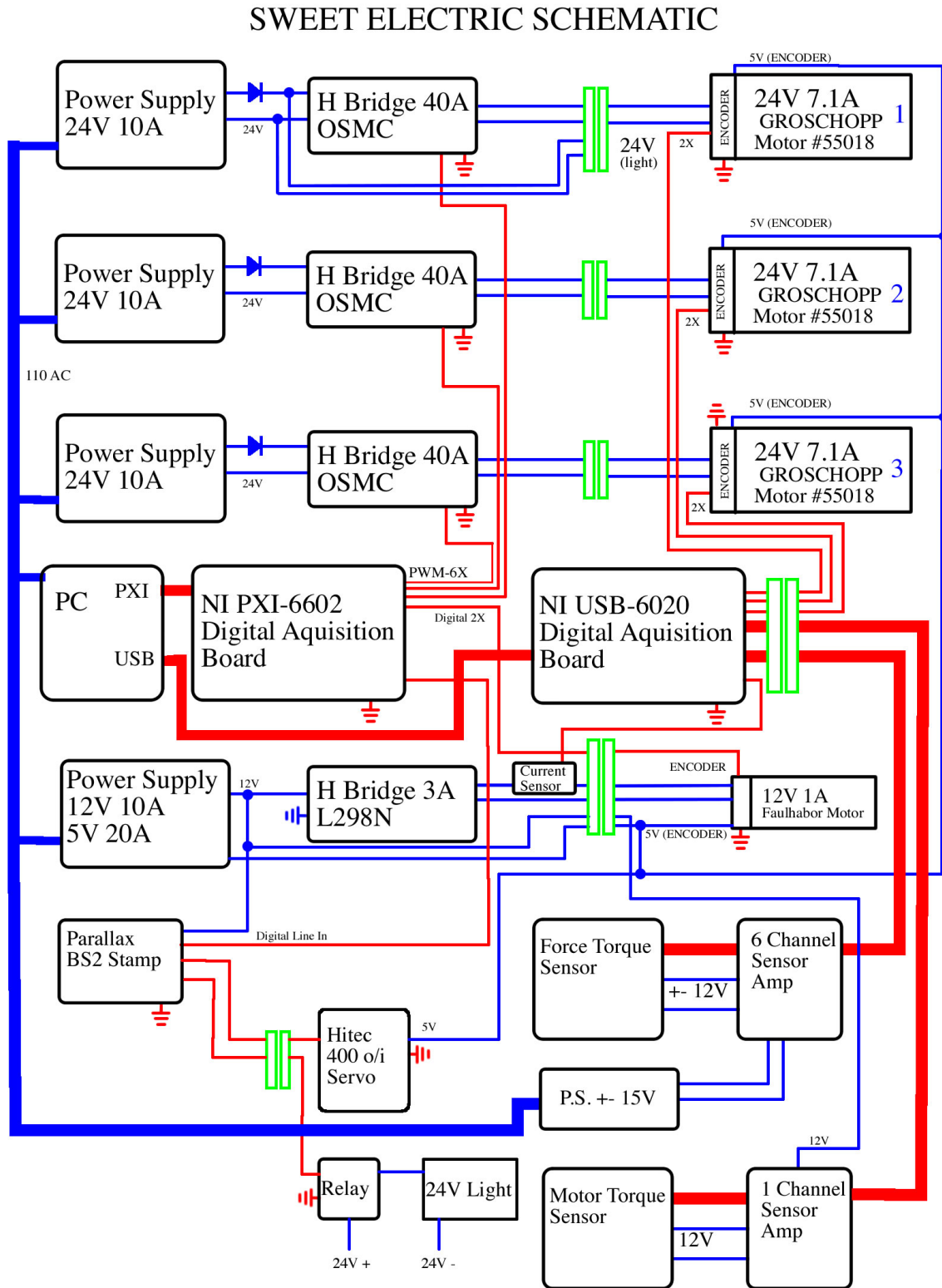


Figure A.8: Main SWEET Schematic

A.0.7 INA126 Instrumental Amplifier

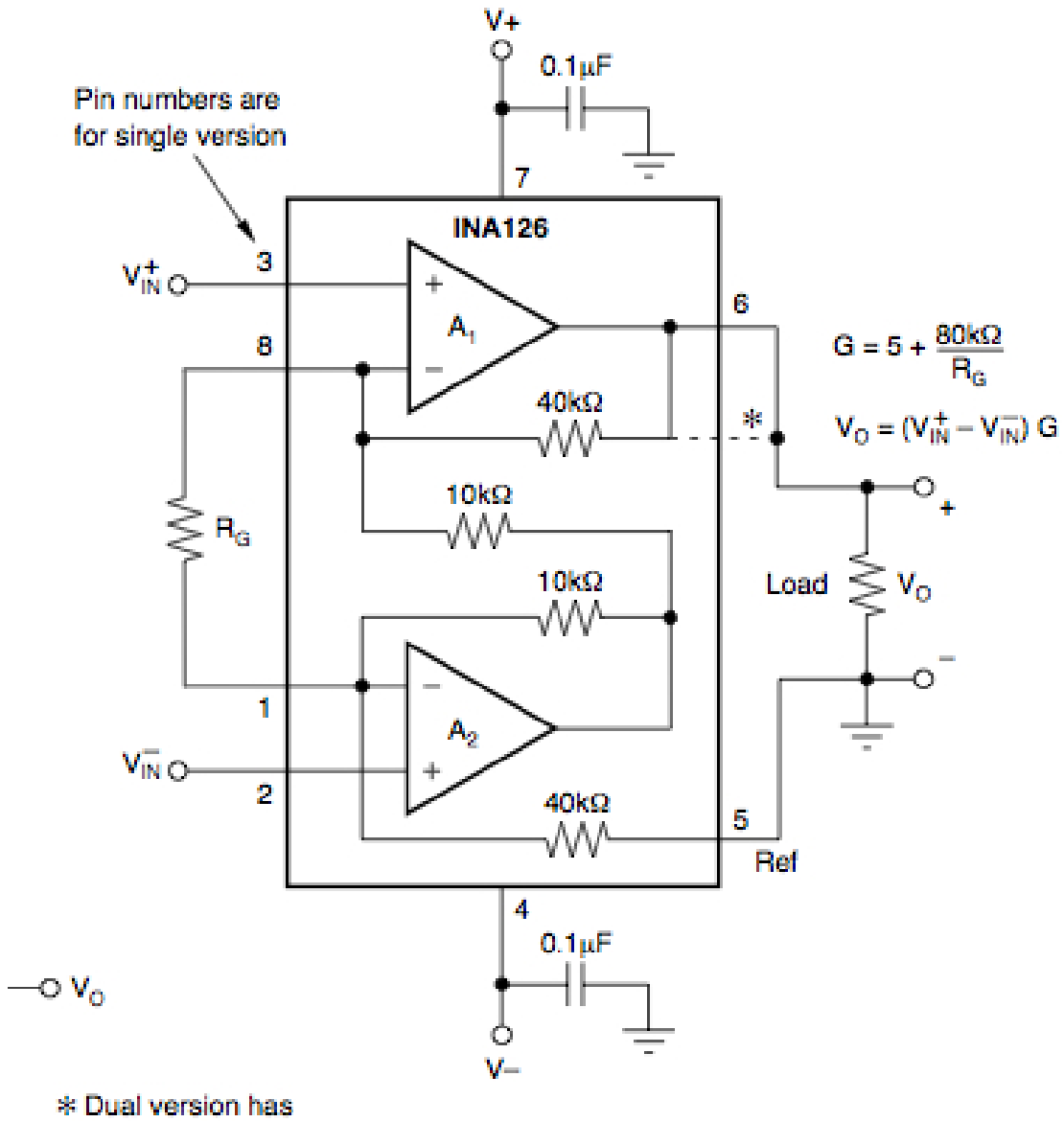


Figure A.10: INA126 Amplifier

A.0.8 Current Sense

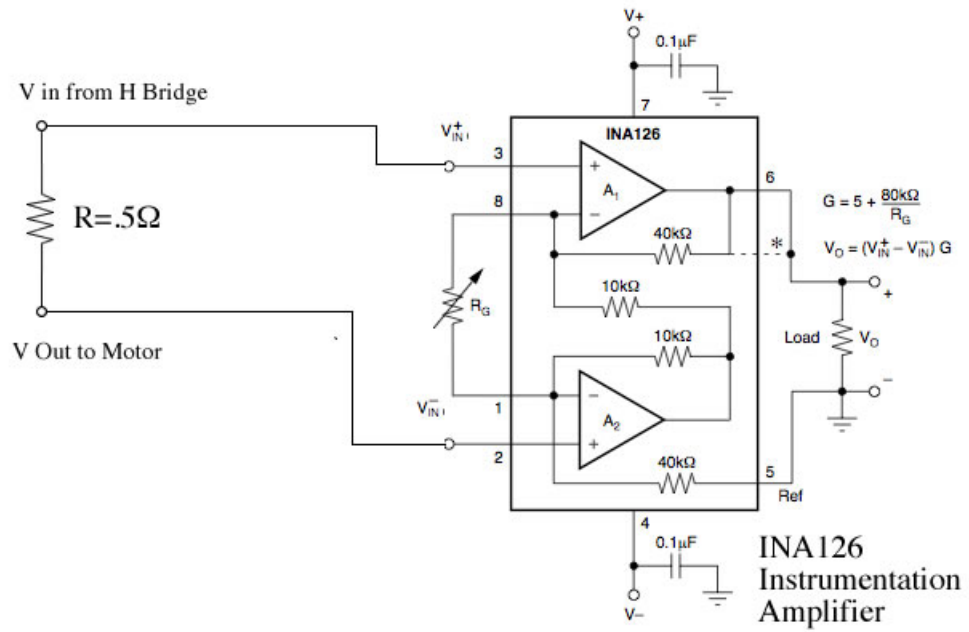


Figure A.11: Current Sense Schematic

A.0.9 Motor Torque Sensor

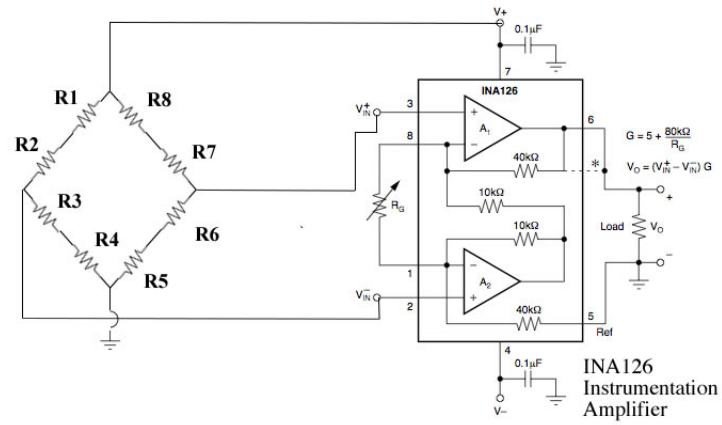


Figure A.12: Motor Mount Torque Sensor and Amplifier Circuit

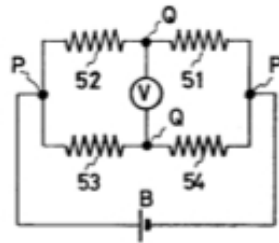


FIG. 9a

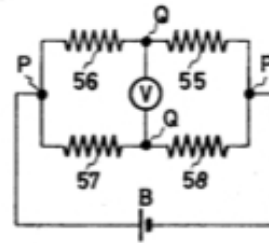


FIG. 9b

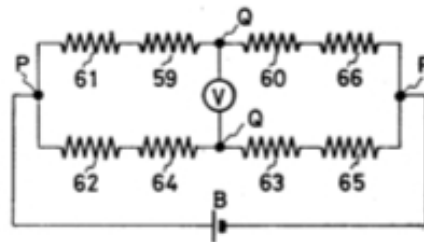


FIG. 9c

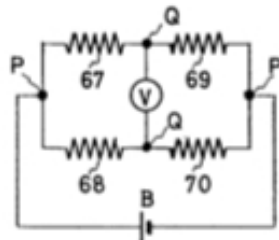


FIG. 9d

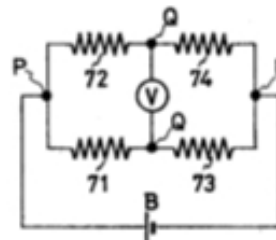


FIG. 9e

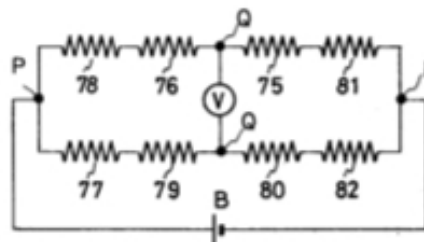


FIG. 9f

Figure A.13: Force Torque Sensor Schematic [33]

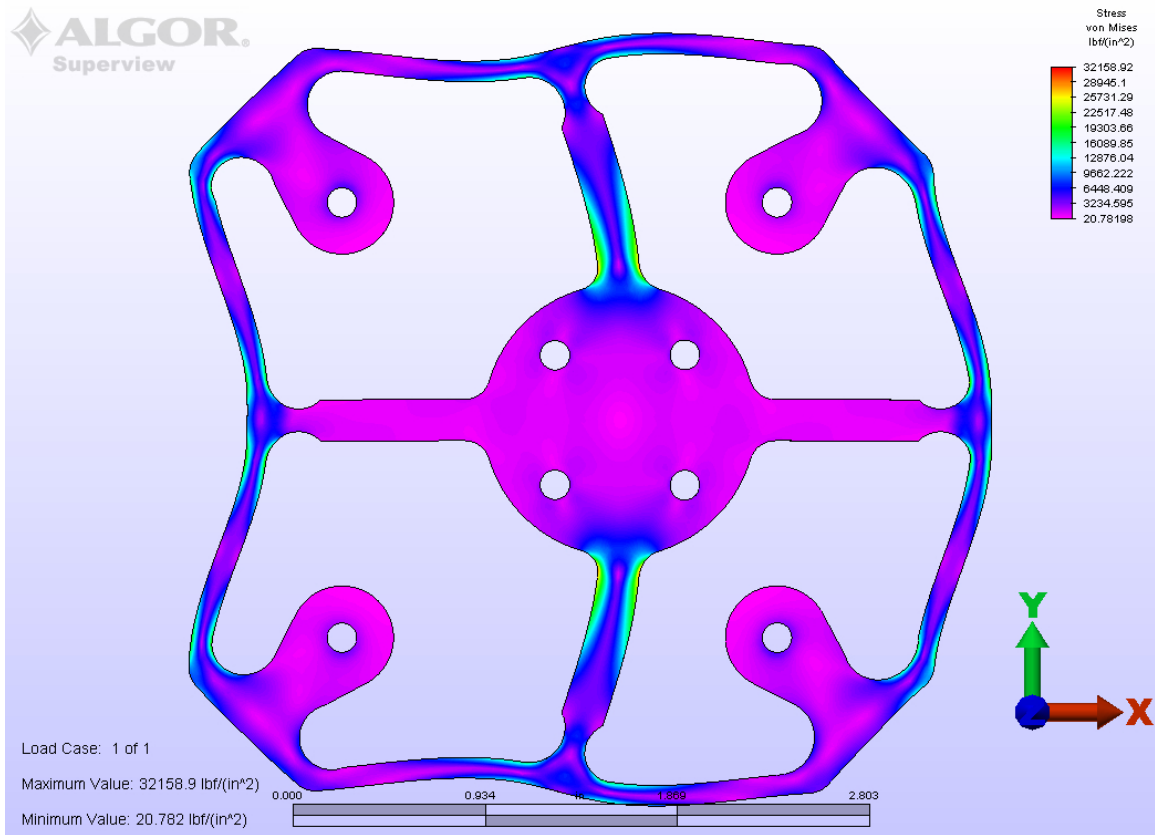


Figure A.14: Exaggerated stress of FT sensor along X axis

Appendix B:Code

A.0.11 Post Processor Code

```

#include <stdio.h>
#include <kiss-compat.h>
#include <string.h>
#include <math.h>
/*****
// Dan Flippo 12-31-08          *****
// version 11 *****
// 5-05-09 REFINED THE OUTPUT AND FITTED FOR POWER VALUES IN TEXT FILES *****
// 2-06-09 ADDED SECOND ORDER CURVE FIT AND ROOT EQUATIONS BACK IN *****
// 1-28-09 FITTED FOR LARGER DATA DUMP FILES *****
// 1-26-09 FIXED SOME GLITCHES *****
// 1-22-09 ADDED 3RD ORDER CURVE FIT, CUBIC EQUATION, AND WORST TRIAL THROW OUT *****
// 1-21-09 ADDED HALF-OMEGA VALUE READING *****
// 9-28-09 ADDED STANDARD DEVIATION *****
// 9-30-09 ADDED STANDARD DEVIATION FOR EACH TRIAL TO MEASURE DRIFT IN EVERY TRIAL *****
// Program to read in data from SWEET data files and do post processing on it *****
// then saves all averaged data in one file, specifically used for Equilibrium tests *****
// Program then curve fits 2nd order curve to data and calculates omega result *****
// trials is the variable for how many trials are done, only work up to 9 *****
// Col is number of columns in text file *****
// oNum is number of omega pts *****
/*****
float SM(float x[],int n);
int main()
{
char path[]="0000.txt",charset,fTail[]=".txt",fHead[]="0",element;
char header[]="Omega: Fx: Fy: V: I: Fx:cal Fy:cal POWER: STD Fx STD Fy STD VSTD I";
int i,j,row=0,kk,k,rows,avgcol,jj=1,trials=5,oNum=7,c,t,flagj=9999,flagk=9999,di,endBL=30,bl=0,cap,Cap=260,startBL=25,iiii;
int col=5,ccc; //change this if not taking power readings
int bigsigk=0,bigsigi=0,bigsigcol=0;
float dataArray[130000][col],data,avgArray[trials][col],sum,omega[30][col],sumTrials,xSlope,ySlope,xInt,yInt,base,xbar,summ,sigma[col];
float sig,sigmat[oNum*2][col][trials],bigsig=0;
char date[10],yn,element1,word[6];
FILE *PTR,*PTRW;
int filenum=oNum,startData=100,oCount=0,scrap=0,iii;
float omegal[100],fy[100],fx[100],sumOSqr[100],sumOCube[100],sumOQuad[100],sumOX[100],sumOY[100],sumO2X[100];
float sumO2Y[100],sumOFifth[100],sumOSixth[100],sumOSixth[100],distance,worst;
float numer,a,aa,b,bb,ca,cc,fxcal,fycal,theta=.8394,oCalcN,oCalcP,sumO3X[100],A0[3],A1[3],A2[3],A3[3],sumO3Y[100],D;
float ucube,pcube,qcube,vcube,root1,root2,root3;
float y1,y2,y3,phi,TT,UU;
double NUMERATOR,N,P,Q,R,S,T,U,V,VV,W,WW,X,XX,Y,YY;
PTRW=fopen("00-000-averages.txt","w");if (PTRW==NULL){printf("PTRW File opening error");return(0);}
printf("\nPLEASE INPUT CALIBRATION PARAMETERS\n\nWHAT IS SLOPE FOR Fx? ");
scanf("%f",&xSlope);
printf("WHAT IS INTERCEPT FOR Fx? ");
scanf("%f",&xInt);
printf("WHAT IS THE SLOPE FOR Fy? ");
scanf("%f",&ySlope);
printf("WHAT IS INTERCEPT FOR Fy? ");
scanf("%f",&yInt);scanf("%c",&yn);
printf("BASE LINE ZERO'ING? ");scanf("%c",&yn); if (yn=='y'|yn=='Y'){bl=1;}
printf("DATA WILL BE CALIBRATED USING THESE EQUATIONS:\n\nFx = %.3f*Fv (+) %.3f Fy = %.3f*Fv (+) %.3f\n\n",xSlope,xInt,ySlope,yInt);
printf("PROCESSING FILES\n");
printf("opening file ");
fprintf(PTRW,"%s",header);//prints header and calibration EQ
for(k=0;k<oNum;k++){//this section goes in the outer loop and reads in the different omega's
if (path[2]=='-'){path[2]='1';k=k-1;}//toggling between - and 1 to get half omega values.
else {path[2]='-';}
if (k<10) {path[1]='0'+k;} else {path[0]='1';path[1]='0'+(k-10);} //this sequences base 10
for(j=0;j<trials;j++){path[3]='0'+j;} //this goes in the second loop for the trials usually 0-4.

cap=Cap;//reset cap value after each trial
//printf(".");//progress periods

PTR=fopen(path,"r"); if (PTR==NULL){flagj=j;flagk=k;break;} //opens up new trial file and checks connection
//printf(" : %s",path);
row=0;
while(!feof(PTR))//loop goes to end of file
{//printf("hitting second loop\n");
element=' '; kk=0;

/*****
//*****scan in trial file*****
for(i=0;i<(col+2);i++){ //scans across the column after the col header
fscanf(PTR,"%f",&data); //saves all the values to dataArray which is a
dataArray[row][i]=data; //2 dimension array that stores all of one trial data
/*****
row=row+1;//advance row count
fscanf(PTR,"%c",&element);fscanf(PTR,"%c",&element);fscanf(PTR,"%c",&element);} //eat up extra symbols
fclose(PTR);
//*****
//*****ADD UP ROWS IN EACH TRIAL AND SAVE IN AVGARRAY 2D ARRAY*****
for(i=0;i<(col);i++){//for loop for columns ADDING UP ROWS, THIS SCROLLS THRU COLUMNS
{sum=0;base=0;if (cap>row){cap=row;} //printf("startData=%d, row=%d cap=%d\n",startData,row,cap);
for (rows=startBL;rows<=endBL;rows++){//for loop for rows,THIS SCROLLS THRU ROWS
base=base+dataArray[rows][i];}

for (rows=startData;rows<=cap;rows++){

sum=sum+dataArray[rows][i]-bl*base/(endBL-startBL+1);
}
}
}
}

```

```

base=0;
avgArray[j][i]=sum/(cap-startData+1); //averages amounts with first XX pts taken out stores in 2 dim array
//*****
for(i=0;i<col-2;i++){sig=0;
for(rows=startData;rows<=cap;rows++){ sig=sig+pow((dataArray[rows][i]-avgArray[j][i]),2);}
sigmat[oCount][i][j]=sqrt(sig/(cap-startData+1));
printf("col[%d]=%f \n",i,sigmat[oCount][i][j]);
if(sigmat[oCount][i][j]>bigsig){bigsig=sigmat[oCount][i][j];bigsigk=oCount;bigsigi=i;bigsigcol=j;}
}
printf("that was trial [%d] of omega=[%d] \n",j,oCount);
//*****FINDING STANDARD DEVIATION FOR DATA IN USABLE SECTION OF EACH TRIAL*****

} //trial loop end
//*****FIND WORST FX IN EACH TRIAL AND EXCLUDE IT FROM THE AVERAGE*****
sumTrials=0;distance=0;scrap=0;worst=0;
for(t=0;t<trials;t++){sumTrials=sumTrials+avgArray[t][1];} //gets average of all trials
for(t=0;t<trials;t++){distance=pow((sumTrials/trials)-avgArray[t][1],2);if(distance>worst){worst=distance;scrap=t;}}
//printf("t=%d avgArray=%f\n",t,avgArray[t][1]); //compares
scrap=999; //if on then find worst algorith is off

//*****SUM UP EVERY COLUMN OF EVERY TRIAL AND SAVE IT TO OMEGA ARRAY*****

for(c=0;c<(col);c++){sumTrials=0;
sumn=0; //****
for(t=0;t<trials;t++){if(t!=scrap){sumTrials=sumTrials+avgArray[t][c];} //****
xbar=sumTrials/((float)trials);
omega[oCount][c]=xbar;
for(t=0;t<trials;t++){sumn=sumn+pow((avgArray[t][c]-xbar),2);}
sigma[c]=sqrt(sumn/trials);} //making 2 dim array of trial averages //****

//*****
//printf("Fx for omega[%d] = %f\n",oCount,omega[oCount][14]);
//*****Print final values to output file*****
fprintf(PTRW,"%n%.4f ",-(float)oCount/200); //goes to 200 if doing half counts
for(avgcol=1;avgcol<col;avgcol++){ //prints out first section of columns
fprintf(PTRW,"%n%.4f ",omega[oCount][avgcol]);}
fprintf(PTRW,"%n%.4f ",xSlope*omega[oCount][1]*xInt); //print to file Fx Calibration
fprintf(PTRW,"%n%.4f ",ySlope*omega[oCount][2]*yInt); //print to file Fy Calibration
fprintf(PTRW,"%n%.4f ",fabs(omega[oCount][3]*omega[oCount][4])); //print out calc power
for(iiii=1;iiii<col;iiii++){ //scrolls through all the std deviation columns
fprintf(PTRW,"%n%.4f ",sigma[iiii]);} //print out std deviation
//*****
oCount++; //if(oCount==1){oCount=2;} //index up the count

} //omega loop end
//ifprintf(PTRW,"%nAVERAGE %s",date);
fprintf(PTRW,"%nlargest sigma is %f at omega=%f trial=%d col=%d\n",bigsig,(float)bigsigk/2,bigsigcol,bigsigi);
fprintf(PTRW,"%nLimits are %d to %d\n",startData,cap);
fclose(PTRW);
printf("largest sigma is %f at omega=%f trial=%d col=%d\n",bigsig,(float)bigsigk/2,bigsigcol,bigsigi);
//*****ERROR STATEMENTS AND PROGRESS CONCLUSIONS*****
printf("\nPARAMETERS WERE %d TRIALS OF %d DIFFERENT OMEGA VALUES\n",trials,oNum);
if(flagj!=9999){printf("ERROR: PROGRAM ONLY PROCESSED %d OF %d TRIALS AT OMEGA VALUE %f\n",flagj,trials,-(float)flagk/10);}
if(k!=(oNum)){printf("ERROR: PROGRAM ONLY PROCESSED %d OF %d OMEGA VALUES\n",k-1,oNum);}
printf("ALL SUCCESSFULLY PROCESSED DATA WAS SAVED TO consolidated-average.txt\n");

//*****DATA CURVE FITTING AND EQUALIBRIUM CALCULATION*****

//*****
// Dan Flippo 1-11-09
// Program to do curve fitting for 2nd and 3rd order polynomials
//
//*****

//filenum=(oNum)*2;
filenum=oCount;
fycal=ySlope;fxcal=xSlope;
//*****READ IN DATA FROM FILE*****
PTR=fopen("consolidated-average.txt","r");
if(PTR=NULL){printf("file not found\n");return(0);}

element=' ';
while(element != '\n'){fscanf(PTR,"%c",&element);} //eats up header in file
//fscanf(PTR,"%f",&omegal[0]);fscanf(PTR,"%f",&fx[0]);fscanf(PTR,"%f",&fy[0]);fscanf(PTR,"%f",&data);fscanf(PTR,"%f",&data);
//fscanf(PTR,"%f",&data);fscanf(PTR,"%f",&data);fscanf(PTR,"%f",&data);fscanf(PTR,"%f",&data);fscanf(PTR,"%f",&data);
for(row=0;row<filenum;row++){
//for(ccc=0;ccc<col;ccc++){
//if(ccc==0){fscanf(PTR,"%f",&omegal[row]);}
//else if(ccc==2){fscanf(PTR,"%f",&fy[row]);printf("fy[%d]=%f\n",row,fy[row]);}
//else if(ccc==1){fscanf(PTR,"%f",&fx[row]);}
//else {
fscanf(PTR,"%f",&data);
fscanf(PTR,"%f",&data);
fscanf(PTR,"%f",&data);
fscanf(PTR,"%f",&data);
fscanf(PTR,"%f",&data);
fscanf(PTR,"%f",&data);
fscanf(PTR,"%f",&data);
fscanf(PTR,"%f",&omegal[row]);
fscanf(PTR,"%f",&fx[row]);
fscanf(PTR,"%f",&fy[row]);
}
}

```

```

//printf("fy=f\n",fy[row]);
for(iiii=0;iiii<9;iiii++){
fscanf(PTR,"%f",&data);//eat up rest of columns
}
//printf("last=f\n",fy[row]);
}
//*****FILLING ARRAYS*****
for(i=0;i<filenum;i++){
fy[i]=fy[i]*fycal+yInt;
fx[i]=fx[i]*fxcal+xInt;
sum0Sqr[i]=pow(omegal[i],2);
sum0Cube[i]=pow(omegal[i],3);
sum0Quad[i]=pow(omegal[i],4);
sum0X[i]=omegal[i]*fx[i];
sum0Y[i]=omegal[i]*fy[i];
sum02X[i]=pow(omegal[i],2)*fx[i];
sum02Y[i]=pow(omegal[i],2)*fy[i];
sum0fifth[i]=pow(omegal[i],5);
sum0sixth[i]=pow(omegal[i],6);
sum03X[i]=pow(omegal[i],3)*fx[i];
sum03Y[i]=pow(omegal[i],3)*fy[i];}
//*****

//*****SOLVING FOR QUADRATIC COEFFICIENTS*****
P=SM(omegal,filenum); //*****
Q=SM(sum0Sqr,filenum); //*****
R=SM(sum0Cube,filenum); //*****
S=SM(sum0Quad,filenum); //*****
T=SM(fx,filenum); TT=SM(fy,filenum); //*****
U=SM(sum0X,filenum); UU=SM(sum0Y,filenum); //*****
V=SM(sum02X,filenum); VV=SM(sum02Y,filenum); //*****
numer=filenum*Q*S+2*P*Q*R-pow(Q,3)-pow(P,2)*S-filenum*pow(R,2); //*****
a=(filenum*Q*V+P*R*T+P*Q*U-pow(Q,2)*T-pow(P,2)*V-filenum*R*U)/numer; //*****
b=(filenum*S*U+P*Q*V+Q*R*T-pow(Q,2)*U-P*S*T-filenum*R*V)/numer; //*****
cA=(Q*S*T+Q*R*U+P*R*V-pow(Q,2)*V-P*S*U-pow(R,2)*T)/numer; //*****
aa=(filenum*Q*VV+P*R*TT+P*Q*UU-pow(Q,2)*TT-pow(P,2)*VV-filenum*R*UU)/numer; //*****
bb=(filenum*S*UU+P*Q*VV+Q*R*TT-pow(Q,2)*UU-P*S*TT-filenum*R*VV)/numer; //*****
cc=(Q*S*TT+Q*R*UU+P*R*VV-pow(Q,2)*VV-P*S*UU-pow(R,2)*TT)/numer; //*****
//*****
printf("Fx=%f*Omega^2+f*0omega+f \n",a,b,cA);
printf("Fy=%f*Omega^2+f*0omega+f \n",aa,bb,cc);
for(iii=0;iii<2;iii++){
if(iii==1){a=0;b=0;cA=0;}
//*****EQUATING THE TWO EQUATIONS TO FIND THE EQUALIBRIUM POINT*****//*****
a=a*tan(theta);b=b*tan(theta);cA=cA*tan(theta);//taking in account for SR2 geometry //*****
oCalcN=(-(bb-b)-sqrt(pow(bb-b,2)-4*(aa-a)*(cc-cA)))/(2*(aa-a));//figure roots //*****
oCalcP=(-(bb-b)+sqrt(pow(bb-b,2)-4*(aa-a)*(cc-cA)))/(2*(aa-a));//figure roots //*****
printf("2nd order ROOTS ARE %f AND %f\n",oCalcN,oCalcP); //*****
//*****

//*****SOLVING FOR QUADRATIC COEFFICIENTS*****
T=SM(sum0fifth,filenum); //*****
U=SM(sum0sixth,filenum); //*****
V=SM(fx,filenum); VV=SM(fy,filenum); //*****
W=SM(sum0X,filenum); WW=SM(sum0Y,filenum); //*****
X=SM(sum02X,filenum); XX=SM(sum02Y,filenum); //*****
Y=SM(sum03X,filenum); YY=SM(sum03Y,filenum); //*****
//*****

//*****
for(i=0;i<2;i++){if(i==1){V=VV;W=WW;X=XX;Y=YY;}
NUMERATOR=(U*pow(P,2)*S - pow(P,2)*pow(T,2) - 2*U*P*Q*R + 2*P*Q*S*T + 2*P*pow(R,2)*T - 2*P*R*pow(S,2) ((CONT))
+ U*pow(Q,3) - 2*pow(Q,2)*R*T - pow(Q,2)*pow(S,2) + 3*Q*pow(R,2)*S - U*filenum*Q*S + filenum*Q*pow(T,2) - pow(R,4) +((CONT))
+ U*filenum*pow(R,2) - 2*filenum*R*S*T + filenum*pow(S,3));
A0[i]=-(R*(Q*(T*X - 2*S*Y + U*W) - P*(T*Y - U*X) + pow(S,2)*W + 2*S*T*V) - pow(S,3)*V + pow(R,3)*Y + pow(Q,2)*(T*Y - ((CONT))
U*X) - pow(R,2)*(S*X + ((CONT))
T*W + U*V) - Q*(W*S*T - X*pow(S,2) - U*V*S + V*pow(T,2)) + P*(Y*pow(S,2) - X*S*T - U*W*S + W*pow(T,2)))/NUMERATOR;
A1[i]=-(pow(R,3)*X - Q*(S*(R*X + T*V) + P*(T*Y - U*X) + pow(R,2)*Y - 2*R*T*W - R*U*V) + S*(P*(R*Y - U*V) - pow(R,2)*W +((CONT))
T*X*filenum + ((CONT))
U*W*filenum + pow(Q,2)*(S*Y - U*W) + pow(S,2)*(R*V - Y*filenum) + P*(pow(T,2)*V - R*T*X) - pow(R,2)*T*V - ((CONT))
pow(T,2)*W*filenum + R*T*Y*filenum ((CONT))
- R*U*X*filenum)/NUMERATOR;
A2[i]=-(pow(R,3)*W + Q*(T*(R*V - Y*filenum) - pow(R,2)*X + P*U*W + U*X*filenum) + pow(Q,2)*(R*Y - U*V) + ((CONT))
pow(S,2)*(Q*V - X*filenum) - ((CONT))
S*(Q*(P*Y + R*W) + T*(P*V - W*filenum) + pow(R,2)*V - 2*P*R*X - R*Y*filenum) + T*(pow(P,2)*Y - P*R*W) -((CONT))
P*pow(R,2)*Y - pow(P,2)*U*X + ((CONT))
P*R*U*V - R*U*W*filenum)/NUMERATOR;
A3[i]=-(R*(S*(P*W - 2*Q*V + X*filenum) - T*(P*V - W*filenum) + pow(Q,2)*X + 2*P*Q*Y) + pow(R,3)*V - pow(Q,3)*Y + ((CONT))
pow(S,2)*(P*V - W*filenum) - ((CONT))
pow(R,2)*(P*X + Q*W + Y*filenum) + T*(X*pow(P,2) - W*P*Q + V*pow(Q,2) - X*filenum*Q) + S*(W*pow(Q,2) - X*P*Q - ((CONT))
Y*pow(P,2) + Y*filenum*Q)/NUMERATOR;
if(i==0&&iii==0){printf("\n\nFx =%f*a2^3 + %f*a2 + %f\n",A3[i],A2[i],A1[i],A0[i]);}
else if(iii==0){printf("Fy =%f*a2^3 + %f*a2 + %f\n",A3[i],A2[i],A1[i],A0[i]);}
}
//*****EQUATING THE TWO EQUATIONS TO FIND THE EQUALIBRIUM POINT*****
A0[0]=A0[0]*tan(theta);A1[0]=A1[0]*tan(theta);A2[0]=A2[0]*tan(theta);A3[0]=A3[0]*tan(theta);//taking in account for SR2 geometry//
if(iiii==1){A0[0]=0;A1[0]=0;A2[0]=0;A3[0]=0;}
pcube=(3*(A1[0]-A1[1])/(A3[0]-A3[1])-pow((A2[0]-A2[1])/(A3[0]-A3[1]),2))/3;
qcube=(2*pow((A2[0]-A2[1])/(A3[0]-A3[1]),3)-9*(A2[0]-A2[1])*(A1[0]-A1[1])/(A3[0]-A3[1])/(A3[0]-A3[1])+27*(A0[0]-A0[1])/(A3[0]-A3[1]))/27;
D=pow(pcube/3,3)+pow(qcube/2,2);

```

```

//Fight you K-State Wildcats for alma matter fight fight fight, glory in the combat
for the purple and the white, faithful to our
colors we will always be fighting ever fighting for a kstate victory fight fight fight!
if(D<0){phi=acos(-qcube/2/sqrt(pow(fabs(pcube),3)/27));
y1=2*sqrt(fabs(pcube)/3)*cos(phi/3);
y2=-2*sqrt(fabs(pcube)/3)*cos((phi+3.1415926)/3);
y3=-2*sqrt(fabs(pcube)/3)*cos((phi-3.1415926)/3);}
else{
ucube=pow(-qcube/2+sqrt(D),.3333);
vcube=pow(-qcube/2-sqrt(D),.3333);
y1=(A2[0]-A2[1])/(A3[0]-A3[1])/3;y2=989999;y3=989999;}
root1=y1-(A2[0]-A2[1])/(A3[0]-A3[1])/3;
root2=y2-(A2[0]-A2[1])/(A3[0]-A3[1])/3;
root3=y3-(A2[0]-A2[1])/(A3[0]-A3[1])/3;
if(!!!=0){
printf("\n\nROOTS = %f,%f,%f\n\n",root1,root2,root3);
if(root1<0 && root1>-.16){printf("Omega predicted at Theta = %f is %f\n",theta,root1);}
if(root2<0 && root2>-.16){printf("Omega predicted at Theta = %f is %f\n",theta,root2);}
if(root3<0 && root3>-.16){printf("Omega predicted at Theta = %f is %f\n",theta,root3);}
else{printf("Fy crosses zero at: %f %f %f\n\n\n",root1,root2,root3);}}
}
float SM(float x[],int n)
{ float sum=0;int i;
for(i=0;i<n;i++){sum=sum+x[i];}
return(sum);
}

```

A.0.12 Test Procedure Populator Code

```

\label{it}
/* Includes the Standard IO Library */
#include <stdio.h>
#include <kiss-compat.h>
//#include <kiss-graphics.h>
//#include <kiss-serial.h>
//#include <kiss-create.h>
//#include <kiss-input.h>

/*****
// Dan Flippo 1-08-09          *****
// version 1 *****
// Program to Populate test procedure files for omega forces experiments          *****
// Specifications are set via the terminal window and a txt file is produced          *****
/*****

int main()
{ int omega,trialRow;
char path[]="00-OMEGA.txt",yn,header[]="ID time Vx Vy Vth w Fx Fy Tth";
float r,rx,ry,dt,tLength,base,maxOmega,w;
FILE *PTR;
/*****INPUT STAGE*****
printf("\n\nPOPULATING PROGRAM VERSION 1\n\nDO YOU WISH A STANDARD TIME 10 sec dt=.1 sec and base = 1.5 sec? ");scanf("%c",&yn);
if(yn == 'y'){tLength=10;dt=.1;base=1.5;rx=.287274;ry=.325374;r=.108745;maxOmega=.15;}
else{printf("\n\nPOPULATING PROGRAM VERSION 1\n\nWHAT IS THE TIME LENGTH OF THE TEST? ");scanf("%f",&tLength);
printf("WHAT IS THE DELTA T FOR THE TEST? ");scanf("%f",&dt);
printf("HOW LONG OF A BASE LINE IN SECONDS? ");scanf("%f",&base);
printf("WHAT IS Rx? ");scanf("%f",&rx);
printf("WHAT IS Ry? ");scanf("%f",&ry);
printf("WHAT IS r? ");scanf("%f",&r);
printf("WHAT IS THE MAX OMEGA VALUE? ",&maxOmega);scanf("%f",&maxOmega);}
printf("WHAT IS W? ");scanf("%f",&w);
/*****WRITE STAGE*****
for(omega=0;omega<=(maxOmega*100);omega++){
if(omega>9){path[1]='0'+omega-10;path[0]='1';}
else{path[1]='0'+omega;}
//path[1]='0'+omega;
printf("path is %s\n",path);
PTR=fopen(path,"w");
fprintf(PTR,"%s",header);
for(trialRow=0;trialRow<=(tLength/dt);trialRow++){
if(trialRow<(base/dt)){fprintf(PTR,"\nBASE %.3f %f %f %f %f %f %f",((CONT))
((float)trialRow*dt),0.0,0.0,0.0,0.0,0.0,0.0);}
else{
fprintf(PTR,"\nTEST %.3f %f %f %f %f %f %f",((float)omega/(100))*ry,((CONT))
((float)omega/(-100))*rx,(float)omega/(-100),w,0,0,0);}
}
fclose(PTR);

}

}

```

A.0.13 Numerical Iteration Program Code

```
/* Includes the Standard IO Library */
#include <stdio.h>
#include <kiss-compat.h>
#include <math.h>
//#include <kiss-graphics.h>
//#include <kiss-serial.h>
//#include <kiss-create.h>
//#include <kiss-input.h>

int main()
{
//this program iterates through two high order equations to satisfy the equation Fx=Fy*cos(theta)
int i,res=4001;//the bigger the res value the more resolution
float Fx,Fy,diff,theta=.839355,hit=0,power=0,FxHit,FyHit,x,x2,x3,x4,x5,x6,oldif=1,score,score2,score3;
for(i=0;i<res+1000;i++)
{
x=(-(float)i/((res-1)*10.0)) ;
x2=pow(-(float)i/((res-1)*10.0),2);
x3=pow(-(float)i/((res-1)*10.0),3);
x4=pow(-(float)i/((res-1)*10.0),4);
x5=pow(-(float)i/((res-1)*10.0),5);
x6=pow(-(float)i/((res-1)*10.0),6);

//Fy = 158593363.51*x5 + 27525704.10*x4 + 1862714.33*x3 + 61769.11*x2 + 1132.92*x + 19.44;//right paint .3 on sand 9-26-09
//Fx = -170594*x3 - 18513*x2 - 734.31*x - 0.3023;

//Fx = -2662.3*x2 - 316.02*x + 0.8818;//.4 right paint on sand 9-26-09
//Fy = 181720*x3 + 21473*x2 + 882*x + 22.28;//

//Fy = 3372411.45948315*x4 + 545609.42175840*x3 + 31990.61609887*x2 + 912.34271092*x + 20.20715267;//.35 right paint on sand 9-26-09
//Fx = -165981.11888109*x3 - 18379.84615384*x2 - 739.59421329*x - 0.82186346;

//Fy = 5948420.40309334*x4 + 989698.32715922*x3 + 59185.79092953*x2 + 1571.86090228*x + 26.87989619;//.5 right paint on sand 9-26-09
//Fx = -2013.60639361*x2 - 251.71396603*x + 1.39599670;//.5 right paint on sand

//Fy = 3372411.46*x4 + 545609.42*x3 + 31990.62*x2 + 912.34*x + 20.21;//.3 left paint on sand 9-26-09
//Fx = -165981*x3 - 18380*x2 - 739.59*x - 0.8219;//.3 left paint on sand 9-26-09

//Fy = 304882956.28051800*x5 + 53539119.70709230*x4 + 3502600.35327850*x3 + 105746.19025795*x2 + ((CONT))
1589.19640058*x + 21.00667489;//.35 left paint on sand 9-26-09
//Fx = -125222.14452213*x3 - 14379.89710290*x2 - 632.89272311*x - 0.20485962;//.35 left paint on sand 9-26-09

//Fy=6029311.67*x4 + 938057.03*x3 + 51941.77*x2 + 1298.11*x + 23.06;//.4 left paint on sand 9-26-09
//Fx=-2569.4*x2 - 312.7*x + 1.3045;//.4 left paint on sand 9-26-09

//Fy = 8533253.80496025*x4 + 1266059.92046509*x3 + 67623.91176451*x2 + 1625.32937817*x + 26.30854706;//.5 left paint on sand 9-26-09
//Fx = -1541420.54024291*x4 - 310944.35760296*x3 - 19945.69402164*x2 - 588.70996278*x + 0.13717185;//.5 left paint on sand 9-26-09

//Fy = 607.7*x2 + 143.24*x + 9.7411;//.3 blank wheel on sand 9-26-09
//Fx = 65731*x3 + 5363*x2 - 155.37*x + 0.9854;//.3 blank wheel on sand 9-26-09

//Fy = 77495*x3 + 8784.4*x2 + 369.56*x + 12.325;//.4 blank wheel on sand 9-26-09
//Fx = 511.58*x2 - 206.37*x + 0.0408;//.4 blank wheel on sand 9-26-09

//Fy = 70023*x3 + 8339*x2 + 328.21*x + 11.299;//.5 blank wheel on sand 9-26-09
//Fx = 52.022*x2 - 153.46*x + 0.9362;//.5 blank wheel on sand 9-26-09

//Fy=5859563.97*x4 + 893053.97*x3 + 47735.13*x2 + 1166.64*x + 18.26;//.3 right wheel on sand 9-26-09
//Fx = -93240*x3 - 9194.2*x2 - 434.69*x + 0.4744;//.3 right wheel on sand 9-26-09

//Fy=5317623.74877357*x4 + 881008.32304662*x3 + 52877.36833258*x2 + 1415.58578064*x + 19.13398174;//.4 right wheel on sand 9-26-09
//Fx = -413.76223776*x2 - 178.48199800*x - 1.36323407;//.4 right wheel on sand 9-26-09

// Fy = 4358137.94047356*x4 + 789680.98176138*x3 + 51954.57349508*x2 + 1508.16746538*x + 21.51105249;//.5 right wheel on sand 9-26-09
//Fx = -61977.15617715*x3 - 6507.68631369*x2 - 312.59592574*x - 2.32424890;//.5 right wheel on sand 9-26-09

//Fy = 174598*x3 + 20239*x2 + 854.7*x + 19.163;//.3 right on sand (8-31-09) 9-26-09
//Fx = -86674*x3 - 7531*x2 - 391.41*x - 1.4127;//.3 right on sand (8-31-09) 9-26-09

//Fy = 6227692.3*x4 + 832414.0*x3 + 37408.4*x2 + 735.5*x + 13.0;//.3 right on sand (8-13-09) 9-26-09
//Fx = 599.29*x2 - 230.25*x + 0.8298;//

//Fx = 5364898*x4 + 585007*x3 + 17629*x2 - 91*x - 1;//.4 right on sand (8-13-09)
//Fy = 108601*x3 + 13420*x2 + 616.65*x + 17.59;//.4 right on sand (8-13-09)

//Fy=150583*x3 + 18727*x2 + 786.5*x + 20.06-.052;//.5 right on sand (8-13-09) with error
//Fx = -1325.5*x2 - 263.14*x - 0.7679+.052;//.5 right on sand (8-13-09) with error

//Fx = -165981.11888109*x3 - 18379.84615384*x2 - 739.59421329*x - 0.82186346+.052;//.35 right paint on sand 9-28-09
//Fy = 3372411.45948315*x4 + 545609.42175840*x3 + 31990.61609887*x2 + 912.34271092*x + ((CONT))
20.20715267-.052;//.35 right paint on sand 9-28-09

//Fx = -152.79*x - 1.417;//.4 right on sand c9-1 50-200 9-30-09
//Fy = 2381718.09*x4 + 455314.10*x3 + 31474.37*x2 + 989.28*x + 16.55;//.4 right on sand c9-1 50-200 9-30-09

//Fy = 48500150.84*x5 + 13360068.56*x4 + 1292377.77*x3 + 56023.15*x2 + 1220.00*x + 15.90;//.3 right on sand 100-200 10-1-09
//Fx = -80779*x3 - 7575.7*x2 - 400.49*x - 1.5777;//.3 right on sand 100-200 10-1-09

//Fy = 6418689.15*x4 + 1052839.90*x3 + 60384.30*x2 + 1513.49*x + 18.84+.052;//.3 right on sand 10-2-09 100-200 1 sec lag
```

```

//Fx= -4433168.79*x4 - 582096.34*x3 - 25472.10*x2 - 618.21*x - 3.25-.052;//.3 right on sand 10-2-09 100-200 1 sec lag
//Fy = 3896394*x4 + 642264*x3 + 39818*x2 + 1167*x + 19+.052;//.4 right on sand 10-2-09 100-200 1 sec lag
//Fx= -2821122*x4 - 374935*x3 - 17527*x2 - 479*x - 3-.052;//.4 right on sand 10-2-09 100-200 1 sec lag

//Fx = -75472.26*x3 - 8092.49*x2 - 367.66*x - 3.19-.052;//.5 right on sand 10-2-09 100-200 1 sec lag
//Fy = 3598711.09*x4 + 703165.14*x3 + 48765.71*x2 + 1463.39*x + 21.79+.052;//.5 right on sand 10-2-09 100-200 1 sec lag

//Fx = -154096*x3 - 16528*x2 - 693.47*x - 1.7254-.052;//.3 left paint 10-6-09 1 sec lag
//Fy = -12224231285*x6 - 2204698283*x5 - 146462536*x4 - 4184574*x3 - 35937*x2 + 596*x + 19+.052;//.3 left paint 10-6-09 1 sec lag

//Fy= 4691633*x4 + 829906*x3 + 51708*x2 + 1426*x + 23+.052;//.4 left paint on sand 10-6-09 1 sec lag
//Fx= -129759*x3 - 13821*x2 - 559.19*x - 0.9737-.052;//.4 left paint on sand 10-6-09 1 sec lag

//Fx = -4146014*x4 - 613704*x3 - 31449*x2 - 752*x - 1-.052;//.5 left paint on sand 10-6-09 1 sec lag
//Fy = 242846*x3 + 30077*x2 + 1252.2*x + 25.787+.052;//.5 left paint on sand 10-6-09 1 sec lag

//Fy = -25112473560*x6 - 4830135738*x5 - 352569095*x4 - 11938826*x3 - 174652*x2 - 358*x + ((COUNT)
19+.052);//.35 left paint on sand 10-6-09 1 sec lag
//Fx = 2206068134*x6 + 372913079*x5 + 21863705*x4 + 357133*x3 - 12794*x2 - 668*x - 2-.052;//.35 left paint on sand 10-6-09 1 sec lag

//Fx= -1799066*x4 - 260962*x3 - 12887*x2 - 378*x - 0;//.4 blank on sand 10-7-09 c10-7 1 sec lag
//Fy = 3604155504*x6 + 869185396*x5 + 81974470*x4 + 3809450*x3 + 90137*x2 + 1050*x + 10;//

//Fy = 542496*x3 + 35017*x2 + 728.55*x + 10.236;//.4 blank partial
//Fx=-1337.5*x2 - 187.84*x - 0.0499;//.4 blank partial 1 sec lag

//Fy = 7689755820*x6 + 1596868265*x5 + 129259168*x4 + 5109133*x3 + 100696*x2 + 922*x + 10+.052;//.4 blank 10-9-09
//Fx = -120060935*x5 - 20141942*x4 - 1193584*x3 - 29541*x2 - 428*x + 1-.052;//.4 blank 10-9-09

//Fx= 136.79*x2 - 121.79*x + 1.3888-.052;//.5 blank c10-09-09
//Fy= 61320*x3 + 7562.7*x2 + 312.29*x + 10.465+.052;//.5 blank on sand c10-09-09

//Fx = -995.1*x2 - 257.13*x - 0.0928-.052;//.3 blank on sand c10-6
//Fy = 1044.7*x2 + 165.42*x + 8.4349+.052;//.3 blank on sand c10-6

//Fy= 4356.5*x2 + 464.56*x + 18.83+.052;//.3 right paint on sand 10-13-09
//Fx = -2996611.82*x4 - 508616.03*x3 - 30331.38*x2 - 877.08*x - 0.00-.052;//.3 right paint on sand 10-13-09

//Fy = 85691402.72*x5 + 18985146.03*x4 + 1648270.86*x3 + 69871.12*x2 + 1519.37*x + 23.28+.052;//.4 right paing 10-13-09
//Fx=-4428835.87*x4 - 694471.49*x3 - 36334.62*x2 - 867.39*x - 0.42-.052;//.4 right paint 10-13-09

//Fy = 4739875.22*x4 + 838460.32*x3 + 53578.78*x2 + 1502.61*x + 26.18+.052;//.5 right paint on sand 10-13-09
//Fx = -136864.34*x3 - 13809.86*x2 - 531.22*x + 0.69-.052;//.5 right paint on sand 10-13-09

//Fy = 129734.85*x4 + 19832.07*x3 + 583.91*x2 + 3.90*x + 1.24+.052;//right .3 padded carpet
//Fx = -18.14*x - 0.15-.052;//right .3 padded carpet

//Fy = -3193.24*x3 - 498.81*x2 - 9.46*x + 1.10+.052;//.3 right unpadded carpet
//Fx = 2326.67*x3 + 287.08*x2 - 8.54*x - 0.11-.052;

//Fy = -770.47*x3 - 184.94*x2 - 5.08*x + 1.17+.052;//.3 left unpadded carpet
//Fx= 1970.10*x3 + 183.71*x2 - 13.18*x + 0.28-.052;//.3 left unpadded carpet

//Fy = 113881.62*x4 + 18357.77*x3 + 494.24*x2 - 1.35*x + 1.18+.052;//.3 omni unpadded carpet
//Fx = -19714.53*x4 - 6222.19*x3 - 674.44*x2 - 29.47*x + 0.14-.052;//.3 omni

//Fx = -43244.73*x4 - 10076.51*x3 - 851.68*x2 - 31.68*x + 0.17-.052;//.5 omni
//Fy = -46131.29*x4 - 6549.49*x3 - 294.06*x2 - 1.26*x + 1.70+.052;//.5 omni unpadded carpet

//Fx = 932.54*x3 + 38.29*x2 - 20.86*x - 0.01-.052;//.3 blank on carpet
//Fy = -46.62*x2 + 4.86*x + 1.25+.052;//.3 blank on carpet

//Fy = 1022.32*x3 + 136.02*x2 + 10.82*x + 1.37-.052;//.4 blank on carpet
//Fx = -50504.48*x4 - 9654.76*x3 - 590.85*x2 - 27.35*x + 0.01+.052;//.4 blank

Fy = 480.87*x3 + 91.32*x2 + 8.37*x + 1.25+.052;//.5 blank on carpet
Fx = 645.72*x3 + 83.65*x2 - 9.99*x + 0.04-.052;//.5 blank

diff=Fy-Fx*tan(theta);
if(fabs(diff)<oldif){printf("hit omega=%f diff=%f power=%f\n",-(float)i/((res-1)*10.0),diff,power);oldif=diff;score=-i/((res-1)*10.0);}
//if(oldif<.005) {hit=-((float)i/((res-1)*10.0));FxFit=Fx;FyHit=Fy;power= 273.7*hit + 56.069;
printf("hit omega=%f diff=%f power=%f\n",-(float)i/((res-1)*10.0),diff,power);}
printf("Fx= %f Fy=%f omega= %f diff=%f\n",Fx,Fy,i/((res-1)*10.0),diff);
}
score2=pow(score,2);
score3=pow(score,3);
//power = -3047.6*score2 + 126.11*score + 47.822;//.3 right paint on sand 9-26-09
//power = -3642.9*score2 + 49.867*score + 51.409;//.35 right paint on sand 9-26-09
//power = 326.12*score + 57.098;//.4 right paint on sand 9-26-09
//power = 4700.9*score2 + 602.11*score + 68.077;//.5 right paint on sand 9-26-09
//power = -3642.9*score2 + 49.867*score + 51.409;//.3 left paint on sand 9-26-09
//power = -3862.3*score2 + 3.8927*score + 49.35;//.35 left paint on sand 9-26-09
//power = 273.7*score + 56.069;//.4 left paint on sand 9-26-09
//power = 6167.8*score2 + 647.54*score + 65.698;//.5 left paint on sand 9-26-09
//power = 71.4*score + 34.533;//.3 blank on sand 9-26-09
//power = 6.371*score + 40.555;//.4 blank on sand 9-26-09
//power = 5.9149*score + 44.439;//.5 blank on sand 9-26-09
//power = 280.56*score + 42.258;//.3 right wheel on sand 9-26-09
//power = 5196.1*score2 + 615.04*score + 52.251;//.4 right wheel on sand 9-26-09
//power = 7482*score2 + 771.04*score + 61.1;//.5 right wheel on sand 9-26-09

```

```
//power = 64.953*score + 35.223; //.3 right on sand 8-13-09
//power = -3819.7*score2 - 121.98*score + 39.204; //.4 right on sand 8-13-09
//power = 167852*score3 + 19321*score2 + 893.35*score + 44.611; //.3 right on sand 10-2-09
//power = 2898.1*score2 + 397.51*score + 47.495; //.4 right on sand 10-2-09
power = 3996.*score2 + 480.92*score + 55.912; //.5 right on sand 10-2-09
printf("power=%f at Wp=%f\n",power,score);
}
```

A.0.14 Parallax Stamp Code for Servo and Light Control

```
' {$STAMP BS2sx}
sp VAR Byte
i VAR Byte

sp=10

main:
FOR i=1 TO 200
GOSUB gox
NEXT

FOR i=1 TO 200
GOSUB goy
NEXT

FOR i=1 TO 200
GOSUB gotheta
NEXT

GOSUB clear

END

clear:
LOW 0
LOW 1
LOW 2
LOW 3
LOW 4
LOW 5
RETURN

gox:
'DEBUG "x "
PULSOUT 0, sp*260
PULSOUT 5, sp*260
RETURN

goy:
'DEBUG "y "
PULSOUT 1, sp*150
PULSOUT 2, sp*300
PULSOUT 5, sp*150
RETURN

gotheta:
'DEBUG "theta "
PULSOUT 1, sp*300
PULSOUT 3, sp*300
PULSOUT 5, sp*300
RETURN
```


Test Procedure File for Drag Test with $F_D = -.5V$.

```
ID time Vx Vy Vth w Fx Fy Tth
NN1 0 0 0 0 0 0 0 0
NN1 0 0 0 0 0 0 0 0
NN1 0 0 0 0 0 0 0 0
NN1 0 0 0 0 0 0 0 0
NN1 0 0 0 0 0 0 0 0
NN1 2 0 0 0 0 0 0 0
NN1 2.1 0 0 0 0 0 0 0
NN1 2.2 0 0 0 0.2 0 0 0
NN1 2.3 0 0 0 0.4 0 0 0
NN1 2.4 0 0 0 0.6 0 -0.5 0
NN1 2.5 0 0 0 0.8 0 -0.5 0
NN1 2.6 0 0 0 1 0 -0.5 0
NN1 2.7 0 0 0 1.2 0 -0.5 0
NN1 2.8 0 0 0 1.4 0 -0.5 0
NN1 2.9 0 0 0 1.6 0 -0.5 0
NN1 3 0 0 0 1.8 0 -0.5 0
NN1 3.1 0 0 0 2 0 -0.5 0
NN1 3.2 0 0 0 2 0 -0.5 0
NN1 3.3 0 0 0 2 0 -0.5 0
NN1 3.4 0 0 0 2 0 -0.5 0
NN1 3.5 0 0 0 2 0 -0.5 0
NN1 3.6 0 0 0 2 0 -0.5 0
NN1 3.7 0 0 0 2 0 -0.5 0
NN1 3.8 0 0 0 2 0 -0.5 0
NN1 3.9 0 0 0 2 0 -0.5 0
NN1 4 0 0 0 2 0 -0.5 0
NN1 4.1 0 0 0 2 0 -0.5 0
NN1 4.2 0 0 0 2 0 -0.5 0
NN1 4.3 0 0 0 2 0 -0.5 0
NN1 4.4 0 0 0 2 0 -0.5 0
NN1 4.5 0 0 0 2 0 -0.5 0
NN1 4.6 0 0 0 2 0 -0.5 0
NN1 4.7 0 0 0 2 0 -0.5 0
NN1 4.8 0 0 0 2 0 -0.5 0
NN1 4.9 0 0 0 2 0 -0.5 0
NN1 5 0 0 0 2 0 -0.5 0
NN1 5.1 0 0 0 2 0 -0.5 0
NN1 5.2 0 0 0 2 0 -0.5 0
NN1 5.3 0 0 0 2 0 -0.5 0
NN1 5.4 0 0 0 2 0 -0.5 0
NN1 5.5 0 0 0 2 0 -0.5 0
NN1 5.6 0 0 0 2 0 -0.5 0
NN1 5.7 0 0 0 2 0 -0.5 0
NN1 5.8 0 0 0 2 0 -0.5 0
NN1 5.9 0 0 0 2 0 -0.5 0
NN1 6 0 0 0 2 0 -0.5 0
NN1 6.1 0 0 0 2 0 -0.5 0
NN1 6.2 0 0 0 2 0 -0.5 0
NN1 6.3 0 0 0 2 0 -0.5 0
NN1 6.4 0 0 0 2 0 -0.5 0
NN1 6.5 0 0 0 2 0 -0.5 0
NN1 6.6 0 0 0 2 0 -0.5 0
NN1 6.7 0 0 0 2 0 -0.5 0
NN1 6.8 0 0 0 2 0 -0.5 0
NN1 6.9 0 0 0 2 0 -0.5 0
NN1 7 0 0 0 2 0 -0.5 0
NN1 7.1 0 0 0 2 0 -0.5 0
NN1 7.2 0 0 0 2 0 -0.5 0
NN1 7.3 0 0 0 2 0 -0.5 0
NN1 7.4 0 0 0 2 0 -0.5 0
NN1 7.5 0 0 0 2 0 -0.5 0
NN1 7.6 0 0 0 2 0 -0.5 0
NN1 7.7 0 0 0 2 0 -0.5 0
NN1 7.8 0 0 0 2 0 -0.5 0
NN1 7.9 0 0 0 2 0 -0.5 0
NN1 8 0 0 0 2 0 -0.5 0
NN1 8.1 0 0 0 2 0 -0.5 0
NN1 8.2 0 0 0 2 0 -0.5 0
NN1 8.3 0 0 0 2 0 -0.5 0
NN1 8.4 0 0 0 2 0 -0.5 0
NN1 8.5 0 0 0 2 0 -0.5 0
NN1 8.6 0 0 0 2 0 -0.5 0
NN1 8.7 0 0 0 2 0 -0.5 0
NN1 8.8 0 0 0 2 0 -0.5 0
NN1 8.9 0 0 0 2 0 -0.5 0
NN1 9 0 0 0 2 0 -0.5 0
NN1 9.1 0 0 0 2 0 -0.5 0
NN1 9.2 0 0 0 2 0 -0.5 0
NN1 9.3 0 0 0 2 0 -0.5 0
NN1 9.4 0 0 0 2 0 -0.5 0
NN1 9.5 0 0 0 2 0 -0.5 0
NN1 9.6 0 0 0 2 0 -0.5 0
NN1 9.7 0 0 0 2 0 -0.5 0
NN1 9.8 0 0 0 2 0 -0.5 0
NN1 9.9 0 0 0 2 0 -0.5 0
NN1 10 0 0 0 2 0 -0.5 0
NN1 10.1 0 0 0 2 0 -0.5 0
NN1 10.2 0 0 0 2 0 -0.5 0
NN1 10.3 0 0 0 2 0 -0.5 0
NN1 10.4 0 0 0 2 0 -0.5 0
```

```
NN1 10.5 0 0 0 2 0 -0.5 0
NN1 10.6 0 0 0 2 0 -0.5 0
NN1 10.7 0 0 0 2 0 -0.5 0
NN1 10.8 0 0 0 2 0 -0.5 0
NN1 10.9 0 0 0 2 0 -0.5 0
NN1 11 0 0 0 2 0 -0.5 0
NN1 12 0 0 0 0 0 -0.5 0
```

Test Procedure File for Static Friction Test.

```
D time Vx Vy Vth w Fx Fy Tth
NN1 2 0 0 0 0 0 0 0
NN2 2.1 0 0 0 0.05 0 0 0
NN3 2.2 0 0 0 0.1 0 0 0
NN4 2.3 0 0 0 0.15 0 0 0
NN5 2.4 0 0 0 0.2 0 0 0
NN6 2.5 0 0 0 0.25 0 0 0
NN7 2.6 0 0 0 0.3 0 0 0
NN8 2.7 0 0 0 0.35 0 0 0
NN9 2.8 0 0 0 0.4 0 0 0
NN10 2.9 0 0 0 0.45 0 0 0
NN10 3 0 0 0 0.5 0 0 0
NN10 3.1 0 0 0 0.55 0 0 0
NN10 3.2 0 0 0 0.6 0 0 0
NN10 3.3 0 0 0 0.65 0 0 0
NN10 3.4 0 0 0 0.7 0 0 0
NN10 3.5 0 0 0 0.75 0 0 0
NN10 3.6 0 0 0 0.8 0 0 0
NN10 3.7 0 0 0 0.85 0 0 0
NN10 3.8 0 0 0 0.9 0 0 0
NN10 3.9 0 0 0 0.95 0 0 0
NN10 4 0 0 0 1 0 0 0
NN10 4.1 0 0 0 1.05 0 0 0
NN10 4.2 0 0 0 1.1 0 0 0
NN10 4.3 0 0 0 1.15 0 0 0
NN10 4.4 0 0 0 1.2 0 0 0
NN10 4.5 0 0 0 1.25 0 0 0
NN10 4.6 0 0 0 1.3 0 0 0
NN10 4.7 0 0 0 1.35 0 0 0
NN10 4.8 0 0 0 1.4 0 0 0
NN10 4.9 0 0 0 1.45 0 0 0
NN10 5 0 0 0 1.5 0 0 0
NN10 5.1 0 0 0 1.55 0 0 0
NN10 5.2 0 0 0 1.6 0 0 0
NN10 5.3 0 0 0 1.65 0 0 0
NN10 5.4 0 0 0 1.7 0 0 0
NN11 5.5 0 0 0 1.75 0 0 0
NN12 5.6 0 0 0 1.8 0 0 0
NN12 5.7 0 0 0 1.85 0 0 0
NN10 5.8 0 0 0 1.9 0 0 0
NN11 5.9 0 0 0 1.95 0 0 0
NN12 6 0 0 0 2 0 0 0
NN12 6.1 0 0 0 2.05 0 0 0
NN10 6.2 0 0 0 2.1 0 0 0
NN11 6.3 0 0 0 2.15 0 0 0
NN12 6.4 0 0 0 2.2 0 0 0
NN12 6.5 0 0 0 2.25 0 0 0
NN10 6.6 0 0 0 2.3 0 0 0
NN11 6.7 0 0 0 2.35 0 0 0
NN12 6.8 0 0 0 2.4 0 0 0
NN12 6.9 0 0 0 2.45 0 0 0
NN10 7 0 0 0 2.5 0 0 0
NN11 7.1 0 0 0 2.55 0 0 0
NN12 7.2 0 0 0 2.6 0 0 0
NN12 7.3 0 0 0 2.65 0 0 0
NN10 7.4 0 0 0 2.7 0 0 0
NN11 7.5 0 0 0 2.75 0 0 0
NN12 7.6 0 0 0 2.8 0 0 0
NN12 7.7 0 0 0 2.85 0 0 0
NN10 7.8 0 0 0 2.9 0 0 0
NN11 7.9 0 0 0 2.95 0 0 0
NN12 8 0 0 0 3 0 0 0
NN13 9 0 0 0 0 0 0 0
```

A.0.16 Design Equations for SWEET

All dimensions in cm.

$$\alpha_1 := \frac{\pi}{3} \quad \beta := 0 \quad r := 6$$

$$\alpha_2 := \pi \quad \theta := 0 \quad R_\theta := \begin{pmatrix} \cos(\theta) & \sin(\theta) & 0 \\ -\sin(\theta) & \cos(\theta) & 0 \\ 0 & 0 & 1 \end{pmatrix}$$

$$\alpha_3 := \frac{-\pi}{3} \quad \gamma := \frac{\pi}{4} \quad \text{length} := .30$$

$$J_{1f} := \begin{bmatrix} \sin(\alpha_1 + \beta + \gamma) & -\cos(\alpha_1 + \beta + \gamma) & -\cos(\beta + \gamma) \\ \sin(\alpha_2 + \beta + \gamma) & -\cos(\alpha_2 + \beta + \gamma) & -\cos(\beta + \gamma) \\ \sin(\alpha_3 + \beta + \gamma) & -\cos(\alpha_3 + \beta + \gamma) & -\cos(\beta + \gamma) \end{bmatrix} \cdot \begin{pmatrix} 1 & 0 & 0 \\ 0 & 1 & 0 \\ 0 & 0 & \text{length} \end{pmatrix}$$

$$C_1 := \begin{pmatrix} \cos(\alpha_1 + \beta + \gamma) & \sin(\alpha_1 + \beta + \gamma) & \text{length} \cdot \sin(\beta + \gamma) \\ \cos(\alpha_2 + \beta + \gamma) & \sin(\alpha_2 + \beta + \gamma) & \text{length} \cdot \sin(\beta + \gamma) \\ \cos(\alpha_3 + \beta + \gamma) & \sin(\alpha_3 + \beta + \gamma) & \text{length} \cdot \sin(\beta + \gamma) \end{pmatrix} \quad \begin{array}{l} J_{1f} \text{ is the rolling matrix} \\ C_1 \text{ is the sliding matrix} \end{array}$$

$$C_1 = \begin{pmatrix} -0.259 & 0.966 & 0.212 \\ -0.707 & -0.707 & 0.212 \\ 0.966 & -0.259 & 0.212 \end{pmatrix} \quad J_{1f} = \begin{pmatrix} 0.966 & 0.259 & -0.212 \\ -0.707 & 0.707 & -0.212 \\ -0.259 & -0.966 & -0.212 \end{pmatrix}$$

$$\text{trans} := R_\theta^{-1} \cdot J_{1f}^{-1} \quad T := R_\theta \cdot J_{1f}$$

$$\text{trans} = \begin{pmatrix} 0.644 & -0.471 & -0.173 \\ 0.173 & 0.471 & -0.644 \\ -1.571 & -1.571 & -1.571 \end{pmatrix} \quad T = \begin{pmatrix} 0.966 & 0.259 & -0.212 \\ -0.707 & 0.707 & -0.212 \\ -0.259 & -0.966 & -0.212 \end{pmatrix}$$

want to know the max rpm for 25 cm/sec speed in X or Y direction:

$$X_{\text{matrix}} := \begin{pmatrix} 25 \\ 0 \\ 0 \end{pmatrix} \quad \text{phi} := \frac{R_\theta \cdot J_{1f} \cdot X_{\text{matrix}}}{r}$$

$$\text{phi} = \begin{pmatrix} 4.025 \\ -2.946 \\ -1.078 \end{pmatrix} \quad \text{phi}_{\text{rpm}} := \frac{60 \cdot \text{phi}}{2 \cdot \pi}$$

$$\text{phi}_{\text{rpm}} = \begin{pmatrix} 38.433 \\ -28.135 \\ -10.298 \end{pmatrix} \quad \begin{array}{l} \text{Motors need to be capable of rpm from -40 to +40} \\ \text{With } \gamma = 45 \end{array}$$

All dimensions in cm.

$$\alpha_1 := \frac{\pi}{3} \quad \beta := 0 \quad r := 6$$

$$\alpha_2 := \pi \quad \theta := 0 \quad R_\theta := \begin{pmatrix} \cos(\theta) & \sin(\theta) & 0 \\ -\sin(\theta) & \cos(\theta) & 0 \\ 0 & 0 & 1 \end{pmatrix}$$

$$\alpha_3 := \frac{-\pi}{3} \quad l := .30 \quad | = \text{length wheels are from center}$$

$$J_{1f} := \begin{bmatrix} \sin(\alpha_1 + \beta + \gamma) & -\cos(\alpha_1 + \beta + \gamma) & -l \cdot \cos(\beta + \gamma) \\ \sin(\alpha_2 + \beta + \gamma) & -\cos(\alpha_2 + \beta + \gamma) & -l \cdot \cos(\beta + \gamma) \\ \sin(\alpha_3 + \beta + \gamma) & -\cos(\alpha_3 + \beta + \gamma) & -l \cdot \cos(\beta + \gamma) \end{bmatrix} \quad J_{1f} \text{ is the rolling matrix}$$

$$C_1 := \begin{pmatrix} \cos(\alpha_1 + \beta + \gamma) & \sin(\alpha_1 + \beta + \gamma) & l \cdot \sin(\beta + \gamma) \\ \cos(\alpha_2 + \beta + \gamma) & \sin(\alpha_2 + \beta + \gamma) & l \cdot \sin(\beta + \gamma) \\ \cos(\alpha_3 + \beta + \gamma) & \sin(\alpha_3 + \beta + \gamma) & l \cdot \sin(\beta + \gamma) \end{pmatrix} \quad C_1 \text{ is the sliding matrix}$$

$$C_1 = \begin{pmatrix} 0.5 & 0.866 & 0 \\ -1 & 0 & 0 \\ 0.5 & -0.866 & 0 \end{pmatrix} \quad J_{1f} = \begin{pmatrix} 0.866 & -0.5 & -0.3 \\ 0 & 1 & -0.3 \\ -0.866 & -0.5 & -0.3 \end{pmatrix}$$

$$\text{trans} := R_\theta^{-1} \cdot J_{1f}^{-1} \quad T := R_\theta \cdot J_{1f}$$

$$\text{trans} = \begin{pmatrix} 0.577 & 0 & -0.577 \\ -0.333 & 0.667 & -0.333 \\ -1.111 & -1.111 & -1.111 \end{pmatrix} \quad T = \begin{pmatrix} 0.866 & -0.5 & -0.3 \\ 0 & 1 & -0.3 \\ -0.866 & -0.5 & -0.3 \end{pmatrix}$$

want to know the max rpm for 25 cm/sec speed in X or Y direction:

$$X_{\text{matrix}} := \begin{pmatrix} 25 \\ 0 \\ 0 \end{pmatrix} \quad \text{phi} := \frac{R_\theta \cdot J_{1f} \cdot X_{\text{matrix}}}{r}$$

$$\text{phi} = \begin{pmatrix} 3.608 \\ 0 \\ -3.608 \end{pmatrix} \quad \text{phi}_{\text{rpm}} := \frac{60 \cdot \text{phi}}{2 \cdot \pi}$$

$$\text{phi}_{\text{rpm}} = \begin{pmatrix} 34.458 \\ 4.873 \times 10^{-15} \\ -34.458 \end{pmatrix} \quad \text{Motors need to be capable of rpm from -35 to +35} \\ \text{With omnidirectional wheels } \gamma = 0$$

Torque requirements:

table weight = TW
 table radius = Tr
 Fine Sand Density = rho.sand
 Sandstone density = rho.stone
 Avg depth of medium = d
 Aluminum density = rho alum
 Table aluminum thickness = Tt

$$Tr := 68.58\text{cm}$$

$$\rho_{\text{sand}} := 1201 \frac{\text{kg}}{\text{m}^3}$$

$$\rho_{\text{stone}} := 2323 \frac{\text{kg}}{\text{m}^3}$$

$$d := 15.\text{cm}$$

$$\rho_{\text{alum}} := 2560 \frac{\text{kg}}{\text{m}^3}$$

$$Tt := 2\text{cm}$$

$$r := 6\text{cm}$$

$$TW := \pi \cdot Tr^2 \cdot Tt \cdot \rho_{\text{alum}} + \pi \cdot Tr^2 \cdot d \cdot \frac{(\rho_{\text{sand}} + \rho_{\text{stone}})}{2}$$

$$TW = 466.17 \text{ kg}$$

$$MA = F = \text{torque} \quad \text{acc} := 25 \frac{\text{cm}}{\text{sec}^2}$$

$$F_x := TW \cdot \text{acc}$$

$$F_y := 0\text{N}$$

$$\tau_{\theta} := 0 \cdot \text{N} \cdot \text{m}$$

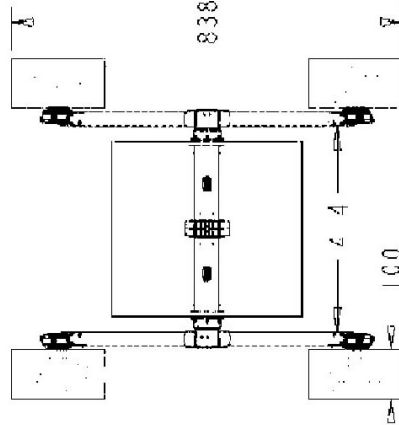
$$F := \begin{pmatrix} F_x \\ F_y \\ \tau_{\theta} \\ r \end{pmatrix}$$

$$\tau := r \cdot J_{1f} \cdot R_{\theta} \cdot F$$

$$\tau = \begin{pmatrix} 6.056 \\ 0 \\ -6.056 \end{pmatrix} \text{J}$$

Worst case rotational torque needed:

SR2



Max speed 25 cm/sec

$$V := 25 \frac{\text{cm}}{\text{sec}} \quad \text{rotcenter} := 43\text{cm}$$

Component of V perp to center rot

$$V_t := V \cdot \sin\left(43 \cdot \frac{\pi}{180}\right) \quad V_t = 0.17 \frac{\text{m}}{\text{s}}$$

Rotation around center

$$\omega := \frac{V_t}{\text{rotcenter}} \quad \omega = 0.397 \frac{\text{rad}}{\text{sec}}$$

$\omega_t :=$

$$X := \begin{pmatrix} 0 \\ 0 \\ \omega_t \end{pmatrix}$$

$$\text{phi} := \frac{J_{1f} \cdot R_{\theta} \cdot X}{r} \quad \text{phi}_{\text{rpm}} := \frac{60 \cdot \text{phi}}{2 \cdot \pi} \quad \gamma = 0$$

$$\text{phi} = \begin{pmatrix} -2.5 \\ -2.5 \\ -2.5 \end{pmatrix} \frac{1}{\text{ms}} \quad \text{phi}_{\text{rpm}} = \begin{pmatrix} -23.873 \\ -23.873 \\ -23.873 \end{pmatrix} \frac{1}{\text{ms}} \quad \text{units are screwed up due to mathcad not letting me put in differing units in one matrix}$$

The values for ω for worst case spinning are within the max for worst case linear motion.

What about torque for worst case: Where table is all the way to one side and it is spinning with $\alpha = .5 \text{ rad/sec}^2$ and is moving in the X direction at full acceleration.

$$I := \frac{1}{2} \cdot TW \cdot Tr^2 + TW \cdot (Tr)^2 \quad l := 30\text{cm} \quad \alpha := .5 \frac{\text{rad}}{\text{sec}^2}$$

$$\text{acc} := .25 \frac{\text{m}}{\text{sec}^2}$$

$$F_x := \text{acc} \cdot TW$$

$$F_y := 0\text{N} \quad \tau_\theta := I \cdot \alpha \quad \tau_\theta = 164.437 \text{ J}$$

$$F := \begin{pmatrix} F_x \\ F_y \\ \frac{\tau_\theta}{r} \end{pmatrix} \quad F_x = 116.542 \text{ N}$$

$$\tau := r \cdot J_{1f} \cdot R_\theta \cdot F$$

$$\tau = \begin{pmatrix} -43.275 \\ -49.331 \\ -55.387 \end{pmatrix} \text{ J} \quad 500 \text{ inch} \cdot \text{pounds of torque}$$

Need to go with smaller table or put les on it.